

**MONITORING THE METABOLISM OF THIOLS/DISULFIDES IN THE
EXTRACELLULAR SPACE OF ORGANOTYPIC HIPPOCAMPAL SLICE CULTURES
BY ONLINE MICROFLUIDIC ANALYSIS COUPLED WITH ELECTROOSMOTIC
SAMPLING**

by

Juanfang Wu

B.S. Chemistry, Tongji University, 2003

M.S. Chemistry, Tsinghua University, 2006

Submitted to the Graduate Faculty of

The Dietrich School of Arts and Sciences

in partial fulfillment of the requirements for the degree of

Doctor of Philosophy

University of Pittsburgh

2013

UNIVERSITY OF PITTSBURGH
THE DIETRICH SCHOOL OF ARTS AND SCIENCES

This dissertation was presented

by

Juanfang Wu

It was defended on

June 25th, 2013

and approved by

Xinyu Liu, Assistant Professor, Department of Chemistry

Adrian Michael, Professor, Department of Chemistry

Valerian Kagan, Professor, Department of Environmental and Occupational Health

Dissertation Advisor: Stephen G. Weber, Professor, Department of Chemistry

Copyright © by Juanfang Wu

2013

Reproduced with permission from

Wu, J.; Ferrance J.P.; Landers, J.P.; Weber, S.G., *Anal. Chem.* 2010, 82(17):7267-7273

Wu, J.; Xu, K.; Landers, J.P.; Weber, S.G., *Anal. Chem.* 2013, 85 (6), 3095-3103

**MONITORING THE METABOLISM OF THIOLS/DISULFIDES IN THE
EXTRACELLULAR SPACE OF ORGANOTYPIC HIPPOCAMPAL SLICE
CULTURES BY ONLINE MICROFLUIDIC ANALYSIS COUPLED WITH
ELECTROOSMOTIC SAMPLING**

Juanfang Wu, PhD

University of Pittsburgh, 2013

Sulfur-containing compounds, such as glutathione (GSH), cysteamine (CSH), homocysteine (Hcy), cysteine (Cys) and their disulfides, are critical for maintaining various cellular functions. Concentration profiles of these compounds in biological samples are useful for evaluating cellular physiological status and diagnosing diseases. Traditional quantitative methods involve tedious sample pretreatment and are not suited to dealing with submicroliter samples. We have developed a microfluidic system for online analysis of thiol-containing compounds in the extracellular space of rat organotypic hippocampal slices cultures (OHSCs). This system is also capable of monitoring ectoenzymatic activity involved in the metabolism of thiols/disulfides.

A microfluidic chip capable of derivatization, multiple injection, separation, and quantitation was designed and coupled to a homemade confocal laser induced fluorescence detector with a multifunctional control program. The microfluidic system was evaluated in an on-chip kinetic study of the reduction of oxidized glutathione (GSSG) catalyzed by glutathione reductase (GR, EC 1.8.1.7) followed by derivatization of GSH with ThioGlo-1. The separation of analytes was successfully achieved within 4.5 s and 9 mm separation length. The linear range of

the system is up to 50 μM (GSH). The mass and concentration detection limits are 10^{-18} mol and 4.2 nM, respectively. Based on GSH growth rates, the apparent Michaelis constants of GR were determined to be 40 ± 11 μM (GSSG) and 4.4 ± 0.6 μM (β -NADPH). Electroosmotic sampling of the extracellular fluid of OHSCs was further coupled to a microfluidic device for *in situ* quantitation of endogenous aminothiols in OHSCs, by which CSH (10.6 ± 1.0 nM), Hcy (0.18 ± 0.01 μM) and Cys (11.1 ± 1.2 μM) were separated and evaluated simultaneously. Using this method, we also observed the complete biodegradation of coenzyme A (CoA) in the extracellular space of OHSCs and determined the kinetic parameters of this sequential multi-enzyme reaction in *in situ*. Metabolism of cystamine (CSSC) and pantethine (PSSP) in OHSCs have also been investigated and the percentage yields of CSH from CSSC and PSSP after ~ 55 s exposure time to OHSCs were $91\% \pm 4\%$ and $0.01\% - 0.03\%$, respectively, which explains the differences of the drugs in clinical effectiveness and toxicity.

TABLE OF CONTENTS

PREFACE.....	XVII
1.0 INTRODUCTION.....	1
1.1 FUNCTIONS AND METABOLISM OF AMINOTHIOLS	2
1.1.1 Biological functions of GSH/GSSG	2
1.1.2 Metabolism of GSH/GSSG	3
1.1.3 Biological functions of CoA and Cys/cystine.....	6
1.1.4 Metabolism of CoA and Cys/cystine	8
1.2 CURRENT METHODS FOR DETERMINATION OF AMINOTHIOLS .	11
1.2.1 Sample collection and pretreatment	11
1.2.2 Separation based methods	13
1.2.3 Non-separation based methods.....	16
1.3 MICROFLUIDIC DEVICES WITH CONFOCAL LASER-INDUCED FLUORESCENCE DETECTION	17
1.3.1 Theory of miniaturization.....	17
1.3.2 Confocal laser induced fluorescence (LIF) detection	22
1.3.3 Microfluidic chip and thiols determination.....	25
2.0 DEVELOPMENT OF A CONFOCAL LASER INDUCED FLUORESCENCE DTECTION SYSTEM.....	27

2.1	OPTIMIZATION OF OPTICAL COMPONENTS OF THE CONFOCAL LIF DETECTOR	28
2.1.1	Laser	28
2.1.2	Microscope objective	32
2.1.3	Photon detector	34
2.1.4	Filter set, lens and mirrors.....	38
2.2	DESIGN AND ASSEMBLY OF AN OPTO-MECHANICAL SYSTEM.....	40
2.3	DEVELOPMENT OF A CONTROL PROGRAM USING LABVIEW	44
2.4	SYSTEM OPTIMIZATION AND PRELIMINARY EXPERIMENTS.....	50
2.4.1	Beam alignment	50
2.4.2	Laser beam profile measurement.....	53
2.4.3	Noise experiments and system performance testing.....	61
2.4.3.1	Noise sources.....	61
2.4.3.2	Identification of different noise sources	63
2.4.3.3	Noise reduction	68
2.4.3.4	System performance testing	78
3.0	ON-CHIP MONITORING OF THE REDUCTION OF OXIDIZED GLUTATHIONE BY GLUTATHIONE REDUCTASE.....	81
3.1	INTRODUCTION	82
3.2	EXPERIMENTAL SECTION.....	84
3.2.1	Chemicals and reagents.....	84
3.2.2	Design and fabrication of the microfluidic chip	85
3.2.3	Reaction between ThioGlo-1 and GSH.....	87

3.2.4	Enzyme kinetics measurement	88
3.3	RESULTS AND DISCUSSION	89
3.3.1	Derivatization of GSH with ThioGlo-1	89
3.3.2	Microfluidic capillary electrophoresis	94
3.3.3	Enzyme kinetic study	99
3.4	CONCLUSIONS	104
4.0	AN <i>IN SITU</i> MEASUREMENT OF EXTRACELLULAR AMINOTHIOLS IN OHSCS BY INTEGRATION OF ELECTROOSMOTIC SAMPLING AND MICROFLUIDIC ANALYSIS	106
4.1	INTRODUCTION	107
4.2	EXPERIMENTAL SECTION.....	110
4.2.1	Chemicals and reagents.....	110
4.2.2	Design of a microfluidic chip coupled with electroosmotic sampling	111
4.2.3	Instrumentation	113
4.2.4	Optimization of the separation conditions for aminothiols	114
4.2.5	OHSCs preparation and characterization	115
4.2.6	Measurement of extracellular aminothiols in OHSCs using single capillary mode	116
4.2.7	Electroosmotic sampling from OHSCs using dual-capillary.....	117
4.3	RESULTS AND DISCUSSION	120
4.3.1	Optimization of separation conditions of aminothiols for microfluidic analysis	120
4.3.2	Microfluidic analysis of samples with high conductivity	125

4.3.3	High sample conductivity affects flow-gated sample injection analysis of samples	126
4.3.4	The function of an auxiliary channel in integrating electroosmotic sampling and microfluidic analysis	133
4.3.5	The effect of electroosmotic sampling conditions on OHSCs	134
4.3.6	Evaluation of the extracellular Cys, Hcy, and CSH concentration in OHSCs.....	135
4.3.7	Comparison of single and dual capillary modes in electroosmotic sampling	140
4.4	CONCLUSIONS	150
5.0	TRACKING THE METABOLISM OF TWO DRUG COMPOUNDS AND COA IN OHSCS.....	151
5.1	INTRODUCTION	152
5.2	EXPERIMENTAL SECTION.....	156
5.2.1	Chemicals and reagents.....	156
5.2.2	Preparation of OHSCs	157
5.2.3	Microfluidic chip design and instrumentation.....	157
5.2.4	Online sampling experiments	159
5.3	RESULTS AND DISCUSSION	160
5.3.1	Calibration and quantitation.....	160
5.3.2	CSSC is converted more rapidly than PSSP to CSH	165
5.3.3	Enzymatic degradation of CoA: CSH.....	170
5.3.4	Enzymatic degradation of CoA: PSH	174

5.4 CONCLUSIONS	176
APPENDIX A	178
APPENDIX B	182
APPENDIX C	184
APPENDIX D	186
APPENDIX E	190
APPENDIX F	192
APPENDIX G	194
BIBLIOGRAPHY	195

LIST OF TABLES

Table 1. Proportionalities of mechanical parameters in relation to the characteristic length l	21
Table 2. Main parameters of BCL-020-405-CL2005 DPSS laser	31
Table 3. Main parameters of LUCPLFLN 40x objective	34
Table 4. Main parameters of H5784-01 PMT module.....	37
Table 5. Main parameters of the emission filter	40
Table 6. Main parameters for data collection	45
Table 7. Connection between levels of DIOs and the state of the state of the electrode	46
Table 8. Gaussian fitting results for three measurements	58
Table 9. Equations and parameters for nonlinear curve fitting of the beam width and D_z	59
Table 10. Environmental noises experiment.....	64
Table 11. rms noise from different background sources.....	65
Table 12. Scattering experiment	65
Table 13. Laser beam and PMT stability analysis	66
Table 14. Signal averaging experiment	70
Table 15. Low pass filter experiment	73
Table 16. Vibration experiment	74
Table 17. Effect of signal averaging for the new system.....	76
Table 18. Effect of the low pass filter for the new system	77

Table B-1. Parameters and results for the standard addition method 182

Table F-1. Linear fitting results for the calibration curves of CSH, Hcy and Cys 193

LIST OF FIGURES

Figure 1. Metabolism of GSH in cell.....	4
Figure 2. Metabolic interactions between astrocytes and neurons in GSH metabolism.....	5
Figure 3. GSH pathways in the detoxification of ROS.....	6
Figure 4. Biosynthesis and biodegradation of CoA.....	9
Figure 5. Cys metabolic pathway.....	10
Figure 6. Structures of common derivatizing agents	14
Figure 7. Sketch of a typical confocal LIF detector.....	24
Figure 8. Excitation and emission spectra of GSH labeled with ThioGlo-1	30
Figure 9. Schematic view of the confocal LIF system.....	41
Figure 10. Top view of aluminum platform of stage A	42
Figure 11. Top view of the platform of stage C.....	43
Figure 12. Photograph of the confocal LIF detector.....	44
Figure 13. Setup of three DIOs and two HV relays for a single HV output channel	46
Figure 14. Screenshot of the user interface of “MAS LAB”	50
Figure 15. Sketch of the microfluidic chip for simple tests.....	52
Figure 16. Setup of two iris diaphragms in the parallel alignment.....	53
Figure 17. Setup for the laser beam profile measurement	54
Figure 18. Results from laser beam profile measurements at different D_z	58

Figure 19. Nonlinear curve fitting of the beam width to D_z	60
Figure 20. Various rms noise sources for a photoluminescence measurement	62
Figure 21. Relationship between E_t/σ_t and E_t when noises are contributed by laser and PMT ..	67
Figure 22. Photograph of the microfluidic chip during the experiment	68
Figure 23. Results from signal averaging experiment	70
Figure 24. FFT results showing the effect of low pass filter with different cutoff frequency	73
Figure 25. FFT results showing the effect of racquetballs in the vibration experiment	74
Figure 26. Effect of averaging for the new system	77
Figure 27. FFT results showing the effect of low pass filter with different cutoff frequency	78
Figure 28. Relationship between the fluorescence intensity and (a) PMT control voltage and (b) laser power	80
Figure 29. Linearity between fluorescence signal and analyte concentration	80
Figure 30. Layout of the microfluidic chip used for enzyme analysis.....	87
Figure 31. Reaction between ThioGlo-1 and thiols	89
Figure 32. pH effect on the reaction of ThioGlo-1 and GSH	90
Figure 33. Change of RFU with time for the reaction of ThioGlo-1 and GSH	91
Figure 34. Kinetic experiments for GSH and ThioGlo-1	92
Figure 35. Global linear fitting of the data from seventeen kinetic curves.....	93
Figure 36. Effect of 1, 6-diaminohexane on the separation of PFH, ThioGlo-1 and GSH*	96
Figure 37. Effect of 1, 6-diaminohexane in reagent reservoir on the enzyme kinetic analysis	98
Figure 38. Electropherograms for on-chip enzyme kinetic study.....	101
Figure 39. Calibration curve established based on the relative peak area of GSH*	102
Figure 40. Lineweaver-Burk plots to determine the enzyme kinetic parameters	104

Figure 41. Layout of the microfluidic chip and single capillary electroosmotic sampling	113
Figure 42. Schematic views of single and dual capillary modes in the electroosmotic sampling	119
Figure 43. Separation of aminothiols mixtures using 20 mM Tris-HCl buffers at pH 7.5 and 8.0	121
Figure 44. Separation of aminothiols mixtures using 20 mM Bis-Tris propane buffers with various pH.....	123
Figure 45. Effect of Bis-Tris propane concentrations on the separation of aminothiols mixtures at pH 8.0.....	124
Figure 46. Effect of 1, 6-diaminohexane on the separation of aminothiols mixtures.....	124
Figure 47. Viability assessment for OHSCs	126
Figure 48. Effect of buffer conductivity on the flow-gated injection	128
Figure 49. Concentrations, conductivities and velocities during injection.....	132
Figure 50. Effect of auxiliary channel on the relative ThioGlo-1 concentration.....	134
Figure 51. Electropherogram of analytes from electroosmotic sampling of OHSCs	136
Figure 52. Reconstructed plot of PMT reading vs time for all injection in one run.....	137
Figure 53. Hcy peak height vs injection # in a single run.....	139
Figure 54. Electrophoretic behavior of GSH	142
Figure 55. Single capillary sampling through membrane of the standing insert placed in the Petri dish.....	143
Figure 56. Single capillary sampling from CA3 of OHSCs	144
Figure 57. Dual capillary sampling directly from solution in Petri dish	145
Figure 58. Comparison of two cases in dual capillary electroosmotic sampling from OHSCs..	148

Figure 59. Dual capillary electroosmotic sampling from OHSCs	149
Figure 60. Proposed CoA biodegradation pathways.....	154
Figure 61. Sketch of the microfluidic device integrated with online electroosmotic sampling .	159
Figure 62. Simulated electric field and current density in both OHSC and sampling capillary during online perfusion experiment.	161
Figure 63. Progress curves for CSH and PSH based on peak heights and migration times	162
Figure 64. Inhibition of the pantetheinase by 8-cyclopentyl-1, 3-dipropylxanthine (DPCPX)..	164
Figure 65. The formation of CSH from CSSC and PSSP through disulfide exchange and catalysis by pantetheinase.....	165
Figure 66. Series of electropherograms obtained from online sampling in the CA3 region of OHSCs	167
Figure 67. The conversion of drug compounds in the CA3 region of OHSCs during electroosmotic sampling	169
Figure 68. Electropherograms obtained from online electroosmotic sampling of the CA3 region in OHSCs	172
Figure 69. Representative electropherograms from online electroosmotic sampling of the CA3 region in OHSCs	172
Figure 70. Michaelis-Menten fittings based on CSH and PSH	174
Figure A-1. Equivalent circuit of the microfluidic chip	178
Figure B-1. Calibration curves used in the standard addition method for CSH, Hcy and Cys...	183
Figure C-1. Estimation the tissue volume being sampled.....	184
Figure D-1. Plot of plateau peak height, H, as a function of peak height growth rate, dH/dt	189
Figure F-1. Calibration curves CSH, Hcy and Cys.....	192

PREFACE

I would like to thank my advisor, Dr. Stephen G. Weber for his guidance and for offering me the exciting opportunity to carry out this project and pursue my doctoral degree in his laboratory. He patiently discussed with me and guided me whenever I met problems in research. It is a great pleasure to have such a great chance to be his student. I would like to thank Dr. Jerome Ferrance at the University of Virginia for giving me many useful and valuable suggestions in designing the confocal laser induce fluorescence detection system. He also shared with me a lot of helpful experiences in working with microfluidic devices. I am also gratefully to Dr. James Landers' lab at the University of Virginia for making glass chips. I would like to express my gratitude to my committee members, Prof. Valerian Kagan, Prof. Xinyu Liu and Prof. Adrian Michael for their kind assistance in helping me to prepare this dissertation. I would like to thank past and current members of the Weber group for their supports during my research and stay in Pittsburgh. I would also like to thank my family and their continuous support. I thank all the staff in electronic shop and machine shop for their assistant in building detection system. In addition, I would like to thank National Institute of Health for generous financial support.

1.0 INTRODUCTION

A portion of this work is adapted from the master's thesis "*Online determination of extracellular glutathione in organotypic hippocampal slice cultures with a microfluidic device and confocal laser-induced fluorescence detection system*", Juanfang Wu (2010)

Sulfur-containing compounds, such as glutathione (GSH), cysteamine (CSH), homocysteine (Hcy) and cysteine (Cys), are critical for maintaining various cellular functions.¹ Each of these molecules contributes to the cellular pool of organic sulfur and sulfur homeostasis.² Changes in the plasma or urine concentration of these compounds and their oxidized disulfide forms are indications of diseases or cellular dysfunction.¹ Current methods for determination of these aminothiols from a variety of biological samples are reviewed in the following section. The integration of sampling, sample transport, and microfluidic analysis will increase automation, improve sample integrity, reduce sample dilution, and reduce cost in time and reagents in the determination of aminothiols. More importantly, such integration makes possible online monitoring of target analytes and reactions with minimal delay and excellent time resolution, which is a necessary step towards the ultimate goal of understanding dynamic changes in living systems.

1.1 FUNCTIONS AND METABOLISM OF AMINOTHIOLS

1.1.1 Biological functions of GSH/GSSG

Adult human brain cells use ~20% of the oxygen needed by the body, which generates reactive oxygen species (ROS) at a high rate through oxidative metabolism.³ Compared with other organs, brain is especially vulnerable to ROS because it is rich in lipids with unsaturated fatty acids.⁴ Maintaining brain functions relies on an effective antioxidant system.⁴ GSH (γ -GluCysGly) is a well-known antioxidant.⁵⁻⁷ GSH and its oxidized form, GSSG, are the most abundant intracellular low molecular weight thiol/disulfide couple.^{8,9} The cytosolic GSH concentration in astrocyte cultures is up to 8 mM,^{10,11} which is higher than the GSH concentration in neurons (0.1-4 mM).^{12,13} In contrast, the intracellular GSSG concentration is less than 1% of that of GSH.^{14,15} Generally, the physiological redox potential (E_h) for GSH/GSSG couple ranges from -260 mV to -150 mV in cells depending on different cellular status, such as proliferation, differentiation and apoptosis.¹⁶ The redox potential of GSH is usually used as an *in vivo* indicator of oxidative stress.¹⁶ GSH can react with ROS directly or with the help of enzymes.³ It works together with other antioxidants, such as ascorbate and α -tocopherol to form a firm cellular defense system against reactive oxygen species (ROS) in brain.^{5,9,17-19} GSH also plays a key role in the detoxification of cellular xenobiotics.^{4,20} GSH is a cofactor in isomerization reactions and a safe form for storing and transporting Cys.^{10,20,21} In addition, GSH is essential for regulating cell proliferation,²²⁻²⁴ apoptosis^{23,25-27} and maintenance of the thiol redox potential in cells.^{22,28}

Although the extracellular concentration of GSH in brain is in the low micromolar range, which is much lower than that in the intracellular space,^{29,30} this portion of GSH also has many functions in brain.¹⁰ Extracellular GSH released by astrocytes is the precursor of neural GSH

synthesis.^{3, 10, 31} GSH also acts as a detoxifying agent for toxic compounds such as glutamate by forming γ -glutamyl glutamate.³²⁻³⁴ In addition, GSH and γ -glutamyl peptides act as agonists and modulators of glutamate receptors (NMDA and AMPA) in brain.³⁵⁻³⁸ GSH is also involved in the metabolism of leukotrienes which have neuroendocrine and excitatory functions in brain.¹⁰ GSH released to extracellular space is also found to contribute to the GSH concentration in the cerebrospinal fluid.³⁹ The extracellular concentration of GSH is found to be elevated upon the onset of cerebral ischemia, which is effective in scavenging the ROS formed in the insulted brain tissue.^{30, 40, 41}

GSH has many biological functions and disturbing GSH metabolism and redox homeostasis can lead to a number of diseases.^{10, 31, 42-44} Monitoring the distributions and concentrations of GSH and related metabolites can provide valuable information regarding oxidative stresses and responses of biological samples. It will also facilitate the analysis of the enzyme activities and cellular interactions involved in GSH metabolism.

1.1.2 Metabolism of GSH/GSSG

The synthesis of GSH in brain cells the same way as in other tissues.³¹ The synthesis of GSH in the cytoplasm begins with the formation of the dipeptide γ -glutamylcysteine (γ GluCys) catalyzed by glutamate cysteine ligase (EC 6.3.2.2). This dipeptide reacts with glycine to generate GSH catalyzed by GSH synthase (EC 6.3.2.3) as shown in Fig. 1.^{10, 14, 21} Both steps are adenosine triphosphate (ATP)-consuming steps. Feedback inhibition of γ GluCys ligase by GSH controls the product's steady state concentration.⁴⁵

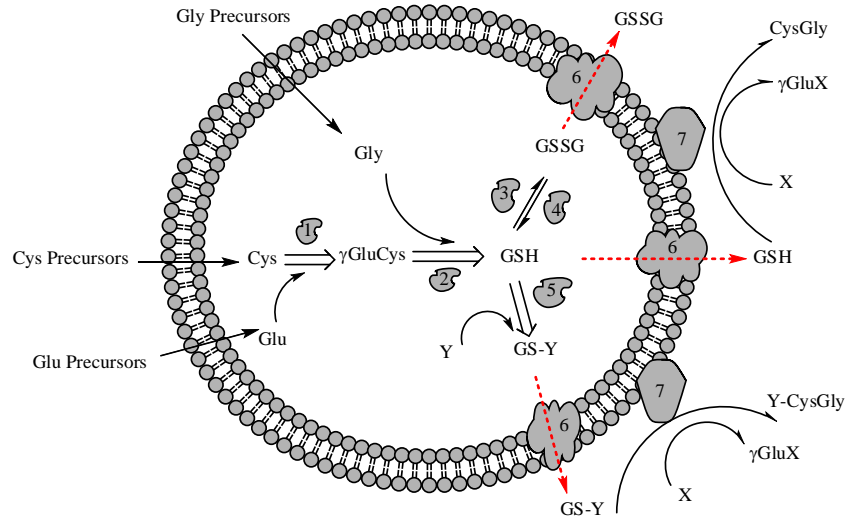


Figure 1. Metabolism of GSH in cell^{10, 31}

X represent acceptors of the γ -glutamyl moiety transferred by γ -glutamyl transpeptidase from glutathione. Y is a substrate of glutathione-S-transferase. 1-7 represent different enzymes involved in this metabolism cycle. 1. glutamate cysteine ligase; 2. glutathione synthase; 3. glutathione peroxidase; 4. glutathione reductase; 5. glutathione-S-transferase; 6. multidrug resistance proteins; 7. γ -glutamyl transpeptidase.

Astrocytes and neurons use different precursors to synthesize GSH in the cytosol.^{3, 46-48} Astrocytes prefer to use extracellular glutamate and cystine, the disulfide from the oxidation of Cys, as GSH precursors.⁴⁹ However, neurons can only use extracellular Cys as precursor.⁵⁰ and the best extracellular glutamate source for neurons is glutamine.⁵¹ Astrocytes can be a source of GSH for neurons as shown in Fig. 2.^{10, 31} GSH released from astrocytes will be first metabolized to CysGly by the ectoenzyme, γ -glutamyl transpeptidase (γ GT, EC. 2.3.2.2).³¹ CysGly cannot be taken up by neurons directly; instead it must be hydrolyzed by aminopeptidase N (ApN, EC 3.4.11.2) to Cys, which can be used for neuronal GSH synthesis.^{31, 52} As the concentration of Cys in the extracellular space is maintained at low concentration due to its toxicity, GSH synthesis in neurons strongly depends on the Cys provided by the neighboring astrocytes.^{10, 31} Neurons also

rely on the glutamine exported by astrocytes as a source of glutamate in neuronal GSH synthesis.³¹ Astrocytes play a key role in the defense of neurons against ROS by supplying the precursors for neuronal GSH synthesis.^{3, 19, 53}

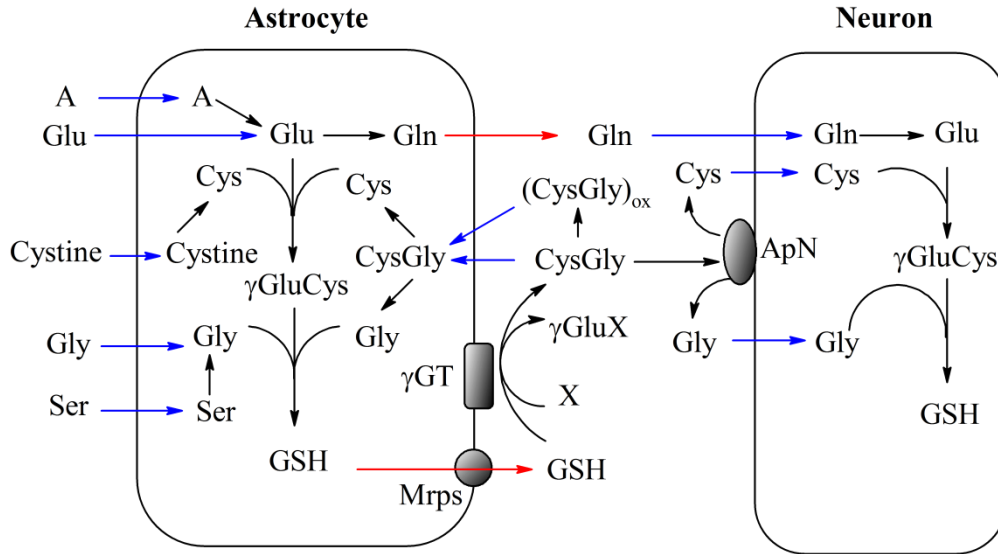


Figure 2. Metabolic interactions between astrocytes and neurons in GSH metabolism^{10, 31}

A represents amino acid to be metabolized by astrocytes to produce glutamate. X represents an acceptor of the γ -glutamyl moiety transferred by γ GT from GSH.

GSH is involved in several metabolic pathways.³ In the detoxification of ROS, GSH reacts directly with radicals or forms glutathione disulfide (GSSG) with peroxides under the catalysis of glutathione peroxidase (GPx, EC. 1.11.1.9) as shown in Fig. 3.^{3, 31} GSSG can be converted back into GSH intracellularly at the presence of NADPH by glutathione reductase (GR, EC 1.8.1.7),³ or exported out of the cells.³¹ GSH can also be conjugated with a variety of electrophilic xenobiotics to form less toxic and more hydrophilic GSH-S-conjugates by glutathione S-transferases (GSTs, EC 2.5.1.18).⁵⁴ These products can then be excreted from cells,⁵⁴⁻⁵⁶ and become the substrates of γ GT to form CysGly conjugates.¹⁰ Finally, intracellular

GSH can be directly released to the extracellular space,^{19, 33, 34, 57-60} although the release of GSH from brain cells has been reported mainly for astrocytes.^{31, 58} Under unstressed conditions, astrocytes release GSH but not GSSG.^{58, 61, 62} On the contrary, during oxidative stress, an effective release of GSSG has been reported as a mechanism of cellular self-defense.^{15, 63} Neurons, microglial cells and oligodendrocytes only excrete a marginal amount of GSH.⁶¹ The transporters that are in charge of the export of GSH, GSSG and GSH S-conjugates to the extracellular space are members of the family of multidrug resistance proteins (MRPs for human transporters; Mrps for the transporters of other species).^{31, 64}

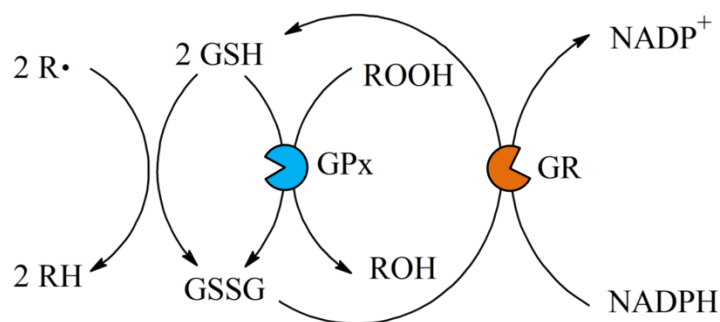


Figure 3. GSH pathways in the detoxification of ROS³

GSH reacts with radical (R•) directly and GSH reacts with peroxides (ROOH) catalyzed by GPx. The regeneration of GSH is achieved by glutathione reductase (GR) and cofactor NADPH.

1.1.3 Biological functions of CoA and Cys/cystine

Coenzyme A (CoA) is an essential cofactor for about 4% of all known enzymes.^{65, 66} In the intracellular space of animal tissues, CoA is distributed mainly in cytosol, mitochondria and peroxisomes with estimated concentrations of 0.02-0.14 mM, 2.2-5 mM and 0.7 mM, respectively.⁶⁵ CoA is an ideal acyl carrier and carbonyl-activating group due to its reactive thiol group in cells.^{65, 67} CoA is a cofactor of oxidative metabolism of carbon substrates and the synthesis of many cellular structural components.⁶⁸ The last product of CoA biodegradation,

CSH, exists in a relatively low concentration in the tissue.⁶⁹ It has been recognized as a vital source of taurine, the second most abundant amino acid in mammalian tissues.⁷⁰ It also plays an active role as a potent radio-protective agent against DNA-induced radiation damage, and a neuroprotective agent against neurodegenerative diseases.⁷¹ The endogenous concentration of free CSH in brain tissue homogenates is usually below the detection limits of the most sensitive detection methods (<10 nmol/L).^{69, 72-74} Development of analytical methods to measure the concentration of CSH in biological samples and its production rate through CoA biodegradation are vital for understanding its metabolic fate. This data is also critical for evaluating the kinetic parameters of the sequential multi-enzyme reactions involved in CoA catabolism.

Due to the efficient reduction of cystine to Cys by GSH in the intracellular space, cystine is maintained at very low concentration in normal cells.⁷⁵ Accumulation of abnormal high amount of cystine in lysosomes will result in cystinosis, a lysosomal storage disorder.⁷⁶ The intracellular Cys concentration is relatively higher than that of cystine and usually on the order of 0.1 mM.⁷⁷ High concentration of Cys in the tissue is neurotoxic and cytotoxic. Cys at 1 mM concentration is the lethal threshold via NMDA receptors.⁷⁸ Cys is the rate-limiting precursor in intracellular GSH biosynthesis.^{50, 79} It is also indispensable in the synthesis of protein, CoA, taurine and inorganic sulfur.¹ Due to the ability to form inter-chain or intra-chain disulfide bond with other cysteine residues, Cys is critical in controlling the tertiary structure of proteins.⁸⁰ To fulfill the essential functions of Cys in the synthesis of the metabolites mentioned above at a relatively low concentration, GSH is used effectively as the major redox buffer for cellular Cys.¹ In the extracellular space, however, Cys and its oxidized form cystine is the predominant low molecular weight thiol/disulfide pool found in human plasma with a 20 to 50-fold higher concentration than that of GSH/GSSG.^{81, 82} The plasma concentration of Cys is normally at 10 to

25 μM , which is much lower than that of the cystine (50-150 μM).⁸³ This ratio of Cys/cystine concentration is quite different from that of GSH/GSSG in the plasma. It has been reported that the acid soluble fraction of total cysteine composed of 5.9% Cys and 83.1% cystine in rat plasma compared to 28% GSH and 9.5% GSSG.⁸⁴ The physiological redox potential, E_h , of Cys/cystine couple is around -80 mV in normal human plasma, which is more oxidized compared to -137 mV for GSH/GSSG.^{8, 84, 85} Like Cys, tissue concentration of Hcy exists at low concentration in tissue, as excessive Hcy is toxic to cells.^{1, 86} In the extracellular space, Hcy is readily oxidized and exists at low concentrations.¹ Only trace amounts (0.05-0.3 μM) of free Hcy (1-2% of total homocysteine) exist in its reduced form in plasma.⁸⁷ Hcy works effectively as an essential intermediate metabolite, which connects the methionine (Met) and Cys metabolic cycles.^{1, 88}

Changes in the concentrations of Cys and Hcy or their oxidized forms in biological systems usually indicate dysfunctions of related metabolic cycles or problems with cellular processes.²³ For example, the Hcy concentration in plasma/serum is considered to be a biomarker of clinical disorders, such as Alzheimer's disease and cardiovascular disease, while the concentrations of Cys and its oxidized form are indicators of oxidative damage.¹ Therefore, measuring the concentration profiles and metabolism of these compounds in biological samples would provide useful information in evaluation of biological conditions and disease diagnosis.

1.1.4 Metabolism of CoA and Cys/cystine

Cys, as well as pantothenic acid and ATP, are well known as the three basic substrates for the biosynthesis of CoA.¹ Starting from these substrates, CoA can be biosynthesized in the cytosol through five well-established steps with the aid of multiple enzymes as shown in Fig. 5.^{65, 68, 89}

However, relatively little is known about CoA degradation and even less is known about the regulation and kinetic characteristics for this sequential multi-enzyme reactions and its turnover rate.^{1, 65, 68, 88} The degradation of pantetheine (PSH) to pantothenic acid and CSH is identified as the last step in the CoA degradation pathway.^{65, 68, 88} This process is catalyzed by Vanins, which comprise a group of membrane-associated extracellular pantetheinases (EC 3.5.1.92).⁶⁵ CSH will be further oxidized to hypotaurine and finally taurine under the catalysis of CSH dioxygenase.⁸⁸

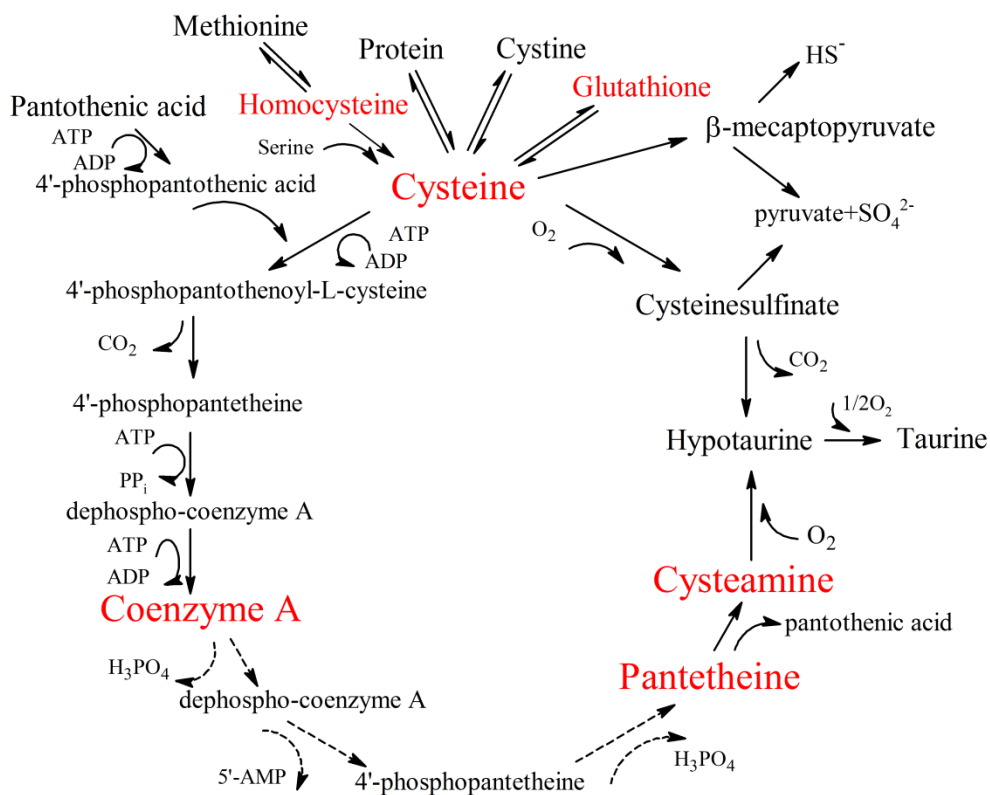


Figure 4. Biosynthesis and biodegradation of CoA⁸⁸

As a semi-essential amino acid of human, Cys can either be obtained from dietary intake or biosynthesized from methionine (Met) and serine (Ser) in the cytosol through a transsulfuration pathway with Hcy, a non-protein-forming sulfur amino acid, as one of the key intermediates.^{1, 90} Hcy may also be converted back to Met through remethylation catalyzed by cystathionine β-synthase (EC 4.2.1.22) or be released to the extracellular space.^{86, 91} Cys

participates actively as a precursor for biosynthesis of proteins and several other essential molecules including GSH, CoA, taurine, inorganic sulfur and cystine as shown in Fig. 4.^{1, 88} For clarity purposes, multistep pathways are represented by bold arrows. Cys can be oxidized by cysteine dioxygenase (CDO) (EC 1.13.11.20) to form cysteinesulfinate in the cytosol, which will then be metabolized into taurine and CO₂ or into pyruvate and sulfate.⁸⁸ Besides, Cys can also be converted to pyruvate and sulfide through β-mecaptopyruvate.¹ In the oxygenated extracellular space, Cys is readily auto-oxidized to cystine.^{83, 92} Cystine can be transported into the intracellular space again for the biosynthesis of GSH or desulfurized through β-cleavage by cystathionine γ-lyase to form pyruvate, ammonia and thiocysteine; the last product can be converted back to Cys by releasing the sulfide.¹ These final products from Cys metabolism are much less toxic than Cys itself.⁸⁸

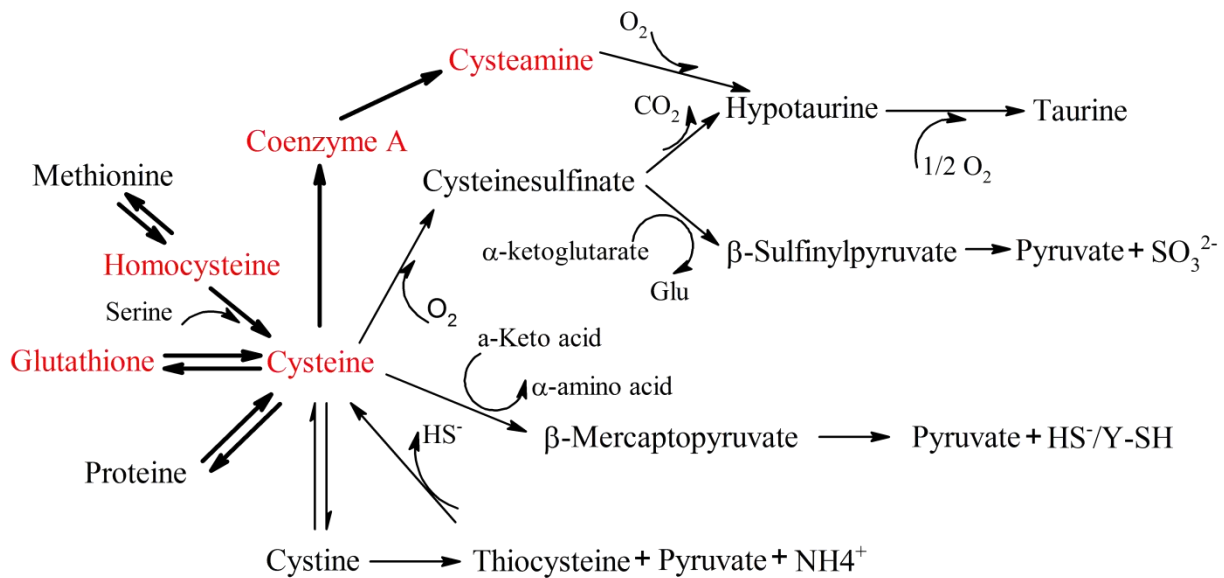


Figure 5. Cys metabolic pathway^{1, 88}

1.2 CURRENT METHODS FOR DETERMINATION OF AMINOTHIOLS

1.2.1 Sample collection and pretreatment

The most common bio-specimens used in the thiol assay are extracellular fluid, cells, tissue, and even a partial of a specific organ *in vivo*.⁹³ To study the thiols in the intracellular fluid, cells must first be separated from their matrix by centrifugation and then lysed. The lysate could then be stored at -80 °C for further analysis.⁹⁴ For single cell analysis, the lysis step can be achieved right before or after cells are introduced into the analysis system.⁹⁵⁻⁹⁷ Procedures for preparing plasma from a blood sample is similar to those described for erythrocytes, except that the plasma portion is collected and stored for further use.^{98, 99} When the matrix is tissue, there are usually several choices for sample collection. If the total GSH in the tissue is of interest, the sample could first be homogenized and diluted in EDTA buffer. The resultant solution is then sonicated for a short time depending on the kind of tissue. The mixture is further treated with centrifugation and the supernatant is eligible for storage and analysis.¹⁰⁰ The incubation medium is also an informative source for monitoring the efflux of GSH from slice cultures to the extracellular space. The incubation medium of the slice can be collected at certain intervals and the concentration of analytes can be determined after separation and detection.^{34, 101} Microdialysis is a good choice for sampling extracellular GSH *in vivo* with relatively good spatial resolution and small damage to tissue.¹⁰² The membrane region of a probe is usually made of semipermeable membrane materials with a specific molecular weight cutoff. This tiny probe could be inserted into a specific region of a tissue or experimental animal for analysis. During the operation, perfusion fluid with a calibrator is pumped through the probe at a low and constant flow rate, usually between 0.1 and 5.0 $\mu\text{L}/\text{minute}$. The molecules below the cutoff weight of the

membrane may undergo exchange in both directions across the membrane based on the concentration gradient. The dialysate containing analyte and calibrator will then be collected for assay.¹⁰² This method has been widely used for in vivo analysis of extracellular GSH in rat brains.^{29, 30, 103, 104} Our lab has developed an electroosmotic sampling method, which uses electroosmotic flow (EOF) as the driving force for collecting interstitial fluid in organotypic hippocampal slice cultures (OHSCs).^{105, 106} Compared to microdialysis, this method does not require extra pumps, allows high recovery of the analytes, and has better spatial and time resolution.

For offline analysis, it is often the case that samples containing thiols will be stored for hours, days or months before the measurement. Special precautions must be taken to prevent artificial errors introduced by improper sample pretreatment procedure. Oxidation and proteolysis are two major factors that lead to transformation of one form of thiol to another.⁹³ For example, at pH values greater than 7, GSH undergoes auto-oxidation to form GSSG. Meanwhile, γ GT coexisting in the samples with thiols will reach its optimum activity at neutral pH, which catalyzes the first step of GSH proteolysis.⁹³ Thus, it is necessary to keep the pH value of the buffer below neutral and store samples in refrigeration to minimize autoxidation and proteolysis of the thiols. It is also helpful to precipitate the proteins from the sample by acidification and centrifugation, addition of organic solvent modifier or ultrafiltration to minimize proteolysis, which will also improve the separation efficiency in high-performance liquid chromatography (HPLC) and capillary electrophoresis (CE).^{93, 107} Moreover, it has also been suggested to add redox quenching buffers composed of HCl, ascorbic acid and diethylenetriaminepentaacetic acid into the system to restrain thiol oxidation.¹⁰⁸ Chromophore or fluorescence tags are often used to block thiol groups and prevent oxidation.⁹⁸ Inhibitors of γ GT

and chelating agents of ferrous ions like 1,10-phenanthroline or EDTA have also been used to prevent oxidation and proteolysis to a certain extent.¹⁰⁹ For online analysis achieved under normal conditions (room temperature, physiological buffer), samples are collected and derivatized right before the separation and measurement. The errors caused by autoxidation are greatly reduced as these reactions take place on the time scale of hours.¹¹⁰⁻¹¹³

1.2.2 Separation based methods

So far, many analytical methods have been applied to analyze thiol containing compounds from different biological sources or matrixes. These methods have been summarized in several informative review articles.^{93, 114} The dominant methods can be classified into two categories, separative and non-separative.⁸⁵ Among all the separative methods, HPLC and CE are the most common techniques widely used in various applications.¹¹⁰ Other methods such as thin layer chromatography (TLC), gas chromatography (GC) and the newly developed microfluidic technique have also appeared in some works.^{93, 107, 115} Common detection techniques applied in separative methods include the UV-Vis absorbance, the electrochemical detection (ECD), the mass spectrometry (MS) and the fluorescence (FL).^{93, 107} Because thiol compounds usually lack of strong chromophores or fluorophores, it is normally required to label them with chromophoric or fluorescent tags to enhance the detection limit in optical detection.⁹³ Due to its specificity, reactivity and selectivity, the thiol group is a more popular target of derivatization than the carboxylic and amino groups. Derivatization of the thiol group also protects it from being oxidized in the following experiments.⁹³ The most widely used reagents to introduce a chromophore tag are Ellman's reagent (5, 5'-dithio-(bis-2-nitrobenzoic) acid, DTNB), Sanger's

reagent (1-fluoro-2,4-dinitrobenzene, DNFB), monoiodoacetic acid (MIAA), N-ethylmaleimide (NEM) and its analogues; the famous reagents used for fluorophore introduction include *o*-phthalaldehyde (OPA), monobromobimane (mBBr) and 4-aminosulfonyl-7-fluoro-2,1,3-benzoxadiazole-4-sulfonate (SBD-F).^{93, 107, 114, 116} Some structures of the above reagents are shown in Fig. 6.

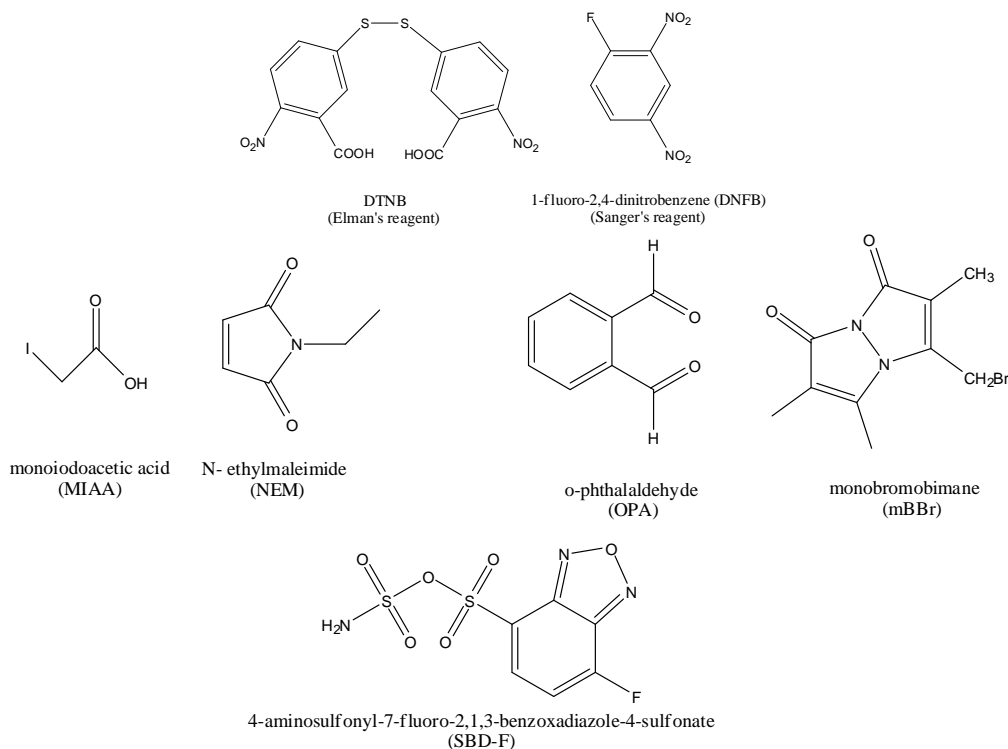


Figure 6. Structures of common derivatizing agents

HPLC is a well-known chromatographic technique used for its advantages in high efficient separation, identification, quantitation, as well as purification of analytes of interests from mixtures. Analytes are separated in an HPLC column based on the differences in retention times caused by the equilibrium distribution of solutes between the stationary phase and mobile phase.¹¹⁷ Most thiol analysis performed by HPLC uses octadecylsilica gel (ODS) as the stationary phase and is performed by reversed-phase (RP) mode.¹¹⁴ Detectors such as UV, ECD, ECD, FL and MS are compatible with HPLC.¹¹⁴ GSH and related compounds in rabbit eye tissue

have been separated by HPLC-UV with post-column derivatization.¹⁰⁰ Microdialysis has been coupled to HPLC for *in vivo* monitoring of extracellular GSH concentration in rat brains using either FL or EC detections.^{30, 104} A 2D HPLC-FL has also been applied in analyzing trace amount of GSH and GSSG in minute plasma samples.⁹⁹ A detailed summary of HPLC techniques in determination of thiols can be found in some good review papers.^{93, 107, 114, 118}

CE is another separative technique widely used in thiol determination. Under a strong electric field, ionic and neutral species can be separated in a capillary based on the differences in the charge and frictional forces.¹¹⁹ Different from HPLC, CE uses EOF as a driving force rather than hydraulic pressure, which results in a plug flow profile instead of parabolic laminar flow profile.¹²⁰ Unlike HPLC, there is no mass transfer between phases in CE. As a result, band-broadening in CE is much less significant than that in HPLC, which contributes to its higher separation efficiency.¹²¹ Meanwhile, because the internal diameters of capillary used in CE are usually within the range of 20 μm -100 μm , CE requires lower volume of sample for analysis than HPLC does.¹²² In addition, high voltage applied in the CE system enables the separation to be completed at high speed within several minutes.¹²² Because of all these advantages, CE has been widely used in analysis of biological samples. CE coupled to laser induced fluorescence (LIF) method has been reported to measure the total plasma thiols. After offline reduction and derivatization of the plasma samples, baseline separation of CysGly, Hcy, Cys and GSH was achieved within 5-9 minutes.⁹⁸ The same method has also been applied to measure protein-bound GSH in cultured cells.¹²³ Microdialysis has been coupled to CE-LIF by a flow-gated interface for continuously monitoring thiols *in vivo* in the caudate nucleus of the rat brain, where analytes were derivatized before entering into the separation capillary and detected by a laser-induced fluorescence detector after separation with LODs (detection of limits) in the range of 20-40

nM.^{29, 124} Determination of the intracellular thiols from a single human erythrocyte has also been achieved using CE-LIF.⁹⁵ More examples can be found in other review papers.^{93, 107, 114}

1.2.3 Non-separation based methods

The non-separative methods used for determination of thiol compounds mainly include spectrophotometry, spectrofluorimetry and amperometry.^{93, 107} The major advantage of non-separative methods is that there is no need to separate the analytes of interest from the matrices. In order to obtain accurate and reliable results, non-separative methods require highly selective ways to detect the analytes from a complicated background. High selectivity detection can be achieved through labeling of the analyte with special tag molecules. Determination of GSSG and GSH have been reported using a spectrophotometric method, which is based on the UV-Vis absorbance change resulting from the redox of added reagents along with that of GSH/GSSG.¹²⁵ GSH has been selectively measured in the presence of Cys by using a GSH selective fluorescence probe, 5-maleimidyl-2(*m*-methylphenyl)benzoxazole.¹²⁶ The measurement of GSH/GSSG redox potential in the cytosol and mitochondria *in vivo* has been achieved by applying genetically encoded redox sensitive green fluorescent protein probes (roGFPs) followed by fluorescence imaging.¹²⁷⁻¹³⁰ Electrochemical sensors have also developed for selective detection of thiols.^{131, 132} In addition, nuclear magnetic resonance (NMR) has been used for *in vivo* determination of the GSH in the human brain¹³³ and measurement of GSH redox status in both intracellular and extracellular compartments of human erythrocytes in a non-separative way.¹³⁴

1.3 MICROFLUIDIC DEVICES WITH CONFOCAL LASER-INDUCED FLUORESCENCE DETECTION

1.3.1 Theory of miniaturization

The concept of miniaturized total analysis systems (μ TAS) or the lab-on-a-chip (LOC) system was first brought forward by Manz et al. in 1990. They envisioned a system that incorporates all sample handling steps, including sample pretreatment, chromatographic or electrophoretic separation, and detection, close together on one device.¹³⁵ This idea was promoted by rapid development of techniques in the field of micro-electro mechanical systems (MEMS) in the 1980s and the urgent practical needs of miniaturization, integration and portability in biotechnology, pharmacology, medical diagnostics and forensics. Generally, the LOC system can be viewed as the shrinkage of various normal laboratory functions on a single chip. The connection of these functions on chip is achieved by controlling the fluid flow between different function modules at micrometric length scales. The study of fluid flow circulating in artificial microsystems later became a popular research topic, microfluidics.¹³⁶ Although the original aim of miniaturization was to enhance the analytical performance of the μ TAS as a new generation of chemical sensor, it was recognized that the miniaturized device not only enables faster and more efficient transportations and separations, but also dramatically reduces the amount of required sample, carrier, reagent or mobile phase.¹³⁵ Attracted by these advantages, many research groups have joined their efforts in the field of microfluidics since 1994. A lot of pioneering works in the development of the theory, technologies, analytical operations and applications are summarized in some excellent reviews.¹³⁷⁻¹⁴⁰

Flow injection (FI), chromatography and capillary electrophoresis (CE) are three analytical techniques commonly used in experiments performed on microfluidic device.¹³⁵ FI is a liquid handling technique that is capable of introducing a series of sample zones with a well-defined volume into a continuously flowing carrier reagent with high reproducibility and sampling rate.¹⁴¹ These features make FI a popular method for automatic sample introduction in micro-channels.¹⁴² Chromatography and electrophoresis are two separation methods based on different mechanisms. Unlike the traditional capillary column, microfluidic channels are usually more complicated with a two dimensional channel network, and the lengths of these channels are usually shorter than that of the capillary column used in traditional CE and capillary HPLC. However, the existing theories of chromatographic and electrophoretic separations will still apply to the separation behaviors on a microfluidic chip.¹¹⁷

Chromatographic separation is based on the different equilibrium distribution of analytes between the stationary and the mobile phases. Different distribution coefficients among analytes lead to various retentions in chromatographic analysis and result in the separated analyte bands.¹¹⁷ The extent of the band spreading directly determines the efficiency and performance of the separation.¹¹⁷ Band broadening in a chromatogram occurs when the solutes travel through both inside and outside the separation column, the latter is usually known as the extra-column band broadening resulting from sample injection, detection step and the dead volume in the connecting tubing.¹⁴³ In an ideal experiment, analytes of interest will be introduced into the system as a narrow zone and travel through the column at a same constant rate. However, in practice, the velocity for individual solute molecules are not always the same, which constitutes the origin of band-broadening. There are three major contributions to the difference in the velocity as the solutes travel through the column: (1) the resistance to mass transfer between

phases; (2) the flow differences with radial position in the column, which is due to the parabolic flow profile of the laminar flow when a pressure gradient is applied to an open-tubular column. The radial mass transfer of the solute, however, helps to reduce the band spreading by mixing the analyte molecules with different velocity; (3) the longitudinal molecular diffusion.^{117, 143} The overall plate height H (or the height of an equivalent theoretical plate, HETP) can be expressed in Eq. 1 to describe the band-broadening inside an coated capillary column and is an important parameter for measuring column efficiency.¹¹⁷

$$H = H_S + H_M + H_L \quad (1)$$

where H_S , H_M and H_L are terms of stationary phase mass transfer, mobile phase effect and longitudinal diffusion, respectively. By studying the origin and mechanism, a mathematical expression for each term can be derived as in Eq. 2, Eq. 3 and Eq. 4.

$$H_S = \frac{qk'}{(1+k')^2} \frac{d_f^2}{D_S} \bar{v} \quad (2)$$

$$H_M = \frac{1 + 6k' + 11k'^2}{24(1+k')^2} \frac{r^2}{D_M} \bar{v} \quad (3)$$

$$H_L = \frac{2D_M}{\bar{v}} \quad (4)$$

Where q is shape factor of the liquid stationary phase dispersed on the surface of a solid support. k' is the capacity factors, d_f is the characteristic distance of the liquid stationary phase, such as the film thickness or droplet diameter; r is the inner radius of the column; \bar{v} is the mean flow velocity of the mobile phase; D_S and D_M are the solute diffusion coefficient in the stationary and mobile phase, respectively.¹¹⁷

Compared with chromatography, the HETP for the ideal CE experiment has no contribution from resistance to mass transfer between phases. Meanwhile, the flow velocity driven by electroosmotic flow (EOF) has a flat flow profile rather than a parabolic shape as in

the chromatographic analysis.^{119, 144} Therefore, only the longitudinal diffusion term contributes to the final separation efficiency when band broadening caused by Joule heating, injection and analyte interaction with the capillary wall are all minimized¹⁴⁵ and that is why CE usually has a theoretical plate number approaching several hundred thousand,¹⁴⁶ which is usually 10- to 100-fold higher than that of a chromatographic separation.¹²¹ Besides, technically, it is much easier and space-saving to apply EOF as a driving force on a compact microfluidic device than to integrate series of mechanically moving parts, such as micro valves and pumps as used in chromatographic analysis.¹³⁷ From these points of view, CE is a better choice to achieve separation of analytes on chip than chromatography.

Proportionality consideration is a convenient approach to predict the trends of physical parameters of a simple flow system during the miniaturization, especially when there is little knowledge of the material constants.¹⁴⁷ Typically, physical parameters of interest can be expressed as functions of the variables to be miniaturized, space (l) and time (t). There are two situations for a simple three-dimensional downscaling process based on the scaling factor l , *time-constant system* and *diffusion-controlled system*. The time-constant system assumes that the timescale keeps constant when the system is miniaturized. It is applicable to the simple transportation system and flow injection analysis (FIA) system.¹⁴⁷ In a *diffusion-controlled system*, molecular diffusion, heat diffusion and flow characteristics determine the separation efficiency, such as in a chromatographic or an electrophoretic system.¹⁴⁷ In these systems, time is proportional to l^2 . Proportionalities of selected physical parameters in relation with the scaling factor, l , are summarized in Table 1 for these two systems.^{135, 136, 147, 148}

Table 1. Proportionalities of mechanical parameters in relation to the characteristic length l

	Time-constant system	Diffusion-controlled system
Time, t	<i>const.</i>	l^2
Space, l	l	l
Linear velocity, u	l	l^{-1}
Volume flow rate, F	l^3	l
Pressure drop, Δp (laminar flow)	<i>const.</i>	l^{-2}
Voltage drop, ΔV (EOF)	l^2	<i>const.</i>
Electric field, V/L , E (EOF)	l	l^{-1}
Reynolds number, Re	l^2	<i>const.</i>
Joule heat, Q	l^3	l^3
Plate number	---	<i>const.</i>

According to Table 1, in a *time-constant system*, if the pressure drop remains constant during the miniaturization, the analysis time that relies on the linear velocity will keep unchanged. However, the consumption of the sample and carrier reagent will be decreased considerably. For, example, a 10-fold decrease in the dimension would result in a 1000-fold reduction of the sample and reagent consumption determined by the volume flow rate. In a diffusion controlled system, the time scale is treated as a surface.¹³⁵ Therefore, a downscale to 1/10 of the original size will lead to 100 fold decrease in the analysis time while the voltage and the separation efficiency (plate number) remain constant for an electrophoretic system. A higher voltage drop can be applied to a downscaled system as the Joule heat will be tremendously reduced and the heat dissipation will also be promoted when the surface-to-volume ratio is increased, which will contribute to an even faster analysis and higher separation efficiency.¹⁴⁹ This evidence supports that EOF is more advantageous than pump-driven flow for miniaturized systems.

1.3.2 Confocal laser induced fluorescence (LIF) detection

Currently, various detection methods have been applied to microfluidic devices, which include FL, ECD, chemiluminescence detection (CL), electrochemiluminescence detection (ECL), MS and other less commonly used detection methods, for example, surface plasmon resonance (SPR), thermal lens microscopy (TLM), time-scanning Fourier transform spectrometry, flame analyzer and atomic/molecular emission detector and so on.^{137-140, 150} In a typical microfluidic analysis, the volume of sample is confined by the dimensions of the microchannel, usually on the order of a few hundred picoliters to low nanoliters. Meanwhile, analytes of interest are usually present in extremely low concentrations.¹⁵¹ The limited sample volume and concentration requires microfluidic analysis to be coupled with highly sensitive detection methods.¹⁵⁰ Compared with other detectors, laser induced fluorescence (LIF) detection is one of the most sensitive detection methods widely used in microfluidic analysis.^{150, 151} Under the best conditions, the concentration limit of detection (LOD) is on the order of 100 fM and the mass LOD of about a few tens of molecules has been achieved.¹⁵¹ Presently, LIF has become a standard detection method for microfluidic analysis with low LOD and high selectivity, although the sample to be analyzed must be naturally fluorescent or capable of being labeled with fluorescent tag.¹⁵⁰

To achieve ultrasensitive fluorescence detection, it is necessary to increase the signal-to-noise ratio (S/N).¹⁵¹ In molecular photoluminescence spectrometry, the signal is directly proportional to the incident radiant power under most conditions.¹⁵² Therefore, using a laser as the an excitation source will provide greater irradiance compared to conventional light sources without excitation wavelength selector.¹⁵² The noise for the photoluminescence comes from two main sources, the shot and flicker noise in the analyte luminescence signal and the blank noise including the amplifier readout noise, dark current noise, background luminescence and

scattering signal.¹⁵² Confocal optical arrangement is capable of achieving highly sensitive fluorescence detection by increasing the S/N through elimination of the scatter or out-of-focus light.^{151, 153, 154} In conventional fluorescence setup, the entire field of sample both in focus and out of focus will fluoresce like a three-dimensional incoherent light source when excited by the incident light.¹⁵⁵ Mathematically, the image formed by an ideal optical system at the detector is a convolution of the object with the defocused point spread function (DPSF).¹⁵⁶ On the contrary, in a confocal LIF system, the detection volume is minimized by a laser beam focused onto the specimen for maximizing the S/N .^{151, 157} The fluorescence signal collected at the focal point of the objective forms an image before the detector where there is a pinhole as a spatial filter conjugated to the focal point of the objective.¹⁵⁵ Due to this spatial filter, the detector only detects fluorescence generated from the focal point on optical slice with a submicron thickness, typically at best 0.5 μm .^{158, 159} All other light rays, such as fluorescence coming from out-of-focus planes, or fluorescence from the focal plane, but not at the focal point, and laser light reflected or scattered from the cover glass and channel walls, will be blocked and filtered out by spectral and spatial filters before they reach the detector.¹⁵⁹ In summary, the confocal LIF detection has higher axial resolution than normal FL detection and is able to control the depth of field.^{160, 161} It also works well to eliminate or reduce background noise and improve the S/N .^{154, 162} All of these advantages make the confocal LIF one of the most ultrasensitive techniques for microfluidic devices.^{151, 154} Fig. 7 is sketch of a typical confocal LIF setup.^{154, 155, 163} A laser is used as the light source to produce an intense and spatially and spectrally constrained point source of illumination. The beam first passes through a laser line exciter filter and is reflected by the dichroic filter positioned at 45° and focused onto the sample stream in the microchannel via a microscope objective. A pinhole is placed in front of the detector at the optical position that is

exactly where the fluorescence from the focal point of the objective is focused after the tube lens. A band pass emission filter is placed after the pinhole to exclude light at unwanted wavelengths. The straight line in Fig. 7 represents the fluorescence signal produced by the sample on the focal plane, which is focused right at the pinhole, thus capable of passing through the pinhole and finally reaches the detector. The dashed blue line denotes the fluorescence generated by the sample above the focal plane. As the image of the out-of-focus fluorescence forms a much larger disk at the pinhole, only a very small portion of this light will pass through the pinhole and contributes negligibly to the ultimate signal at the detector.¹⁶⁴ In a true confocal system, the excitation volume depends on the objective NA and the diameter of the entering laser beam, while the collection volume depends on NA and the spatial filter diameter.¹⁵¹

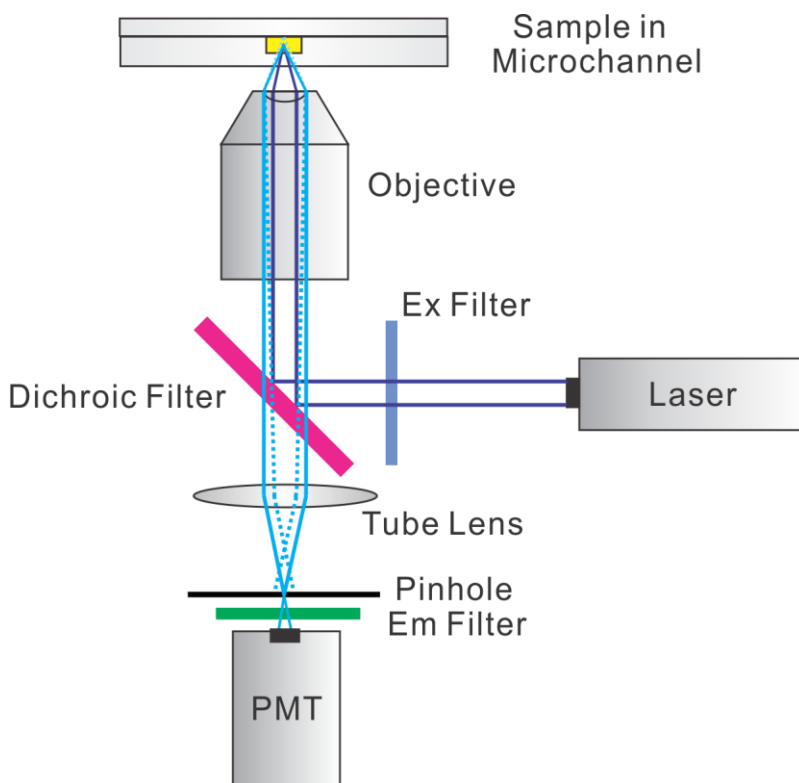


Figure 7. Sketch of a typical confocal LIF detector

Since the first introduction of LIF as a detection technique for CE in 1985 by Gassmann, Kuo and Zare,¹⁶⁵ LIF has attracted a lot of research interest because of its high sensitivity extended to the single molecule concentration.¹⁵⁷ Early pioneering papers in LIF detection¹⁶⁶⁻¹⁶⁹ laid solid experimental and theoretical foundations for subsequent research in the field of ultrasensitive confocal LIF detection¹⁷⁰⁻¹⁷² coupled to micro-analytical systems. Recently, various laser sources and detectors have been introduced into the LIF system.¹⁷³⁻¹⁷⁵ Parameters of optical components and its arrangements are further discussed according to their effects on experimental results.^{151, 154, 176} More studies were aimed at applying confocal LIF for single cells and single molecule analysis in microfluidic devices.^{176, 177}

1.3.3 Microfluidic chip and thiols determination

With the development of a microfluidic system and its attractive advantages in handling small amounts of samples, research on separation and determination of thiol compounds from biological samples has been switched from traditional analytical techniques, such as CE and LC, to the more integrated microfluidic platform.¹¹⁴ Currently, a majority of studies in measurement of intracellular GSH together with reactive oxygen species (ROS) on microfluidic devices treat these two molecules as model compounds to demonstrate the performance of on-chip single cell analysis^{96, 97, 178-181} or as signaling molecules to evaluate the apoptosis and oxidative stress of cells.¹⁸²⁻¹⁸⁴ These studies were either achieved after offline extraction of cellular components or through direct single cell analysis on the microfluidic chip and the signals from the labeled molecules have been measured using LIF^{96, 97, 178-184} or CL detection.¹⁸⁵

Simultaneous determination of individual thiols in mixture solutions has been a research focus. Hcy, Cys, GSH and/or N-acetylcysteine (NAC) in a standard mixture,^{186, 187} or in the blood samples,¹⁸⁸ the human plasma^{189, 190} and the red blood cell lysate,^{115, 191} have been successfully analyzed on a microfluidic chip coupled to an electrochemical detector with LODs ranging from submicromolar to low micromolar and an analysis time of several minutes. The intracellular concentration of GSH, Cys and hemoglobin (Hb) in individual red blood cells from cancer patients were simultaneously determined using a microfluidic chip coupled to CL detection and the results were compared with samples from healthy subjects indicating a tremendous increase in GSH and Cys concentrations in samples from cancer patients.¹⁹² GSH in a mixture with other biological anions, NO_2^- , ascorbic acid and tyrosine at pH 11 in a standard mixture has been separated and analyzed in a microfluidic chip integrated with the EC detection.¹⁹³ Cys, in a mixture of native amino acids, has been successfully separated and analyzed on microfluidic chip with either EC¹⁹⁴ or LIF detection.¹⁹⁵

Thiol containing drugs are widely used for treating many diseases. The analysis of these thiol drugs in standard mixtures or from biological samples has also obtained some research interest. For example, microfluidic electrophoresis integrated with online labeling and post-column CL detection has been used for simultaneous quantitation of four thiol drugs including 2-mercaptopropionylglycine (2-MPG), captopril (CP), 6-thioguanine (6-TG) and 6-mercaptopurine (6-MP) with LODs in the range of 8.9-13.5 nM.¹⁹⁶

2.0 DEVELOPMENT OF A CONFOCAL LASER INDUCED FLUORESCENCE DETECTION SYSTEM

This part of work is adapted from the master's thesis "*Online determination of extracellular glutathione in organotypic hippocampal slice cultures with a microfluidic device and confocal laser-induced fluorescence detection system*", Juanfang Wu (2010)

Several aspects must be considered in building a confocal laser induced fluorescence (LIF) detection system. 1) Selection of an optimized set of optical components based on the analytes of interest. Parameters for a specific optical component, such as the type and wavelength of the laser, cut-on and cut-off wavelength of a filter set, magnification and numeric aperture (NA) of the microscope objective, etc., must meet goal of the research. Meanwhile, different parameters of various optical components must be compatible with each other to achieve the best optical performance. 2) Design and assembly of an opto-mechanical system. This usually includes designing a platform for accommodating the microfluidic device and choosing series of holders and stages to support and arrange optical components in the light path. A good arrangement of optical components will not only ease the beam alignment, but also increase the sensitivity and decrease the detection limit. 3) Development of a multi-task controlling program. Computer remote control allows for automation of detection and measurement. It should be capable of

achieving different functions, such as data collection and averaging, voltage and current monitoring, high voltage power supply (HVPS) manipulating, and sampling control with a user-friendly interface.

2.1 OPTIMIZATION OF OPTICAL COMPONENTS OF THE CONFOCAL LIF DETECTOR

2.1.1 Laser

Laser beams are well-known for their beneficial qualities such as high collimation, monochromaticity, coherent and high radiance.¹⁵² These characteristics allow for the directional delivery of intense irradiance with high spectral purity to the sample.¹⁹⁷ According to confocal theory, only the fluorescence signal generated from the focal point will be detected by the detector; the photoluminescence signal is mostly proportional to the incident radiant power, it is therefore necessary to use a laser as an excitation source and focus it into a small spot to get a strong signal.¹⁵²

One of the most important criteria in choosing a suitable laser source is its wavelength. It must match the absorbance spectrum of the analyte. As the derivatizing reagent of thiols in the following experiments is ThioGlo-1 (the reason of choosing this dye will be further discussed later), the excitation and emission spectra of aminothiols labeled with this dye must be examined. Fig. 8 shows the excitation (emission wavelength: 513 nm) and emission (excitation wavelength: 379 nm) spectra of labeled GSH taken with a SpectraMax M2 (Molecular Devices, Sunnyvale, CA). The spectra were taken right after mixing of the GSH in deionized H₂O and ThioGlo-1 in

DMSO at final concentrations of 52 μM and 20 μM , respectively at 24.8 $^{\circ}\text{C}$. Fig. 8 shows that the excitation and emission maxima are 370 nm and 502 nm for ThioGlo-1 conjugated with GSH, which are different than the literature values (excitation wavelength: 379 nm and emission wavelength: 513 nm) provided by the product catalog. This may be caused by the different experimental conditions under which the spectra were taken. The laser with wavelength a little higher than 400 nm was chosen for several reasons. First, although 370 nm is the peak excitation wavelength for the GSH-ThioGlo-1 conjugate, it falls out of the wavelength range of visible light (380–750 nm) for the human eye. Thus it may cause some difficulty in beam alignment. Second, the closer the wavelength is to the ultraviolet portion of the spectrum, the more chance that other analytes in the sample and different materials in optical path may be excited and fluoresce, which will increase the background signal. Third, it is less expensive to get a laser with longer wavelength.

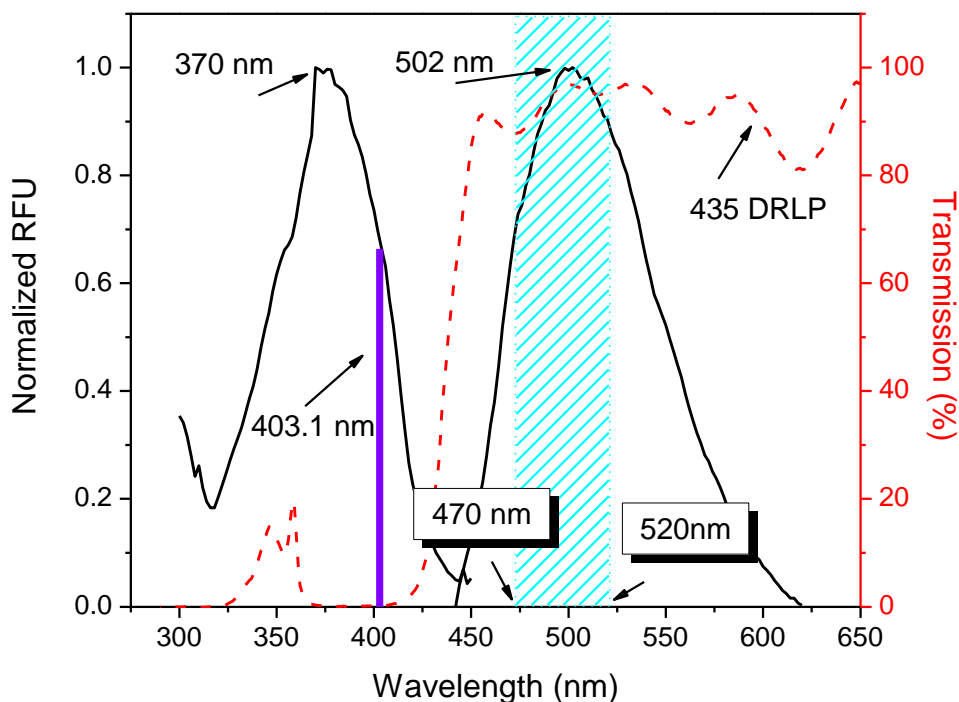


Figure 8. Excitation and emission spectra of GSH labeled with ThioGlo-1

Another factor that dominates the selection of a laser is its operational modes. Generally, continuous-wave (cw) lasers have better spatial coherence than pulsed lasers and may be focused to a few micrometers spot size.¹⁶⁷ Meanwhile, pulsed lasers tend to have much higher intensity in a very short time compared with cw lasers;¹⁵² this will lead to saturation and photo-degradation of dye, which should be avoided during the measurement. Finally, the stability of the laser is of vital importance to obtain shot noise limited performance and high LOD.¹⁶⁷

The most widely used lasers mainly include gas lasers, dye lasers, solid-state lasers, and semiconductor lasers and chemical lasers.¹⁵² The diode pumped solid-state (DPSS) laser use a semiconductor diode laser as pump source to pump a doped laser crystal. Rather than giving off the fundamental laser frequency of the lasing medium, the second harmonic generated by the doubling crystal is transmitted as the final laser beam.¹⁹⁸ DPSS lasers produce stable and narrow

laser beam with good mode quality throughout the visible spectrum at a relative low cost. Meanwhile it also possesses characteristics of a diode laser, such as a compact size and high optical efficiency.¹⁹⁸ A DPSS cw laser produced by CrystaLaser (Reno, NV) was chosen as the illumination source. It is equipped with an adjustable power supply controller. Table 2 lists some of the main parameters for this laser obtained from the manufacturer. The output power for our system is adjustable from 0 mW to 20 mW. A Gaussian 20 mW beam focused to a 1 μm radius spot size will produce a peak irradiance of over 10^6 W/cm^2 and in real operation the irradiance should be held to a value less than 10^5 W/cm^2 to eliminate saturation and possible photodegradation in fluorescence detection.¹⁶⁷ Thus output power range of 0 to 20 mW suffices for our system.

Table 2. Main parameters of BCL-020-405-CL2005 DPSS laser

Parameters	Values
Wavelength	403.1 nm
Output Power	Up to: 20 mW
Transverse Mode	TEM ₀₀ mode, $M^2 = 1.2$
Longitudinal Mode	Several longitudinal modes
Beam Diameter ($1/e^2$)	1 mm
Beam Divergence	0.6 mrad (full angle)
Output Stability	1% over 24 hours
Noise (rms)	< 0.5%
Operation Voltage	90 to 250 VAC
Dimension (mm)	30 x 30 x 120

2.1.2 Microscope objective

The microscope objective is one of the core optical components in a confocal LIF system. In a confocal setup, the objective will be used to focus the laser beam into a tiny spot onto the sample in the microfluidic channel and to collect the fluorescence signal generated by the sample and transmits it into the following optical path. There are several key parameters that determine the performance of an objective.

Numerical aperture (N.A.) is defined as the refractive index (n) of the immersion medium times the sine of the angle made by the marginal ray with the optical axis. It is closely related with the light collection efficiency as shown in Eq. 5¹⁶⁷

$$\text{Collection Efficiency} = \sin^2\left[\frac{\arcsin\left(\frac{N.A.}{n}\right)}{2}\right] \quad (5)$$

Therefore a lens of high N.A. is required to obtain high collection efficiency. For example, without special immersion medium, a lens with N.A. of 0.6 will collect 10% of the emitted light, while a lens with a N.A. of 0.1 will only collect 0.3%. Objectives with higher magnification usually have greater N.A.

Optical aberrations occur in various forms for objectives, which include spherical aberration, chromatic aberration and other geometrical aberrations. Expensive objectives usually have higher level of correction than the inexpensive ones. In a confocal LIF system, the excitation source is a single wavelength laser beam and the fluorescence signal has a narrow band width. Therefore, it is not necessary to use objectives with highest correction level. Most transmitted light objectives are designed to image specimens that are covered by a cover glass. The thickness of this small cover slip is standardized at 0.17 mm for most applications. General-purpose objectives are designed for this thickness. However, some special objectives have a

correction collar adjustment of the internal lens elements to compensate for the variation in thickness of the cover glass. Because the thickness of the base glass has a thickness of 1.0-1.1 mm, it is important to choose an objective with higher allowance for the thickness of the cover glass. The working distance (W.D.) is the distance between the front objective pupil lens and the closest surface of the cover glass when the specimen is in focus. In most cases, the W.D. is inversely related to the magnification of the objective. It is safer to have an objective with 3 mm or longer W.D due to the mechanical platform for the microfluidic devices.

A LUCPLFLN 40x objective from Olympus (Center Valley, PA) has been selected to use in our confocal LIF system. It belongs to the UIS2 (infinity-corrected) series and is a plan-fluorites objective with a cover glass correction collar from 0-2 mm. The W.D. for this objective is between 2.7-4 mm, which is also within the safe distance for our system. The light collection efficiency is also acceptable under a N.A. of 0.6. Table 3 includes some of the main parameters for this objective obtained from the manufacturer. A LUCPLFLN 20x objective with focal length of 9.0 mm and W.D. of 6.6-7.8 mm is also used in some of the experiments mentioned below to test the performance of the system.

Table 3. Main parameters of LUCPLFLN 40x objective

Parameters	Value
Focal Length (mm)	4.5
N.A.	0.6
W.D. (mm)	2.7-4
F.N.	22
Cover Glass Thickness (mm)	0-2
Immersion	No
Correction Ring	Yes
Ultra Wide Anti-reflection Coating	Yes
Bright field	Excellent
Dark field	Good
DIC	Excellent
Polarized Light	Good
Fluorescence (B, G Excitation)	Excellent
UV Fluorescence (at 365nm)	Excellent

2.1.3 Photon detector

Fluorescence signals generated by the sample must be converted into electrical signals for post-processing, analysis and storage. Photon detectors are sensors of light or other electromagnetic radiation that are capable of translating optical signals into electrical signals. Photoemissive devices, such as vacuum phototubes and photomultiplier tubes, form one of the major classes of photo detectors. For a vacuum phototube, photocurrent will be generated upon

the strike of photons towards the photocathode with energy larger than the threshold energy of photosensitive material. The anodic current will cause a voltage drop across the load resistor, which can be measured and recorded. The photomultiplier tube (PMT) is a type of vacuum phototube with additional dynodes, which can provide electron multiplication or gain. The operating voltage for PMTs is usually between 500 V to about 1200 V with gains of 10^6 .^{152, 199}

pn-Junction devices, such as photodiodes (PDs), are another class of photon detectors. The main component of PDs is the *pn*-junction diode. Under reverse bias, a limiting current directly proportional to the incident radiant power can be measured when the production rate of the charge carrier induced by light largely exceeds that which results from thermal processes. PDs are simple, very small in size and have excellent linearity over six to seven decades of incident radiant power. However the responsivity (the ratio of the rms signal output to the rms incident radiant power evaluated at a particular wavelength and incident power) of PDs is typically much lower than that of PMTs due to the lack of the internal gain.¹⁵² Avalanche photodiodes (APDs) can be viewed as PDs with gain, which are typically operated in the reverse breakdown region of the *pn*-junction diodes and provide best signal to noise (S/N) performance with an internal gain between 200-1000.²⁰⁰ Typically, APDs have a high responsivity unmatched by PDs and excellent performance at 650 nm unmatched by PMT.^{152, 200}

To choose a suitable detector for a certain application, important factors such as gain, quantum efficiency (QE) or responsivity, S/N, wavelength region, response time and cost must be considered.^{152, 201} As mentioned above, the internal gain of APD is much smaller than that of PMT. PMT usually has a smaller QE value (the ratio of the number of photoelectrons ejected to the number of incident photons, this value can be converted from responsivity) than that of APD and PD. For example, a gallium-arsenide-phosphide (GaAsP) cathode found in the most sensitive

PMTs has QEs of 40% compared to the 85% peak QEs offered by APDs.^{152, 200} PMT has peak responsivity around 300-400 nm and the maximum detection range of 800 nm while PD and APD maintain high responsivity in the range of 400-1100 nm and are widely used in the red or near infrared range.²⁰⁰ Most PMTs provide little responsivity in the NIR spectral region (beyond 850 nm), but APD and PD are sensitive up to 1100 nm.²⁰¹ At high signal level, APD and PMT have similar S/N in the visible spectral range.²⁰⁰ APD has better S/N at wavelengths longer than 650 nm due to high QE in the long wavelength region.²⁰⁰ At low signal level, PMTs offer a better S/N than PD and APD with an amplifier, where PMT is operating in the shot-noise limit while S/N of APD and PD is limited by the amplifier and dark noise.^{200, 201} The rise times for both PMT and APD are all very short (1-10 ns) and they are applied in experiments requiring fast responses.¹⁵² In general, PMT is widely used at very low light level while APD is used where the light level is too low for a standard PD but too bright for a PMT or when a magnetic field is present.

In our case, the emission light has a peak wavelength around 500 nm; meanwhile the signal from the confocal LIF system is relatively weaker than that in normal fluorescence detection. Based on the above discussion, a head-on metal package PMT module H5784-01 from Hamamatsu Photonics (Bridgewater, NJ) was selected as the photon detector of the system. Some of the main parameters for this PMT module provided by the manufacturer are listed in Table 4.

Table 4. Main parameters of H5784-01 PMT module

Parameters		Value
Cathode Type		Multi-alkali
Peak Sensitivity Wavelength (nm)		400
Spectral Response (nm)		300-850
Frequency Bandwidth (kHz)		DC to 20
Max. Output signal Voltage		10 V
Current-to-Voltage Conversion Factor (V/ μ A)		1
Sensitivity Adjustment Range		1:10 ⁴
Cathode: Radiant Sensitivity (mA/W) ^{*1}		60
Anode	Radiant Sensitivity (V/nW) ^{*1*2}	30
	Voltage Output Depending on PMT Dark	0.4 (typ.)
	Current (mV) ^{*2,*3}	4 (max.)
Settling Time (s) ^{*4}		2
Rise Time (ns)		0.78
Gain ^{*2}		4 x 10 ⁵
Effective Area: diameter Φ (mm)		8
Dimension (mm)		22 x 22 x 60
Ripple Noise (peak to peak) (mV) ^{*2,*5}		2 (max.)

*1: Measured at the peak sensitivity wavelength;

*2: Control voltage is +0.8 V;

*3: After 30 minute storage in darkness;

*4: The time required for the output to reach a stable level following a change in the control voltage from +1.0 V to +0.5 V;

*5: Cable RG-174/U, Cable length 450 mm, Load resistance = 1 M Ω , Load capacitance = 22 pF.

There are several major advantages of using this PMT as the detector. First, our desired wavelength of 500 nm is near the peak sensitivity wavelength of this PMT. Second, the dark

current and the ripple noise of this module are very low. Third, it is quite compact and includes a low-power consumption high-voltage power supply and a low noise amplifier together with a metal package photomultiplier tube. Fourth, the head-on type has a circular input window with a diameter of 8 mm, which is much easier than a side-on module during beam alignment. Last but not least, the rise time for this module is fast, which fits for detection following separation carried out in the microchannels.

2.1.4 Filter set, lens and mirrors

There are two kinds of filters in our detection system, spatial filters and spectral filters. A pinhole can be used as the spatial filter of the system. The diameter of the aperture depends on the area of the sample we want to analyze. The smaller the area of the sample we want to analyze, the narrower the aperture should be, and therefore less noise from the background would pass through the pinhole. Several pinholes with various fixed aperture diameters ranging from 50 μm to 600 μm were tested to optimize the aperture size. The selection of spectral filter set largely depends on the light source used and the excitation and emission spectra of the analyte (see Fig. 8). A set of spectral filters usually includes an excitation filter, a dichroic filter and an emission filter. An excitation filter is placed after the light source, which is used to block light with unwanted wavelength from entering the system. A dichroic filter not only reflects the laser beam but also allows the passage of fluorescence signal collected by the objective while effectively reflecting other light with wavelength below the cut-on wavelength of the dichroic filter. An emission filter can be a long pass filter or a band pass filter depending on the actual experiment. A band pass filter serves to capture the most specific energy from the analyte rather than to

capture the entire spectral region. Therefore, a filter with narrow bandwidth is effective in reducing potential background artifacts.

A XF2040 (435DRLP) filter and a 3rd 470-520 nm band pass filter as were selected as the dichroic filter and the emission filter in the confocal system, respectively, both of which were obtained from Omega Optical, Inc. (Brattleboro, VT). The diameter of the dichroic filter is 22 mm. The transmission spectrum of this 435DPLP is shown in Fig. 8. The 50% peak transmission is at 435 nm, and the transmission at 403 nm and 500 nm are around 0.19% and 96.8% respectively. This is compatible to wavelength of DPSS laser and the emission spectrum of the analyte. The key parameters for the emission filter are listed in Table 5. The 3rd millennium band pass filter applies Alpha technology and has very sharp edge steepness. It also applies a special coating assembly aimed at eliminating auto-fluorescence, improving transmitted wave front and lengthening filter life. Transmission range of this filter covers the emission peak of our analyte with the peak transmission of 83%. The excitation filter was not added because the monochromaticity of the DPSS laser source is very good and the reflected laser line would be eliminated by the dichroic and emission filter before reaching the detector.

Because the fluorescence collected by the infinity corrected objective will travel as infinity parallel rays after it passes through the objective, it is necessary to have a lens after the objective to focus the fluorescence signal to the pinhole. The focal length of this lens depends on approximate location of the pinhole in the system. An achromat doublet (G063215000, Linos Photonics, Inc, Milford, MA) with a focal length of 120 mm and clear aperture of 25.4 mm was selected for the system. It consists of a convex crown glass lens with low dispersion and a concave flint glass lens with a high dispersion to correct for both spherical and chromatic aberrations.

Another important optic component in the system is the front surface mirror used to redirect the light path 90° to another channel. A silver elliptical plane mirror (G340523000, Linos Photonics, Inc., Milford, MA) with a size of 22.4 x 31.5 mm was selected for our system. It has the highest reflection (>95%) for 450 nm to 12 μm wavelength and a surface flatness of 1/10 λ.

Table 5. Main parameters of the emission filter

Parameters	Value
Cut-On (nm)	470
Cut-Off (nm)	520
Average Transmission (%)	83
Edge Tolerance (nm)	±3
Attenuation Range (nm)	UV-1.3 x Cut-Off
Attenuation (OD)	>>5
Diameter (mm)	25

2.2 DESIGN AND ASSEMBLY OF AN OPTO-MECHANICAL SYSTEM

In order to reduce noise from vibration, the whole opto-mechanical assembly was built upon a 19" x 23" composite breadboard (NT54-252, Edmund Optics Inc., Barrington, NJ). We adopted a parallel mode in assembling the laser and collection optics, where the laser beam and fluorescence signal entering the detector are parallel with each other as indicated in Fig. 9. Arranging the laser (5), the optical tower and the stage C for the pinhole (6), the emission filter (7) and the PMT (8) on a single rail with engraved scales eased beam alignment. This linear arrangement also saved a lot of space for stage A.

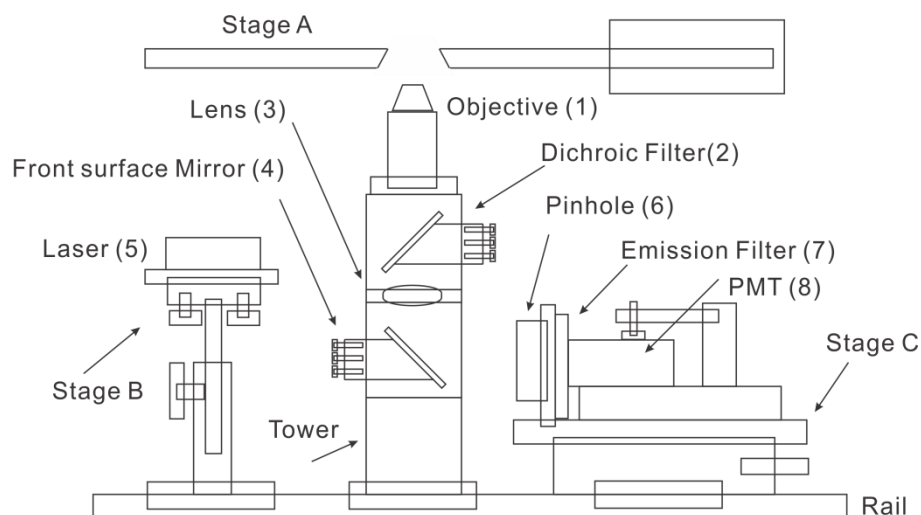


Figure 9. Schematic view of the confocal LIF system

Stage A was used to hold and control the location of the microfluidic device and the cell dish. It is composed of an aluminum platform and an x, y, z-translational stage mounted on a heavy duty rod. This 3D stage allowed the adjustment of as low as 1 μm in each dimension. The design of the aluminum platform on stage A is shown in Fig. 10 and is drawn to scale. An aperture with a size of 40 mm x 15 mm was located close to the center of this platform, which had a trapezoidal cross section and provided an easy access for the objective to the bottom of the microfluidic devices. Four plastic slide bars were fixed around the aperture by screws to hold the device in position. The aluminum platform was fixed to the x, y, z-linear translational stage through the connector located on the top right corner of this platform. Five circular wells with a diameter of 35 mm served as holders for cell dishes.

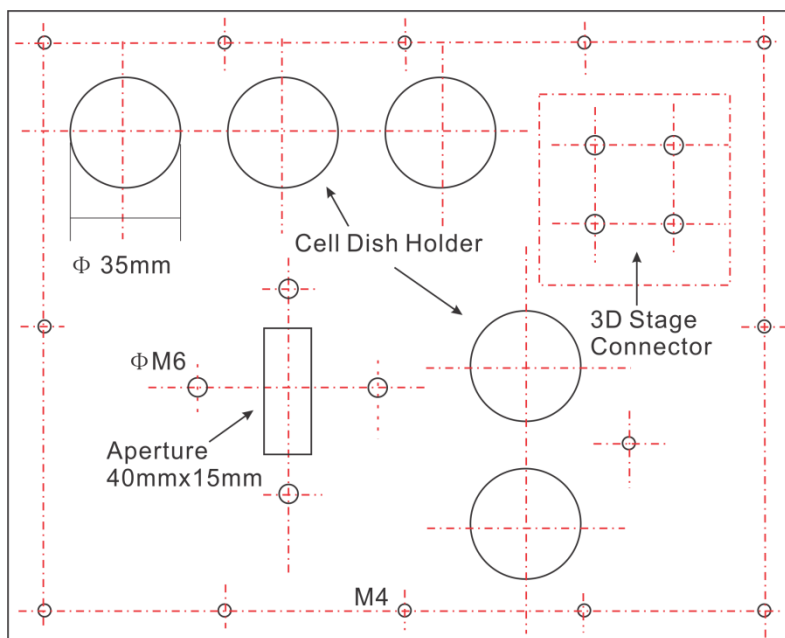


Figure 10. Top view of aluminum platform of stage A

The main part of stage B was a small tilt table sitting on the optical rail. The laser head was mounted on top of it horizontally with output of the beam directed towards the dichroic filter. The angle of the beam could be finely adjusted by turning three spring thumbscrew adjusters at the bottom. The height of the beam could be regulated by the height of the post below the table.

Stage C had an x-linear stage attached to the opposite side of the rail. It assembles three optical components together, the pinhole, the emission filter and the PMT. Fig. 11 is a platform of this stage. A square holder with a 33 mm x 33 mm through hole in the middle was attached to the left side of the platform. This holder was used to mount the pinhole positioner on one side and the emission filter holder on the other side. The size of this holder was specially calculated to make sure the pinhole and emission filter was closely attached to each other in order to avoid miscellaneous light coming from the environment. The head of the PMT was right against the holder of emission filter and the centers of the pinhole, emission filter and PMT photon sensitive surface were adjusted to the same height.

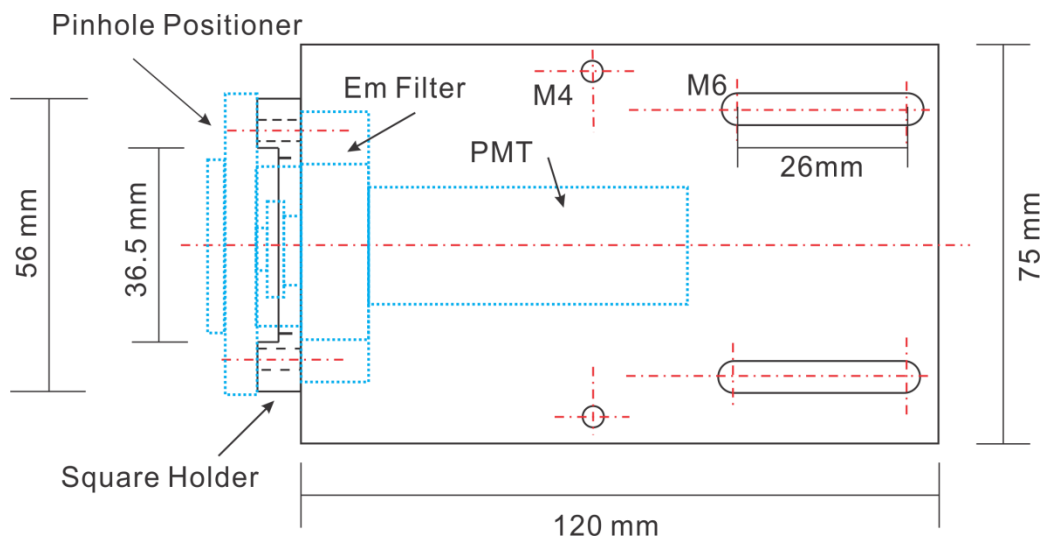


Figure 11. Top view of the platform of stage C

The other important part of the system is the optical tower standing in the middle of the rail. It was composed of three 40 mm cube frames piled on top of each other. The top of the tower held the objective (1), which was mounted on top of the first cube with an adaptor. The dichroic filter (2) was fixed on a beam-steering mirror holder and mounted inside the first cube. It reflected the incoming laser beam parallel to the rail toward the objective perpendicular to the rail. The front surface mirror (4) was fixed on a second mirror holder and resided in the second cube. It reflected the focused signal by the lens (3) mounted in a plate between the first and second cubes and directed it towards the pinhole. This two steering mirror holders had three thumbscrew adjusters for fine adjustment of the angle and the position of the mirror. A photograph of the confocal LIF detector is given in Fig. 12.

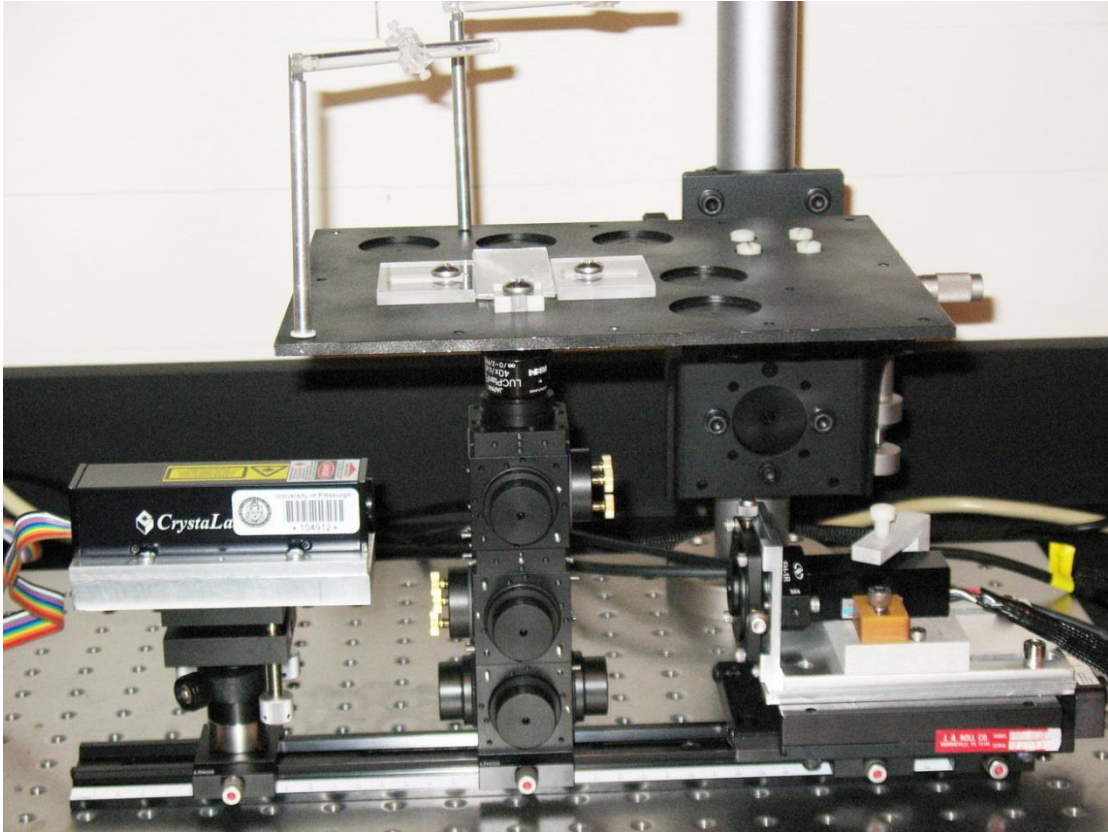


Figure 12. Photograph of the confocal LIF detector

2.3 DEVELOPMENT OF A CONTROL PROGRAM USING LABVIEW

The control program, named “Microfluidic Analysis System (MAS LAB)” used to control the detection system was developed using LabVIEW (version 8.2 National Instruments, Austin, TX), which is commonly used for data acquisition, instrument control, and industrial automation. Based on the functions to be achieved in real experiments, the control program can be divided into four modules: (1) data acquisition (analog input); (2) control and monitoring of high voltage power supply (HVPS) (analog input/output and digital I/O); (3) control of PMT sensitivity (analog output and digital I/O); (4) control of electrokinetic sampling (digital I/O). Two

multifunction data acquisition (DAQ) devices (NI PCI-6221 and a NI PCI-6733), two CB-68LPR I/O connector blocks, one SHC68-68-EPM cable, one SH68-68-EP cable and a RTSI Bus Cable were obtained from National Instruments to cooperate with the program.

Data acquisition is the main function of the control program. Current signals from the PMT were first converted into voltage by its internal amplifier and then were transferred to the DAQ device. A digitizer on the device applied an accurate internal sample clock to determine the sampling rate (up to 250 kS/s) and converted the input signal to digital values. These data were temporarily stored in a buffer region allocated by the program, then averaged and plotted on a chart in the front panel (user interface) during the experiment. Meanwhile, data would also be recorded in a user specified file and could be exported for analysis. The main parameters that can be controlled by user on the front panel are listed in Table 6.

Table 6. Main parameters for data collection

Parameters		Value
Channel	Max. (V)	10
	Min. (V)	-10
Sampling Rate (kS/s)		0-250
Averaging	Type	Linear/ Exponential
	Time (ms)	10/20/50/100
	Windows for DC and RMS (linear only)	Rectangular
		Hanning
		Low Side Lobe
	Output Function	DC only
		RMS only
DC and RMS		
File/Process Control		Save/Run/Stop

The state and voltage of two high voltage power supply (HVPS) racks, each of which had four positive or negative output channels, were controlled by using twenty-four digital

input/output (DIO) channels and eight analog output channels of two DAQ devices. There were three states for each individual output channel, namely “disable/float”, “output” and “GND”, which could be accomplished by the cooperation of three DIOs. Fig. 13 and Table 7 show how three DIOs are capable of controlling two HV relays (relay 1 and relay 2) and an enable/disable switch of the output channel to achieve three different states. Users could control the states and output voltage of these eight HV channels with the option of presetting the experiment time. All channels were automatically disabled after the completion of the experiment. There were additional four charts on the front panel, which served as monitors of voltage and current for one positive HV channel and one negative HV channel.

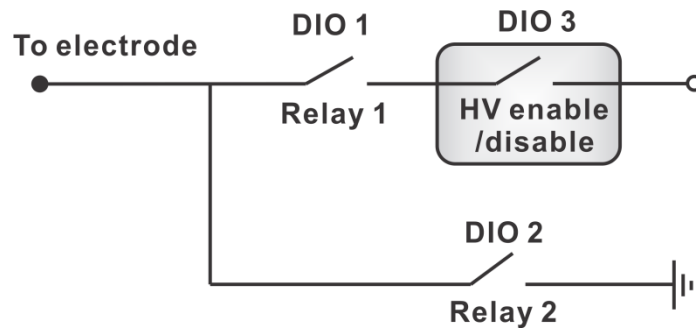


Figure 13. Setup of three DIOs and two HV relays for a single HV output channel

Table 7. Connection between levels of DIOs and the state of the state of the electrode

Level of DIOS			State of HV channel
DIO1	DIO2	DIO3	
1	0	1	Output
0	0	0	Disable/Float
0	1	0	GND

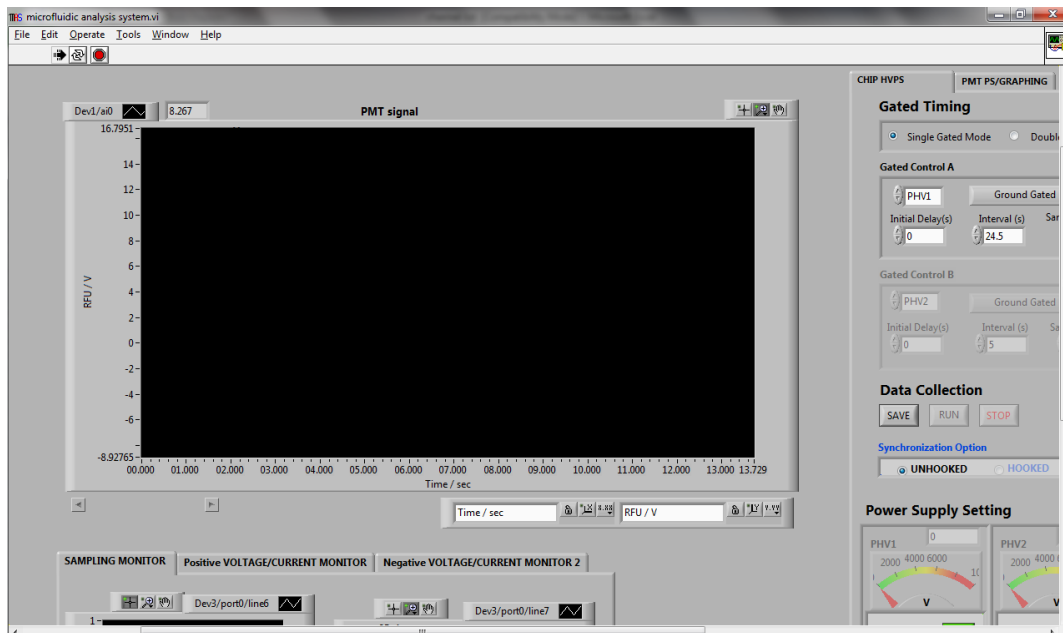
The PMT module used in our system had a built-in low-power consumption (± 15 V) high voltage power supply and a low noise amplifier. It also had an additional pinout to adjust the PMT sensitivity using an external low voltage. One of the analog output channels on PCI-6221

was assigned to adjust this control voltage ranging from 0.25 V to 0.9 V. In an experiment, users could adjust the value of the control voltage and had the option to lock this voltage at a certain value.

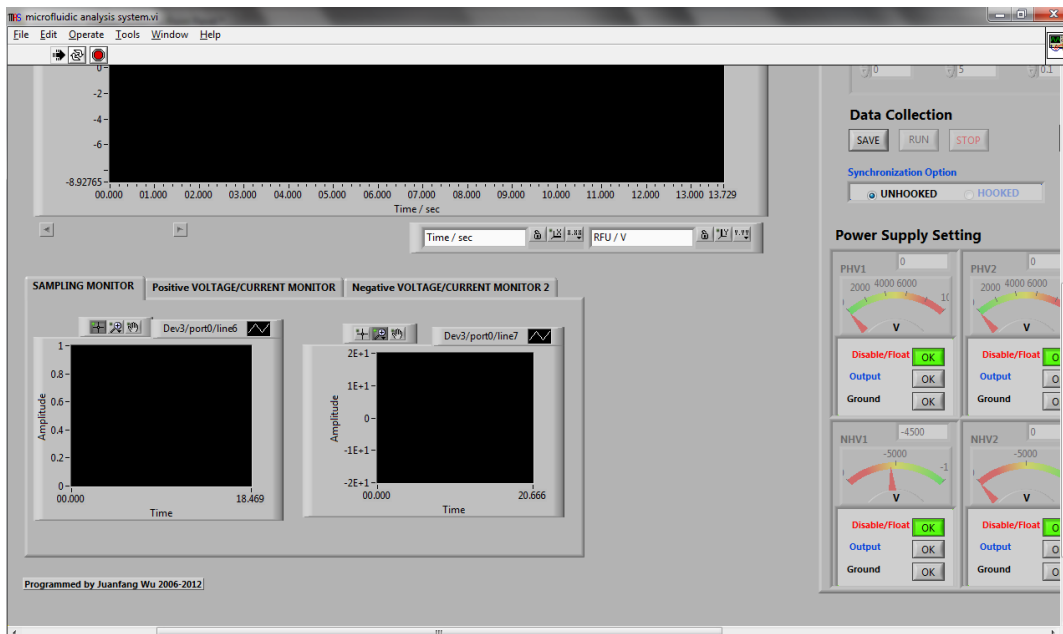
Electrokinetic gated sampling was performed on the microfluidic chip for continuous injecting sample into separation channel for analysis. In an experiment, users had the options to select “single gated mode” or “double gated mode”. In the “single gated mode”, one 32-bit counter of PCI-6221 controlled either a positive output channel or a negative output channel to generate an output signal switching between “float (injection)” and “GND” or “output” (analysis) based on the parameters specified by the user, which included “initial delay”, “interval”, “sampling time” and “repeat”. In the “double gated mode”, two 32-bit counters could simultaneously control two individual channels using specified parameters by the user. The program also had a synchronization option, which allowed the gated sampling to start at the same time as the data acquisition.

Finally, the program had a safe “SHUT DOWN” button. If anything unusual happened in the middle of an experiment, the user could disable all HV output channels, gated sampling, PMT control voltage, data acquisition and reinitialize everything into its default value by clicking this button. Screenshots of the user interface are given in Fig. 14.

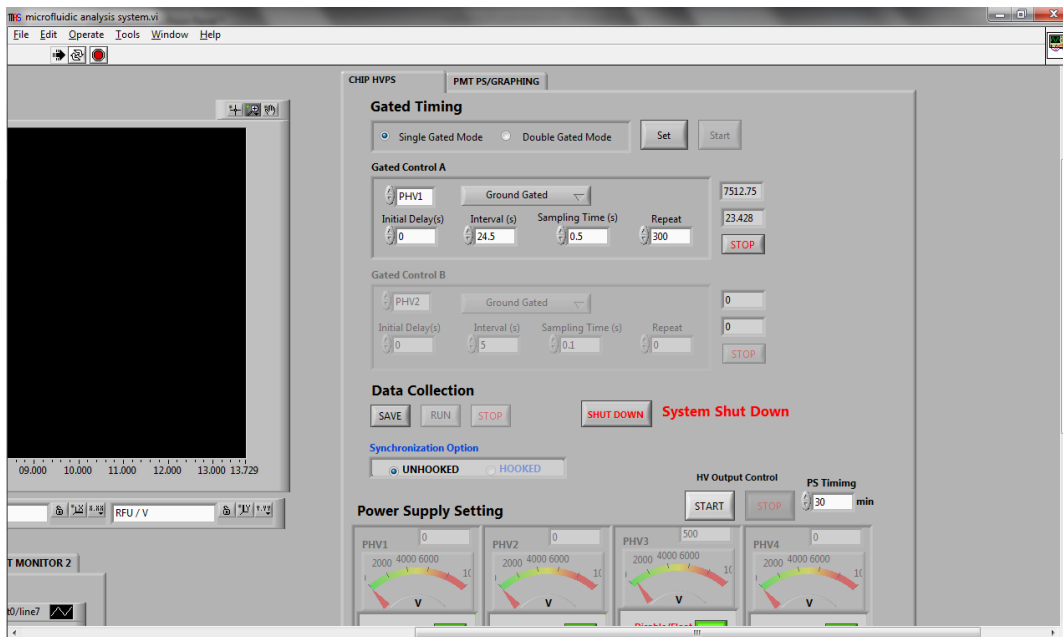
(a) PMT signal acquisition



(b) Monitoring of gated sampling, HV current and voltage



(c) Controlling of electrokinetic gated sampling



(d) Controlling of HVPS racks



(e) Controlling of PMT sensitivity and data averaging

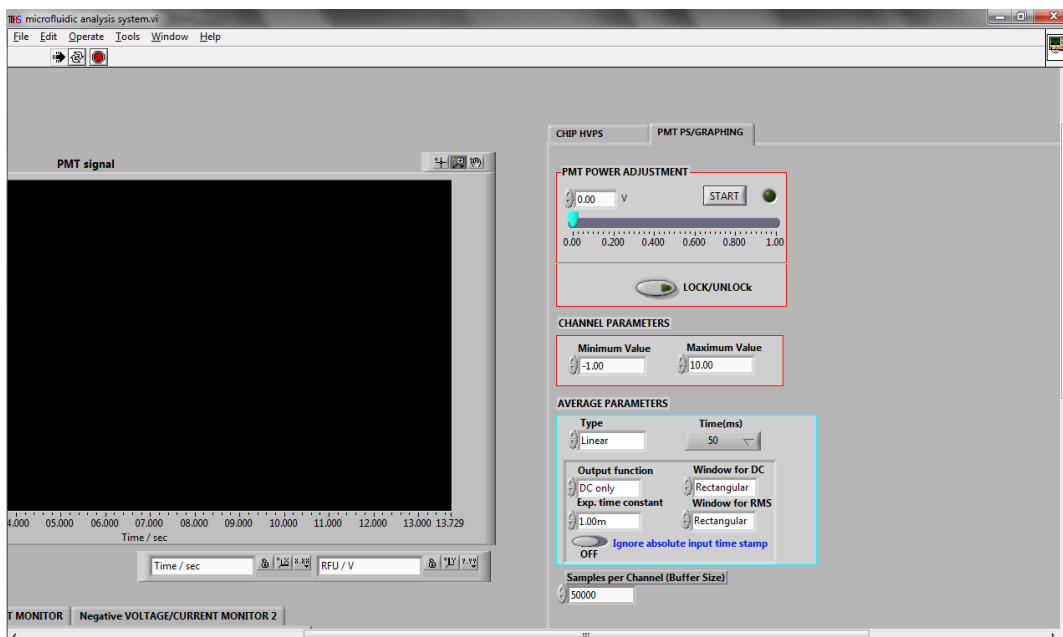


Figure 14. Screenshot of the user interface of “MAS LAB”

2.4 SYSTEM OPTIMIZATION AND PRELIMINARY EXPERIMENTS

2.4.1 Beam alignment

After the stage A, B, C and optical tower were assembled with optical components as shown in Fig. 12, beam alignment was performed to optimize the light path for best detection. A plain glass slide (25 mm x 75 mm, 1 mm thickness) with a fluorescent label on one side was used to assist the alignment of the laser beam. The cover glass was placed on the stage A at the location where the aperture was. After turning on the power supply, the laser beam was reflected 90° by the dichroic filter towards the objective and formed a bright fluorescent spot on the glass slide.

The diameter of the spot became larger when the glass slide was moved away from the focal plane by adjusting the height of the stage A, which could be used to test the location of the focal plane. Meanwhile, the shape of the fluorescent spot could be used to identify the direction of the laser beam. Three thumbscrews on the beam-steering mirror holder were adjusted so that the shape of the fluorescent spot was round, which indicated that laser beam was positioned along the light path of the objective and perpendicular to the platform of stage A. An eclipsed spot appeared when the beam hit the inner barrel of the objective lens.

After the excitation beam had been optimized, the glass slide was replaced by a simple test microfluidic chip as shown in Fig. 15. The bottom glass of the chip had a thickness of 1.0-1.1 mm. The diameter and the depth of the big round reservoir on the chip were about 6.7 mm and 1.8 mm, respectively. The depth of the channel on the chip was around 20 μm . About 50 μL of freshly prepared solution of ThioGlo-1 (0.5 μM) and GSH solution (0.1 μM) were loaded into the reservoir. A piece of fluorescent label would be placed in front of the pinhole facing the front surface mirror at a distance of ~ 10 cm. The height of the stage A was adjusted so that the laser beam was focused on the middle of the solution and a bright spot ($\phi \approx 1$ mm) could be detected on the fluorescent label. The thumbscrews of the dichroic filter holder were then finely adjusted so that three distinguished spots appeared on the fluorescent label and were clearly separated from each other. Among them, two spots were the images formed by a very small portion of laser beam reflected by the objective and the bottom glass of the microfluidic chip and only one of them was the true image of the fluorescence signal from the sample. The real signal image could be distinguished from the other two by changing the fluorescent label into a plain white paper. The image formed by the fluorescence signal had a unique color close to cyan, while the other two images formed by the reflection light had a color close to indigo like the color of the

laser beam. The image of the fluorescence signal must be separated from the images of the reflected light to prevent a noisy optical background.

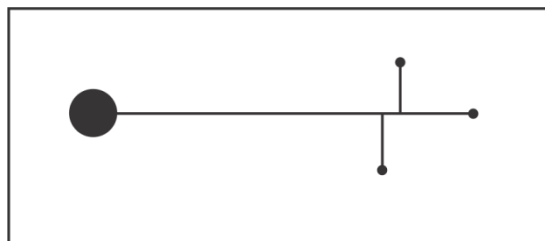


Figure 15. Sketch of the microfluidic chip for simple tests

In order to make sure that the focused fluorescence signal beam was in parallel with the rail, two iris diaphragms with the minimum aperture diameter of 1 mm were used to facilitate the alignment. A sketch of this setup is presented in Fig. 16. The emission filter was temporarily removed from stage C and placed between the front surface mirror and the paired iris diaphragms. The iris diaphragm A was placed at 10 cm away from the center of the front surface mirror. Iris diaphragm B was in parallel with A and the distance between them was about 2.5 cm. The height of diaphragms A and B were carefully adjusted so that the centers of both iris diaphragms were at the same level as the pinhole on stage C. A fluorescent label was placed between two iris diaphragms, both of which were closed down. Three thumbscrews on the beam steering holder of front surface mirror were finely adjusted so that a light spot was formed on the fluorescent label. Then, the label was removed and placed after iris diaphragm B. The angle of the mirror was further adjusted so that the focused signal beam could pass through the second diaphragm and formed a light spot on the label.

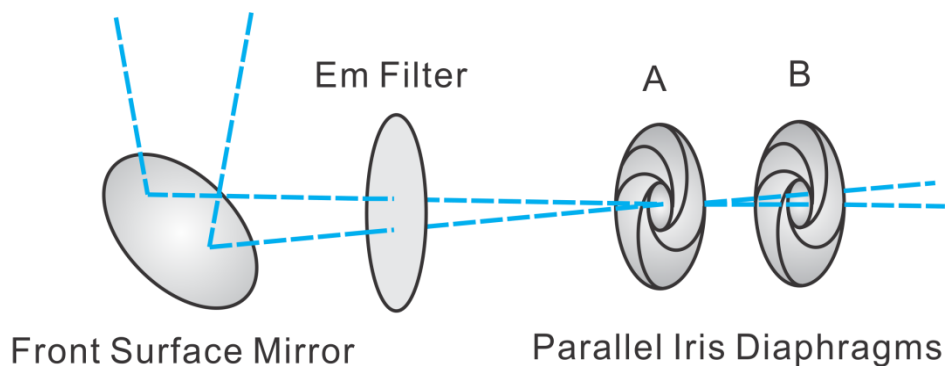


Figure 16. Setup of two iris diaphragms in the parallel alignment

After the focused beam was aligned in parallel with the rail, a 400 μm pinhole, the emission filter and the PMT would be fixed on stage C as shown in Fig. 12. The position of the pinhole would then be finely adjusted with the thumbscrews on the pinhole positioner, so that the focused beam was aimed at the center of the pinhole. After turning on the control program and PMT, fluorescence signals could be read on the chart on the front panel. The positions of stage A and the pinhole would be further tuned until a maximum signal could be detected.

2.4.2 Laser beam profile measurement

In the confocal LIF system, the laser beam is focused by the objective onto the sample inside the microchannel. It is useful to have a full picture of the intensity profile of the focused laser beam in order to optimize the dimension of the channel and other related parameters. Ideally, a laser beam can be depicted as a Gaussian intensity profile, which theoretically has a TEM_{00} mode. In the following experiment, a simple method is presented for measuring the laser beam intensity profile. The result will be further compared to that from theoretical calculation.

The setup used to measure the laser beam profile is presented in Fig. 17. A thin blade with a small aperture (red) in its center was bonded to a plain glass slide with a thickness of 1

mm. The collar ring on the 40x LUCPLFLN objective was adjusted to the corresponding position to compensate for the thickness of the glass slide. The platform of stage A was temporarily removed and the holder in Fig. 15 was fixed on the heavy-duty rod, so that the aperture on the blade was directly above the objective installed on the optical tower. A low power detector (818-UV, Newport, Irvine CA) with an active diameter of 1.13 cm was also fixed on the rod at a height just above the blade with its active surface facing the aperture on the blade. The distance between the detector and the front objective pupil lens was fixed to be about 2.8 cm. The adjustment factor for the power meter (1815-C, Newport, Irvine CA) connected to the detector was set to be 3.81×10^3 W/A for 400 nm wavelength measurements.

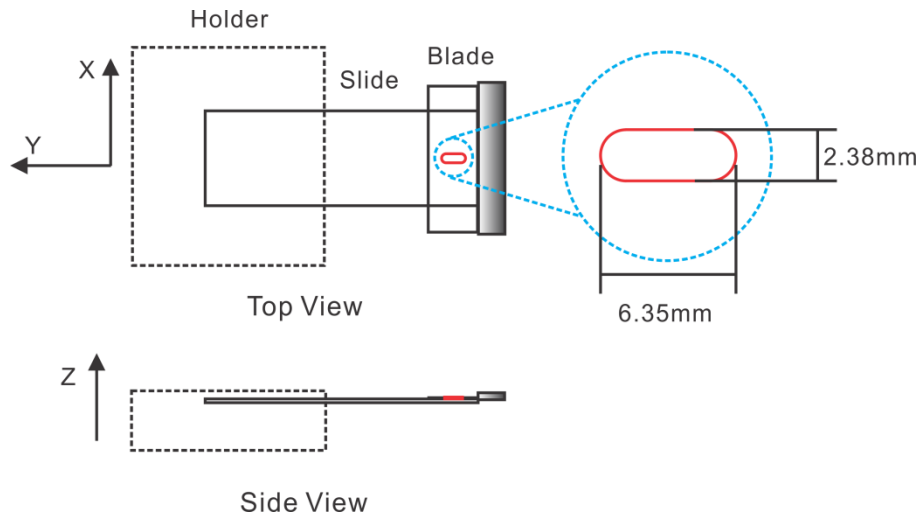


Figure 17. Setup for the laser beam profile measurement

At the beginning of the experiment, the height of the glass slide was slowly decreased until the bottom of the glass slide was just in contact with the front surface of the objective pupil lens. The reading of the z-axis micrometer drive was recorded. The glass slide was then lifted up ~2 mm above the objective and the reading of z-axis micrometer drive was recorded again. The actual distance between the surface of pupil lens and the bottom of the glass slide, D_z (z is the

propagation direction of the focused laser beam), was calculated from the difference between two readings of the micrometer drive at different heights. When the height of the glass slide was fixed, the y-axis linear stage was adjusted so that the laser beam passed through the center of the aperture on the blade. After that, the micrometer drive on the x-axis was turned to a position where the laser beam was fully blocked by one side of the blade and the reading on the power meter was 0.00 mW. The x-axis drive was then turned back slowly step by step until the reading on the power meter reached its maximum. Readings of the power meter and the micrometer drive in each step were recorded for further analysis. This whole process was repeated when the height of the glass slide was changed to other values in z-axis.

The relationship between the laser beam power readings and x-axis positions at different D_z , (2.507 mm (a1), 3.250 mm (b1), 4.030 mm (c1)) are plotted in Fig. 16. Each step in our experiment along the x-axis can be treated as a definite integration of the laser beam power unblocked by the blade. The results therefore could be differentiated and fitted to the Gaussian intensity profile of a theoretical TEM_{00} mode according to Eq. 6.

$$y = y_0 + \frac{A}{w\sqrt{\pi/2}} e^{-2\left(\frac{x-x_c}{w}\right)^2} \quad (6)$$

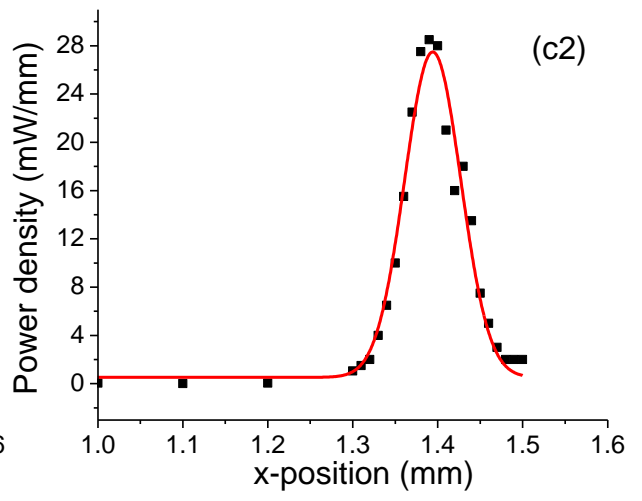
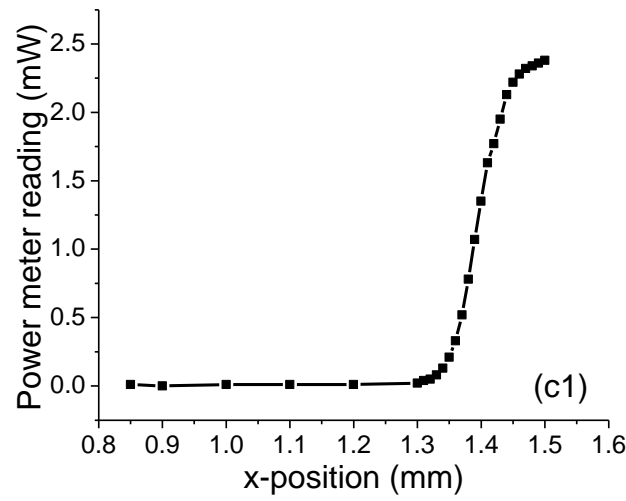
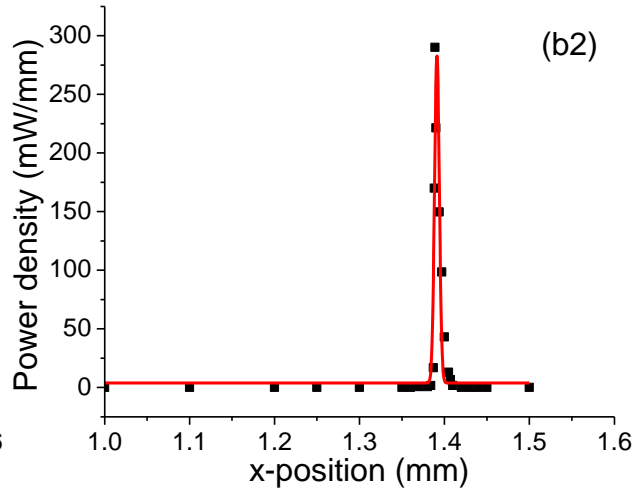
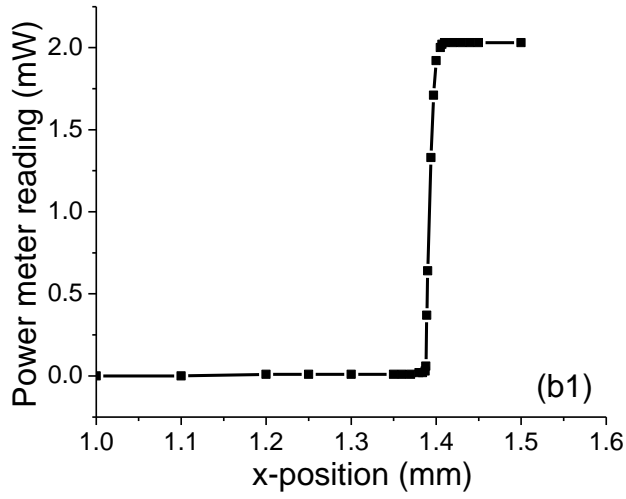
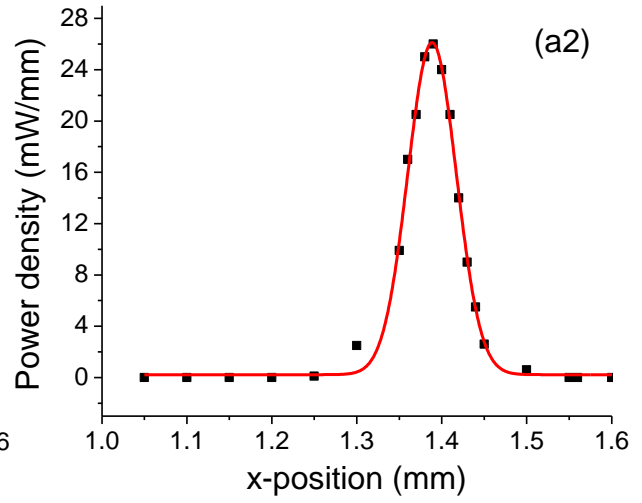
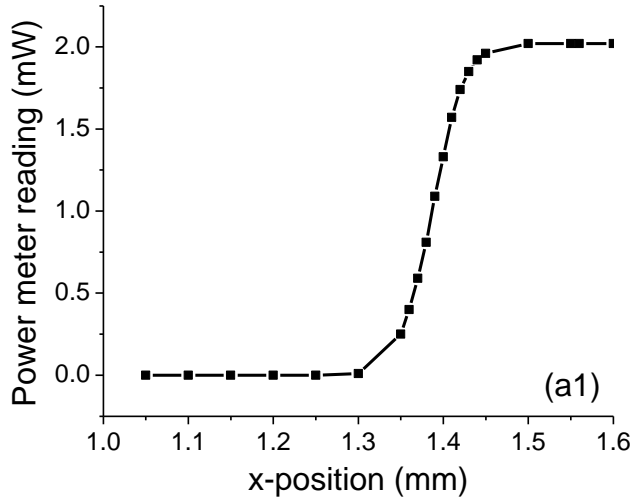
Where y_0 , x_c , w and A are the offset, center, width and area of the Gaussian distribution, respectively. In an irradiance distribution of the Gaussian TEM_{00} beam, the beam intensity can be expressed by²⁰²

$$I(r, z) = I_0 \left(\frac{w_0}{w(z)}\right)^2 e^{-2\left(\frac{r}{w(z)}\right)^2} \quad (7-a)$$

Or

$$I(r, z) = \frac{2P}{\pi w(z)^2} e^{-2\left(\frac{r}{w(z)}\right)^2} \quad (7-b)$$

Here, z is the distance the wave has propagated from the plane where the wavefront is flat ($z = 0$ is the location of a Gaussian waist); $w(z)$ is the beam width defined as the radius of $1/e^2$ contour after the beam has propagated a distance z ; w_0 is the beam width of the waist defined as the radius of the $1/e^2$ contour at the Gaussian waist; I_0 is the beam intensity of $1/e^2$ contour at the Gaussian waist; P is the total beam power; and r is the radical distance from the center of the beam. Comparing Eq. 6 and Eq. 7, it is not difficult to find out that the y_0 , x_c , w and A in Eq. 6 obtained from experiments correspond to the offset for the power density, beam center, beam width (radius of the $1/e^2$ irradiance contour) and total beam power, respectively. The fitting constants for three runs are listed in Table 8. It is obvious from the Fig. 18 that the power density (mW/mm) of the laser beam in run b is much larger than that in run a or c. The D_z in run b is 3.250 mm, which falls into the listed W.D. range of this objective (2.7-4 mm).



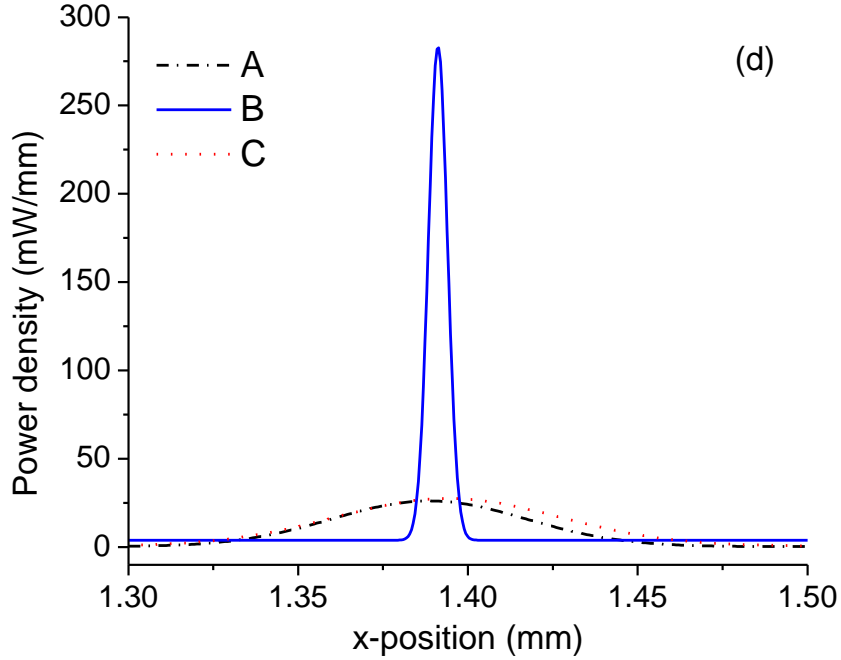


Figure 18. Results from laser beam profile measurements at different D_z

$a_1 = 2.507$ mm; $b_1 = 3.250$ mm; $c_1 = 4.030$ mm; The results are then differentiated and fitted to Gaussian distribution and plotted in a2, b2, c2, respectively. Three Gaussian fits are plotted together in plot d for comparison.

Table 8. Gaussian fitting results for three measurements

Run #	D_z (mm)	A (mW)	x_c (mm)	w (mm)	y_0 (mW/mm)	Peak density (mW/mm)	R^2
a	2.507	1.85	1.389	0.057	0.223	25.9	0.973
b	3.250	1.97	1.391	0.006	3.84	280	0.867
c	4.030	2.24	1.394	0.066	0.528	27.0	0.996

When Gaussian beam propagates through a simple lens, the output beam will still have a Gaussian intensity profile. Therefore, it is reasonable to fit our results by using the propagation equation for a laser beam. In practice, a beam quality factor, M^2 , is generally used to describe the

deviation of a real laser beam from an ideal Gaussian beam. The radius of the $1/e^2$ contour after a real beam has propagated a distance z , $w_r(z)$, can be expressed by Eq. 8²⁰³

$$w_r(z) = w_{0r} \left[1 + \left(\frac{\lambda M^2}{\pi w_{0r}^2} (z - z_0) \right)^2 \right]^{1/2} \quad (8)$$

Where λ is the wavelength of the beam; w_{0r} is the radius of the $1/e^2$ irradiance contour of a real beam at the beam waist and z_0 is the location of the beam waist along the direction of wave propagation. In our experiment, D_z can be related with z by

$$D_z = z - d \quad (9-a)$$

$$D_{z0} = z_0 - d \quad (9-b)$$

Where d is the thickness of the glass slide and D_{z0} is the distance between the front objective pupil lens and the bottom glass slide when the beam waist is located at the top surface of the glass slide (ignoring any effect caused by the finite thickness of the blade in our experiment).

Replacing z and z_0 with D_z and D_{z0} will give

$$w_r(D_z) = w_{0R} \left[1 + \left(\frac{\lambda M^2}{\pi w_{0r}^2} (D_z - D_{z0}) \right)^2 \right]^{1/2} \quad (10)$$

The parameters and results from nonlinear curve fitting based on Eq. 10 are given in Table 9 and Fig. 19.

Table 9. Equations and parameters for nonlinear curve fitting of the beam width and D_z

Known variable		$\lambda = 403.1 \times 10^{-6} \text{ mm}$				
		$M^2 = 1.2$				
Dependent Variable		W_R (width of the Gaussian distribution from Table 9)				
Independent Variable		D_z (see Table 9)				
Results	Parameters	w_{0r} (μm)	Value	1.9	Error	0.04
		D_{z0} (mm)		3.204		0.013
	R^2	0.99724				

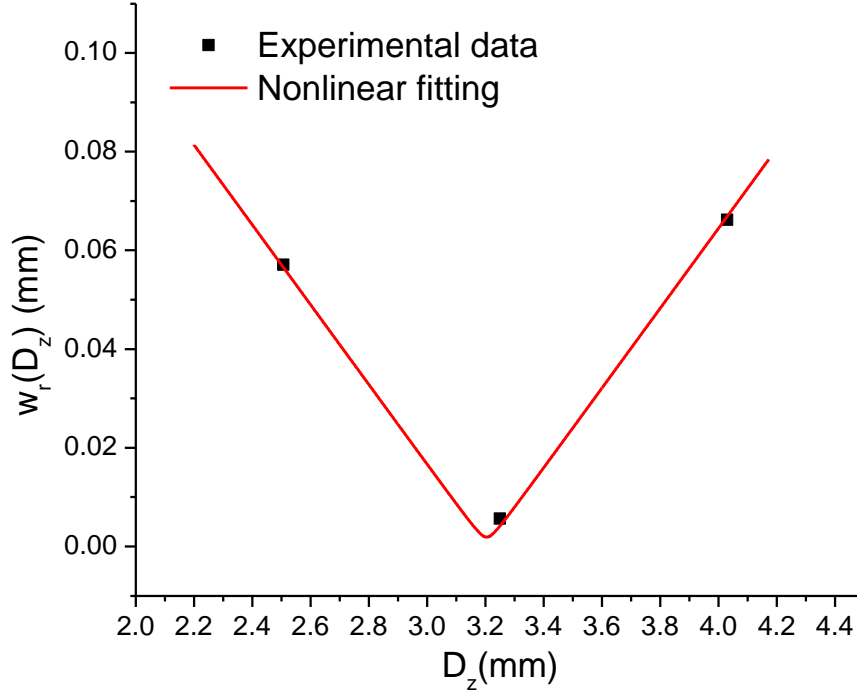


Figure 19. Nonlinear curve fitting of the beam width to D_z

Table 9 gives two important parameters obtained from nonlinear curve fitting. One is the radius of the beam waist, w_{0r} , which is around $1.9 \mu\text{m}$. The other is the W.D. of this objective with a 1 mm thick glass slide, D_{z0} , which is 3.205 mm (Strictly speaking, W.D. $\neq D_{z0}$, but they are very close to each other in our case.)

Meanwhile, it is possible to calculate the radius and the location of the beam waist after a spherical Gaussian beam passes through a train of lenses by using method developed by S. A. Self in 1983.²⁰⁴ If the waist of the input beam represents the objective and the waist of the output beam represents the image, the relationship between the objective distance s , image distance s'' , and focal length of the lens under paraxial conditions is given by Eq. 11:

$$\frac{1}{s + \left(\frac{z_R}{M^2}\right)^2 / (s - f)} + \frac{1}{s''} = \frac{1}{f} \quad (11)$$

Where z_R is the Rayleigh range (the distance over which the beam radius increased by a factor of $\sqrt{2}$ or the distance from the waist at which the wavefront curvature is a maximum) of the input beam defined by Eq. 12

$$z_R = \frac{\pi w_{0r}^2}{\lambda} \quad (12)$$

The magnification, m , is given by

$$m = \frac{w_{0r}''}{w_{0r}} = \frac{1}{\sqrt{\{[1 - (s/f)]^2 + [(z_R/M^2)/f]^2\}}} \quad (13)$$

where w_{0r}'' is the width of a real output beam waist. In most cases, the beam waist is designed to be very close to the output surface of the laser. Therefore we can assume that the w_{0r} is 0.5 mm and s is ≈ 130 mm for our setup. The focal length for 40x objective is 4.5 mm. z_R , s'' and w_{0r}'' can be calculated from Eq. 11, 12, 13 are 1947 mm, 4.501 mm and 1.391 μm , respectively, which indicates that the waist of the output beam is not exact at the focal plane of the objective, but 1 μm away. However, the beam width at the focal plane is very close to that of the beam waist based on the fitting results obtained in Fig. 19. The results from the beam profile experiments are consistent with what we got from the theoretical calculation.

2.4.3 Noise experiments and system performance testing

2.4.3.1 Noise sources

Identification of the dominant noise sources is of vital importance for optimizing experimental variables systematically and improving the instrumental design to obtain a better S/N. The total noise observed in a measurement may arise from several sources, among which one or two noise sources are dominant. For a photoluminescence measurement, the total signal, E_t , equals to the

summation of the analytical luminescence signal E_S and the blank signal E_{bk} , where E_{bk} includes contributions from the background luminescence signal, the dark current and scattering. Similarly, the rms noise in the total signal, σ_t , has contributions from analytical signal noise (σ_S) and the blank signals noise (σ_{bk}). σ_S is mainly due to analytical signal shot noise, $(\sigma_S)_s$ and flicker noise $(\sigma_S)_f$. σ_{bk} is originated from noise in the background signal noise, σ_B , and the total dark current noise, σ_{dt} . Furthermore, σ_B can be divided into background signal shot noise, $(\sigma_B)_s$ and flicker noise $(\sigma_B)_f$. On the other hand, σ_{dt} includes the actual noise in the dark current, σ_d , and the amplifier-readout noise, σ_{ar} . Finally, σ_d is contributed from the dark current shot noise, $(\sigma_d)_s$, and the excess noise, $(\sigma_d)_{ex}$. The rms noise from different sources can be added up quadratically if all of them are assumed to be totally uncorrelated. The affiliation among all these various noise sources is summarized in Fig. 20. It can be concluded that there are three primary noises sources existing in the analog signal processing: the noise in the analytical signal, the noise in the background signal, and the noise from the dark current and amplifier-readout system.¹⁵²

$$\begin{aligned}
 \sigma_t^2 &= (\sigma_S)_s^2 + (\sigma_S)_f^2 + (\sigma_B)_s^2 + (\sigma_B)_f^2 + (\sigma_d)_s^2 + (\sigma_d)_{ex}^2 + \sigma_{ar}^2 \\
 &\quad \underbrace{\hspace{10em}}_{\sigma_S^2} \quad \underbrace{\hspace{10em}}_{\sigma_B^2} \quad \underbrace{\hspace{10em}}_{\sigma_d^2} \\
 &\quad \underbrace{\hspace{15em}}_{\sigma_{dt}^2} \\
 &\quad \underbrace{\hspace{20em}}_{\sigma_{bk}^2} \\
 &\quad \underbrace{\hspace{25em}}_{\sigma_t^2}
 \end{aligned}$$

Figure 20. Various rms noise sources for a photoluminescence measurement

S/N is an important parameter of the system. Mathematically, it is defined as

$$\frac{S}{N} = \frac{E_S}{\sigma_t} \quad (14)$$

For a confocal LIF system with a PMT as fluorescence signal monitor, the main sources of $(\sigma_S)_s$ are shot noise, including the quantum noise and PMT multiplication noise. $(\sigma_S)_f$ is mainly due to the variation in laser radiance resulted from the fluctuation in the electrical power, temperature or vibrations. Besides, the vibration of the whole setup, especially the sample stage also contributes to the flicker noise in analytical signal. σ_B mainly comes from background scattering and luminescence noises, such as the noise of scattering light from the wall of the microchannel, and noises of light from computer monitor or other additional light sources in the room. It is worth to notice that laser flicker noise is also related with σ_B , because just like the analytical fluorescence, the background fluorescence and scattering signals are also proportional to the radiant power of excitation source and will be affected equivalently as the analytical signal by the source flicker noise. σ_{dt} is relatively weak compared with other noises mentioned above according to the listed values provided the manufacturer.¹⁵²

2.4.3.2 Identification of different noise sources

Several experiments were designed to test the rms noises from different sources and identify the dominant one(s) in the system. The first experiment mainly was designed to test the environmental noises such as the luminescence from computer monitor and a weak ceiling lamp. The laser power was set to be 3.0 mW and PMT control voltage was 0.556 V. No cover glass was placed on the sample stage and stage C was not shielded with light tight cover. The sampling rate was 10 Hz. A LUCPLFLN 20 x objective is used in the system. The results of this experiment are summarized in Table 10.

Table 10. Environmental noises experiment

Parameters	Only monitor on	Only lamp on	Monitor On and Lamp On	Monitor off and Lamp off
σ_{bk} (mV)	2.460	2.165	3.338	0.428
E_{bk} (mV)	0.494	7.578	8.674	0.206

Laser power is 3.0 mW; PMT control voltage is 0.556 V; 20x objective; Sampling rate is 10 Hz; No cover glass on the stage; sample is not loaded; no light tight cover over the stage C.

It is indicated by the Table 10 that the main blank signal and noises (without chip) in this experiment were resulted from background luminescence of the computer monitor and ceiling lamp. The dark current and amplifier readout contributed only a very small portion of the blank signal and noise with values of only 0.206 mV and 0.428 mV, respectively. As the noise from the computer monitor, σ_M , ceiling lamp, σ_L , and total dark current noise, σ_{td} , are independent, they can be added quadratically as follows

$$\sigma_{bk} = \sqrt{\sigma_M^2 + \sigma_L^2 + \sigma_{td}^2} \quad (15)$$

Based on Eq. 15 and the data in Table 10, the rms noises and signal from different sources and their contribution (%) can be calculated as in Table 11. It is obvious that ceiling lamp contributed 93.7% of the background signal. Meanwhile noises from computer monitor and ceiling lamp accounted for 55.6% and 42.7% of the total noises, respectively. Therefore, it was necessary to turn off the ceiling lamp and shield the stage C with a light tight cover during the experiments to minimize these background noises.

Table 11. rms noise from different background sources

Parameters	Monitor Only (Calc.)	Lamp Only (Calc.)	Total Dark Current (Expt.)	Monitor, Lamp and total dark current	
				Calc. ^{*1}	Expt. ^{*2}
σ_{bk} (mV)	2.422	2.122	0.428	3.248	3.338
%	55.6	42.7	1.74		
E_{bk} (mV)	0.288	7.372	0.206	7.866	8.674
%	3.66	93.7	2.62		

*1 Obtained by adding the values in the first three columns.

*2 Obtained from Table 10 under the conditions when computer monitor and ceiling lamp are both on.

The following experiment was designed to study the noises from the scattering and reflecting light from the cover glass. Most of the basic parameters for this experiment were same with that in the first experiment, except that a cover glass of 1 mm thickness was placed on the sample stage and the laser power was increase to 7.4 mW. Ceiling lamp was kept off for all the experiments discussed below. The total signal and rms noise from scattering light are summarized in Table 12.

Table 12. Scattering experiment

Parameters	Scattering Expt.	Total dark current (from Table 10)	Scattering light (Calc.)
σ_{bk} (mV)	0.662	0.428	0.505
E_{bk} (mV)	0.485	0.206	0.279

Laser power is 7.4 mW; PMT control voltage is 0.556 V; 20x objective; Sampling rate is 10 Hz; with cover glass on the stage; sample is not loaded; both computer monitor and ceiling lamp are off, no light tight cover over the stage C.

Compared with σ_{dt} in the first experiment, the result in the scattering experiment where computer monitor was off showed a little increase in its value. This was due to the noise of scattering light from the cover glass. Assuming that σ_{dt} was the same for both experiments, the contribution of signal and noise from the scattering light could be estimated to be 0.279 mV and

0.505 mV, respectively, which were relatively weak compared with the noise from the computer monitor and ceiling lamp.

In the third experiment, the laser head and PMT were temporarily removed from the system and lined up with several neutral density filters between them. The heights of the PMT and laser were adjusted so that laser beam was just aimed at the active surface of the PMT. The goal of this experiment was to test the noise contributed by the laser and PMT together. Like the scattering experiment, the sampling rate for this experiment was 10 Hz and the experiment was carried out when the ceiling lamp and computer monitor were both off. Results and main parameters of this experiment are listed in Table 13.

Table 13. Laser beam and PMT stability analysis

Run #	Laser Power (mW)	Neutral Density Filter (OD)	σ_t (V)	E_t (V)	S/N (E_t/σ_t)
1	3.00	4	0.014	5.861	413
2	10.0	5	0.007	1.538	220
3	15.0	5	0.008	2.418	286

Sampling rate is 10 Hz; ceiling lamp and computer monitor are both off; PMT control voltage 0.375 V.

In this experiment, the laser beam could be treated as the analytical signal. The noise sources in this experiment composed of the shot noise of PMT and laser flicker noise. Based on the results from the first noise experiment, total dark noise only accounted for a small portion of the total noise. Table 13 shows that the total rms noise from PMT and laser increased when the analytical signal was enhanced. Linear fitting of $\lg(E_t/\sigma_t)$ against $\lg(E_t)$ in Fig. 21 shows that S/N was directly proportional to $(E_t)^{0.46}$, which further demonstrates that the shot noise was the dominant source of noise as the exponent was close to 0.5.

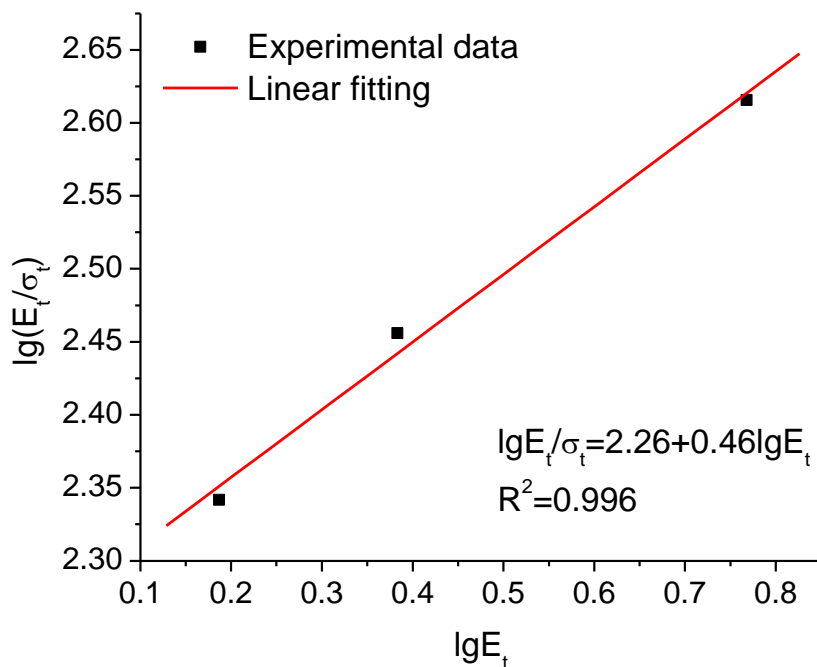


Figure 21. Relationship between E_t/σ_t and E_t when noises are contributed by laser and PMT

Finally, the real sample was tested when the stage C was shielded with a light tight cover. The ceiling lamp was kept off throughout the experiment, but the computer monitor was not turned off, which was required to monitor and control the experiments. A 40x objective was installed in the system. Newly prepared sample solution, which contained 0.50 mM ThioGlo-1 and 0.10 mM GSH in 50 mM Tris-HCl buffer (pH=7.0), was loaded into the large reservoir on microfluidic chip shown in Fig. 15. The sample was then introduced into the channel by applying vacuum at the other end of the channel. The level of the stage A was finely adjusted so that the laser beam was focused onto the solution inside the channel. PMT control voltage was set to be 0.5 V and the laser power was fixed at 3.0 mW. The total rms noise was 0.084 V, while the total signal was 6.896 V (Table 14). Fig. 22 is a picture of microfluidic chip with sample in reservoir taken during the experiment. Compared with the rms noise in the previous experiments, it is

obvious that analytical signal shot noise and flicker noise accounted for a large percentage of the total noise.

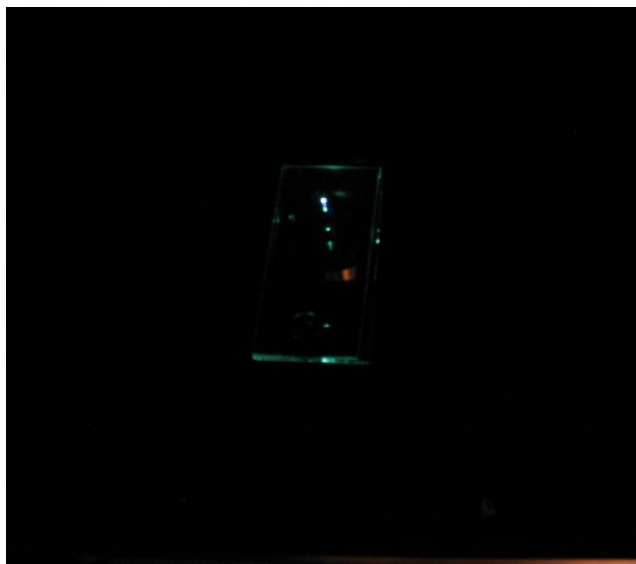


Figure 22. Photograph of the microfluidic chip during the experiment

2.4.3.3 Noise reduction

Three different methods will be applied to reduce the noise in our system, averaging and low pass filter, reduction of stage vibration. As we already know that the analytical and background shot noise, $(\sigma_s)_s$, is a fundamental noise is due to the random emission of photons from a source and the random fluctuation in the PMT gain due to the random nature of secondary emission of electrons in the dynodes. The probability of photon counts in a certain integration time can be described with the Poisson probability distribution with a well-defined mean and variance. As the magnitude of the shot noise power is independent of frequency, it belongs to white noise (or Gaussian noise).¹⁵² When the expected value of noise is zero, after performing signal averaging, the expected value of the output signal is statistically close to the mean. While the expected value of the rms noise will be reduced to $1/\sqrt{n}$ of the original rms noise based on the error propagation formula and quadratic addition (additive variances) property, where n is the

number of points used in the averaging. Therefore, the S/N will be enhanced to \sqrt{n} of the value before signal averaging is performed. It must be noticed that signal averaging doesn't correct for pink noise or interference noise. In addition, proper correction must be done before it is applied to signal with a time-dependent drifting characteristics.²⁰⁵

When applying averaging in experiments, attention must be paid to some practical limits, such as the sample clock rate of the DAQ device, the processor's speed, buffer size. Besides, all samples taken for averaging should come from a range of time where the real signal varies little in amplitude compared with the error that you are trying to eliminate. In other words, it is necessary to know the maximum frequency component of a signal. In our system, the resolution is acceptable when using a sampling rate of 20 Hz (50 ms/point) for a peak with a standard deviation of 0.1 s (about 10 points per signal peak (5σ)). If we set the sample clock rate of the DAQ device to be 10000 Hz and the number of averaged points to be 100, the temporal resolution for the system will remain to be 10 ms (100 Hz). Because the number of averaged points in one period will be 100 and the rms noise will decrease to 1/10 of its original value.

Averaging is simply achieved by using "averaging function" in control program. The averaging time was fixed to be 50 ms, but the sample clock rate was changed from 20, 100, 1000, 10000 and 100000 Hz. In this case, the temporal resolution (50 ms or 20 Hz) was maintained at a same level for all the experiments while different numbers of points, n , were averaged. PMT control voltage was adjusted to be 0.5 V and the laser power was set to be 3.0 mW. Sample solutions, which contained 0.50 mM ThioGlo-1 and 0.10 mM GSH in 50 mM Tris-HCl buffer at pH 7.0, was introduced into the microchannel of the microfluidic chip shown in Fig. 15 by applying vacuum at the other end of the channel. A 40x objective was used to focus the laser beam into the center of the channel. The results are shown in Table 14 and Fig. 23.

Table 14. Signal averaging experiment

Sample Clock Rate	Averaged Points	Averaged time (ms)	E_t (V)	σ_{avg} (V)	S/N (E_t/σ_{avg})
20	1	50	6.896	0.084	82
100	5	50	6.916	0.030	227
1000	50	50	6.889	0.014	492
10000	500	50	6.863	0.013	531
100000	5000	50	6.852	0.011	614

Laser power is 3.0 mW; PMT control voltage is 0.5 V; 40x objective; averaging time is 50 ms (sampling rate 20 Hz); ceiling lamp is off and computer monitor is on; light tight cover over the stage C; laser is focused to the center of the channel.

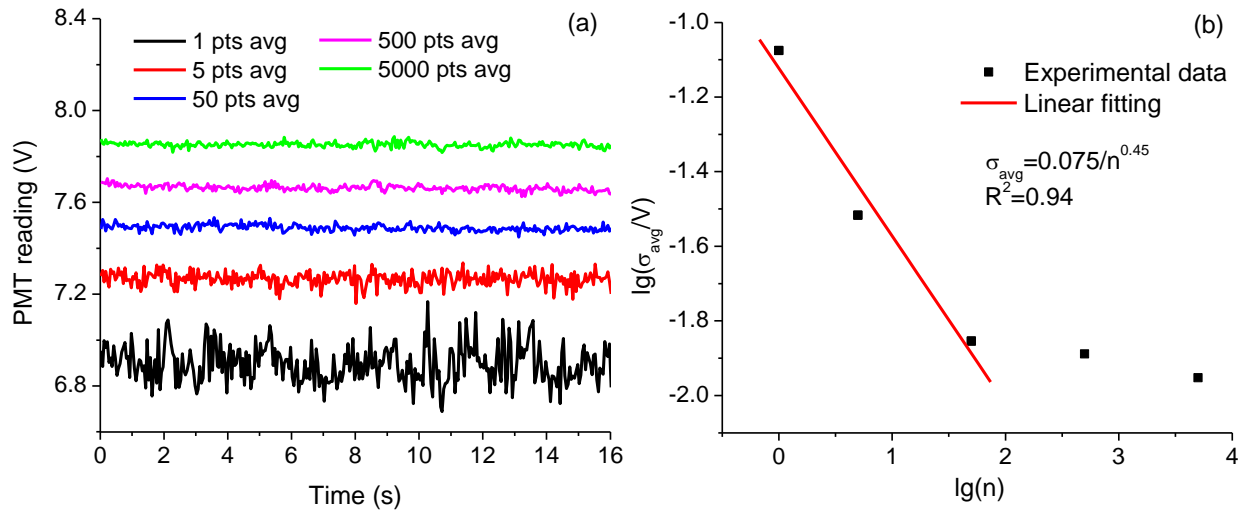


Figure 23. Results from signal averaging experiment

(a) PMT signals obtained when different averaged points (pts) are applied; (b) linear fitting of averaged rms noise to the number of averaged points in the log plot.

The linear regression of the first three data points indicates that the averaged rms noise level, σ_{avg} , is kept decreasing linearly as the number of averaged points, n , is increasing within a certain range (0-50 points). σ_{avg} is proportional to $(n)^{-0.45}$, which is consistent with what is predicted by the theory (-0.5 is the theoretical exponent of n). However, this linearity changes after the number of averaged points reaches a certain level, which is ~ 50 pts in our case. This

phenomenon implies that there are some other noise sources with certain frequencies in our system, which cannot be removed by performing signal averaging. Those noises must be removed by applying other methods.

The function of an electronic low pass filter is to restrict the bandwidth of the input signal so that the aliases caused by the noise with frequency higher than Nyquist frequency can be removed. Nyquist frequency is defined as half of the sampling frequency in a sampling system. Aliasing exists when the frequency of a signal or noise is higher than the Nyquist frequency. When the highest frequency component of interest in the measurement is higher than the Nyquist frequency, the signal of interest will be under sampled and the sampling rate will generate an incorrect low frequency alias. Meanwhile, the actual signal usually contain noises with frequencies that is higher than the Nyquist frequency, aliases of these frequencies will be added to the signal of interest, distort the otherwise correct signal and generate a noisy background.²⁰⁶

The alias frequency f_a of a signal or noise with high frequency equals to the minimum absolute value of the difference between the frequency of the input signal, f , and the closest integer multiple of the sampling rate, Nf_s , as given by Eq. 16

$$f_a = |f - Nf_s|_{\min} \quad (16)$$

It can be deduced from the above equation that signal must be sampled at a rate no less than twice the highest frequency component of interest in the signal ($f_s > 2f$) in order to capture the highest frequency component of interest and prevent aliasing.²⁰⁷ In practice, the sampling rate must be set high enough (about 5 to 10 times the highest frequency components in the signal) to obtain accurate measurements in the output data. Meanwhile, to prevent aliasing of noises with high frequencies, it is often necessary to add a low pass filter to attenuate frequencies higher than

the Nyquist frequency and restrict the bandwidth of the input signal before the analog-to-digital converter (ADC) in the DAQ device.

In the following experiment, a Wavetek 852 dual Hi/Lo variable filter (Willtek, Germany) was added between the signal output end of PMT and DAQ device. PMT control voltage was adjusted to be 0.5 V and the laser power was set to be 3.0 mW. Newly prepared sample solutions containing 0.50 mM ThioGlo-1 and 0.10 mM GSH in 50 mM Tris-HCl buffer at pH 7.0 was loaded into the big reservoir of the microfluidic chip shown in Fig. 15. A 40x objective was used to focus the laser beam into the center of the reservoir. The sample clock rate was kept at 1000 Hz throughout the experiment and no averaging was performed. The cut off frequency of the filter was changed from 10 Hz to 5000 Hz. Under each specific frequency, the experiment was repeated for 10 runs and each lasted for ~15 s. Before using with Fast Fourier Transform (FFT) to extract the character frequency of the noise, all data sets were treated with the methods described by Morgan and Weber.²⁰⁷ Briefly, a smoothed curve was obtained for each run by using adjacent averaging. This smoothed curve was then subtracted from each original curve, respectively. The resulted data sets were finally treated with FFT and averaged. The results after adding a low pass filter is summarized in Table 15 and Fig. 24. It can be seen from the data that the analytical signal is accompanied by noises with several characteristic frequencies around 20 Hz, 30 Hz, 45 Hz and 60 Hz. When the cutoff frequency of the low pass filter is decreased, noise with frequencies higher than the cut-off frequency disappears and the total rms noise level goes down, too. Besides, the frequencies of the noise are concentrated below 100 Hz, therefore when the cut off frequency is higher than 100 Hz, the low pass filter has no obvious effect for decreasing the total rms noise.

Table 15. Low pass filter experiment

Cut Off Freq. (Hz)	E_t (V)	σ_t (V)	S/N (E_t/σ_t)
No filter	5.449	0.049	111
5	5.313	0.006	864
50	5.530	0.037	150
500	5.548	0.035	159
5000	5.520	0.037	150

Laser power is 3.0 mW; PMT control voltage is 0.5 V; 40x objective; sample clock rate is 1000 Hz; ceiling lamp is off and computer monitor is on; light tight cover over the stage C; laser is focused to the center of the reservoir.

Channel A of the dual Hi/Lo filter is used with 0 dB gain and flat amplitude.

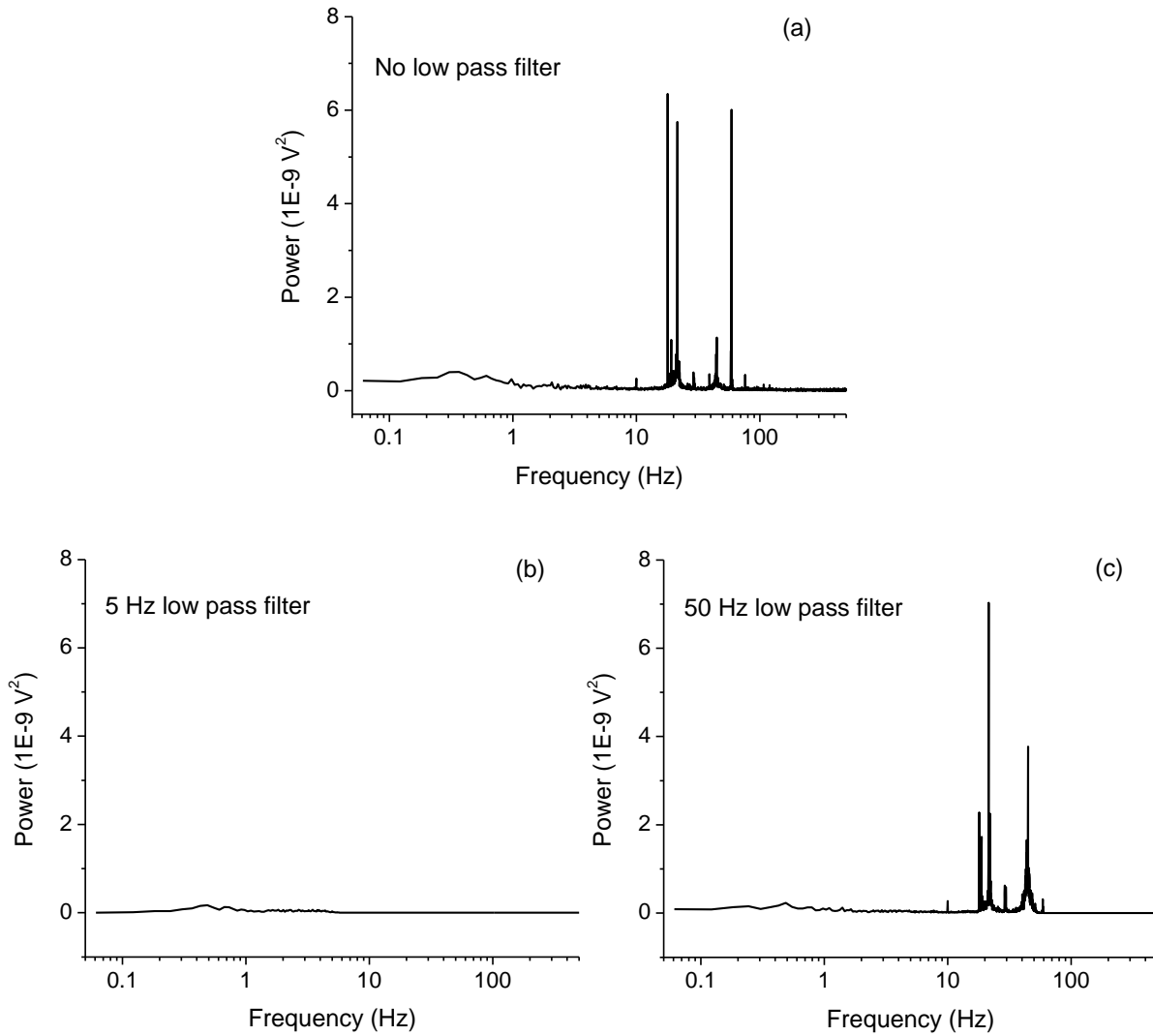


Figure 24. FFT results showing the effect of low pass filter with different cutoff frequency

(a) No filter; (b) 5 Hz; (c) 50 Hz.

Further experiments proved that some of the noises with frequencies lower than 100 Hz were caused by the vibration of the lab bench (and the building) to the sample stage. In the following experiments, a rubber layer was placed under the platform of stage A and all the steel screws on this platform were replaced with plastic ones to dampen and mitigate the transference of vibrations from the bench to sample platform. Fluorescence signals from newly prepared ThioGlo-1 (0.50 mM) and GSH (0.10 mM) mixture loaded inside the big reservoir of the same microfluidic chip (Fig. 15) were collected with or without four racquetballs added under the optical breadboard. According to the results (see Table 16 and Fig. 25), there is a distinguishable change in the noise intensity, which proves that the sources for these noise are related with vibration.

Table 16. Vibration experiment

With racquetballs?	E_t (V)	σ_t (V)	S/N (E_t/σ_t)
Yes	6.712	0.024	282
No	6.583	0.051	128

*1 laser power is 3.0 mW; PMT control voltage is 0.4 V; 40 x objectives; light tight cover over the stage C; sampling rate is 1000 Hz, no averaging and low pass filter; laser is focused to the center of the reservoir.

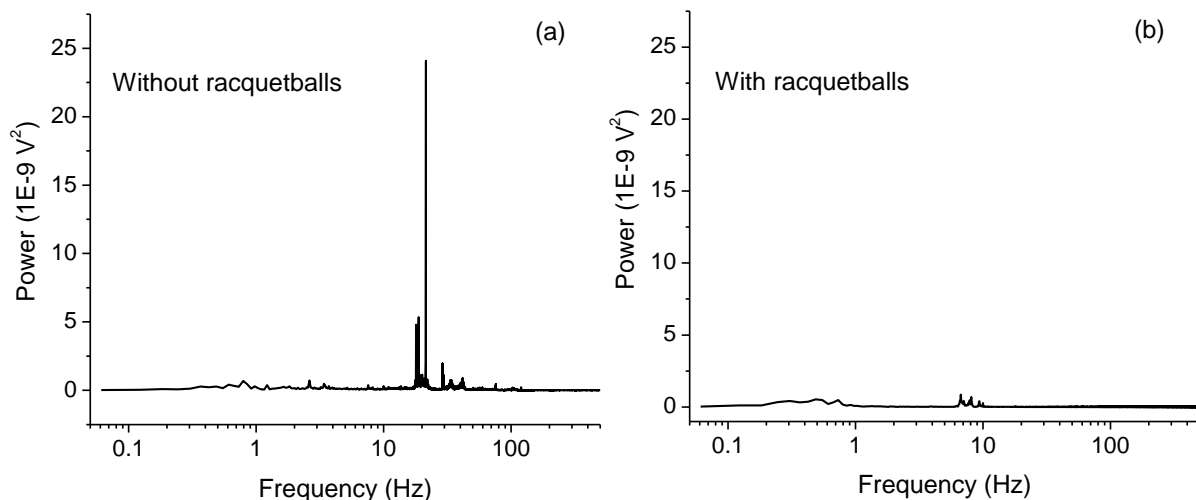


Figure 25. FFT results showing the effect of racquetballs in the vibration experiment

(a) No racquetballs; (b) with racquetballs under the breadboard.

To further reduce the noises and increase the S/N, a heavy-duty aluminum frame stage was specially designed and made to accommodate the confocal LIF detection system. The whole breadboard, on which the detection system was built, was hanged in the air with four elastic ropes fixed to the roof of the frame stage. Black light tight curtains were installed on four sides of the frame stage to minimize the light from environment. In addition, the platform of stage A was supported from below with a spring tension rod to dampen the vibration and give addition support. Beam alignment was performed after the detection system was installed into the frame stage.

The following experiments showed the effects of averaging and low pass filter on the new system where transference of vibrations from the bench to sample platform was effective blocked. Sample containing 10.7 μM GSH and 50 μM ThioGlo-1 was loaded into the big reservoir of the same microfluidic chip as before. The control voltage of PMT was set at 0.5 V while the laser beam of 3.0 mW was focused on the center of the reservoir by a 40 x objective. The results from averaging experiment for the new system were summarized in Table 17 and Fig. 26. Compared with the results for the old system (Table 14, Fig. 23), it is clearly that the fluorescence response of the new system is much better than the old system. Fluorescence signal of a 10 times diluted sample in the new system is as high as one third of the signal of an undiluted sample in the old system using the same PMT control voltage and laser power. Meanwhile, the best S/N obtained from averaging in the new system is three times higher than that of the old system. Fig. 26 shows that, unlike that in the old system, data averaging effectively decreases the rms noise until the number of the averaging points reaches 500 for a system. This is consistent with the fact that averaging will be most effective when flick noise generated by vibration is pre-removed from the system and white noise becomes the dominant

noise source. The results from Low pass filter experiment are summarized in Table 18 and Fig. 27. The S/N values shown in Table 18 are also better than that in Table 15. The best S/N obtained under 5 Hz cut-off frequency for the new system is 2.6 times higher than that for the old system. Fig. 27 indicates that the noise power is decreased by two orders of magnitude for the new system compared to that of the old system. The special frequencies below 100 Hz in Fig. 24 (a) disappear in Fig. 27 (a). By applying a low pass filter with 5-500 Hz cut-off frequency, the rms noise is further decreased as shown in the power spectrum. It must be pointed that although the low pass filter is effective in reducing the aliases of noises with high frequency, noises at frequencies of 10 Hz, 60 Hz and 180 Hz can be introduced into the system by the low pass filter as shown in Fig. 27 (c) and (d). Frequencies at 60 Hz and 180 Hz are most likely picked up from the power line hum and its harmonics. Based on these results, a low pass filter with 50 Hz cut-off frequency and 500 points data averaging will be applied in the further experiment unless otherwise specified.

Table 17. Effect of signal averaging for the new system

Sample Clock Rate	Averaged Points	Averaged time (ms)	E_t (V)	σ_{avg} (V)	S/N (E_t/σ_{avg})
20	1	50	2.408	0.0248	97
100	5	50	2.211	0.010	214
1000	50	50	2.333	0.004	648
10000	500	50	2.167	0.001	1477
100000	5000	50	2.265	0.001	1878

Laser power is 3.0 mW; PMT control voltage is 0.5 V; 40 x objective; averaging time is 50 ms (sampling rate 20 Hz); no low pass filter; the whole system is covered with light tight curtains; laser is focused to the center of the reservoir.

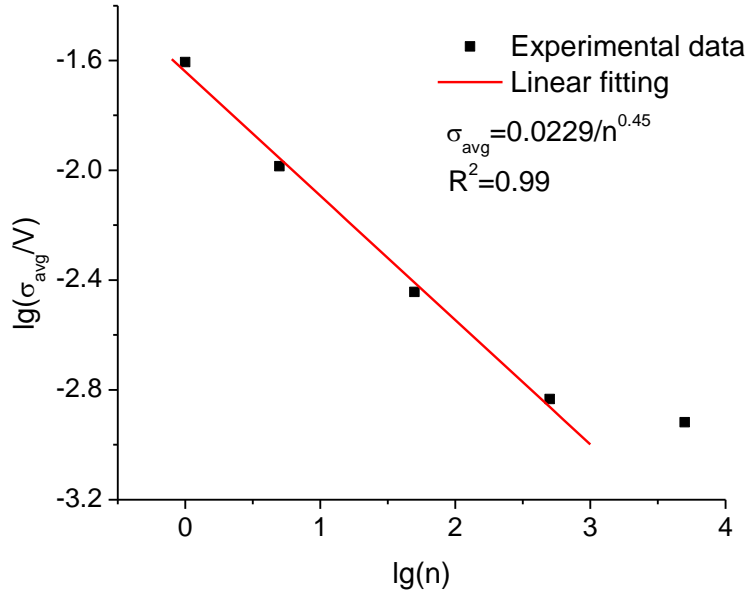


Figure 26. Effect of averaging for the new system

Table 18. Effect of the low pass filter for the new system

Cut Off Freq. (Hz)	E_t (V)	σ_t (V)	S/N (E_t/σ_t)
No filter	2.186	0.024	92
5	2.110	0.001	2255
50	2.137	0.002	1083
500	2.126	0.004	505
5000	2.164	0.012	184

Laser power is 3.0 mW; PMT control voltage is 0.5 V; 40 x objective; sample clock rate is 1000 Hz; no averaging is performed; the whole system is covered with light tight curtains; laser is focused to the center of the reservoir; only channel A of the dual Hi/Lo filter is used with 0 dB gain and flat amplitude.

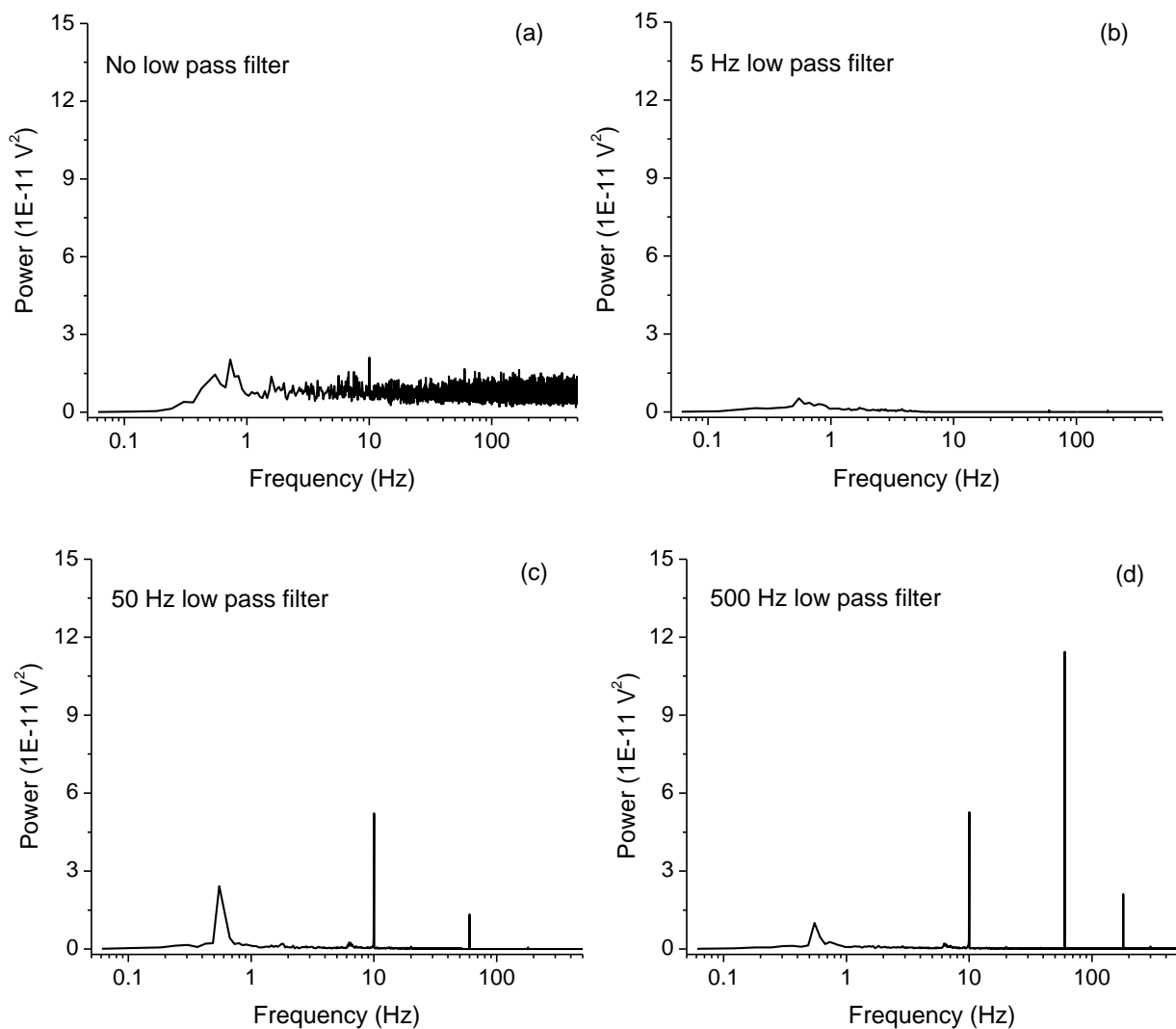


Figure 27. FFT results showing the effect of low pass filter with different cutoff frequency

(a) No filter; (b) 5 Hz; (c) 50 Hz; (d) 500 Hz.

2.4.3.4 System performance testing

The performances of the detection system, which include the relationship between fluorescence responses and PMT control voltage/laser power and the linearity of the signal response related to the analyte concentration. The following experiments were carried out in the old system where the breadboard was directly placed on top of a lab bench. In PMT control voltage experiment, sample solution, which contained 50 μM ThioGlo-1 and 10.7 μM GSH, was

loaded into the big reservoir on microfluidic chip in Fig. 15. The averaging time was set to be 50 ms when the sample clock rate was 1000 Hz. The cutoff frequency of the low pass filter was adjusted to 10 Hz. The laser beam with a power of 3.0 mW was focused on the sample with a 40x objective. Fig. 28 (a) indicates an optimal range of PMT control voltage where E_t/σ_t reached its highest level. The experiment conditions in laser power experiment were similar to those in PMT control voltage experiment, except that the control voltage for PMT was fixed at 0.5 V while laser power varied in different runs. Fig. 28(b) shows that the fluorescence from the analyte would not increase boundlessly when the power of laser was enhanced. This is mainly because the optical saturation of the absorbance transition for the analyte will arrive finally under a high irradiance of the beam. A significant fraction of the analyte will be raised to the excited state and the number of photons absorbed per second approaches the spontaneous emission rate under the first approximation. The increase in the laser power thereafter will only lead to photo degradation of the sample.¹⁶⁷

Sample solutions with different concentration of ThioGlo-1 and GSH were also used to test the linearity of fluorescence response to the analyte concentration. All other conditions were same as the previous experiments. Results from linearity experiments are given in Fig. 27. When the PMT control voltage was set at 0.5 V and laser power was adjusted to 3.0 mW, the linear range for GSH ([GSH]: [ThioGlo-1] = 1:5) for the current setup spanned from 0-49.7 μ M (analyte with higher concentration was not tested under the current condition, as the high optical intensity would cause the saturation and damage of the PMT). The detection limit was estimated to be 1.45 nM (Eq. 17) with the mass detection limit as low as 10^{-18} mol:

$$LOD = \frac{3\sigma_{bk}}{slope} = \frac{3 \times 4.42 \times 10^{-5}}{0.09151} = 1.45 \text{ nM} \quad (17)$$

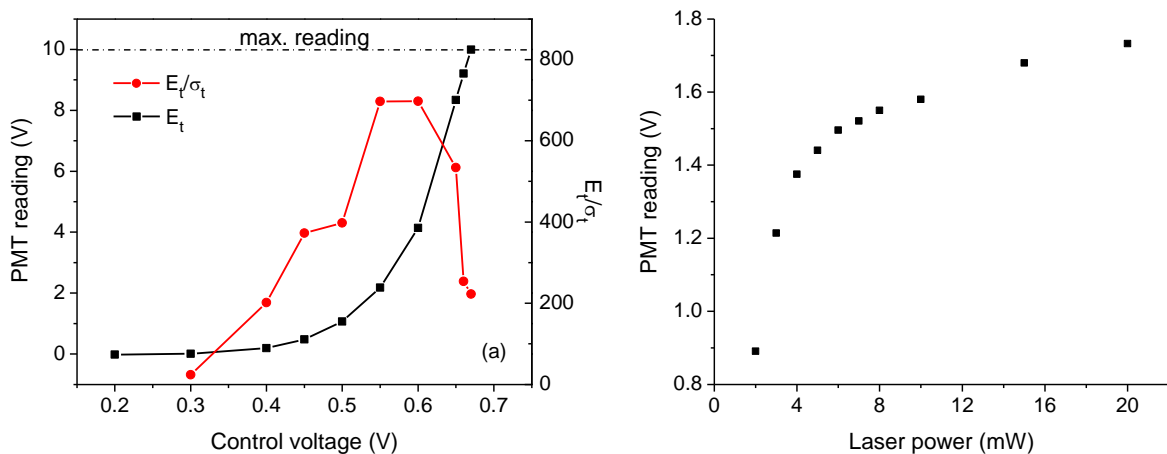


Figure 28. Relationship between the fluorescence intensity and (a) PMT control voltage and (b) laser power

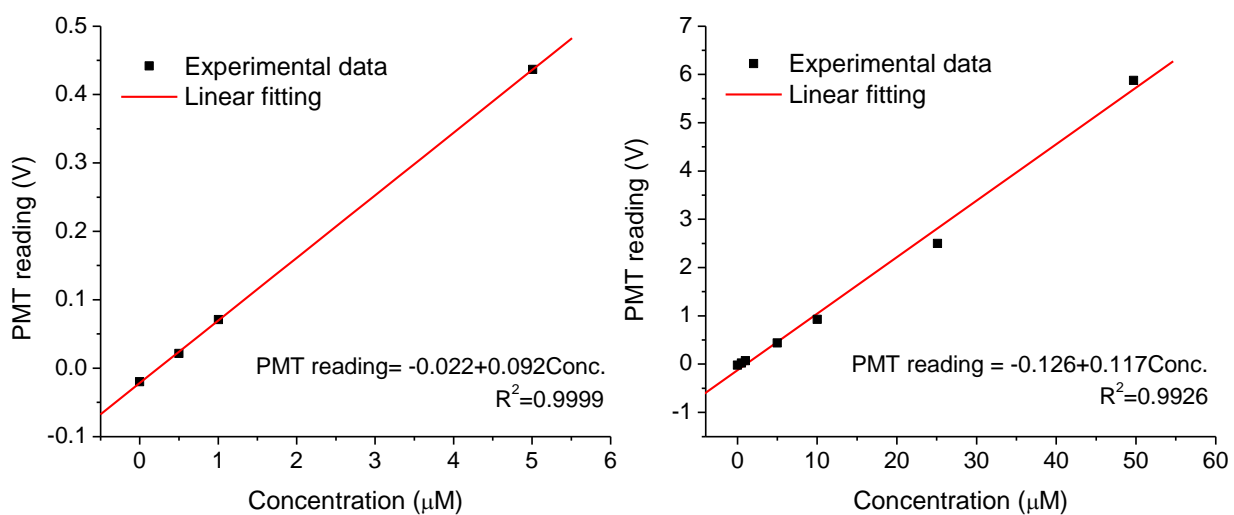


Figure 29. Linearity between fluorescence signal and analyte concentration

Note: due to the existence of photobleaching, data collected in the first 50 s was not used in the calculation.

3.0 ON-CHIP MONITORING OF THE REDUCTION OF OXIDIZED GLUTATHIONE BY GLUTATHIONE REDUCTASE

Part of the following work has been published in *Analytical Chemistry* **2010**, 82(17):7267-7273

A microfluidic chip has been designed, which integrates the precolumn derivatization, continuous flow gated sampling, separation and detection on a single device. We validated this device for monitoring GSH level by studying the kinetics of glutathione reductase (GR, EC 1.8.1.7), an enzyme that catalyzes the reduction of GSSG to GSH in the presence of β -NADPH (β -nicotinamide adenine dinucleotide phosphate, reduced form) as a reducing cofactor. We demonstrate here that the fluorogenic, thiol-specific reagent, ThioGlo-1, reacts rapidly enough for efficient precolumn derivatization. The second order rate constant for the reaction of GSH and reagent (pH 7.5, room temperature) is $2.1 \times 10^4 \text{ M}^{-1}\text{s}^{-1}$. During the experiment, GSH being generated in the enzymatic reaction was labeled with ThioGlo-1 as it passed through a mixing channel on the microfluidic chip. Derivatization reaction products were introduced into the analysis channel every 10 s using flow gated injections of 0.1 s. Baseline separation of the internal standard, ThioGlo-1, and the fluorescently labeled GSH was successfully achieved within 4.5 s in a 9 mm separation channel. Relative standard deviation of the peak area, peak height, and full width at half maximum (FWHM) for the internal standard were 2.5%, 2.0%, 1.0%, respectively with migration time reproducibility for the internal standard of less than 0.1%

RSD in any experiment. The GSH concentration and mass detection limit were 4.2 nM and $\sim 10^{18}$ mol, respectively. The Michaelis constants (K_m) for GSSG and β -NADPH were found to be 40 ± 11 μ M and 4.4 ± 0.6 μ M, respectively, comparable with those obtained from UV/Vis spectrophotometric measurements. Our system is capable of integrating derivatization, injection, separation and detection for continuous GSH determinations.

3.1 INTRODUCTION

The ubiquitous tripeptide, GSH acts as an anti-oxidant in cells.²⁸ It is particularly important for its ability to react with reactive oxygen species (ROS) directly or indirectly making it a principal component of an organism's antioxidant response.³ Compared with other organs, brain is especially vulnerable to ROS because it is rich in lipids with unsaturated fatty acids.^{4, 208} Oxidized glutathione, GSSG, is reduced to GSH by the NADPH-dependent enzyme GR. Alterations in this energy (NADPH)-redox (GSH/GSSG) "axis" occur in aging, and are thought to be responsible for the progress of neurodegenerative diseases.^{209, 210} Efflux rates of GSH from astrocytes through hemichannels can be gated by changes in the concentration of extracellular Ca^{2+} ,⁶⁰ and hypoxia-ischemia.²¹¹ Thus, there is an interest in continuous monitoring of GSH, and related thiols in the extracellular space of tissues, including brain with good temporal resolution.^{3, 60, 212} Both electrochemical^{213, 214} and fluorescence detection^{215, 216} of GSH and other thiols has been used with high performance liquid chromatography and capillary electrophoresis. Determination of GSH and related thiols on microfluidic chips has been performed using UV,²¹⁷ and electrochemical detection.¹⁸⁹ Laser induced fluorescence (LIF) detection^{179, 180, 190} on microfluidic chips used offline derivatization of GSH and other thiols. Despite the need for the

derivatization, LIF is widely applied for its robust nature and consistent calibration compared to electrochemical detection. Also, labeling of the thiol group reduces its reactivity during the analysis, protecting it from degradation.⁹³ Qin¹⁸² and Ling⁹⁷ *et al.* briefly mentioned the use of 2,3-naphthalene dicarboxaldehyde (NDA) for on-column derivatization of GSH by simply including the fluorescent tag in the electrophoresis buffer. However, as the derivatization process was carried out simultaneously with separation, this approach is not optimal. The goal of this work is to improve the analysis platform for thiols, including the speed of the separation, the detection limit of the determination, using a derivatizing reagent that is thiol-specific, and doing continuous analysis.

The published reaction times for fluorogenic labeling of thiols are fairly long, which commonly range from several minutes to an hour.²¹⁸⁻²²² Some of them even require heating for a fast and complete derivatization.^{219, 222} We and others have used a commercial fluorescent tag, ThioGlo-1²²³ (N-(2-carbomethoxy-9-methoxy-3-oxo-3H-naphtho [2,1-b] pyran-10-yl) maleimide) for labeling thiols in intact cells,²²⁴⁻²²⁶ cell homogenates or supernants.^{225, 227} Others have shown the potential of ThioGlo reagents for labeling thiols before HPLC analysis.²²⁸ These derivatizations were performed offline with a 20-minute reaction time. In this work, we determined the reaction rate at pH 7.5 for the derivatization of GSH by ThioGlo-1 and demonstrated the feasibility of using ThioGlo-1 for online derivatization of GSH.

GR is a flavoprotein that catalyzes the β -NADPH-dependent reduction of GSSG to GSH and maintains a suitable intracellular thiol/disulfide redox potential for an organism.^{229, 230} Maintaining an adequate level of reduced cellular GSH over GSSG is especially important for cells to fight against oxidative stresses and xenobiotics.^{10, 26} The kinetics and mechanism of the GR catalyzed reactions have been studied.²²⁹⁻²³² The most widely used tool to analyze the

kinetics and mechanism of GR is UV/Vis absorbance as described by Racker,²³³ which relies on the decrease in the absorbance at 340 nm of NADPH. Transferring the enzyme reaction from the traditional cuvette or well plate to microchannels with LIF detection not only reduces the consumption of samples and reagents, but also has much higher sensitivity compared with that of UV/Vis absorbance detection. Meanwhile, interferences caused by other chemicals that coexist with the target compound, such as enzyme, by product, unreacted substrates would be eliminated from the detection by separation, which ensures more reliable results.

In the following research, we used the reaction catalyzed by GR as a model system to validate the online derivatization, multiple injection, separation and detection of GSH with good temporal resolution on an integrated microfluidic platform. GSH concentration in the enzyme reaction mixture was measured using an online precolumn derivatization and a 4.5 s electrophoretic separation. In any given experiment, the reproducibility of the migration times of the internal standard was excellent, less than 0.1% relative standard deviation. The obtained kinetic constants for GR are comparable with those obtained through traditional methods.

3.2 EXPERIMENTAL SECTION

3.2.1 Chemicals and reagents

ThioGlo-1 was purchased from Calbiochem (San Diego, CA). Proflavine hemisulfate salt hydrate (PFH), sodium hydroxide, tris(hydroxymethyl) aminomethane, hydrochloric acid, GR from baker's yeast (suspended in 3.6 M ammonium sulfate, 168 units/mg protein, containing 0.1 mM dithiothreitol, pH=7.0), dimethyl sulfoxide (DMSO), GSH, GSSG disodium salt, β -

nicotinamide adenine dinucleotide phosphate, tetrasodium salt hydrate, and 1,6-diaminohexane were purchased from Sigma-Aldrich Chemical Co. (St. Louis, MO) and used without purification.

Stock solutions of GR, GSSG and β -NADPH were prepared using 20 mM Tris-HCl buffer (pH = 7.5). The concentrations of these solutions were 3.33 units /mL, 13.2 mM, and 2.41 mM, respectively. The stock solutions of PFH and ThioGlo-1 were prepared using Milli-Q water (Millipore Co., Billerica, MA) and DMSO with the final concentrations of 4.74 mM and 2.5 mM, respectively. Stock solutions were aliquoted into small vials and stored at -20 °C and diluted serially to the desired concentrations on the day of experiment. All working solutions were kept on ice during the experiment when not in use. The running buffer for microfluidic chip electrophoresis was 20 mM Tris-HCl buffer (pH = 7.5) with 0.1 mM 1, 6-diaminohexane, unless otherwise specified. All buffers were prepared using Milli-Q water, filtered through Nylon 0.22 μ m filter and degassed by ultrasonication prior to use.

3.2.2 Design and fabrication of the microfluidic chip

The microfluidic chip used in our experiments was fabricated using traditional lithography techniques. Briefly, borofloat glass (1.1 mm) coated with chromium and AZ 1500 photoresist (Telic, Valencia, CA) was exposed to UV light through a negative film mask (Pixels, Charlottesville, VA) containing the design of the channels to be etched. Following development and removal of the underlying chrome, the glass was etched in HF solution containing nitric acid (HF/HNO₃/H₂O:20/14/66) to a depth of 20 μ m. The remaining photoresist and chromium was then removed and the glass cleaned and dried. Uncoated borofloat cover glass was drilled using 1.1 mm diameter diamond tipped drill bits (Kingsley North Inc., Norway, MI) to provide access

holes at the end of each channel. Cover plates were cleaned and aligned with the etched glass plate and the two pressed together to form an initial bond. The device was permanently bonded by thermal annealing at 675 °C for 3.5 hours. The layout of the microfluidic chip and the voltage scheme are shown in Fig. 30. RR, SR, BR, and WR represent reagent reservoir, sample reservoir, buffer reservoir and waste reservoir, respectively. The channels were determined to be ~30 μm wide at the bottom and ~70 μm wide at the top, with a depth of ~20 μm. The total length of the precolumn reaction channel was ~46.3 mm. The detection point (DP) was located 9 mm from the injection cross. Platinum electrodes were placed into all reservoirs to serve as electrical contacts to the high voltage power supply. During each run, the electrodes in reagent reservoir and sample reservoir were kept at ground, while the electrode in waste reservoir was connected to a single channel negative high voltage power supply (UltraVolt, Inc., Ronkonkoma, NY). Sample injection was by a gated approach, which has advantages in shortening the analysis cycle, enhancing the temporal resolution and reducing contamination between reservoirs.^{234, 235} The electrode in buffer reservoir could be switched between “GND” and “floating” to achieve the flow gated sampling. In the “sampling” stage, the electrode in buffer reservoir was set to “float” for a very short period allowing a small segment of the reaction mixture to be directed into the separation channel. In the “separation” step, this electrode was switched back to ground, resulting in electrophoretic separation of the components in the injected aliquot. These steps were computer controlled and repeated automatically to achieve continuous sampling and analysis.

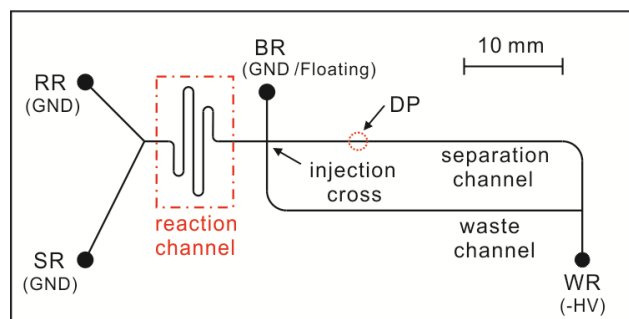


Figure 30. Layout of the microfluidic chip used for enzyme analysis

3.2.3 Reaction between ThioGlo-1 and GSH

A SpectraMax M2 from Molecular Devices (Sunnyvale, CA) was used in measurement of the reaction between ThioGlo-1 and GSH at 25°C. The excitation and emission wavelengths were set at 403 nm and 495 nm, respectively. The reaction between 29.7 μM GSH and 15 μM ThioGlo-1 were monitored in a series of 50.1 mM Tris-Acetate buffers at different pH value ranging from 4 to 9 for optimizing the reaction condition of online precolumn derivatization. The measurement was started right after two reactants were well mixed. The kinetic parameters of the reaction between GSH and ThioGlo-1 in 20 mM Tris-HCl buffer at pH 7.5 were also measured. In order to accurately record the start point of the reaction and establish the baseline, the fluorescence reading was started before GSH and ThioGlo-1 was mixed. At the beginning of the experiment, the cuvette contained only ThioGlo-1 dissolved in 20 mM Tris buffer solution at pH 7.5. The addition of GSH stock solution into the cuvette followed by mixing using a pipette for 2-4 s caused a sharp increase of fluorescence intensity, which marked the start point of the reaction.

3.2.4 Enzyme kinetics measurement

The home-made confocal LIF detection system described in Chapter 2 was used to detect the analyte in the microfluidic experiments. The PMT control voltage was set at 0.5 V and the laser power was adjusted to 3.0 mW. Before each run, mixtures of β -NADPH and GSSG at the desired concentrations were prepared using 20 mM Tris-HCl buffer (pH = 7.5) and transferred into the sample reservoir. Derivatizing reagent, which contains 50 μ M ThioGlo-1 and 1.9 μ M PFH as internal standard, was prepared using 20 mM Tris-HCl buffer (pH = 7.5) with 0.1 mM 1,6-diaminohexane then added into reagent reservoir. Buffer reservoir and waste reservoir were both filled with running buffer. The enzyme catalyzed reaction was initiated by the addition of 10 μ L of GR solution into the substrate mixture in sample reservoir to achieve a final concentration of 7.93×10^{-4} unit/mL unless otherwise specified. The final volume of solution in each reservoir was 200 μ L. Immediately after addition of GR, -6000 V was applied to waste reservoir, while reagent reservoir and sample reservoir were kept at ground and buffer reservoir was switched between two states, “GND” and “floating”. Typically, the sampling time was 0.1 s and the separation time was 9.9 s unless otherwise stated. There were usually 40-50 repeat injections for each sample per run. Before changing to the next sample, the channels were rinsed and reconditioned in sequence with 0.1 M NaOH and running buffer each for 5 minutes by applying -6000 V at waste reservoir and keeping all other reservoirs at ground. All experiments were carried out at room temperature.

3.3 RESULTS AND DISCUSSION

3.3.1 Derivatization of GSH with ThioGlo-1

ThioGlo-1 is selected as a fluorescent derivatizing reagent of GSH based on its distinctive properties compared to other widely used reagents mentioned in Section 1.2.2. ThioGlo-1 is a maleimide derivative of naphthopyranone fluorophore.²²³ It has very low quantum yield before reacting with thiols, while adduct of ThioGlo-1 and GSH has a high quantum yield. The stock solution of ThioGlo-1 in DMSO is very stable and the hydrolyzed products are all inactive with thiol group and have low quantum yield. The hydrolysis rate of the ThioGlo-1 is slower than most other maleimide reagent. Most important, the reaction between ThioGlo-1 and GSH is very fast in buffer solution at pH 7.0.²³⁶

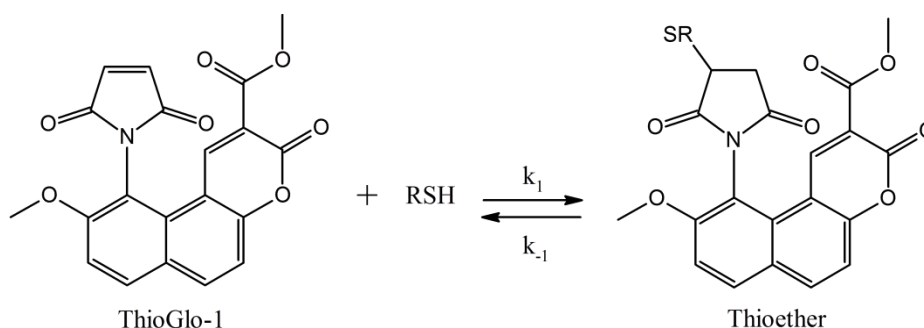


Figure 31. Reaction between ThioGlo-1 and thiols

The reaction between GSH and ThioGlo-1 shown in Fig. 31 was monitored using a commercial spectrofluorometer to test its suitability and optimize the reaction conditions for online precolumn derivatization. Fig. 32 shows the change of the fluorescence intensity (relative fluorescence unit, RFU) with time at different pH value. The fluorescent signal is directly proportional to the concentration of the fluorescent adduct. When pH value is lower than 7, the

reaction between GSH and ThioGlo-1 is relatively slow compared with solutions with higher pH value. Besides, there is a small decrease in the fluorescence intensity when pH value reaches 9, which may due to the fast oxidation of GSH to GSSG at high pH value. Based on this result, Tris buffer at pH 7.5 is selected as the buffer solution for the derivatization of GSH with ThioGlo-1.

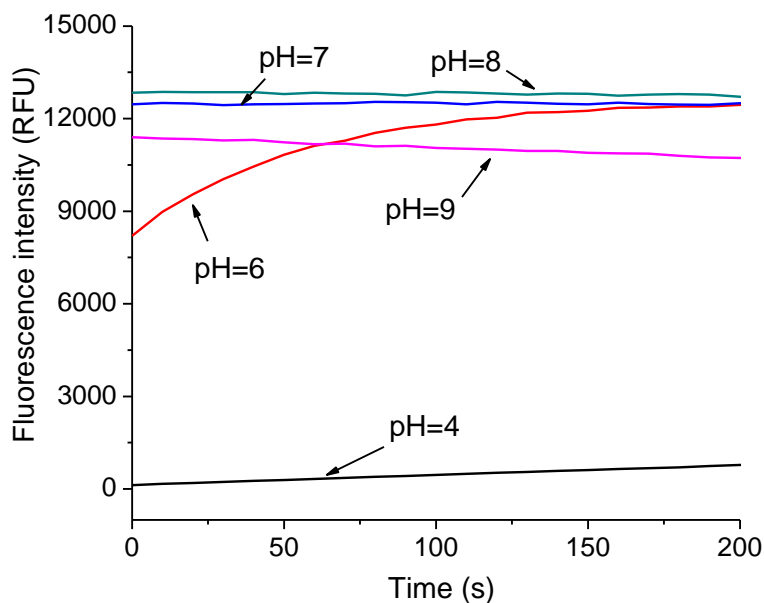


Figure 32. pH effect on the reaction of ThioGlo-1 and GSH

It has been observed that the reaction of GSH and ThioGlo-1 at pH above 7 will be completed in seconds. The complete time course of the reaction between GSH and ThioGlo-1 in 20 mM Tris buffer solution at pH 7.5 shown in Fig. 33 indicates that it takes about 14 s to generate a fluorescent signal equivalent to 95% of the signal intensity at equilibrium when the initial concentrations of GSH and ThioGlo-1 are 5 μM and 25 μM , respectively. Based on this fact, it is reasonable to assume that under the similar conditions the precolumn derivatization in the reaction channel will be nearly complete as long as the online derivatization reaction lasts longer than 14 s.

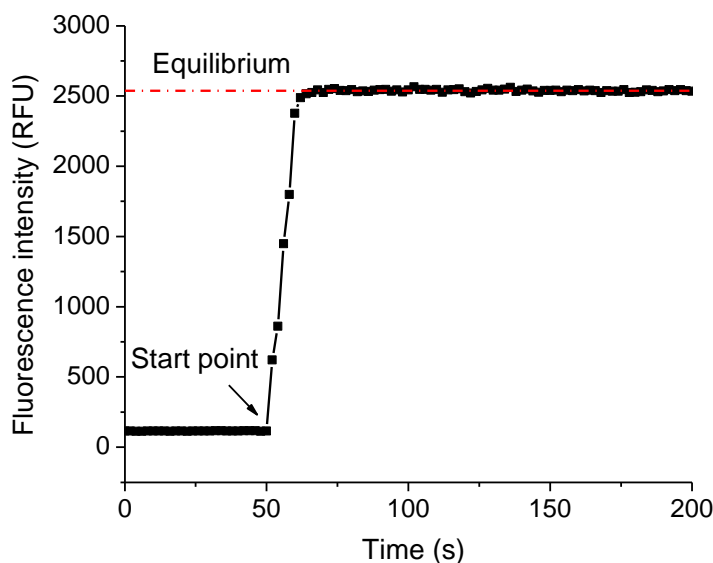


Figure 33. Change of RFU with time for the reaction of ThioGlo-1 and GSH

To obtain the kinetic parameters for the reaction between GSH and ThioGlo-1 in a 20 mM Tris buffer solution at pH 7.5, seventeen complete time courses of the reaction between GSH with initial concentrations ranging from 0 μM to 15 μM and ThioGlo-1 with a fixed concentration of 5 μM were recorded. Fig. 34 (a) shows nine out of the seventeen time progress curves with the initial GSH concentrations of 0.5 μM , 1 μM , 2 μM , 3 μM , 4 μM , 5 μM , 6 μM , 8 μM and 15 μM . These curves were adjusted so that they shared a common starting point at $t = 0$ s for better comparison. The fluctuation of the fluorescence intensity right after $t = 0$ s was caused by mixing using a pipette and these two to three data points will be removed in the following data treatment. The average fluorescence intensities of the product at equilibrium are plotted against various initial concentrations of GSH in Fig. 34 (b). Data points at each concentration are mean $\pm 2 \times$ standard deviation (SD) based on 50 or more fluorescence measurements after equilibriums were reached. It can clearly be seen that when ThioGlo-1 is in excess, the fluorescence intensity of the product is directly proportional to the initial concentration of

GSH. A linear curve fitting (black dash-dot line) gives an R^2 of 0.9982 for the data when the initial GSH concentrations range from 0-5 μM . The equilibrium fluorescent adduct concentration, P_{eq} (M) and the initial GSH concentration, G_0 (M) and ThioGlo-1 concentration, T_0 (M), can be mathematically related according to the definition of equilibrium constant, K (M^{-1}) as shown in Eq. 18. Meanwhile, P_{eq} is directly proportional to the equilibrium fluorescence intensity, I_{eq} (RFU) according to Eq. 19 with coefficients, α (M/RFU) and β (M). Nonlinear fitting (red solid curve) of the data shows K is on the order of 10^8 M^{-1} .

$$K = \frac{P_{eq}}{(G_0 - P_{eq})(T_0 - P_{eq})} \quad (18)$$

$$P_{eq} = \alpha \cdot I_{eq} + \beta \approx \alpha \cdot I_{eq} \quad (19)$$

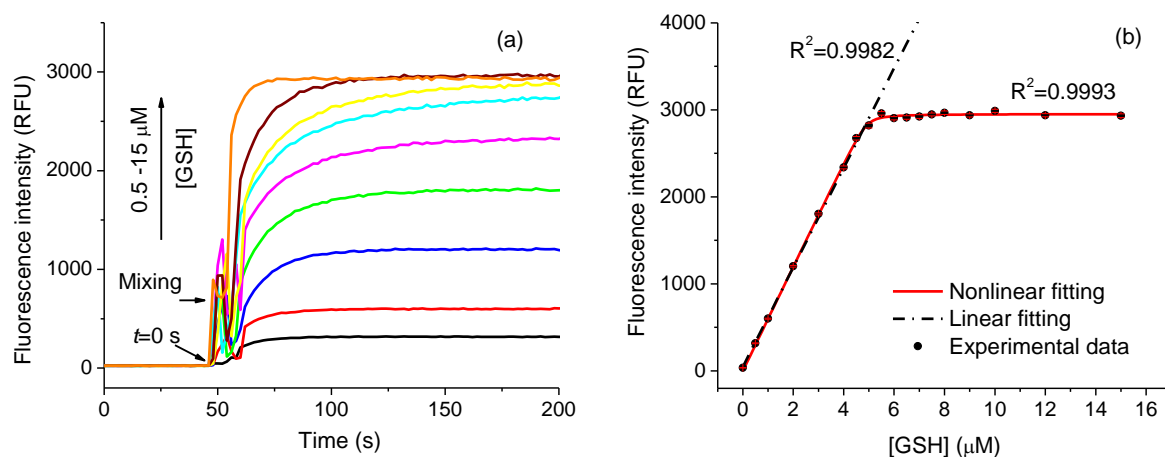


Figure 34. Kinetic experiments for GSH and ThioGlo-1

(a) Time progress curves of the reaction taking place in 20 mM Tris buffer solution at pH 7.5; (b) relationship of the equilibrium fluorescence intensity and the initial GSH concentration.

Based on this approximate equilibrium constant, it is reasonable to assume that the rate constant of the reverse reaction, $k_{-1}(\text{s}^{-1})$, is much smaller than the rate of the forward reaction rate, $k_1(\text{M}^{-1}\text{s}^{-1})$, when the concentrations of GSH and ThioGlo-1 are in the low micromolar range.

Under this assumption, a linear relationship can be derived as indicated in Eq. 20 and 21, with P_t (M) and I_t (RFU) as the concentration and the fluorescence intensity of fluorescent adduct at time t , respectively.

$$\frac{\ln \frac{T_0 - P_t}{G_0 - P_t} - \ln \frac{T_0}{G_0}}{T_0 - G_0} = k_1 t \quad (20)$$

$$P_t = \alpha \cdot I_t + \beta \quad (21)$$

A linear global fitting of the seventeen sets of kinetic data is given in Fig. 35. The value of the slope, k_1 , is $2.1 \times 10^4 \text{ M}^{-1} \text{ s}^{-1}$ with a standard deviation of $2.2 \times 10^2 \text{ M}^{-1} \text{ s}^{-1}$. Based on the above results, k_{-1} can also be estimated, which is on the order of 10^{-4} s^{-1} . Although the reaction between thiols and maleimide is reversible,²³⁷ under our experimental conditions, the reverse reaction does not factor into the detection. Therefore, ThioGlo-1 is suitable for online precolumn derivatization of GSH and quantitative analysis.

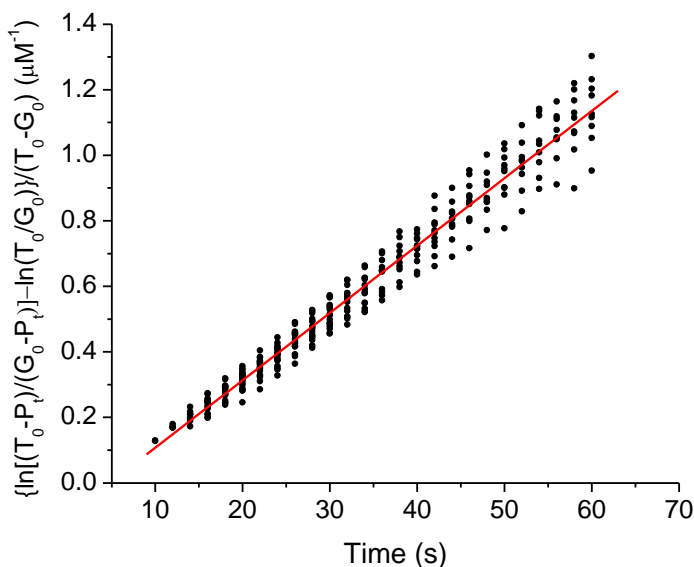


Figure 35. Global linear fitting of the data from seventeen kinetic curves

3.3.2 Microfluidic capillary electrophoresis

Utilizing flow gated injection,²³⁸ the microfluidic chip operates in a continuous sampling/separation mode, which allows continuous monitoring of the changing concentration of the analyte GSH. Another advantage of flow gated injections is that the analyte, reagent, and buffer reservoirs are all kept isolated throughout the experiment. Therefore dilution or contamination of analytes by the other reagents and buffers is reduced compared to a pinched injection, which enables more repeatable and reliable results. Although the flow gated injector is time dependent and electrophoretically biased,^{239, 240} it is possible to use an internal standard to eliminate these problems. The sample volume loaded by the flow gated valve is determined by both the short period of time when the potential at buffer reservoir is floating and the flow rate of the sample streams. The operation of the high voltage relay was controlled by the onboard clock on the data acquisition device, which provided precision in the floating time. However, the flow rate of the sample streams can be affected by changes in the zeta potential, the conditions in the microfluidic channels, differences in the relative liquid levels between buffer reservoir and waste reservoir, and fluctuations of the pH in each reservoir during continuous analysis. To mitigate any effect of the variability in the injection volume, an internal standard, PFH, was added to the reagent reservoir. PFH has an excitation maximum of 445 nm and emission maximum of 511 nm at neutral pH, both of which are suitable for our LIF detector.²⁴¹ Moreover, it is positively charged under the separation conditions and should migrate before the analyte to avoid additional analysis time. Fig. 36 (a) shows the separation of PFH (internal standard, IS), unreacted ThioGlo-1 (dye) and the ThioGlo-1 labeled GSH in the microfluidic chip using 20 mM Tris-HCl buffer (pH = 7.5) as the carrier buffer and running buffer. Sample reservoir was filled with 3 μ M GSH and reagent reservoir was filled with 50 μ M ThioGlo-1 and 1.9 μ M PFH.

Sampling and separation times were 0.1 s and 9.9 s, respectively. Potential applied at waste reservoir was -6000 V, while the reagent and sample reservoir were kept at ground and buffer reservoir was switched between two states, “GND” and “float”.

Although the resolution of the IS and Dye peaks reaches 4.0 in Fig. 36 (a), the IS peak is tailing. This may be caused by electrostatic interactions between the cationic PFH and the negatively charged inner wall of the channel. Supporting this idea, when PFH was used, the channels became clogged, even if the microfluidic chip went through a conditioning step between runs. PFH is relatively insoluble in water, and adsorbed PFH may nucleate precipitation. The addition of aliphatic diamines, especially 1,4-diaminobutane, to the running buffer to neutralize the negative charges on the wall has been investigated by several groups.^{242, 243} For these experiments, 1, 6-diaminohexane was chosen since it is less toxic than other diamines with shorter aliphatic chains. While it will compete for surface adsorption sites with PFH, it will also change the zeta potential at the microchannel wall. Fig. 36 shows a decrease in the mobilities of PFH (IS), unreacted ThioGlo-1 (dye), and ThioGlo-1-GSH adduct (GSH*) as the concentration of 1, 6-diaminohexane in the running buffer varied from 0 mM to 1.0 mM, which is the evidence of a reduced zeta potential and electroosmotic flow rate. Based on these results, a concentration of 0.1 mM 1, 6-diaminohexane was chosen for further experiments based on the separation time needed for the analysis.

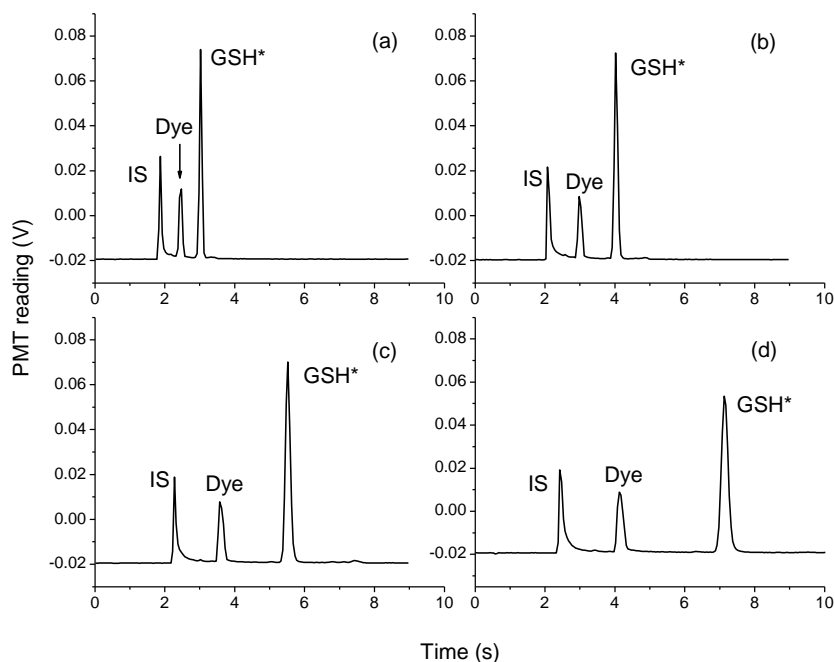


Figure 36. Effect of 1, 6-diaminohexane on the separation of PFH, ThioGlo-1 and GSH*

Sample reservoir was filled with 3 μM GSH in 20 mM Tris-HCl buffer (pH = 7.5) and reagent reservoir was filled with 50 μM ThioGlo-1 and 1.9 μM PFH in the same Tris-HCl buffer. The concentration of 1, 6-diaminohexane in the buffer and waste reservoir varied from (a) 0 mM; (b) 0.1 mM; (c) 0.5 mM; (d) 1.0 mM.

To test the effect of 1, 6-diaminohexane in the reaction channel, electropherograms were obtained with and without 0.1 mM 1, 6-diaminohexane in the reagent reservoir during continuous analysis of GSH produced in the sample reservoir by the enzyme reaction. In this experiment, sample reservoir contained 25 μM GSSG and 50 μM β -NADPH. Reagent reservoir contained 300 μM ThioGlo-1 and 9.5 μM PFH. Experiment was started once GR was mixed with the substrate solution at a final concentration of 5.29×10^{-3} unit/mL in sample reservoir. Sampling and separation times were 0.1 s and 9.9 s, respectively. Potential applied at waste reservoir was -6000 V. It is clear from Fig. 37 that the repeatability is significantly improved from using the

additive. Fig. 37 (c) shows the fluctuation in the FWHM of the GSH-ThioGlo-1 reaction product (GSH*) peaks in both cases. The RSD of the FWHM for GSH* peaks was 2.2% when 0.1 mM 1, 6-diaminohexane was included in reagent reservoir. However, this value increased to 12.8% when 1, 6-diaminohexane was excluded from reagent reservoir. Adding 1, 6-diaminohexane to both the derivatizing reagent and running buffer was helpful for improving the resolution of the separation, reducing the adsorption of PFH and stabilizing the quantitative measurements, especially in continuous sampling. To avoid any interference with the enzyme reaction, 1, 6-diaminohexane was not added to sample reservoir. Applying the above optimized conditions for the separation, the concentration and mass limit of detection for GSH were determined to be 4.2 nM and 10^{-18} mol using ThioGlo-1 as the derivatizing reagent. The repeatability of the continuous injections was evaluated by measuring the peak parameters for the internal standard. The relative standard deviation of the peak area, peak height, FWHM and migration time for the internal standard were found to be 2.5%, 2.0%, 1.0% and less than 0.1%, respectively.

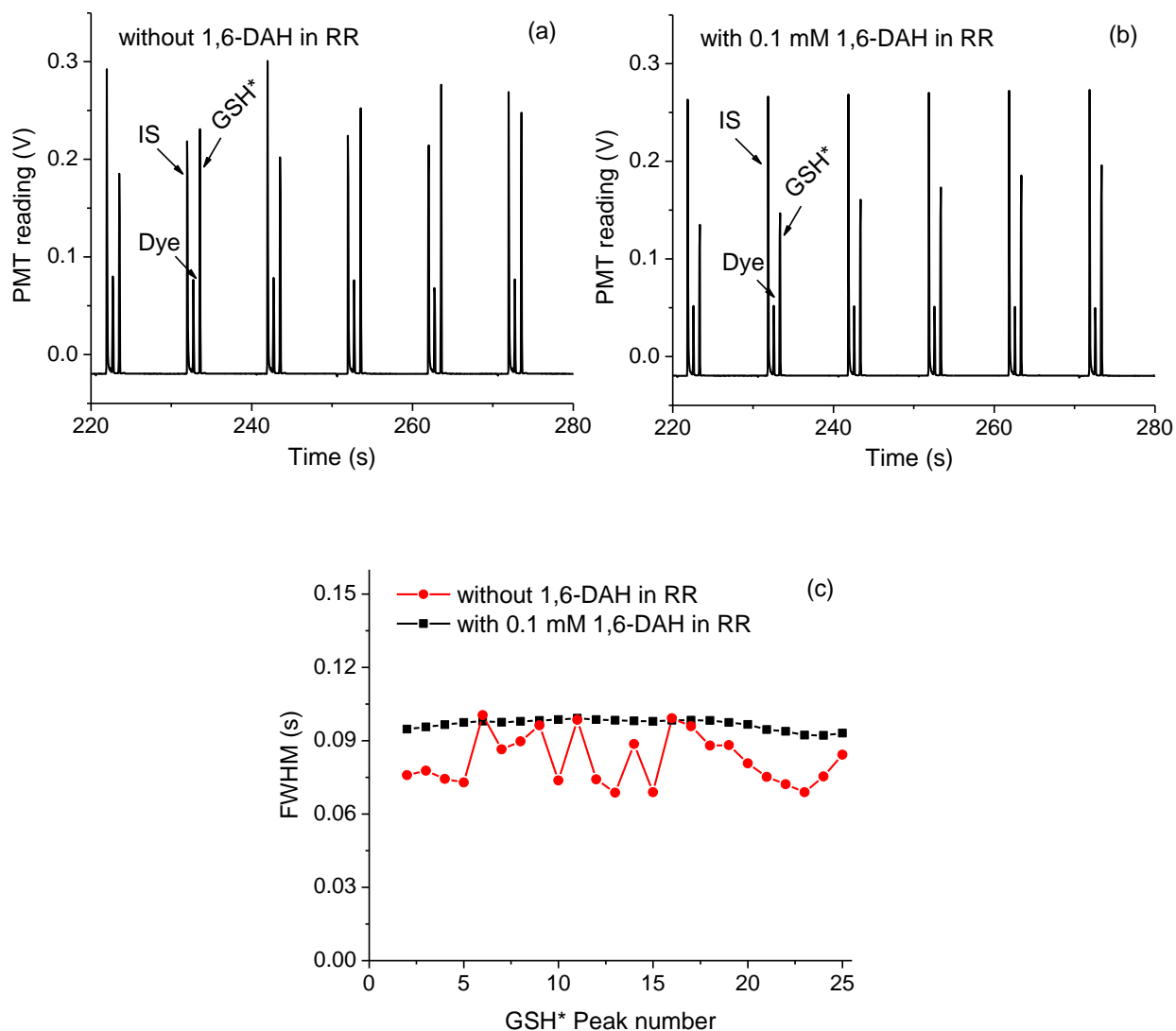


Figure 37. Effect of 1, 6-diaminohexane in reagent reservoir on the enzyme kinetic analysis

(a) No 1, 6-diaminohexane; (b) 0.1 mM 1, 6-diaminohexane; (c) FWHM of the GSH* peaks in both experiments. Sample reservoir contained 25 μM GSSG and 50 μM $\beta\text{-NADPH}$. Reagent reservoir contained 300 μM ThioGlo-1 and 9.5 μM PFH. Experiment was started once GR was mixed with the substrate solution at a final concentration of 5.29×10^{-3} unit/mL in sample reservoir.

3.3.3 Enzyme kinetic study

GR is a well-studied flavoenzyme, which catalyzes β -NADPH-dependent reduction of GSSG to maintain a healthy cellular ratio of [GSH]/[GSSG] as shown by the equation below.^{229, 244}



Numerous studies have demonstrated that in the absence of product inhibition, the double reciprocal plot (Lineweaver-Burk plot) of the reaction rate against one of the two substrates, the other being held constant and saturating, will give a straight line.^{232, 244-248} Thus if we obtain two linear Lineweaver-Burk plots, each of which yields a correct Michaelis constant for the non-saturating substrate, then we know that the derivatization, injection, separation and detection of GSH on this microfluidic platform are reliable.

We utilized the microfluidic chip, and the conditions just developed, to measure the initial forward rate as a function of concentration of one substrate while the concentration of the other substrate was kept at a saturating concentration. As the initial rate was to be measured, inhibition caused by the product was assumed to be negligible. The reaction rate in this case depends only on the concentration of the enzyme-substrate complex, assumed to be nearly constant, therefore; a linear conversion of the substrate to product is predicted. Fig. 38 (a) shows the series of electropherograms obtained for a rate measurement when the initial concentration of GSSG and β -NADPH were 1000 μM and 100 μM GSSG. The electropherograms for all of the injections in this experiment are replotted in parallel in Fig. 38 (b).

The electropherogram in Fig. 38 (a) can be divided into three regions based on the detected peaks. In the first region (0–40 s), no peaks are observed. This is the time needed by the compound with the highest mobility to pass through the reaction and separation channels before being detected. In the second region, located between 40 and 130 s, the IS peaks come out

steadily and the dye peaks start to arrive and gradually become stable. No GSH* peak is detected in this region. GSH* peaks begin to be detected in the third region beginning at approximately 130 s. Calculations based on Ohm's and Kirchoff's laws show that it takes about 106 s for GSH to traverse the reaction channel, i.e., the reaction time is about 106 s. Based on the rate constant determined above, the ThioGlo-1 concentration in the reaction channel, and assuming a pseudo-first order reaction (ThioGlo-1 in excess) the time required to achieve 95% conversion of GSH to GSH* would be 5 s. The time for a complete mixing of dye and GSH in aqueous solution is estimated to be ~2 s, based on the diffusion coefficient of GSH, $D = 6.7 \times 10^{-10} \text{ m}^2/\text{s}$,²⁴⁹ and the channel width, 50 μm . Thus, conversion of GSH to GSH* is virtually complete. Comparison of relative peak areas for the online reaction and offline reaction (5 minutes) shows that the reaction is, in fact, complete. For evaluation of enzyme kinetics, data points were collected once the later peaks demonstrate the expected constant signal (ThioGlo-1 and IS) and a linear increase in the height and area of the GSH* peak due to the enzyme reaction was observed. The first several peaks of GSH* were excluded in the calculation of the initial forward rate. The relative peak area of the GSH* (compared to that of IS) was converted to the concentration of GSH* based on the calibration curve (Fig. 39) obtained under the same conditions as those applied in the enzyme kinetic experiments except that the solution in the sample reservoir contained GSH at known concentrations.

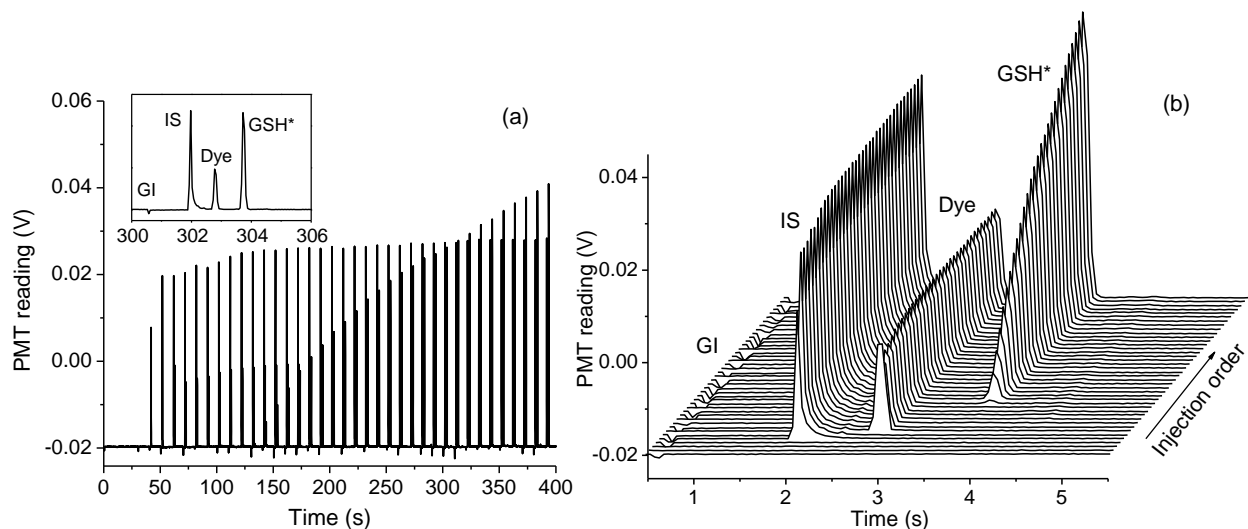


Figure 38. Electropherograms for on-chip enzyme kinetic study

(a) Series of electropherograms obtained in a microfluidic chip with continuous flow gated injection. The concentrations of GSSG and β -NADPH were 1000 μ M and 100 μ M, respectively. The inset magnifies one set of peaks from an injection made between 300 and 309 s. The small valley, GI, around 300.5 s resulted from the flow gated injection. 'IS', 'Dye' and 'GSH*' represent PFH, unreacted ThioGlo-1 and ThioGlo-1-GSH adduct, respectively. (b) Reconstructed plot of PMT reading vs time for all injections in this series.

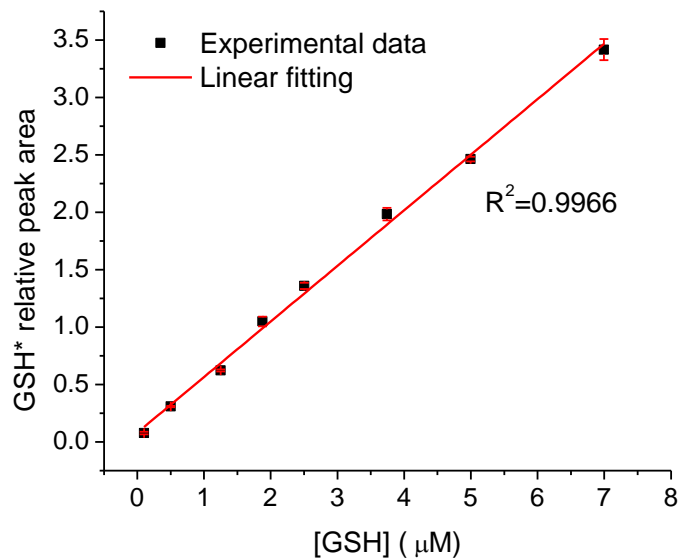


Figure 39. Calibration curve established based on the relative peak area of GSH*

Experimental conditions were same as that in enzyme analysis, except that only GSH was included in sample reservoir. Data are plotted as mean \pm SD for at least 17 injections.

For the enzyme kinetic studies, the concentration of GR was fixed at 7.93×10^{-4} unit/mL; this concentration was chosen to allow the steady state phase of the enzyme catalyzed reaction to last long enough to collect sufficient data while also giving a detectable change in GSH. The appropriate forms of the rate equations for the initial rates are ^{231, 250}

$$v_i = \frac{V_{max}[A]_0[B]_0}{K_{mB}[A]_0 + K_{mA}[B]_0 + [A]_0[B]_0} \quad (23)$$

$$\frac{1}{v_i} = \frac{K_{mB}}{V_{max}} \frac{1}{[B]_0} + \frac{1}{V_{max}} \left(1 + \frac{K_{mA}}{[A]_0}\right) \quad (24)$$

In the above equations, v_i is the initial forward rate obtained under different initial substrate B concentrations, $[B]_0$. $[A]_0$ is the fixed concentration of substrate A. K_{mA} and K_{mB} are the Michaelis constant of substrate A and B, respectively, and V_{max} is the maximum rate. If

substrate A is kept at saturating concentration, $[A]_0$ would be much larger than K_{mA} . Therefore, the term $K_{mA}/[A]_0$ can be neglected and Eq. 24 would be further simplified to

$$\frac{1}{v_i} = \frac{K_{mB}}{V_{max}} \frac{1}{[B]_0} + \frac{1}{V_{max}} \quad (25)$$

A Lineweaver-Burk plot based on Eq. 25 is shown in Fig. 40. The relationship between the initial rate of the forward reaction of GR (the rate at which the GSH concentration changes) and the initial concentration of β -NADPH (1-100 μ M) at a saturating concentration of GSSG (1000 μ M)²⁴⁷ is demonstrated in Fig. 40 (a). The corresponding plot showing the initial rate versus the initial concentration of GSSG (10-1000 μ M) at a saturating concentration of β -NADPH (100 μ M)²⁴⁷ is shown in Fig. 40 (b). The initial concentrations of both GSSG and β -NADPH were chosen to be evenly distributed in the inverse plot. The initial forward rates were obtained by performing linear regression of the GSH concentration vs. time. The apparent K_m of β -NADPH and GSSG for GR obtained from the Lineweaver-Burk plots were $4.4 \pm 0.6 \mu$ M and $40 \pm 11 \mu$ M, respectively. V_{max} values calculated from each plot were close to each other; it was 11.0 ± 1.3 nM/s when the concentration of GSSG was fixed and 10.8 ± 2.6 nM/s when the concentration of β -NADPH was fixed. Errors are the standard error of the mean (SEM).

The K_m values of GSSG and β -NADPH for GR (baker's yeast) measured by Massey et al. were 55 μ M and 3.8 μ M, respectively.²²⁹ Mavis et al. reported similar K_m values of 61 μ M and 7.6 μ M for GSSG and β -NADPH.²⁵¹ The apparent K_m values of GSSG and β -NADPH we obtained using an integrated microfluidic method for evaluation of GR kinetics are comparable with these values.

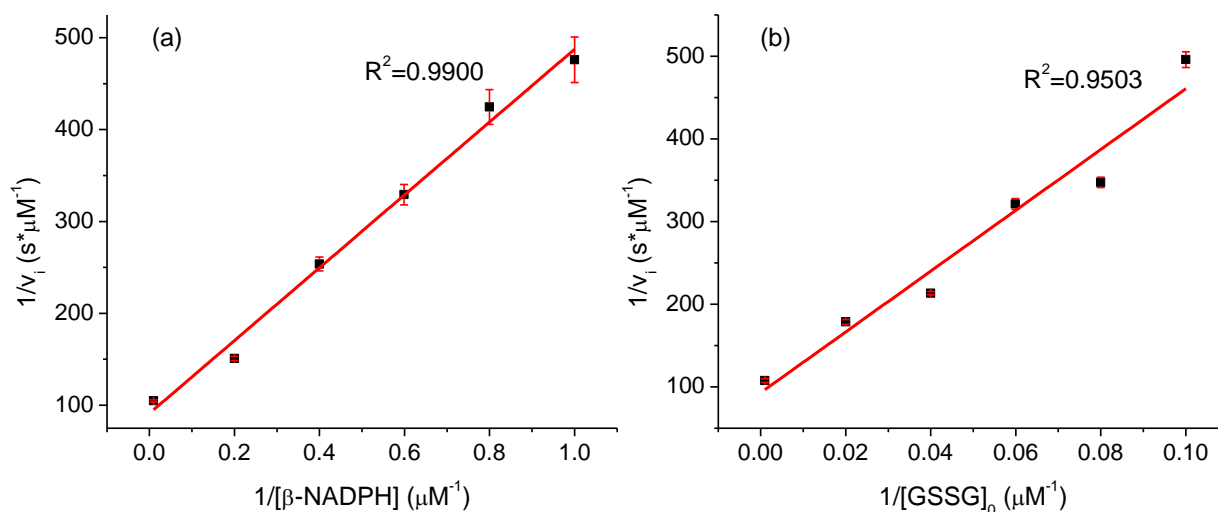


Figure 40. Lineweaver-Burk plots to determine the enzyme kinetic parameters

(a) The initial rate of the forward reaction of GR is plotted against concentration of β -NADPH at 1000 μM GSSG;
 (b) the initial rate of the forward reaction of GR is plotted against concentration of GSSG at 100 μM β -NADPH.
 Error bars are \pm SD ($n = 14$). Note that the initial reaction rate is the expressed as the rate at which GSH concentration changes.

3.4 CONCLUSIONS

We have demonstrated the use of ThioGlo-1 as an online derivatizing reagent for quantitative determinations of GSH. The reagent derivatizes GSH more rapidly than had been thought to be the case. This knowledge was then utilized to develop an integrated microfluidic method for evaluation of enzyme kinetics employing on-chip precolumn derivatization. For the gated separation analysis, PFH as an internal standard minimized variable injection volume effects without added analysis time and 1, 6-diaminohexane addition resulted in stabilization of the peak parameters from GSH, especially during continuous analysis. The sensitivity of the

determinations is excellent with a GSH concentration and mass detection limit of 4.2 nM and 10^{-18} mol. The combination of the simple microfluidic chip with well-chosen chemistry has led to an integrated system capable of continuous monitoring of GSH concentrations.

4.0 AN *IN SITU* MEASUREMENT OF EXTRACELLULAR AMINOTHIOLS IN OHSCS BY INTEGRATION OF ELECTROSMOITIC SAMPLING AND MICROFLUIDIC ANALYSIS

Part of the following work has been published in *Analytical Chemistry* **2013**, 85(6):3095-3103

We demonstrate an all-electric sampling/derivatization/separation/detection system for the quantitation of thiols in tissue cultures. Extracellular fluid collected from rat OHSCs by electroosmotic flow through an 11 cm (length) x 50 μm (ID) sampling capillary is introduced to a simple microfluidic chip for derivatization, continuous flow-gated injection, separation and detection. With the help of a fluorogenic, thiol-specific reagent, ThioGlo-1, we have successfully separated and detected the extracellular levels of free reduced CSH, Hcy and Cys from OHSCs within 25 s in a 23 mm separation channel with a confocal LIF detector. Attention to the conductivities of the fluids being transported is required for successful flow-gated injections. When the sample conductivity is much higher than the running buffer conductivities, the electroosmotic velocities are such that there is less fluid coming by electroosmosis into the cross from the sample/reagent channel than is leaving by electroosmosis into the separation and waste channels. The resulting decrease in the internal fluid pressure in the injection cross pulls flow from the gated channel. This process may completely shut down the gated injection. Using a glycylglycine (Gly-Gly) buffer with physiological osmolarity but only 62% of physiological

conductivity and augmenting the conductivity of the running buffers solved this problem. Quantitation is by standard additions. Concentrations of CSH, Hcy and Cys in the extracellular space of OHSCs are 10.6 ± 1.0 nM (n = 70), 0.18 ± 0.01 μ M (n = 53) and 11.1 ± 1.2 μ M (n = 70), respectively. This is the first *in situ* quantitative estimation of endogenous CSH in brain. Extracellular levels of Hcy and Cys are comparable with other reported values.

4.1 INTRODUCTION

The coupling of sample collection and microfluidic analysis addresses the critical problems that arise in handling small amounts of liquid samples.¹³⁵ Several groups have devised useful approaches to transport samples from cells, tissues, or living animals directly to a microfluidic chip for online analysis.^{153, 252-254} But to the best of our knowledge all the published methods require extra vacuum/pressure pumps for transporting the samples either from a push-pull perfusion probe²⁵² or a microdialysis probe^{153, 253, 254} to the microfluidic chip for further analysis. The addition of these pumps increases the total cost and the complexity of the system.

Electroosmosis is the natural and dominant driving force in CE and microfluidic chips.^{255,}
²⁵⁶ Electroosmosis requires no mechanical pumps but can generate accurate flow rates in the domain of less than one to tens of nL/s depending on the cross sectional area of the conduit.²⁵⁷ In addition, the plug shaped electroosmotic flow creates less solute dispersion than that of parabolic flow in a pressure-driven system. Under an external electric field, solvated cations in the diffuse layer will migrate towards the cathode, dragging the bulk solution. The potential at the shear boundary of the fluid defines the ζ -potential that governs the EOF. Under physiological conditions, the cell surface is naturally negatively charged like that of the wall in a fused silica

capillary or a microfluidic channel.²⁵⁸ We have reported that OHSCs have a ζ -potential of -22.8 mV,²⁵⁹ therefore the EOF generated with an electric field can be used to pump the extracellular fluid out of the tissue for analysis. Our lab has developed an electroosmotic sampling method to extract extracellular fluid from OHSCs into a fused silica capillary. In that work, the sample inside the capillary was then collected for offline HPLC analysis.¹⁰⁶

Cys, Hcy and CSH are three related aminothiols that exist in tissues and body fluids at low levels.^{1, 88} Although Cys is neurotoxic,⁷⁸ it is a rate-limiting synthetic precursor of glutathione in neurons. The latter plays a critical role in defending cells against oxidative stress.¹⁰ In brain, neuronal glutathione synthesis relies on Cys that arises from extracellular hydrolysis of GSH exported from astroglia by γ -glutamyl transpeptidase and aminopeptidase N. This interplay results in an intensive metabolic exchange with astrocytes.³¹ The Cys concentration in plasma is estimated to be in the range of 8-10 μ M,²³ while the concentration of Cys in the extracellular space of rat caudate nucleus and striatum determined by microdialysis is round 2 μ M.^{29, 260} Hcy is an important endogenous molecule in the metabolism of methionine, and it connects the methionine and Cys metabolic cycles.¹ Only trace amounts (0.05-0.3 μ M) of free Hcy (1-2% of total Hcy) exist in its reduced form in plasma.⁸⁷ Changes in the levels of Cys/Hcy or their oxidized forms in biological systems usually indicate dysfunctions of related metabolic cycles or cellular processes. Specifically, cystinosis is due to accumulation of abnormal amounts of cystine in lysosomes.⁷⁶ The Hcy level in plasma/serum is considered to be a biomarker of clinical disorders, such as Alzheimer's disease and cardiovascular disease.¹ Due to their importance, numerous methods have been developed to detect and quantify free or total cysteine and homocysteine in body fluids such as plasma,^{222, 261, 262} urine,^{262, 263} tissue homogenates,²⁶⁴ while fewer studies have been done on the extracellular space of tissues^{29, 260} through microdialysis.

The dominant quantitation methods are HPLC or capillary electrophoresis equipped with UV, FL or mass spectrometry detectors.^{114, 265}

Although CSH is a decarboxylated form of Cys, it is widely believed to be the active terminal product of the synthesis and degradation of CoA in the Cys metabolic cycle.⁶⁸ Albeit at a very low concentration in the tissue,⁶⁹ the oxidation of CSH is believed to be an indispensable pathway for taurine synthesis, the second most abundant amino acid in mammalian tissues.⁷⁰ CSH has many other remarkable roles and biological functions. As an FDA-approved drug for treating cystinosis, CSH can cross the lysosome membrane, react with the cystine to form a mixed disulfide which can be transported out of the lysosome.²⁶⁶ In addition to its potent radio-protective action on DNA-induced radiation damage, CSH, as well as its oxidized form cystamine (CSSC), have been considered as potential neuroprotective agents. Both compounds have shown significant beneficial properties in treating models of neurodegenerative disease, such as Huntington's and Parkinson's diseases.⁷¹ Measuring the CSH concentration in biological samples is vital for understanding its metabolic mechanism and fate. Endogenous CSH levels in different tissue homogenates (brain, liver, kidney, etc),^{72-74, 267-270} urine and plasma^{74, 262, 271} have been reported using HPLC-electrochemical detection^{73, 268, 269}/FL^{72, 74, 268, 270, 271}, CE-LIF²⁶². The published values cover a very wide range, which is most likely due to the inadequate methodology and species differences.^{69, 73} Several workers report that the endogenous concentration of free CSH in brain tissue homogenates is very low and below the detection limits of the most sensitive detection methods (<10 nmol/L).^{69, 72-74} We are unaware of measurements *in vivo* or in *in vitro* preparations such as acute or cultured brain slices.

In this work, we integrated online electroosmotic sampling and microfluidic analysis coupled to confocal LIF detection to evaluate the endogenous free Cys, Hcy and CSH

concentrations in the extracellular space of OHSCs. Compared with publications cited above, the method described here is faster, more sensitive; and to the best of our knowledge for the first time simultaneously evaluates the endogenous Cys, Hcy and CSH in the extracellular space of any tissue.

4.2 EXPERIMENTAL SECTION

4.2.1 Chemicals and reagents

Tris (hydroxymethyl)aminomethane (Tris base), 1,3-bis[tris(hydroxymethyl)methylamino]propane (Bis-Tris propane), hydrochloric acid, sodium hydroxide, dimethyl sulfoxide anhydrous (DMSO), D-(+)-glucose, Gly-Gly, L-Cys, DL-Hcy, CSH hydrochloride, Gey's balance salt solution (GBSS) and nitric acid (70%) were purchased from Sigma-Aldrich Chemical Co. (St. Louis, MO). Hydrofluoric acid (48-50%) was from Fisher Scientific (Pittsburgh, PA). Sodium chloride, potassium chloride and methanol were obtained from Avantor Performance Materials (Center Valley, PA). Potassium phosphate monobasic and calcium chloride dihydrate were from EM Science (Gibbstown, NJ). Opti-MEM, horse serum, Hank's balanced salt solution (HBSS) with phenol red and propidium iodide (PI) were from Life Technologies (Grand Island, NY). ThioGlo-1, sodium bicarbonate and magnesium sulfate anhydrous were purchased from EMD Millipore (Billerica, MA).

Stock solutions of CSH, Hcy, Cys, GSH, γ -Glu-Cys and Cys-Gly were prepared no more than two days before experiments using degassed Milli-Q water (EMD Millipore) and stored at -20 °C. The stock solution of ThioGlo-1 was prepared using anhydrous DMSO with the final

concentration of 2.5 mM. Stock solutions were diluted serially to the desired concentration during the experiments and kept on dry ice when not in use. The artificial cerebrospinal fluid (ACSF) was composed of 128 mM NaCl, 3 mM KCl, 2 mM CaCl₂, 1.2 mM MgSO₄, 0.4 mM KH₂PO₄, 25 mM NaHCO₃ and 10 mM D-glucose.²⁷² Gly-Gly modified ACSF (ggACSF) was prepared by replacing 75 mM NaCl in ACSF with 125 mM Gly-Gly and keeping all other components unchanged. Both solutions were adjusted to pH 7.4 using NaOH. GBSS used during sampling experiments was fortified with 2.7 mM MgSO₄ and 0.5% D-(+)-glucose. The term GBSS used below means “fortified GBSS” unless otherwise specified. PI solution was prepared using GBSS to a final concentration of 0.35 mM and was stored in the freezer. For optimization of the separation conditions, Tris-HCl buffers and Bis-Tris propane buffers at various concentrations and different pH values were used as the running buffer to test their effects in the separation of aminothiols mixture in the microfluidic channel. In some experiments, 1, 6-diaminohexane were also used as an additive of the running buffer. For online sampling experiments, the running buffer of the microfluidic capillary electrophoresis was 40 mM Bis-Tris propane buffer with 15 mM NaCl (pH 8.5) unless otherwise specified. Tris-HCl buffer (20 mM, pH 7.5) was used as the derivatizing buffer for the thiol analytes. All buffers were filtered through 0.1 μm polyethersulfone membrane (EMD Millipore) and degassed by ultrasonication prior to use.

4.2.2 Design of a microfluidic chip coupled with electroosmotic sampling

The fabrication of microfluidic chip was similar as described previously in Section 3.2.2 with some modifications. Briefly, after UV exposure, development and removal of the underlying chromium layer, the AZ 1500 photoresist coated borofloat glass plates was etched in HF solution

(HF/HNO₃:200/30 (v/v)) to a desired depth. The photoresist and chromium remaining on the plate were then removed completely. The etched glass plate was carefully aligned with another uncoated borofloat cover plate pre-drilled with liquid access holes. Permanent bonding between two plates was achieved by annealing at 655 °C for 8 hours. The mask width for all channels is 30 μm and the etching depth is 20 μm. Fig. 41 shows the layout and the photograph of the microfluidic chip coupled with electroosmotic sampling. The total length of the reaction channel from the mixing junction to the injection cross is ~46.3 mm. The detection point (DP) is about 23 mm away from the injection cross. R1, R2, R3 and R4 represent derivatizing reagent reservoir, buffer reservoir, waste reservoir and auxiliary reservoir, respectively. An 11 cm (length) x 50 μm (ID)/360 μm (OD) fused silica capillary tube (Polymicro Technologies, Phoenix, AZ) was connected to the R5 through a NanoPort™ assembly (IDEX Health&Science LLC, Oak Harbor, WA). The free tip of the capillary was positioned by a Sutter MP-285 micromanipulator system (Sutter Instrument Company, Novato, CA) near the surface of an OHSC. Platinum electrodes (0.5 mm diameter, Goodfellow Corporation, Oakdale, PA) made electrical contact with solutions in all reservoirs and the Petri dish (35x10 mm, BD, Franklin Lakes, NJ). During the experiment, the electrodes in R1 and the Petri dish were connected to positive power supplies (UltraVolt, Inc., Ronkonkoma, NY). The electrode in R3 was connected to a negative power supply, while the one in R4 was kept at ground (GND). Flow-gated sampling was achieved through the switching of electrode in R2 between the “GND” (separation) and “floating” (injection) states. The microfluidic chip shown in Fig. 41 can also be used in on-chip experiments by temporally replacing the sampling capillary with reservoir R5. In these experiments, R1 and R5 (or R4) will be connected to positive power supplies, while R4 (or R5) will be disabled. The potential settings in other reservoir will be the same as that in the electroosmotic sampling. Extra caution is

required when working with high voltage power supplies. All voltages were controlled remotely by computer.

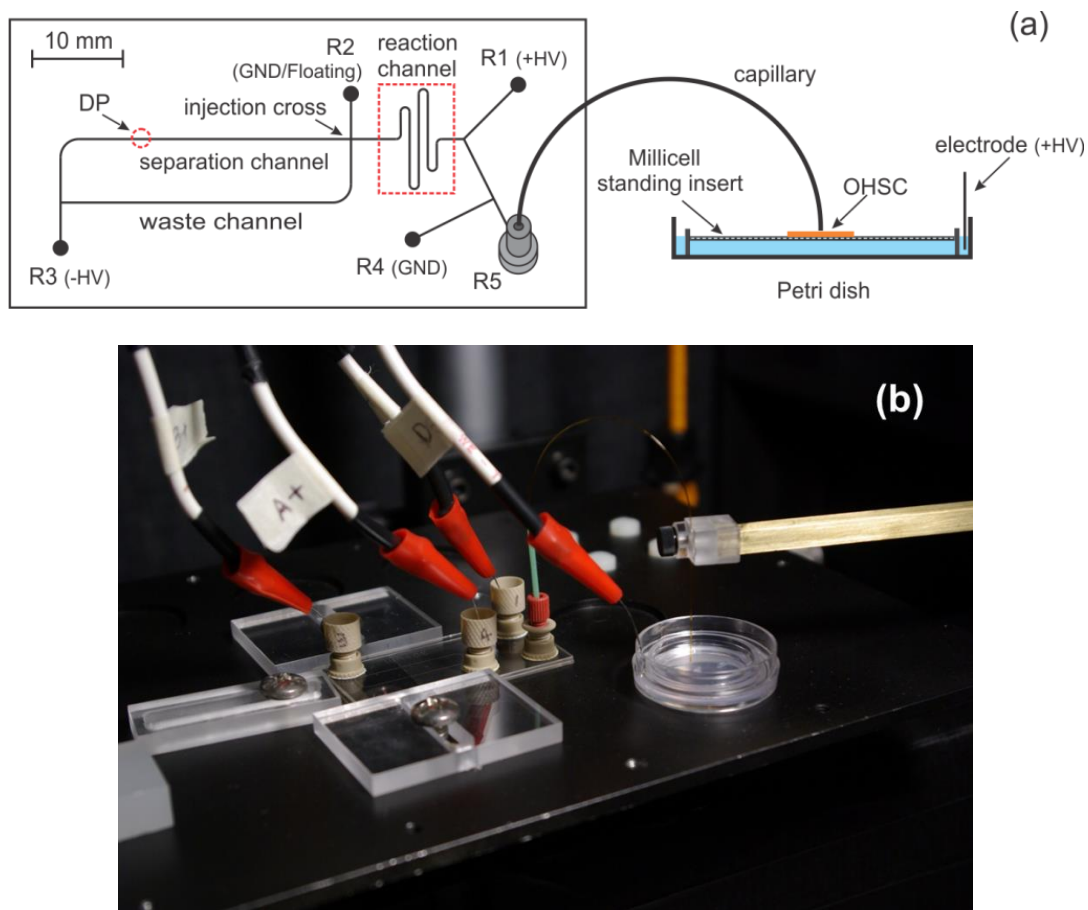


Figure 41. Layout of the microfluidic chip and single capillary electroosmotic sampling
 (a) Sketch view of the system; (b) Photograph of the single capillary electroosmotic sampling

4.2.3 Instrumentation

Detection in the microfluidic experiments was achieved through a home-made confocal LIF detector detection system described in Chapter 2. The PMT control voltage was set at 0.5 V in the optimization experiments and 0.6 V in the online analysis of aminothiols from OHSCs. The laser power was maintained at 3.0 mW. A locally written program in LabView 8.2 (National

Instruments, Austin, TX) was used to control two four-channel high-voltage power supplies, the flow-gated sample introduction, the control voltage of the PMT and the signal collection. An inverted fluorescent microscope IX71 (Olympus, Center Valley, PA) was used to characterize OHSCs. This microscope was equipped with an Olympus U-MWIG2 mirror unit (ex: 520-550 nm; em: 580IF nm; dichroic: 565 nm), an Olympus UPLANAPO 4x objective and a Hamamatsu ORCA-ER digital CCD camera. Laser safety goggles should be worn in the presence of the laser beam.

4.2.4 Optimization of the separation conditions for aminothiols

The separation conditions for microfluidic analysis of aminothiols were optimized using the microfluidic chip shown in Fig. 30. Standard mixture of aminothiols was added into the sample reservoir while ThioGlo-1 solution was transferred into the reagent reservoir. The derivatization of aminothiols was achieved in 20 mM Tris-HCl at pH 7.5 in the reaction channel. Different running buffers were added into the gated reservoir and waste reservoir to test their capability in separating aminothiols. The detection point was located at 27 mm from the injection cross. In the experiments, the electrodes in reagent reservoir and sample reservoir were kept at ground, while the electrode in waste reservoir was connected to -6000 V. The gated reservoir was switched between “GND” and “Floating” to achieve multiple injections with an injection time of 0.1 s. The microfluidic channels were rinsed with NaOH and buffer solutions successively to prevent contamination between runs.

4.2.5 OHSCs preparation and characterization

The procedure for OHSC preparation is adapted from Gogolla's protocol²⁷³ and has been approved by the IACUC of the University of Pittsburgh. Briefly, the hippocampus of a 7 days postnatal Sprague-Dawley rat was removed and sliced (McIlwain tissue chopper, Mickle Laboratory Engineering Co. Ltd., UK) into 350 μm thick transverse sections. After cold incubation, slices with the right morphology were selected and transferred onto the Millicell standing inserts (hydrophilic PTFE membrane, 0.4 μm , EMD Millipore) in a 6-well tissue culture plate (Sarstedt Inc., Newton, NC) containing culture medium (50% Opti-MEM, 25% HBSS with phenol red, 25% horse serum, 0.45% D-(+)-glucose). The OHSCs were usually cultured in the incubator for 6-8 days before any sampling experiments were carried out.

An inverted fluorescent microscope IX71 (Olympus, Center Valley, PA) was used to characterize OHSCs. This microscope was equipped with an Olympus U-MWIG2 mirror unit (ex: 520-550 nm; em: 580IF nm; dichroic: 565 nm), an Olympus UPLANAPO 4x objective and a Hamamatsu ORCA-ER digital CCD camera. Tissue viability was assessed before a set of experiments. PI was added to the culture medium to a final concentration of $\sim 7 \mu\text{M}$. The OHSCs were then cultured overnight. The PI-containing medium was replaced with pre-warmed and gassed GBSS before the fluorescence images were taken. Cell death was assessed by acquiring fluorescence images using the same exposure time as the auto-exposure time for an intentionally killed 100% death control.¹⁰⁵ After that, the GBSS in the 6-well plate was replaced with normal culture medium and OHSCs were taken back to the incubator for future experiments. The assessment of cell death in OHSCs following sampling was also carried out as described above.

4.2.6 Measurement of extracellular aminothiols in OHSCs using single capillary mode

R2 and R3 contain running buffer. R1 contains ThioGlo-1 2.7 μM in 20 mM Tris-HCl buffer (pH = 7.5). R4 and the sampling capillary were filled with 20 mM Tris-HCl buffer (pH = 7.5) with 60 mM NaCl. The final liquid volume in each reservoir was 300~310 μL . OHSCs on culture inserts were transferred from the incubator to a Petri dish containing 1.2 mL pre-warmed and gassed GBSS. Immediately before sampling, an OHSC on an insert was transferred to another Petri dish containing 1.2 mL of ggACSF alone or spiked with the standards at their desired concentrations before the sampling. The free end of the sampling capillary was lowered perpendicularly towards the tissue until it made contact with a thin layer of liquid on the tissue surface (CA3 region) by a Sutter MP-285 micromanipulator system (minimal resolution 0.04 μm). The tip was then raised up 20 μm so that the tissue surface and the capillary tip were connected through a thin layer of liquid. The process was monitored using a Fisher Scientific Stereomaster zoom microscope.

Every sampling experiment was started with a pre-sampling step. In this step, +3000 V were applied to the Petri dish while R4 was grounded. All other reservoirs were floating. This step preserves derivatizing reagent and running buffer while electroosmotically transporting extracellular fluid into the sampling capillary. Six minutes later, the microfluidic chip was switched to the measuring mode. Data collection was initiated and +300 V and -4500 V were applied to R1 and R3, respectively. The voltage on R4/Petri dish was not changed. R2 was switched between two states: “floating” (injection, 0.5 s) and “GND” (separation, typically 24.5 s) to obtain a continuous sequence of separations as described previously.²⁷⁴ The time during which the system is in the online measuring mode varies, but is typically in the 800-1000 s range. This corresponds to 32-40 injections and separations per run. The appearance of the first peaks from the extracellular space typically occurs in the 17th electropherogram. Therefore, we

obtain 16-24 electropherograms corresponding to 6.7-10 minutes of sampling from the tissue. Between each run, the microfluidic chip and the sampling capillary were flushed and reconditioned with NaOH and buffer solutions successively to prevent contamination. All experiments were carried out at room temperature. To prevent byproducts from the oxidation reactions at the Pt electrode in the culture dish from altering the composition of the extracellular space, the Pt electrode was kept 15-20 mm from the sampling region.

4.2.7 Electroosmotic sampling from OHSCs using dual-capillary

Dual capillary setup mode was tested as a comparison of single capillary electroosmotic sampling from OHSCs. Fig. 42 shows the difference between these two sampling modes. In dual capillary mode, the capillary holder has two parallel grooves which can fit two capillaries at the same time. The inner distance between two capillaries is determined by the distance of the grooves, which is 180 μm . Before the experiment, one end of the inlet capillary (15 cm x 50 μm ID) would be immersed into a small glass vial which contains ggACSF buffer only or spiked with GSH and a platinum electrode connecting to a positive power supply. The other end of the inlet capillary would be lowered towards the tissue together with one end of outlet capillary (11 cm x 50 μm ID) until the tip of outlet capillary just made contact with a thin layer of liquid on the tissue surface (CA3 region) by the manipulator. The capillary holder was then raised up 20 μm so that the tissue surface and the outlet capillary were connected through a thin layer of liquid. In this process, it was important to make sure that the tip of inlet capillary also connected with the surface liquid on the tissue. The other end of the outlet capillary will be connected to the microfluidic chip in the same way as that in a single capillary experiment. There is no electrode in the Petri dish in the dual capillary mode. It must be noticed that there is limited freedom to use

only one manipulator to control two capillary at the same time. The relative height of the two capillaries may result in two cases as shown in Fig. 42 (c). Although the distances between the tip of outlet capillary and tissue surface are kept the same in both cases, the distance between the tip of inlet capillary and tissue surface may varies. In case A, the tip of inlet capillary is much closer to the tissue than that of outlet capillary. In case B, the tip of inlet capillary is at the same height as that for the outlet capillary. During the dual capillary sampling experiment, the voltage setup was same as that for the single capillary analysis, except that +3000 V positive potential used to apply to the Petri dish was now switched to the glass vial with a value of +7000 V. Inlet capillary was prefilled with the same solution as in the glass vial and outlet capillary was prefilled with 20 mM Tris-HCl buffer (pH = 7.5) with 60 mM NaCl as in single capillary experiment. Petri dish contained 1.2 mL pre-warmed and gassed GBSS. For comparison purpose, all the solutions contained in the reservoirs are the same as those in single capillary experiment. Similarly, every sampling experiment included a six minutes pre-sampling step, where +7000 V were applied to the Petri dish while R4 was grounded. All other reservoirs were floating.

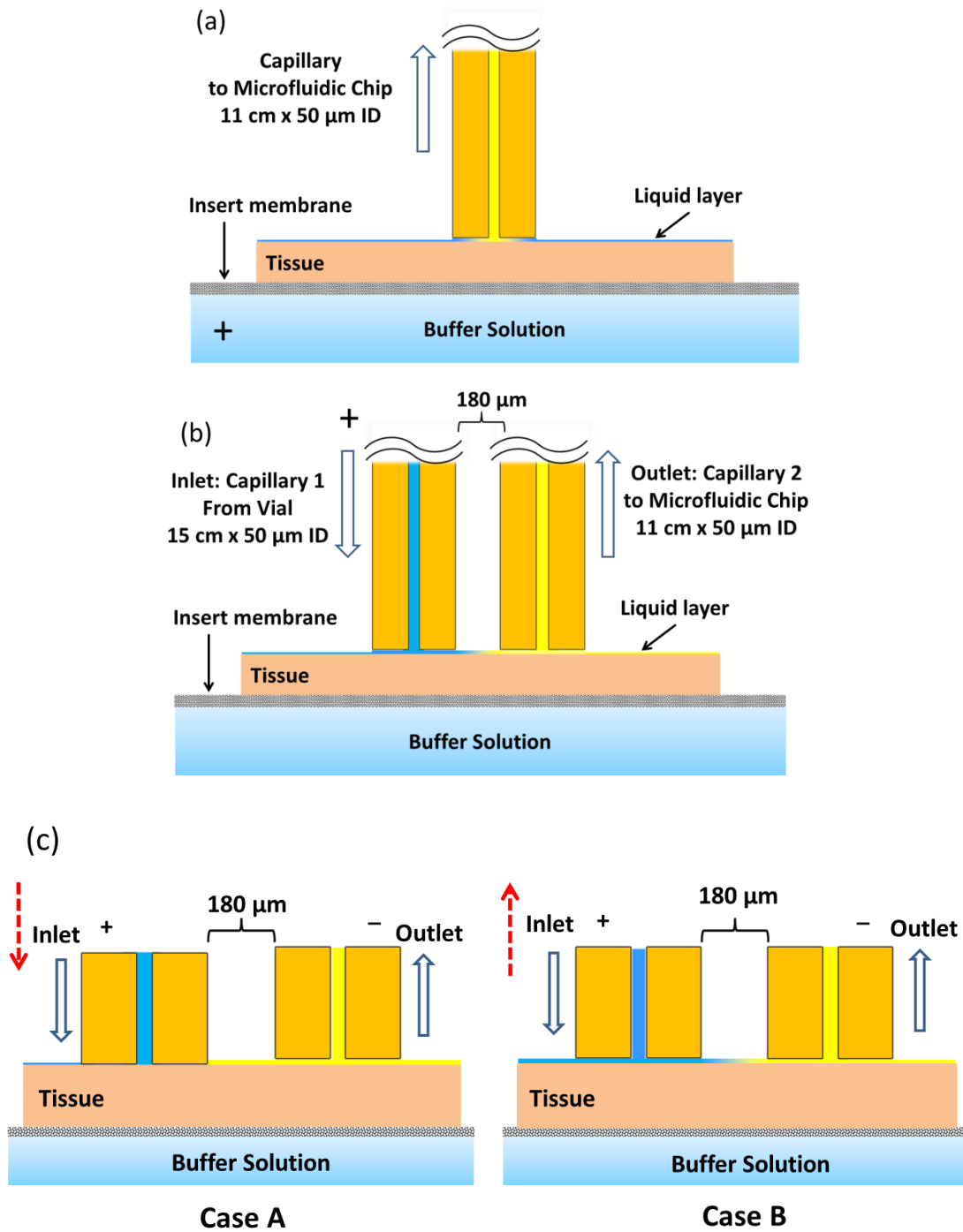


Figure 42. Schematic views of single and dual capillary modes in the electroosmotic sampling (a) Single capillary mode; (b) dual capillary mode; (c) two different cases in dual capillary mode: Case A, inlet capillary lower than outlet capillary; case B, inlet capillary is at the same height as the outlet capillary.

4.3 RESULTS AND DISCUSSION

4.3.1 Optimization of separation conditions of aminothiols for microfluidic analysis

The separation conditions of aminothiols in microfluidic channel were optimized for later online analysis. Tris buffer has been used as the running buffer in the separation of ThioGlo-1 and fluorescent derivatized GSH in the glutathione reductase experiments (Section 3.3.2). However, the separation capacity of this solution was not good for aminothiols mixture including Hcy, Cys, GSH, γ -Glu-Cys and Cys-Gly. Fig. 43 shows the separation of aminothiols using 20 mM Tris-HCl at different pH values. At pH 7.5, unreacted ThioGlo-1, fluorescent labeled Hcy, and Cys peaks were overlapped, while fluorescent labeled GSH, γ -Glu-Cys and Cys-Gly migrated together as a single peak. Although, increasing the pH to 8.0 decreased the average signals for all the peaks, there was a baseline separation of Cys from that of Hcy and ThioGlo-1.

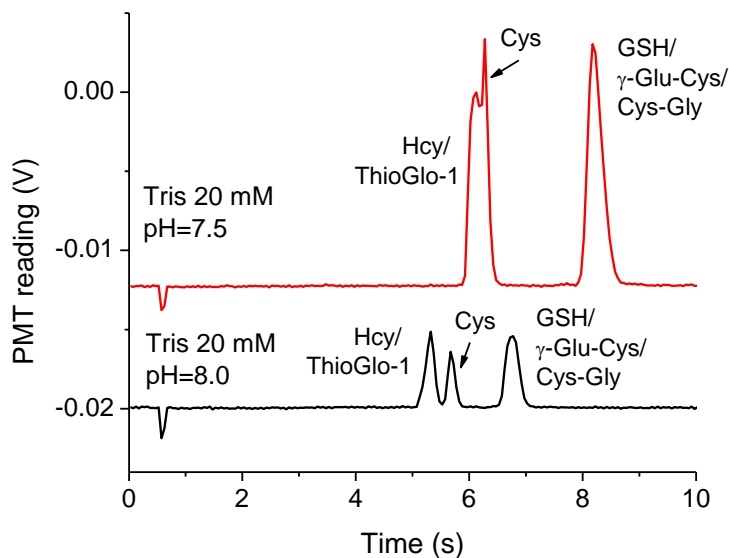


Figure 43. Separation of aminothiols mixtures using 20 mM Tris-HCl buffers at pH 7.5 and 8.0

The concentration of Hcy, Cys, GSH, γ -Glu-Cys and Cys-Gly in the sample reservoir were all 1.0 μ M and the concentration of ThioGlo-1 in reagent reservoir was 5.0 μ M. The labeled peaks belong to the aminothiols derivatized with ThioGlo-1. Hereafter, the names of the aminothiols will be used to mark the peaks of ThioGlo-1 labeled aminothiols.

Bis-Tris propane is another widely used chemical substance in buffer solution with a wider buffering range (pH 6.0 to 9.5) than that of Tris buffer (pH 7.1 to 9.0). The separation performances of Bis-Tris propane buffer solutions at different pH for aminothiols were tested and summarized in Fig. 44. At pH 7, a baseline separation of GSH, Cys-Gly and γ -Glu-Cys were achieved. However, the separation of Hcy, Cys and ThioGlo-1 is not acceptable as indicated by the inset of Fig. 44 (a). The resolutions for peaks of ThioGlo-1, Hcy and Cys are improving together with much shorter migration times for all the peaks as the pH of the running buffer increases. The resolutions for GSH, γ -Glu-Cys and Cys-Gly decreases first when pH of the running buffer varies from 7.0 to 8.0, and then increases a little at pH = 9.0, where Cys-Gly is

baseline separated from the overlapped peaks of GSH and γ -Glu-Cys. The concentration Bis-Tris propane buffer will also affect the separation performance. Fig. 45 indicates that as the concentration of buffer solution is enhanced, the separation of peaks improves with longer migration time. The trends in the change of migration time with pH and concentration are constant with what is predicted by the Debye-Huckel approximation.¹¹⁷ The effect of 1, 6-diaminohexane to the separation of aminothiols was also examined and shown in Fig. 46. The increment in the additive concentration in the running buffer results in an improved separation performance at the cost a longer migration time. The actual separation conditions for the online analysis will be determined by the analytes of interest presenting in the samples and the requirement of analysis time to achieve good temporal resolution.

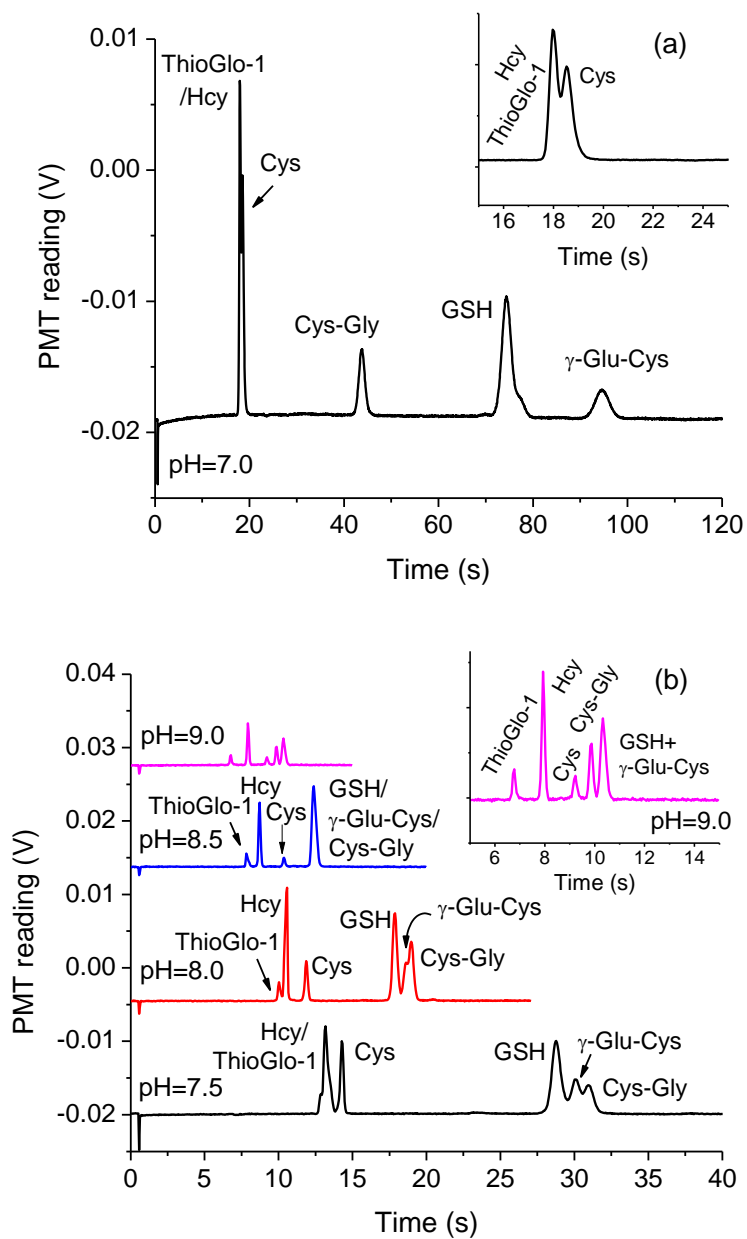


Figure 44. Separation of aminothiols mixtures using 20 mM Bis-Tris propane buffers with various pH. The concentration of each analyte in sample reservoir was 1 μ M each. The concentration of ThioGlo-1 in reagent reservoir was 5 μ M.

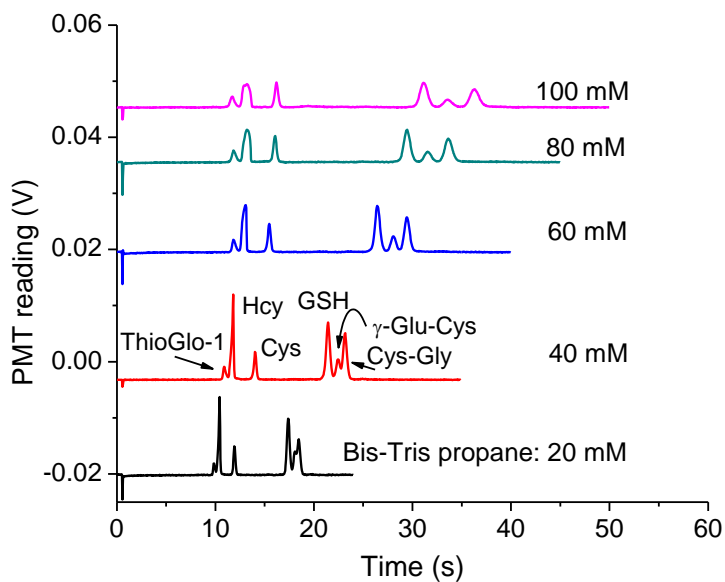


Figure 45. Effect of Bis-Tris propane concentrations on the separation of amino thiols mixtures at pH 8.0

The concentration of each analyte in sample reservoir was 1 μM each. The concentration of ThioGlo-1 in reagent reservoir was 5 μM .

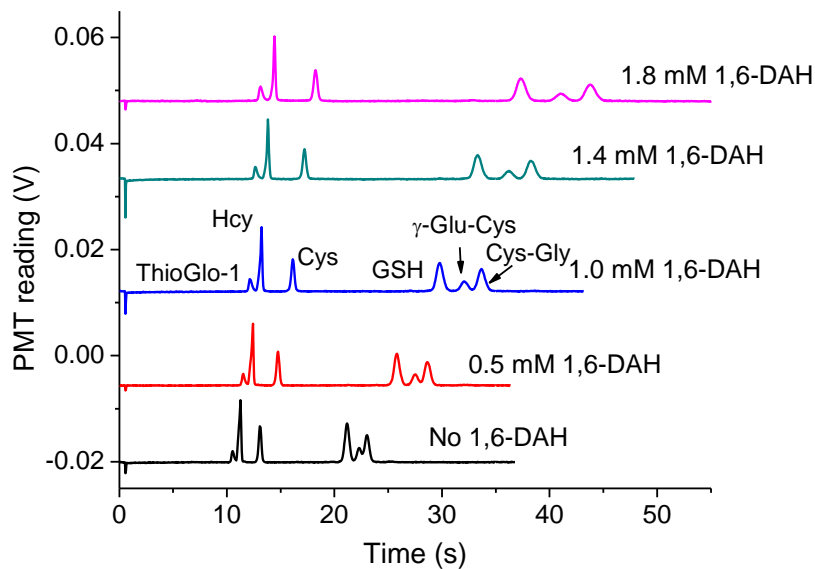


Figure 46. Effect of 1, 6-diaminohexane on the separation of amino thiols mixtures

The concentration of each analyte in sample reservoir was 1 μM each. The concentration of ThioGlo-1 in reagent reservoir was 5 μM . Running buffer is 30 mM Bis-Tris propane buffers at pH 8.0. 1, 6-DAH: 1, 6-diaminohexane.

4.3.2 Microfluidic analysis of samples with high conductivity

Initial experiments drawing ACSF into the chip led to difficulties such as significant Joule heating, gas bubble formation,²⁷⁵ reduced electrophoretic separation efficiency,²⁷⁶ and fast consumption of buffer seen by others. Methods to deal with this problem include reducing the sample conductivity, or diluting samples, and decreasing the electric field strength or applying ac electric fields with dc offsets.²⁷⁵ In our experiments, Gly-Gly, widely used in biochemistry with a buffering range that complements phosphate and bicarbonate (7.5-8.9 at 25 °C), was used as a substitute for some of the NaCl in the ACSF that the OHCSs imbibe. In the following experiments, 75 mM of the NaCl in ACSF was replaced with 125 mM Gly-Gly in ggACSF and the final pH value of 7.4 was adjusted using NaOH solution. The osmolarity for the ggACSF was calculated to be the same as that of the ACSF. The ggACSF's conductivity is 9.6 mS/cm while the conductivity of ACSF is 15.4 mS/cm. We assessed the potential for tissue damage from brief exposure of OHSCs to ggACSF. Fig. 46 (c1) and (c2) show the fluorescence and bright field images of an OHSC which was placed in a Petri dish containing ggACSF for 10 min. By measuring the grey level of the experimental OHSC in Fig. 47 (c1) and comparing it with that of the 100% death control in Fig. 47 (a1) and a live control in Fig. 47 (b1), the percentage of cell death can be calculated according to the Eq. 26.¹⁰⁵

$$\text{death\%} = \frac{\text{experimental OHSC} - \text{live control}}{\text{dead control} - \text{live control}} \times 100\% \quad (26)$$

The results indicate that the death% for the CA3 region (sampled region) was below 1%. Therefore, ggACSF is an effective substitute for the ACSF in electroosmotic sampling.

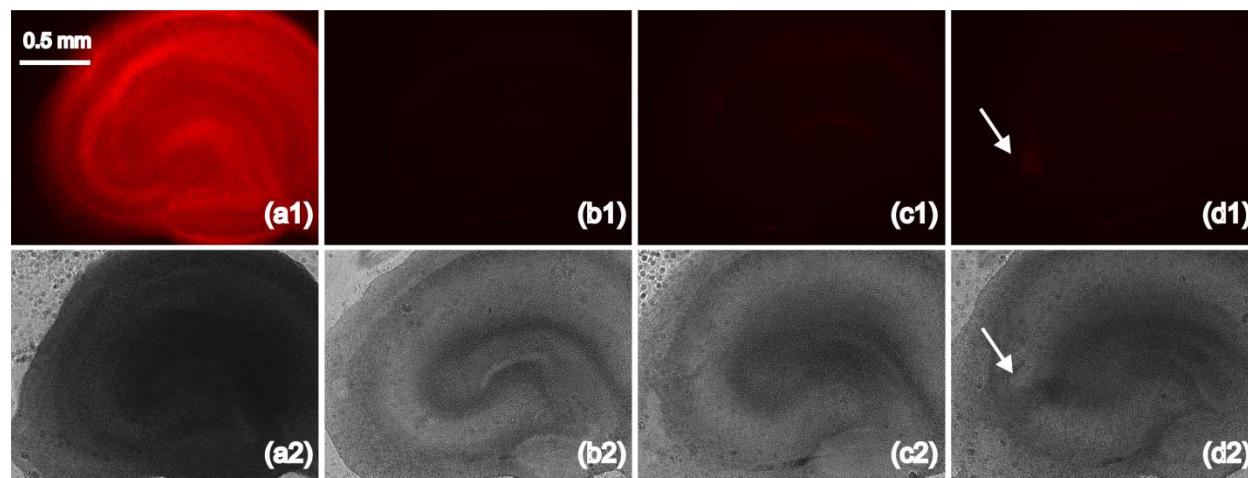


Figure 47. Viability assessment for OHSCs

(a1) fluorescence and a2 bright field are for the 100% death control. (b1) and (b2) are for a live control, which was handled in the same way as the experimental OHSCs, except that it was neither sampled nor exposed to ggACSF. Image (c1) and (c2) are for an OHSC placed on the same culture insert as the sampled OHSC (d1/d2) in a Petri dish containing the ggACSF. The electroosmotic sampling was carried out by applying +3000 V at the Petri dish and GND at R4 for 10 min. The arrows indicate the location where the sampling capillary tip was positioned.

4.3.3 High sample conductivity affects flow-gated sample injection analysis of samples

Normally, the conductivities of the fluids inside the channels during a microfluidic analysis are similar. We found that when the conductivity of the stream from the reaction channel (which contains the sample) is much higher than that of the running buffer (from R2 and R3), flow-gated sample injection will fail. To investigate this, we used a simplified version of the setup shown in Fig. 41 in which the capillary and fitting were removed from R5. An electrode and an appropriate buffer solution were placed in the reservoir thus created. There is no analyte flowing in from the sample branch (from R5). We use the peak from the ThioGlo-1 reagent, which has a very low but non-zero quantum yield in the absence of thiols, as a flow marker. Fig. 48 shows a series of flow-gated injection experiments where the analyte-free sample stream in R5 has the

same (a) or higher (b) conductivity than that of the running buffer. The period from 0 to about 80 s in Fig. 48 (a) and (b) represents the time needed for changes made in the reservoirs to show up at the injection cross. When the conductivity of the solution in R5 was 1.4 mS/cm (20 mM Tris, pH = 7.5) which is the same buffer as in R1, R2, and R3, continuous flow-gated injection generated reproducible ThioGlo-1 peaks. When the low conductivity buffer in R5 was replaced by ACSF (15.4 mS/cm), and following the 80 s period in which the conductivity in the reaction channel changes, the ThioGlo-1 peaks disappear as shown in Fig. 48 (b). To validate that the failure of flow-gated sample introduction is due to the mismatch of the conductivities around the injection cross, the running buffers in R2 and R3 were both replaced with 20 mM Tris-HCl augmented with 60 mM NaCl (pH = 7.5), which increased the conductivity inside the separation channel to 7.3 mS/cm. We estimate the conductivity in the reaction channel to be 4.2 mS/cm with R5 at 15.4 mS/cm and R1 at 1.4 mS/cm. This estimation depends on the conductivities of the fluids as well as the mixing ratio of fluids from R1 and R5 as they enter the reaction channel. Estimation of the mixing ratio accounts for the relevant channel lengths, applied voltages, and channel wall ζ -potentials (which take into account the local ionic strength). When the reaction channel conductivity (~ 4.2 mS/cm) is lower than that of R2/R3 (7.3 mS/cm), reproducible flow-gated injection behavior is recovered as shown in Fig. 48 (c).

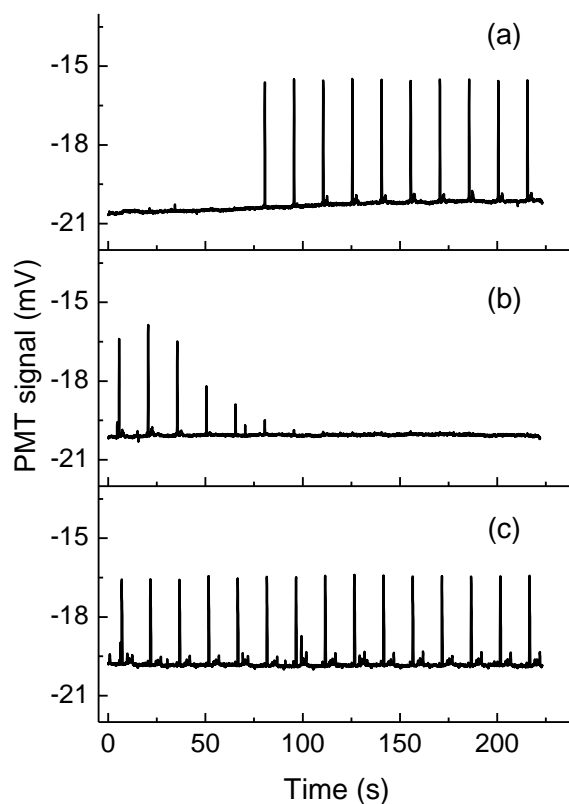


Figure 48. Effect of buffer conductivity on the flow-gated injection

+200 V, +200 V and -4500 V were applied to R1, R5 (no capillary was connected) and R3, respectively. R2 was switched between “GND” (0.5 s) and “floating” (14.5 s) continuously, while R4 was disabled. R1 was filled with 3.4 μM ThioGlo-1 in 20 mM Tris-HCl (pH = 7.5). (a) R2, R3, and R5 have 20 mM Tris-HCl (pH = 7.5). (b) R2 and R3 as in (a), R5 has ACSF (pH = 7.4). (c) R2/R3 has 20 mM Tris-HCl containing 60 mM NaCl (pH = 7.5), R5 same as (b).

To understand this phenomenon better, we simulated it using Comsol v4.3 (COMSOL, Inc., Burlington, MA). The channel lengths, applied voltages, and sample injection time were simulated at 1/10 of their laboratory values. This increases computing efficiency while leaving the critical feature, electric field, equal to the field applied in the laboratory. To avoid confusion, we will refer to laboratory voltages. We simulated injections with the conductivity in R5 ranging

from 1.4 mS/cm to 15.4 mS/cm, while the conductivities of the solutions in all other reservoirs were kept constant at 1.4 mS/cm. In Fig. 49, the injections cross has the same orientation as that in Fig. 41. Fig. 49 shows that the conductivity in R5 has a significant influence on the velocities at the cross. Importantly, at high conductivity, floating R2 does not result in an injection. This can be explained qualitatively as follows.

In the injection step (R2 floating) the current from the reaction (r) channel passes in about equal proportions into the waste (w) and separation (s) channels. As the cross sectional areas are all the same, the current density in the separation and waste channels is about half that of the reaction channel. As the electric field is proportional to the product of current density and resistivity, when the resistivities are the same in all channels, the electric field in the reaction channel E_r is nearly twice as large as that of the separation channel (E_s) or that of the waste channel (E_w). For incompressible liquid, according to the law of the conservation of mass, the total volumetric flow rate (m^3/s) into the cross is equal to that out of the cross which can be expressed as follows:

$$A(v_s + v_w) = A(v_g + v_r) \quad (27)$$

where A is the area (m^2) of the channel cross sections, v_s , v_w , v_g , and v_r are the flow speeds (m/s) in the separation, waste, gated and reaction channels, respectively. Each flow speed is contributed by two terms, the electroosmotic flow and the pressure driven flow. According to Hagen-Poiseuille law, the mean flow speed caused by the pressure drop is inversely proportional to the length of the channel given the same pressure drop between the inlet/outlet of a channel and injection cross. As the channel lengths for the separation, waste and reaction channels are much longer than the gated channel, the contribution from the pressure driven flow is negligible for v_s , v_w , and v_r in comparison with that for v_g . When R2 is floating, there is no electric field in

the associated channel, v_g is contributed only by pressure driven flow. According to the above discussion, the flow speeds in reaction, separation and waste channel are proportional to the electric fields, v_r is equal to $v_s + v_w$. Combining the mass balance expressed as Eq. 27, v_g is zero. This is seen in the simulation, Fig. 49 (c1). Therefore, the sample stream from the reaction channel enters the separation channel when R2 is floating and the injection is successful (Fig. 49 (a1)).

If we keep the conductivities of solutions in R1/R2/R3 unchanged while increasing that of solution in R5, after a certain time the concentrations of the solutions in all channels will reach a new steady state. The conductivities in the waste and reaction channels will be similar and higher than that of the separation channel, which is approximately unchanged. As the parallel waste and separation channels have different conductances, their currents are no longer the same. The current in the waste channel becomes larger than that in the separation channel. Furthermore, as the current in the reaction channel provides the current passing through both the waste and separation channels, and the waste channel has the majority of the current beyond the cross, the ratio of the current in the reaction channel to that in the waste channel is now less than two. As the current densities define the fields, the fields suffer the same change in ratio. Thus, when R2 is floating, E_s and E_w are each greater than one-half of E_r (See Appendix A for detailed equation deduction). Consequently, the mass flow rate leaving the cross is greater than the mass flow rate provided by the reaction channel:

$$v_s + v_w > v_r \quad (28)$$

In order to meet the requirements of Eq. 27 and 28 simultaneously, v_g must be larger than zero. Therefore, during the sample injection step, there is fluid flow from the gated channel through the injection cross due to the decrease in the internal fluid pressure at the cross, even

though R2 is set at “floating” and the contribution of this fluid flow from EO flow is zero (Fig. 49 (c2-4)). A direct result of this flow during the injection step is the reduction in the amount of sample being introduced into the separation channel (Fig. 49 (c2/3)). When the mismatch of the conductivity becomes large, sample introduction will be completely shut down (Fig. 49 (a4)). Fig. 49 (d) simulates the profiles of the ThioGlo-1 peaks along the separation channel at 0.025 s in the separation step after injection of the sample stream for 0.05 s. It is clear that when the conductivity in R5 increases to 11.9 mS/cm, no more samples will be introduced into the separation channel.

In order to keep the conductivity of the solution in R2 balanced with that of the sample stream, the 40 mM Bis-Tris propane buffer (pH = 8.5) was augmented with 15 mM NaCl, which increased the conductivity of the running buffer in R2 to 4.2 mS/cm, comparable to that of sample stream from OHSCs mixed with derivatizing reagent. Another way that may circumvent the flow-gated problem described above is by switching the relay to a negative voltage instead of “floating” for a sample introduction. We have not explored this.

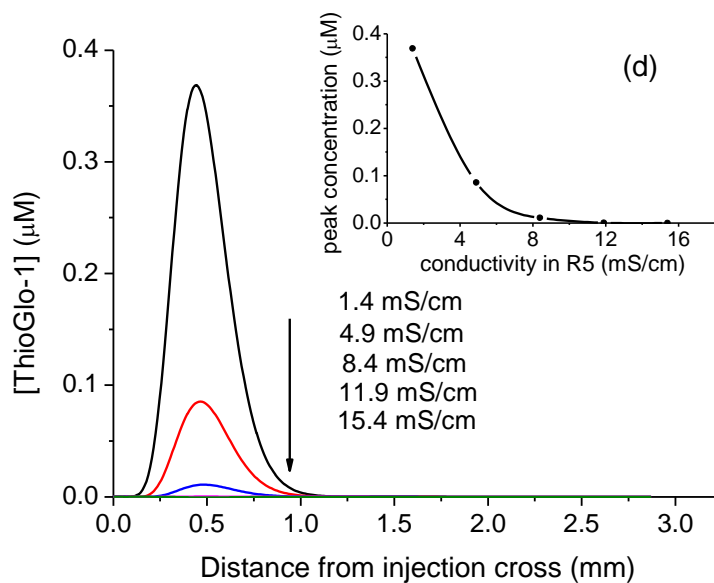
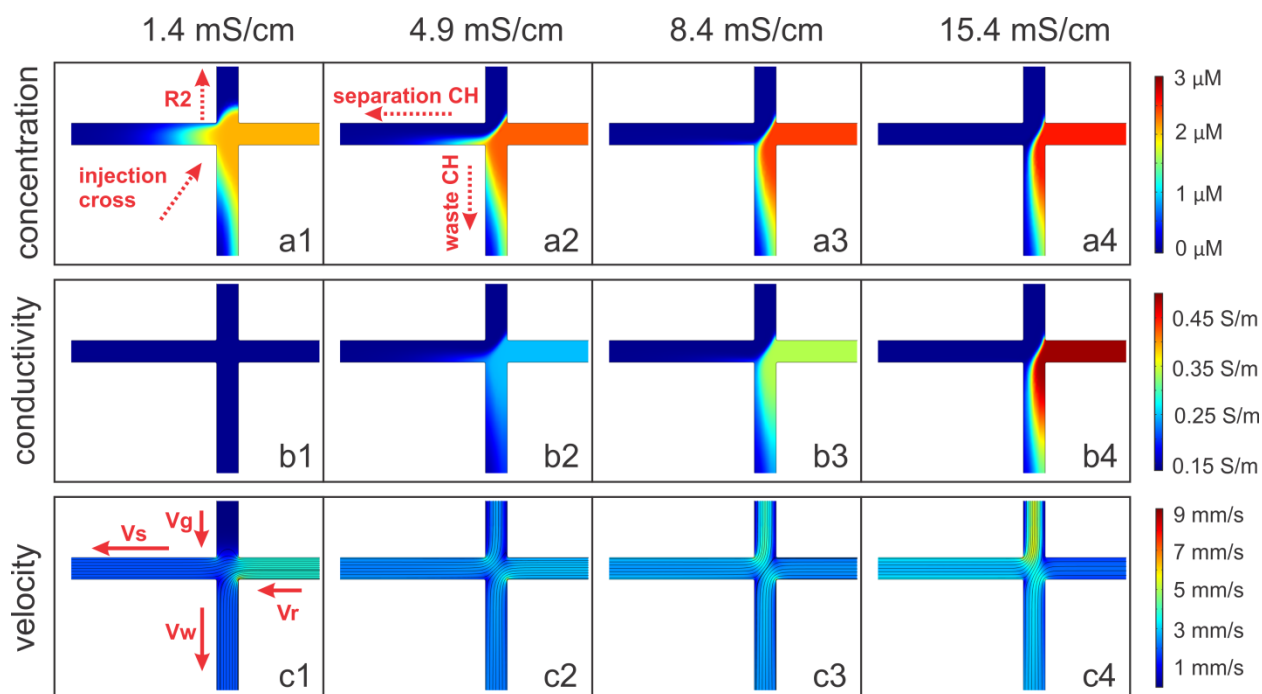


Figure 49. Concentrations, conductivities and velocities during injection

Snapshots of the ThioGlo-1 concentration (a1-4), the buffer conductivity (b1-4) and the velocity of the fluid (c1-4) after 0.05 s of sample injection are for different R5 conductivities. The concentration profiles of the ThioGlo-1 at 0.025 s in the separation step are plotted against the length of the separation channel (d). The peak concentration of ThioGlo-1 is plotted against the R5 conductivity in the inset of (d).

4.3.4 The function of an auxiliary channel in integrating electroosmotic sampling and microfluidic analysis

Controlling the flow rate by adjusting potentials applied to reservoirs is critical to obtaining a reproducible signal. If the sampling step and the microfluidic analysis are directly connected to each other, the potential drop in one process will dramatically affect the following steps. To circumvent this, an auxiliary channel with an additional R4 was added to the microfluidic chip (Fig. 41). By setting R4 to “GND”, the electric field across the sampling capillary is controllable without dramatically affecting the derivatizing reaction. Moreover, it expands the usable potential range that can be applied on the sampling capillary and provides an option to split the sample flow to R4.

To demonstrate the effectiveness of the auxiliary channel, we simulated the effect of changing the potential in the Petri dish on the concentration of the derivatizing reagent in the reaction channel with and without an auxiliary channel (Fig. 50). In this simulation, we again rescaled the capillary length, and the applied voltages to one tenth of their actual values but kept the width of the channel unchanged. Again, voltages stated here are those that would be used in the laboratory. The ThioGlo-1 concentrations at the end of the reaction channel relative to ThioGlo-1 concentration in R1 were recorded, while the potential at the Petri dish was swept from 0 to +10000 V and that at R1 was kept constant at +300 V. It is clear from Fig. 50 that with a grounded auxiliary channel, changing the potential in the Petri dish (x-axis) has much less effect on the relative ThioGlo-1 concentration (y-axis) in the reaction channel than that in the case without the auxiliary channel. At virtually all applied voltages without the auxiliary channel, the reagent concentration is less than its value in R1. With the auxiliary channel,

however, at voltages up to about 3000 V there is little change in the reagent concentration. Thus, we chose to use 3000 V in these measurements.

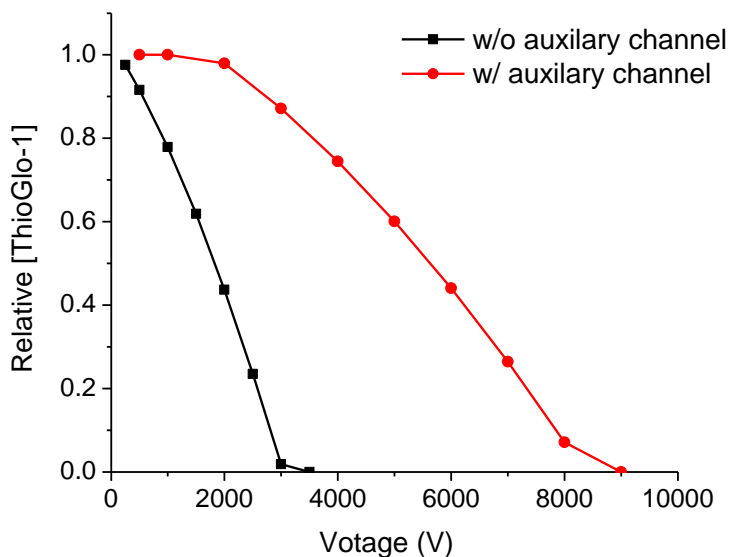


Figure 50. Effect of auxiliary channel on the relative ThioGlo-1 concentration

ThioGlo-1 concentration is sampled at the end of the reaction channel. X-axis is the voltages at the Petri dish (sample).

4.3.5 The effect of electroosmotic sampling conditions on OHSCs

Unlike the offline sampling method,¹⁰⁶ online experiments require continuous transport of the collected sample through the whole sampling capillary before it can enter into the microfluidic chip for analysis. Parameters, such as capillary ID, length, and potential applied at the Petri dish should be adjusted to obtain an appropriate flow rate. We finally selected an 11 cm x 50 μm (ID) capillary with +3000 V applied to the cell dish after trial and error. Also, exposure to the field and current can be damaging.¹⁰⁵ To evaluate the damage that the electroosmotic sampling may cause to CA3, we first did a viability assessment for OHSCs after applying 3000 V to the Petri dish while R4 was at GND for 10 min. All other conditions were the same as that for the pre-

sampling step described in the experimental section. The fluorescent (PI) and bright field images are shown in Fig. 47 (d1/2). According to Eq. 26, the %death of the tissue after sampling is ~10%, which we believe is acceptable in sampling from OHSCs.¹⁰⁵

4.3.6 Evaluation of the extracellular Cys, Hcy, and CSH concentration in OHSCs

Results from online single capillary sampling experiments indicated that there was no detectable GSH, γ -Glu-Cys or Cys-Gly in the samples collected from electroosmotic sampling. GSH was evident in electropherograms when sampling directly from the surface of the hydrophilic PTFE membrane of the standing insert on which the culture sits (when glutathione is present in the medium below), however it was not evident when sampling from tissue. We believe that there are two contributions to this. One is that GSH reacts very rapidly with Gly-Gly in the extracellular space due to the presence of the ectoenzyme γ -glutamyl transpeptidase.²⁷⁷ The other is the electrophoretic bias in sampling. It takes longer for anions to be transported from tissue to the chip than for neutrals or cations under the sampling conditions. In the extreme case, the electroosmotic sampling method may fail to sample out small and highly negatively charged molecules that have electrophoretic mobility equivalent or larger than that of electroosmotic flow with opposite direction. This is mainly due to the relative small ζ -potential of the tissue (-22.8 mV)²⁵⁹ compared with that of the fused silica capillary (-50 mV) and low permeability of the tissue (~10-15 m²),²⁷⁸ even the pressure driven flow induced by the stepwise change in the ζ -potentials at the interface of tissue and sampling capillary will not compensate the difference between the electrophoretic mobility of small negatively charged analytes and electroosmotic mobility in the extracellular space of the tissue.

Based on the analyte of interest presenting in the sample and the requirement of analysis time for a single assay, 40 mM Bis-Tris propane buffer with 15 mM NaCl (pH 8.5) was used as the running buffer in the online analysis. Fig. 50 (a) shows an electropherogram from electroosmotic sampling of an OHSC with ggACSF in the Petri dish. Fig. 51 (b), (c), (d) were obtained using the same conditions, but the ggACSF (Petri dish) was spiked with 99.2 nM CSH, 65.8 μ M Cys and 575 nM Hcy. ThioGlo-1 derivatized peaks of CSH, Hcy, and Cys were identified by comparing the migration times with those of standards. A reconstructed plot of PMT reading vs time for all injections in one run is given in Fig. 52.

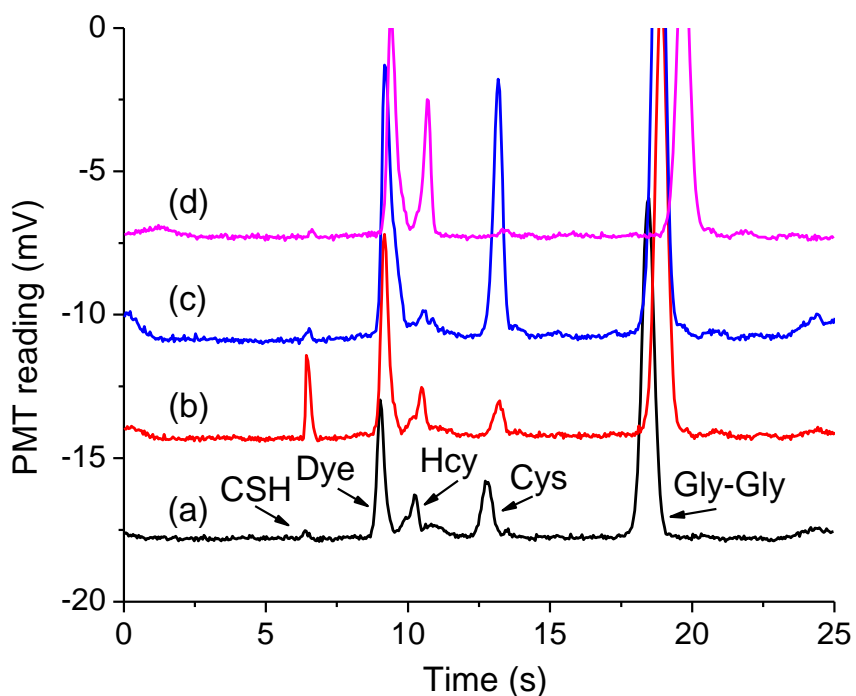


Figure 51. Electropherogram of analytes from electroosmotic sampling of OHSCs

Electroosmotic sampling from an OHSC with (a) ggACSF in the Petri dish, (b) 99.22 nM of CSH in ggACSF, (c) 65.81 μ M of Cys in ggACSF, (d) 574.8 nM of Hcy in ggACSF.

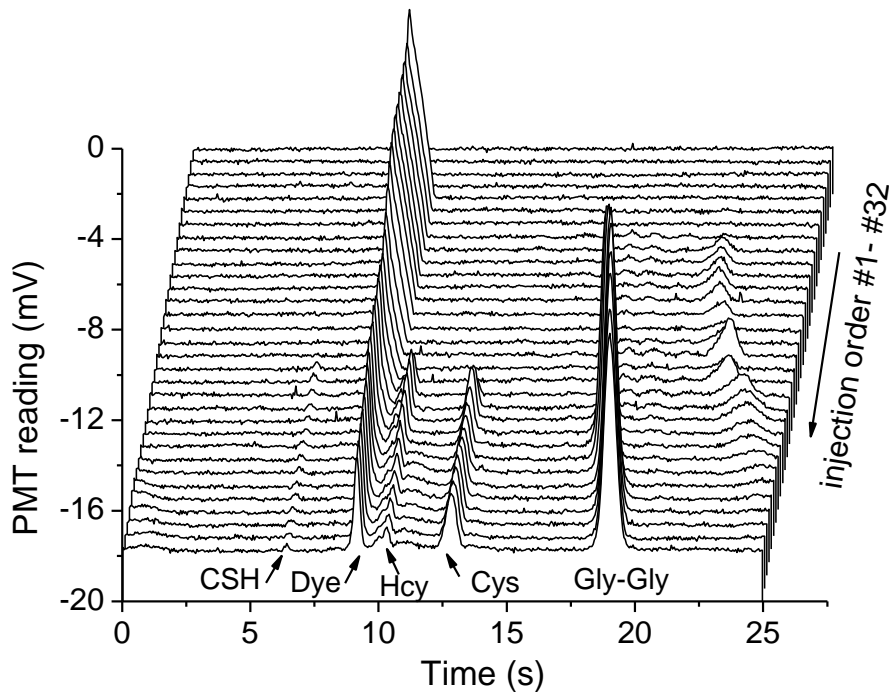


Figure 52. Reconstructed plot of PMT reading vs time for all injection in one run

Electroosmotic sampling was performed on an OHSC with only ggACSF in the Petri dish. Peaks with migration time from 20-25 s are impurities from derivatizing reservoir R1 containing ThioGlo-1.

Some comments on the separation/detection are warranted. The “dye” peak is from the neutral ThioGlo-1, thus it acts as a marker for the electroosmotic velocity in the separation channel. Hcy and Cys are nominally zwitterionic, but in fact at pH 8.5, each has a small negative charge ($pI_{\text{Cys}} = 6.31$; $pI_{\text{Hcy}} = 6.54$,²⁷⁹ estimated without considering the pKa of $-\text{SH}$) consistent with their positions, with respect to each other as well as with respect to the neutral marker, in the observed electropherogram. Finally, we were surprised to see Gly-Gly in the electropherogram. It turns out that amines are reactive with maleimides, though at a much lower rate than thiols.²⁸⁰

In order to convert the output signals to values with a unit of concentration, a calibration curve must be established. In our situation, it is inappropriate to establish standard curves by sampling directly from free solutions containing analytes at various concentrations. The resistance of an OHSC is significantly different from free solution. Alterations in the voltage and current distribution on the chip will lead to different sample-reagent mixing ratios and thus different fluorescent signals for the same analyte concentration. To solve this problem, a calibration curve was created by adding known quantities of the analyte to the ggACSF in the Petri dishes of a series of tissue cultures. To determine the basal concentration of CSH, Hcy and Cys, analyses were carried out on 5-8 tissues for each compound. Three tissues in each group had no added analytes, while the rest had added analyte. As discussed in a previous paper,²⁷⁴ there is a delay from the appearance of the first analyte peak in each analysis until the peak magnitude in the electropherogram reaches a steady value (Fig. 53). Once the steady state is reached, all of the peak heights are taken. Each analysis results therefore include fifty or more determinations. For example, a single reported concentration may result from measurements on six tissue cultures, three with no added analyte and three with different concentrations of analyte in the Petri dish. If ten electrophoretic peaks are used from each of six tissue cultures, then the number of data going into the measured concentration is sixty. A linear regression on these data points leads to a slope for peak height versus concentration. The y-intercept and the slope are used to calculate the resting concentration of that analyte in OHSCs. Standard deviations of the basal concentrations were calculated through propagation of error (see Appendix B for detail information related with the standard addition method). In this way, the measured endogenous concentration of CSH, Hcy and Cys were calculated to be 10.6 ± 1.0 nM ($n = 70$), 0.18 ± 0.01 μ M ($n = 53$) and 11.1 ± 1.2 μ M ($n = 70$), respectively, where n is the number of data points used

in the linear fitting. Errors are the SEM. We also calculated the detection limit based on the RMS noise in 3 second sections of baselines and the slope of the calibration curve. This would be appropriate for deciding if a particular feature in a single electropherogram was actually a peak. The values ($S/N = 3$) are 5.4 nM, 25 nM and 1.4 μM for CSH, Hcy and Cys, respectively. Averaging electropherograms would improve these values. This method is capable of determining CSH in the extracellular space of rat OHSCs. Other methods do not have the requisite low detection limit.^{73, 74} The concentrations for Hcy and Cys are comparable with the published extracellular values of Hcy and Cys.^{29, 87, 260}

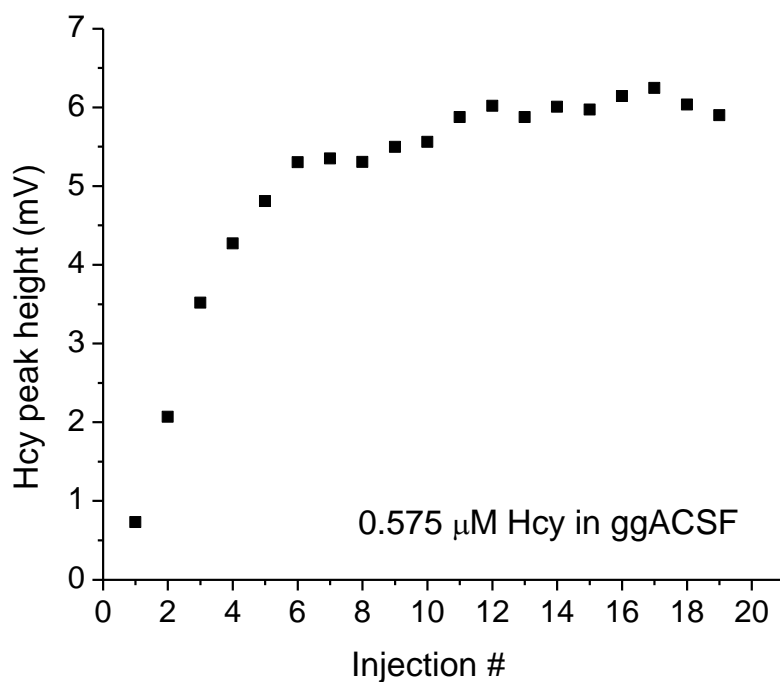


Figure 53. Hcy peak height vs injection # in a single run

Record of the injection number started from the detection of the first Hcy peak in the electropherogram. 0.575 μM of Hcy was added into ggACSF buffer in the Petri dish before the start of electroosmotic sampling from an OHSC.

No new method should go without a thorough consideration of potential confounding issues. It is well known that accurate calibration of a method that samples (or measures directly in) the extracellular space is very difficult, e.g., microdialysis and in vivo voltammetry. A primary source of uncertainty in the current method might be the local uptake and exchange of the aminothiols inside the tissue during sampling, especially when the spiked analytes have concentrations comparable to the basal levels in OHSCs. Cell damage near the sampled region may add uncertainty. On the latter point, we note that the electric field inside the tissue along the sampling direction is highest near the tip of the sampling capillary. Cells near the capillary tip may be electroporated²⁸¹ adding intracellular material to the sample. However, the actual measurements are taken after the signal reaches a steady state. Material from electroporated cells near the tip of the capillary will be present at the early stages of the measurement prior to establishing the steady state. Finally, electroosmotic sampling will suffer a sampling bias based on solute charge and size. With proper calibration, this need not be a problem, but there are some molecules (small and highly negatively charged) that may not be suitable for this method based on the current experimental setup and conditions.

4.3.7 Comparison of single and dual capillary modes in electroosmotic sampling

It has been discussed in Chapter 1 that the synthesis of neuronal GSH relies on the releasing of GSH from the neighboring astrocytes. The concentration of extracellular GSH in brain has been reported to be in the low micro molar range. However, from the online single capillary sampling experiments, there is no detectable GSH shown in the electropherograms. In order to further explore this problem, a dual capillary sampling mode is applied in electroosmotic sampling from OHSCs as a comparison to single capillary sampling. To find out the migration behavior of GSH

under the current separation condition, the microfluidic chip in Fig. 41 was first operated in on-chip mode. Fig. 54 (a) was obtained when the sample reservoir R5 contained ggACSF spiked with 1.234 μM GSH. There was an additional peak just before the location for the peak of Gly-Gly. To further confirm the identities of these peaks, in the following experiment, the analyte of Tris-HCl buffer with 60 mM NaCl and 1.234 μM GSH was added into R4. Fig. 54 (b) showed that there was an obvious decrease in the Gly-Gly peak and an increase in the GSH peak. In the next experiment, we would like to test whether the membrane of the standing insert became an obstacle of electroosmotic sampling of GSH. In this experiment, the tip of the single sampling capillary was lowered down until it made contact with the membrane. The ggACSF buffer solution under the membrane was spiked with 62.24 μM GSH. All other conditions were the same as that described in Section 4.2.6. Fig. 55 proved that GSH could be sampled out successfully without any problem through the membrane.

There are several possibilities that will result in no detectable GSH in extracellular fluid collected through single capillary electroosmotic sampling in CA3 region as shown in Fig. 52. First, the basal concentration of GSH is too low to be detected using this method. Second, the electrophoretic bias of this sampling method may result in much longer migration time for anions like GSH to be transported from tissue to the chip than that for neutrals and cations, or in the worst case, this method may fail to collect GSH due to both the low ζ -potential and low permeability of the tissue. Third, the conversion rate of GSH to CysGly by γGT may increase at the presence of a high concentration of Gly-Gly in ggACSF buffer. To exclude the concentration factor, GSH was added into the ggACSF buffer to a final concentration of 62.24 μM . There was still no GSH peak observed in a ~ 30 minutes online electroosmotic sampling as shown in Fig. 56, which suggested that it may require much longer sampling time for the GSH to reach the

injection cross and the mobility of GSH may be comparable with that of the electroosmotic flow but with opposite direction. Based on the migration time of ThioGlo-1 and GSH shown in Fig. 43 and 44, the electrophoretic mobility of GSH-ThioGlo-1 adduct can be estimated to be $-1.22 \times 10^{-8} \text{ m}^2/(\text{V}\cdot\text{s})$ at $\text{pH} = 7.5$. The electrophoretic mobility of GSH would be more negative than its ThioGlo-1 adduct. According to the reported value of ζ -potential for OHSCs, -22.8 mV ,²⁵⁹ the electroosmotic mobility of tissue would be $1.78 \times 10^{-8} \text{ m}^2/(\text{V}\cdot\text{s})$. The difference between these estimated mobilities is not large.

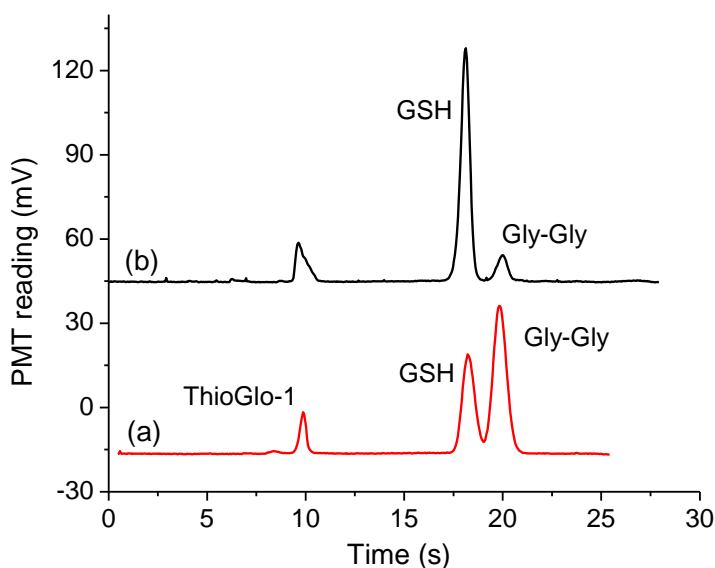


Figure 54. Electrophoretic behavior of GSH

Microfluidic chip shown in Fig. 41 were used. R1: 20 mM Tris-HCl at pH 7.5 with 2.688 μM ThioGlo-1; R2/R3: 40 mM Bis-tris propane buffer with 15 mM NaCl at pH 8.5; R4: 20 mM Tris-HCl buffer spiked with 60 mM NaCl and 1.234 μM GSH at pH 7.5; R5: ggACSF with 1.234 μM GSH. Voltage settings in experiments: (a) R1/R5: 300 V; R2 (GND/floating: 24.5 s/0.5 s); R3: -4500 V; R4: disable; (b) R1/R4: 300 V; R2 (GND/floating: 24.5 s/0.5 s); R3: -4500 V; R5: disable.

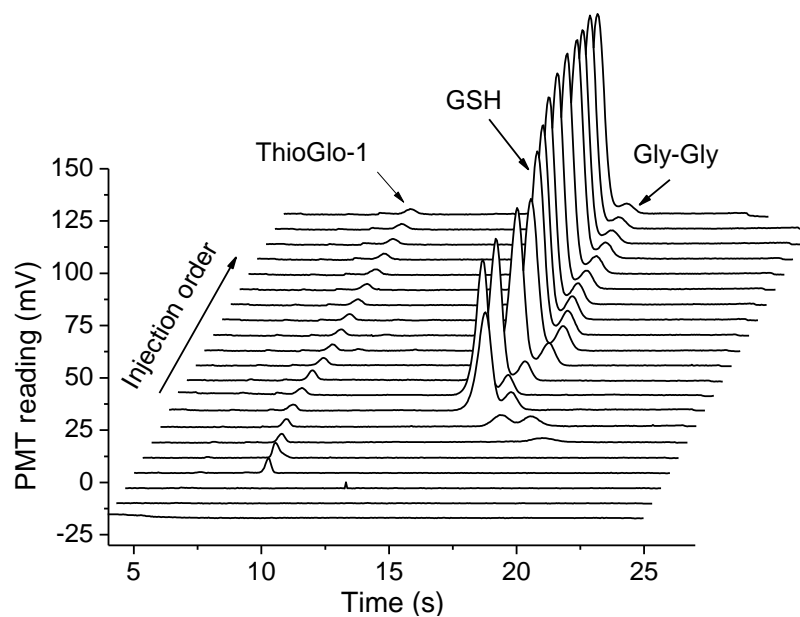


Figure 55. Single capillary sampling through membrane of the standing insert placed in the Petri dish. Petri dish contained 1.2 mL ggACSF spiked with 62.24 μM GSH. All other conditions were same as the single capillary sampling experiment described in Section 4.2.6.

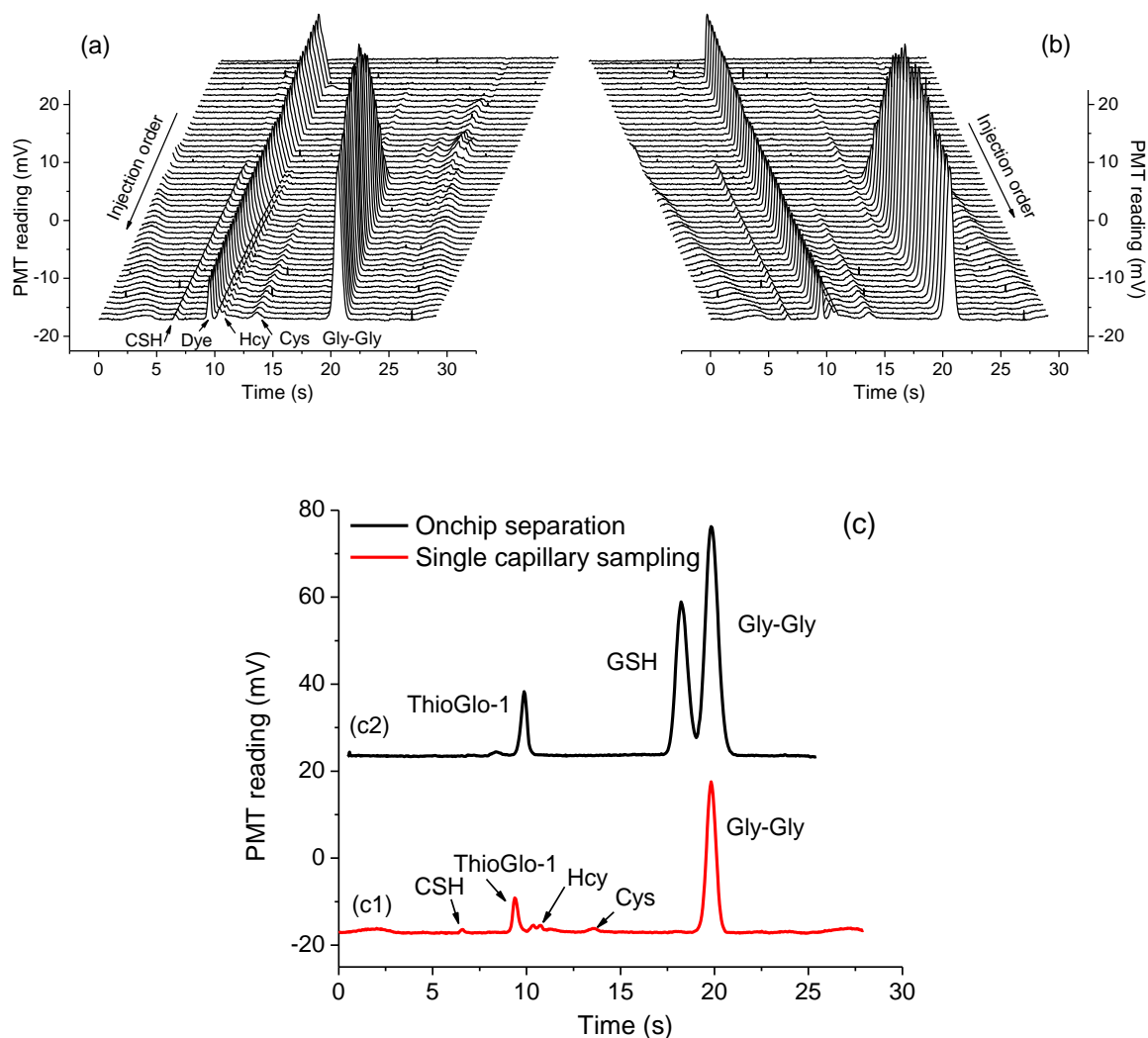


Figure 56. Single capillary sampling from CA3 of OHSCs

Petri dish contained ggACSF spiked with 62.24 μM GSH. All other conditions were same as sampling experiment described in Section 4.2.6. (a) Waterfall plot of all injections in a single run of 1200 s (there was an additional six minutes pre-sampling step) (b) rotated view of the waterfall plot; (c) Comparison of the electropherograms obtained from injection at 950.525 s of this experiment and that of Fig. 54 (a).

The dual capillary sampling was first tested when both tips of the parallel inlet capillary and 2 were immersed into ggACSF in a Petri dish. Inlet capillary and glass vial were prefilled with 62.24 μM GSH doped ggACSF buffer and outlet capillary filled with 20 mM Tris-HCl with

60 mM NaCl at pH 7.5. In the pre-sampling step and at the beginning of the online analysis, +3000 V was applied to the glass vial. All other parameters were same as the single capillary sampling experiment described in Section 4.2.6. At about 626 s, the potential in R1 was decreased to 80 V, which decreased the ratio of the derivatizing reagent in the mixing channel. At about 975 s, the potentials at the glass vial and R1 were increased to +7000 V and +300 V, respectively, so that the electric field applied on the two capillaries was similar to that in the single capillary sampling experiment. GSH appeared finally in the electropherogram as shown in Fig. 57. It must be pointed out that concentration of the GSH in the sample stream is determined by the actual tip-to-tip distance of the two capillary and the mobility of GSH in inlet and outlet capillaries.

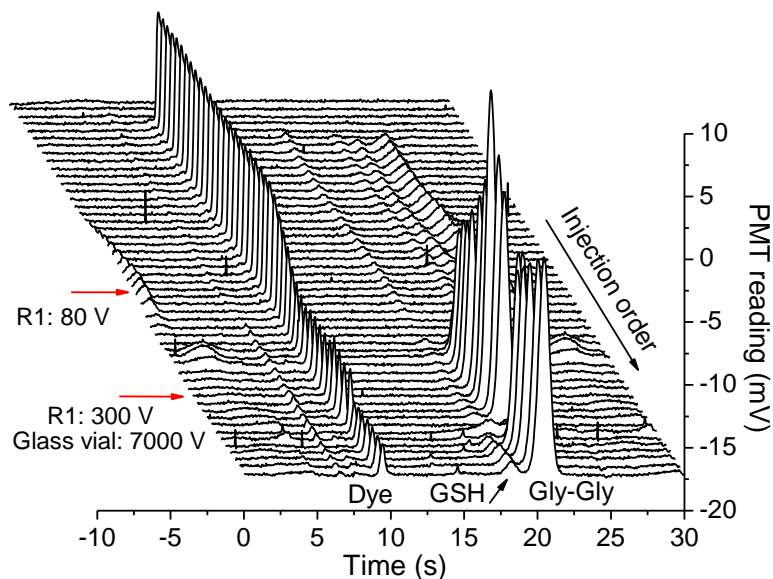


Figure 57. Dual capillary sampling directly from solution in Petri dish

Petri dish contained 1.2 mL ggACSF buffer. Glass vial and inlet capillary contained ggACSF buffer spiked with 62.24 μ M GSH. At beginning, 3000 V was applied to the glass vial; +300 V was applied to R1; at 626 s, the potential at R1 was decreased to 80 V; at 975 s, the potential at R1 was increased to 300 V and potential at the glass vial was increased to +7000 V. All other experiment conditions were described in Section 4.2.7.

It has been discussed in Section 4.2.7 that there are two situations in the dual capillary sampling experiment as shown in Fig. 42 due to the limited freedom in controlling positions of two capillaries simultaneously with only one manipulator. Fig. 58 shows that the electropherograms for these two cases were quite different. In this experiment, glass vial and inlet capillary were filled with ggACSF buffer spiked with 62.24 μM GSH, all other conditions were described in Section 4.2.7. The relative distance between the tip of outlet capillary and tissue surface was kept the same as that in the single capillary sampling experiment, while the tip of inlet capillary was much closer to the tissue surface than that of outlet capillary (case A) or at the same height as that for the outlet capillary (case B). In case A, there is no additional peak migrates before Gly-Gly peak (Fig. 58 (a1/2)). However, in case B, the GSH peak appears in the electropherogram next to the Gly-Gly peak (Fig. 58 (b1/b2)). The overlay of selected electropherograms for these two cases is given in Fig. 58 (c). In another dual capillary sampling experiment, all experimental conditions were same as that for Fig. 58 (b1/b2) except that no GSH was in the glass vial or inlet capillary, however, we still observed an additional peak before the peak of Gly-Gly (Fig. 59 (a)). By comparing the migration time of this peak with that of GSH (Fig. 59 (b)), this additional peak was assigned to basal extracellular GSH of OHSCs with a concentration of $\sim 10 \mu\text{M}$. A possible reason that may explain the difference in the appearance of GSH on the electropherogram in both cases is that in case A when the inlet capillary is very close or touching the tissue surface, electric circuit between two tips of the capillaries is completed by a segment of tissue. Buffer solution from the inlet capillary has to pass through this segment of tissue before being collected by the outlet capillary. As discussed before, GSH has similar electrophoretic mobility as the electroosmotic mobility of the tissue but with opposite direction. The time it requires to collect anions from tissue may be much longer than for neutrals or cations

under the sampling conditions and this time may be longer than the current sampling time. Therefore, there is no GSH observed in the electropherogram in Fig. 58 (a1/2). On the contrary, in case B, the tip of the inlet capillary is at the same height at that of the outlet capillary, the electric circuit between two capillary tips is completed by a parallel circuit composed of a segment of liquid on the tissue surface and a segment of tissue. Due to the low conductivity and permeability of the tissue in comparison to the free solution, most of the buffer solutions from the inlet capillary flows on top of the tissue and then enters the outlet capillary rather than passing through the tissue. Although the electroosmotic mobilities are same on the tissue surface and inside the tissue, the pressure driven flow caused by the mismatch of the ζ -potentials of the capillary and tissue will dramatically increase the velocities of the anions like GSH in the free solution on top of the tissue, which explain the existence of the GSH peaks on the electropherogram in Fig. 58 (b1/b2). However, the low permeability²⁷⁸ of the tissue largely limits the pressure driven flow inside the tissue and thus has little help in speeding up the velocity of GSH. The endogenous GSH in the extracellular space which diffused into the liquid layer on top of the tissue can also be collected by the dual capillary sampling as shown Fig. 59 (a). It is anticipated that by applying the dual capillary electroosmotic sampling in a mode that the inlet capillary is at the same height or higher than the outlet capillary, it is possible to obtain information of the analytes in the extracellular space of OHSCs and metabolic data when specific substrate flows on top of tissue.

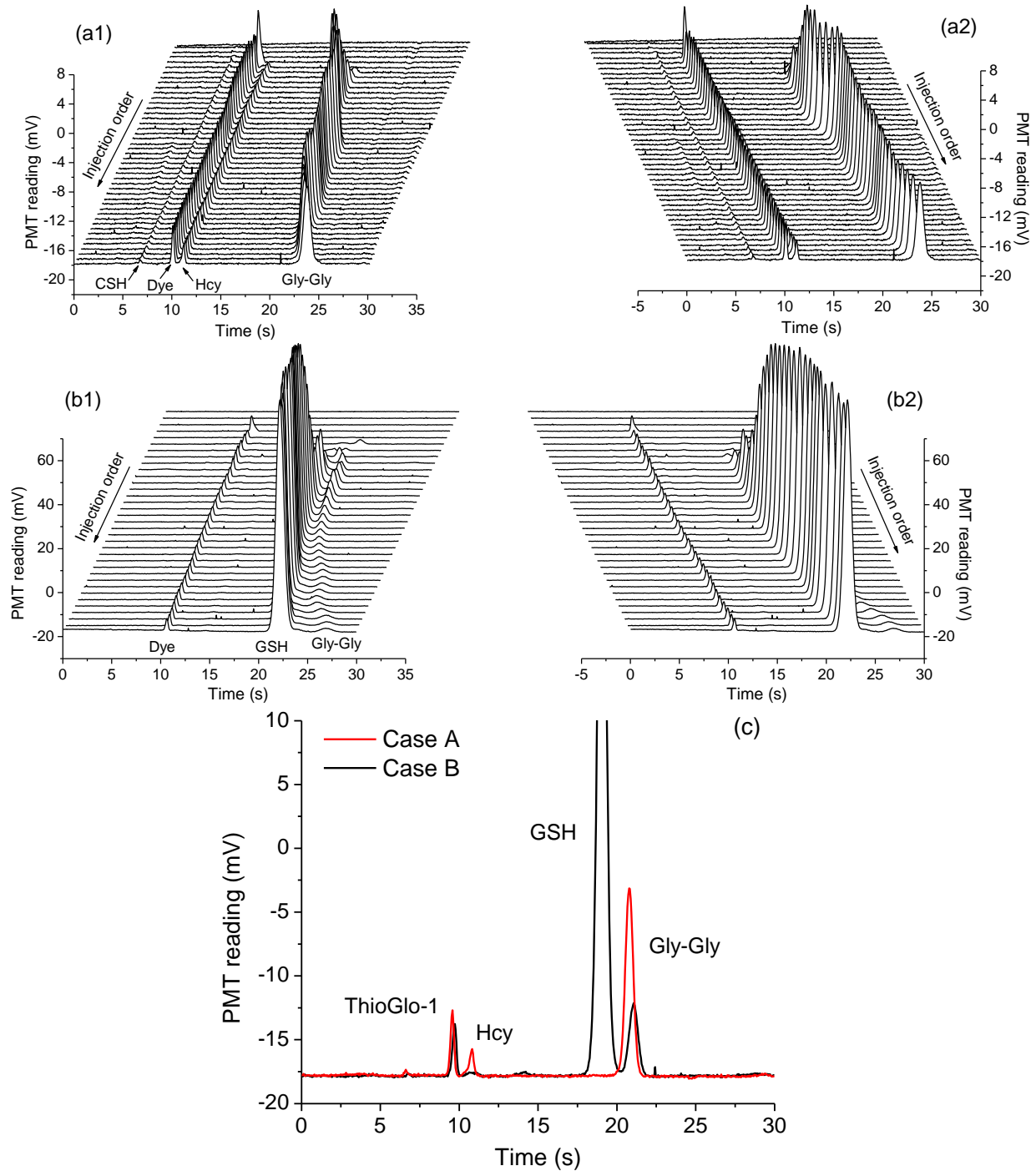


Figure 58. Comparison of two cases in dual capillary electroosmotic sampling from OHSCs

Sampling was performed in CA3 region. Glass vial and inlet capillary were filled with ggACSF buffer spiked with $62.24 \mu\text{M}$ GSH. The dual capillary setups in a1 (a2, rotated view) and b1 (b2 rotated view) were based on case A and case B shown in Fig. 43, respectively. (c) Comparison of the electropherograms obtained from injection at 475.525 s in case A and injection at 481.525 s in case B. Other conditions were described in Section 4.2.7.

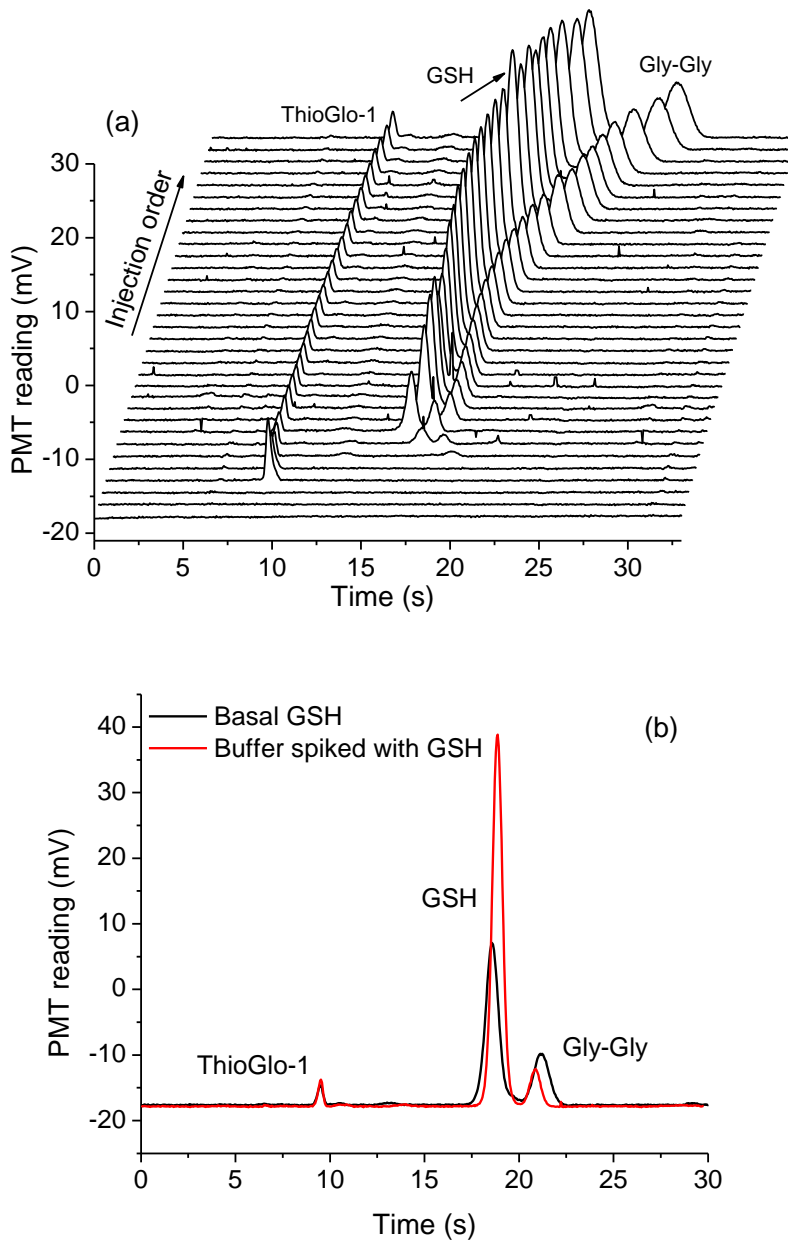


Figure 59. Dual capillary electroosmotic sampling from OHSCs

Sampling was performed in CA3 region. Glass vial and inlet capillary contained ggACSF buffer only. (a) Electropherogram shows the basal GSH. (b) Comparison of the electropherograms obtained from injection at 631.925 s in this experiment and injection at 481.525 s in case B of Fig. 58.

4.4 CONCLUSIONS

We have interfaced electroosmotic sampling and a microfluidic chip-based determination for thiols. High conductivity biological samples lead to many practical problems during microfluidic analysis. We explored the issues of high conductivity samples and the failure in flow-gated injection due to mismatch in conductivities of flows at the injection cross and provided solutions to these problems. The partial replacement of NaCl in the ACSF in the tissue culture dish with Gly-Gly resulted in a 38% decrease in the conductivity and caused negligible damage to OHSCs. Further, the increase of the conductivity of the running buffer using NaCl not only recovered the flow-gated injection but also retained the separation resolution for three aminothiols, CSH, Cys, and Hcy in 15 s. Finally, the incorporation of an auxiliary channel plays a key role in integrating electroosmotic sampling with microfluidic analysis. It expanded the usable range of the electric field across the sampling capillary in comparison to when there is no auxiliary channel. We demonstrated the successful separation of common aminothiols in the microfluidic channel and the coupling of single capillary electroosmotic sampling with a microfluidic chip to achieve *in situ* measurement of the extracellular CSH, Hcy, and Cys in OHSCs. Compared with other reported works, our method has high selectivity, sensitivity and analysis speed. This technique can be applied to monitoring the change of aminothiols level in the extracellular space and measuring the activity of related ectoenzymes in OHSCs. We also compared the single capillary and dual capillary in electroosmotic sampling of OHSCs and found that it is possible to sample the spiked or endogenous GSH out of tissue if tips of the capillaries in a dual capillary mode are connecting the tissue through a thin layer of liquid. The dual capillary sampling mode is a promising technique to study anionic analytes in the extracellular space and other biological information and metabolic process on the tissue surface.

5.0 TRACKING THE METABOLISM OF TWO DRUG COMPOUNDS AND COA IN OHSCS

CSH is the last product of CoA biodegradation. The current knowledge about the formation rate of CSH in mammalian tissues is limited, which hinders the estimation of taurine flux through the CSH pathway. Owing to their ability to generate CSH, cystamine (CSSC) and pantethine (PSSP) are two well-known drug compounds in treating cystinosis. The difference in their effectiveness and side effects can be tracked back to their distinct metabolic behaviors at cellular level. CoA, as an essential cofactor for about 4% of all known enzymes, participates actively in the oxidation of carbon substrates and the synthesis of cellular structural components. Currently, little is known about CoA biodegradation and even less is known about the regulation and kinetic characteristics for this sequential multi-enzyme reaction. We have developed a technique, which integrates electroosmotic sampling with online microfluidic analysis that is capable of tracking the metabolism of CSSC, PSSP and CoA in the extracellular space of organotypic hippocampal slice cultures (OHSCs). In this research, the percentage yields of CSH from CSSC and PSSP after ~55 s exposure time to the OHSCs were $91\% \pm 4\%$ and $0.01\%-0.03\%$, respectively, which can be used to explain the reported differences in the effectiveness and toxicity of these two drugs. Error represents the standard error of the mean. Besides, the kinetic parameters of enzyme reaction catalyzed by pantetheinase were also determined to be $K_{M,C}/\alpha = 4.4 \pm 1.1$ mM and $V_{\max,C} = 29 \pm 3$ nM/s, where α is the percentage yield of PSSP to pantetheine through disulfide

exchange. The degradation of CoA in extracellular space was also observed and based on the formation rate of CSH in the OHSCs, we obtained the overall apparent Michaelis constant and maximum reaction rate for the sequential extracellular CoA degradation in an *in situ* environment, which are $K'_M = 16 \pm 4 \mu\text{M}$, $V'_{\max} = 7.1 \pm 0.5 \text{ nM/s}$. Kinetic parameters obtained *in situ*, although difficult to measure, are better representations of the biochemical flux in the living organism than those from an isolated enzyme *in vitro*. Using these kinetic parameters for the CoA biodegradation is helpful to understand and solve the current challenges related with CoA degradation.

5.1 INTRODUCTION

Endogenous CSH exists at a relatively low concentration in the tissue.⁶⁹ It is the terminal metabolite in CoA degradation.^{65, 68, 88} and also a vital source for taurine.⁷⁰ Beside their therapeutical functions as radio-protective and anti-viral agents, CSH and its disulfide form CSSC are potential neuroprotective candidates in treating neurodegenerative diseases such as Parkinson's disease and Huntington's disease.^{71, 282, 283} CSH and CSSC are also used in the treatment of cystinosis, an autosomal recessive genetic disease.^{284, 285} Cystine trapped inside the lysosome reacts with CSH following the latter's transport across the lysosomal membrane by a specific yet unidentified membrane transporter to form the CSH-cysteine mixed disulfide, which can leave the lysosome with the help of lysosomal lysine transporter.⁷⁶ The disulfide form of pantetheine, PSSP, is also capable of reducing accumulated cystine inside the lysosome but with fewer side effects and lower toxicity in comparison to CSH or CSSC.²⁸⁵⁻²⁸⁸ The ability of PSSP in treating cystinosis relies on the formation of pantetheine from disulfide exchange reaction

with endogenous thiols (e.g. GSH) and then the metabolism of PSH to CSH via pantetheinases.^{285, 289}

CoA is an essential cofactor for about 4% of all known enzymes and is actively involved in more than one hundred different synthetic and degradative reactions^{65, 68}. CoA participates in the oxidation of major carbon substrates for energy production and the synthesis of many cellular structural components⁶⁸. In brain, CoA also plays an essential role in the production of the neurotransmitter acetylcholine⁶⁸. Due to its role in energy metabolism, the tissue concentration of total CoA, including both free CoA and esterified CoA, is especially high in metabolically active tissues such as heart, liver, kidney and brain.^{65, 68, 290, 291} In the intracellular space of animal tissues, CoA is distributed mainly in cytosol, mitochondria and peroxisome with estimated concentrations of 0.02-0.14 mM, 2.2-5 mM and 0.7 mM, respectively.⁶⁵ The biosynthesis of CoA is accomplished in cytosol through five well-established steps with the aid of enzymes starting from three substrates, pantothenic acid (also known as vitamin B₅), ATP, and cysteine^{65, 68, 89, 292}. However, very little is known about CoA degradation and even less is known about the regulation of this process as well as its turnover rate^{1, 65, 68, 88}. Currently, the pathway for CoA degradation is poorly understood. Based on the current information related with identified enzymes that can catalyze this process, there are several proposed routes for CoA biodegradation as shown in Fig. 60. In route I, CoA is first dephosphorylated to dephospho-CoA by acid phosphatase (EC 3.1.3.2) located inside the lysosome and then degraded to 4'-phospho-PSH by the ecto-nucleotide diphosphatase (EC 3.6.1.9) located on the plasma membrane^{65, 68, 293}. CoA has also been reported to be a direct substrate of nucleotide diphosphatase with the products of 3', 5'-ADP and 4'-phospho-PSH through route II^{65, 68, 294}. In route III, a peroxisomal nudix hydrolase (EC 3.6.1.13) is capable of converting CoA to 4'-phospho-PSH and shows very low

activity with dephospho-CoA as the substrate^{65, 294-296}. After further dephosphorylation of 4'-phospho-PSH by acid phosphatase, the product PSH is then degraded to pantothenic acid and CSH, which is catalyzed by membrane-bound extracellular pantetheinase (EC 3.5.1.92)^{65, 68, 88}.

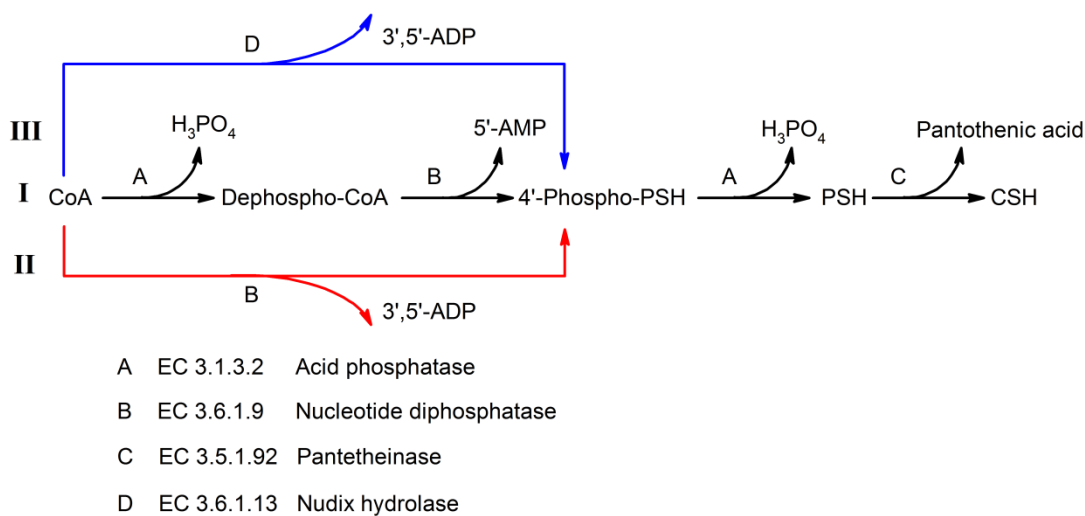


Figure 60. Proposed CoA biodegradation pathways

H₂O in each step is omitted.

Measuring CSH concentration in biological samples and the rate of CSH formation are crucial for evaluating taurine production through the CSH-dependent pathway and better understanding the CoA metabolic turnover rate and mechanism.⁸⁸ It will also clarify the mechanism underlying the differences in the toxicity and beneficial effects of CSSC and PSSP at the molecular level. Currently, there is little knowledge about the rate of CSH formation in mammalian tissues due to the relatively low endogenous concentration of this molecule in tissues and also the technical difficulty in measuring it.^{69, 88} We have reported integrating electroosmotic perfusion with a microfluidic chip for online analysis of fluid perfused through the extracellular space of OHSCs.²⁹⁷ Conveniently, under the influence of an electric field extracellular fluid in the tissues can be drawn into a capillary by the same natural driving force, electroosmotic flow, as that used in the microfluidic chip. The coupling of perfusion, sample transport and

quantitative analyses solves many practical problems. Samples transported directly to a microfluidic device for analysis are more representative of the fluid in the tissue being sampled than samples that undergo several handling steps. This is especially true when the samples volumes are nanoliters or smaller volumes.

The integration of a tissue culture with a micro-analytical system has an added advantage. In intact biological systems, numerous enzyme reactions occur simultaneously with complex inhibiting and activating regulation and feedback among them.²⁹⁸ Therefore, analyzing a metabolic process in an *in situ* model provides a representation of the process that is distinct from and complementary to the determination of the physicochemical properties of the enzymes involved in the process.

In this work, we perfused OHSCs with two drug compounds used to treat cystinosis, CSSC and PSSP, to determine the extent of generation of the active compound, CSH, from each of them. The differences in the metabolism of the two drugs correlate with their clinical effectiveness and tendency to produce side effects. We also monitored the changes in the concentrations of CSH, PSH, Hcy and Cys in the extracellular space of the CA3 region in the OHSCs while perfusing the tissue with CoA. Direct evidence for complete degradation of CoA to cysteamine in the extracellular space of OHSCs was observed, based on which the *in situ* overall kinetic parameters were calculated. To the best of our knowledge, this is the first *in situ* study that directly measures conversion rate of CSH during extracellular CoA degradation in tissues.

5.2 EXPERIMENTAL SECTION

5.2.1 Chemicals and reagents

ACSF was composed of (mM), NaCl (128), KCl (3), CaCl₂ (2), MgSO₄ (1.2), KH₂PO₄ (0.4), NaHCO₃ (25), D-(+)-glucose (10). The ggACSF was prepared by replacing 75 mM NaCl in the ACSF with 125 mM Gly-Gly with all other components unchanged. Both solutions have similar osmolarity (~310 mOsm/L) and pH value (pH = 7.4). NaCl and KCl were obtained from Avantor Performance Materials (Center Valley, PA). CaCl₂ and KH₂PO₄ were from EM Science (Gibbstown, NJ). MgSO₄ and NaHCO₃ were purchased from EMD Millipore (Billerica, MA). Gly-Gly and D-(+)-glucose were from Sigma-Aldrich Chemical Co. (St. Louis, MO).

For tissue culture and characterization, Gey's balance salt solution (GBSS) (Sigma-Aldrich) was supplemented with 2.7 mM MgSO₄ and 0.5% D-(+)-glucose. The culture medium consisted of 50% Opti-MEM, 25% horse serum, 25% Hank's balanced salt solution (HBSS) with phenol red, and 0.45% D-(+)-glucose. Propidium iodide solution was prepared with GBSS at a final concentration of 0.35 mM and stored at -20 °C. All reagents except those mentioned previously were from Life Technologies (Grand Island, NY).

The running buffer for microfluidic electrophoresis consisted of 40 mM Bis-tris propane with 15 mM NaCl at pH 8.5. On-chip thiol derivatizing buffer was 20 mM Tris-HCl at pH 7.5. The sampling buffer preloaded in the capillary was composed of 20 mM Tris-HCl and 60 mM NaCl at pH 7.5. All buffers were filtered through 0.1 µm polyethersulfone membrane (EMD Millipore) and degassed by ultrasonication prior to use. The derivatizing stock solution was made by dissolving ThioGlo-1(EMD Millipore) to anhydrous DMSO at a final concentration of 2.5 mM and stored in freezer. The stock solutions of different thiol/disulfide, CoA (CoA, ~95%)

and CSH, DL-Hcy, L-Cys and D-PSSP, CSSC were prepared by dissolving the solids to degassed Milli-Q water (EMD Millipore) to final concentrations of 7.1 mM, 272.4 mmol/1 mL H₂O, 69.1 mM, 49.7 mM, 182.7 mM/1 mL H₂O, 138.8 mmol/1 mL H₂O respectively. These solutions were stored at -20 °C in aliquots and diluted serially to desired concentrations before use. The pantetheinases inhibitor solution, 8-cyclopentyl-1, 3-dipropylxanthine (DPCPX), was prepared with DMSO to a final concentration of 26.3 mM. All these chemicals were from Sigma-Aldrich Chemical Co..

5.2.2 Preparation of OHSCs

The preparation of OHSCs is modified from Gogolla's protocol²⁷³ and has been described previously. In short, the hippocampal region of 7 days postnatal Sprague-Dawley rat pups was dissected out and chopped into 350 µm thick slices by a McIlwain tissue chopper (the Mickle Laboratory Engineering Co. Ltd., UK). After cold incubation for 30-90 min, slices with the right more morphology were selected and placed onto the Millicell standing inserts (hydrophilic PTFE membrane, 0.4 µm, EMD Millipore) in a 6-well tissue culture plate (Sarstedt Inc., Newton, NC) preloaded with culture medium. The OHSCs were incubated in 5% CO₂ and 95% air for 5-8 days before use. Culture medium was exchanged every 2-3 days. This protocol has been approved by the IACUC of the University of Pittsburgh.

5.2.3 Microfluidic chip design and instrumentation

The design of the microfluidic chip is illustrated in Fig. 61. It is fabricated using lithography techniques as described previously²⁷⁴ with a 30 µm mask width for all channels. The etching

depth is 20 μm and the channel length (solid line) is drawn to scale. The total length of the reaction channel is ~ 46 mm and the distance between the detection point and injection cross is 23 mm. The electrical connection to all liquid access holes, the derivatization (+HV), the sample input (+HV), the auxiliary (ground), the gate (switched between ground and floating through a HV relay) and the waste (-HV) are represented by the short dashed lines as shown in Fig. 60. Microfluidic reservoirs were bought from IDEX Health & Science LLC (Oak Harbor, WA) and adapted to accommodate ~ 500 μL reagents each. An 11 cm (length) x 50 μm (ID)/360 μm (OD) fused silica capillary (long dashed line, Polymicro Technologies, Phoenix, AZ) are connected to the microfluidic chip via a NanoPortTM assembly (IDEX Health & Science LLC) with a minimized dead volume.

The detection of ThioGlo-1 derivatized thiol compounds was accomplished by a home-made laser induced fluorescence (LIF) detector.²⁷⁴ Two four-channel high voltage power supplies (HVPS), flow gated sample introduction, PMT voltage and signal collection are all controlled by a locally written program in LabVIEW 8.2 (National Instruments, Austin, TX). During the experiment, The PMT control voltage was set at 0.6 V and the laser power was maintained at 3.0 mW. An inverted fluorescent microscope IX 71 (Olympus, Center Valley, PA) was used to check and characterize OHSCs.

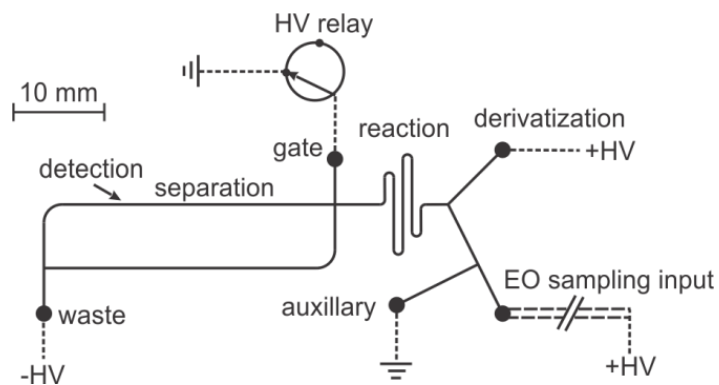


Figure 61. Sketch of the microfluidic device integrated with online electroosmotic sampling

Channel (solid line) lengths are drawn to scale and all channels are 20 μm in depth. The short dashed line represents the electrical connection in each reservoir. Long dashed line labeled with electroosmotic sampling input stands for the fused silica sampling capillary

5.2.4 Online sampling experiments

At the beginning of the experiment, an OHSC was transferred to a Petri dish with 1.2 mL pre-warmed and gassed GBSS and then to another Petri dish containing 1.2 mL of ggACSF alone or augmented with a substrate, inhibitor or drug compound at a desired concentration. Microfluidic chips and sampling capillaries were preconditioned with 1 M NaOH or 0.1 M NaOH, followed by deionized water and the experimental buffers for 5 minutes each. The auxiliary reservoir and the sampling capillary were preloaded with sampling buffer. The gate and waste reservoirs were filled with running buffer. The derivatization reservoir contained 2.7 μM ThioGlo-1 in derivatizing buffer. The liquid volume at each reservoir was 300-310 μL . The electroosmotic sampling setup and voltage settings were described in another paper.²⁹⁷ Briefly, for electroosmotic sampling, the end of the sampling capillary was lowered perpendicularly towards the OHSC by a Sutter MP-285 micromanipulator (Sutter Instrument Company, Novato, CA) until the tip made contact with the thin layer of liquid on the tissue surface in the CA3 region and

then was lifted up 20 μm while remaining in contact with the tissue through the thin layer of liquid. There was a pre-sampling step prior to each experiment. In this step, +3000 V and “GND” were applied to Petri dish and auxiliary reservoir, respectively for 6 min. All other reservoirs were set at “floating”. After this step, +300 V and -4500 V were applied to derivatization and waste reservoirs, respectively. The gate reservoir was switched between sample loading (floating, 0.5 sec) and separation modes (GND, 24.5 sec) alternately using a high voltage relay. Electrical settings at the auxiliary reservoir and the Petri dish were kept unchanged from the pre-sampling step. Extracellular fluid collected by the electroosmotic sampling in the CA3 region of the hippocampal slice was analyzed online with the microfluidic chip with the confocal LIF detector through continuous gated injections. There were about 30-40 repeated injections per run. Experiments were carried out at room temperature.

5.3 RESULTS AND DISCUSSION

5.3.1 Calibration and quantitation

In the process of electroosmotic sampling of the extracellular space of an OHSC with a natural enzyme substrate, the substrate will be metabolized. The conditions used for electroosmotic sampling are always the same, thus the residence time of a particular substrate in the tissue is constant. As the fluid flow is governed by the electric field in the tissue (and in the sampling capillary), the velocity of the sampling buffer/extracellular fluid is not constant. Because the electric field in the tissue is proportional to the current density and the current density decreases away from the opening of the sampling capillary, the fluid velocity is highest near the sampling

capillary (Fig. 62). As a result of this, substrate conversion to product will be highest far from the sampling capillary. We estimate that the residence time of the substrates, t_s , is approximately 55 s (see Appendix C for detailed derivatization).

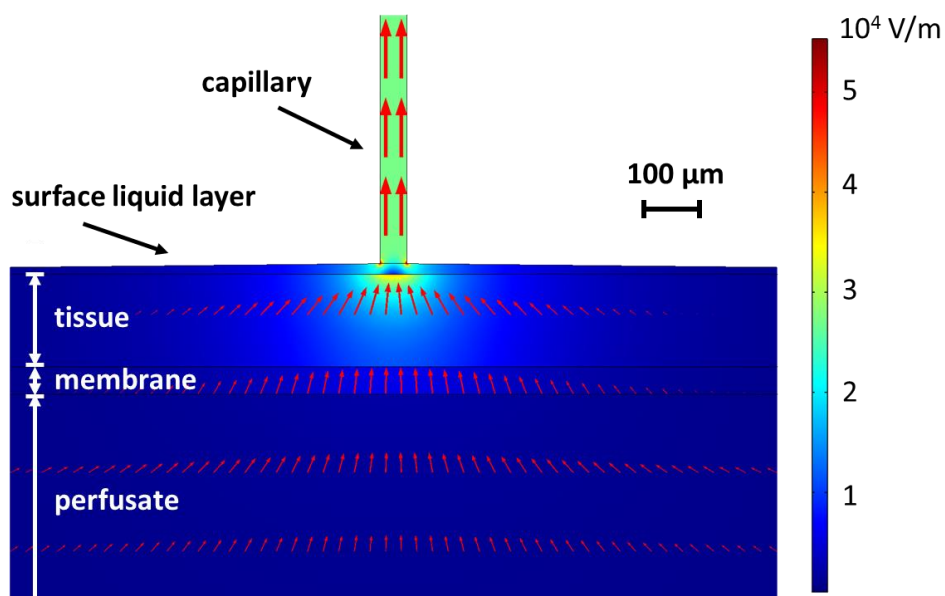


Figure 62. Simulated electric field and current density in both OHSC and sampling capillary during online perfusion experiment.

Parameters are based on the laboratory conditions described in the Experimental Section. Simulation is carried out for the entire region, but only a portion of the capillary, tissue, membrane and perfusate is shown in the plot for clarity purposes. The red arrows indicate the direction and magnitude of the current density (arrow length is logarithmically proportional to the magnitude of the current density) and the color in the background represents the magnitude of electric field, which is much higher inside the sampling capillary than that in OHSCs. Due to the stronger electric field near the capillary lumen, the magnitude of the velocity in that region is highest in the tissue below the sampling capillary.

As described in our previous work^{274, 297} solutes from the tissue arrive at the chip after a short delay time. Peak heights increase over a short time and reach a steady state. Plots of peak height vs. time describe a symmetrical sigmoidal curve. We use the steady state peak heights for

measurements with one exception. PSH has calculated logP values of -0.92 ± 0.72 (Advanced Chemistry Development, ACD/Labs 12.0) and -0.10 (ALOGPS 2.1,²⁹⁹ <http://146.107.217.178/lab/alogps/index.html>). Thus it can pass across the cell membrane through passive diffusion and the volume accessible to PSH is greater than the volume accessible to charged solutes. The peak height of PSH changes more slowly over time as it reaches a steady state in comparison to, e.g. CSH (Fig. 63). In fact, because the time for a single measurement is restricted to about fifteen minutes, in some cases a clear steady state is not reached. In these latter cases, we use the slope (dH/dt) at the inflection point of the sigmoidal curve as the measurement as this slope is directly proportional to the plateau height, H (see Appendix D for equation derivation).

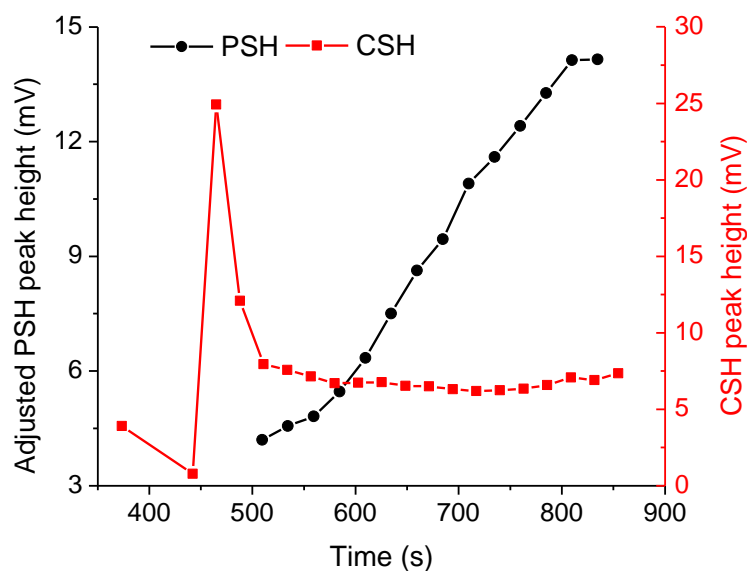


Figure 63. Progress curves for CSH and PSH based on peak heights and migration times

Petri dish contains $21.8 \mu\text{M}$ CoA in ggACSF buffer. Other conditions are same as the online sampling of the CA3 region in OHSCs.

Many of our inferences are based on quantitative determinations of CSH in the sampling fluid. We have determined earlier²⁹⁷ that the basal concentration of cysteamine in OHSCs is 10.6 ± 1.0 nM. Errors for the derived parameters from fittings are the standard error of the mean (SEM), and data points in the plots are shown as mean \pm standard deviation (SD). The calibration procedure is to introduce CSH into the sampling buffer at various concentrations and establish a linear relationship between the signal and the concentration of analyte added in the sampling buffer. It is important to note that this process provides a measurement that is not sensitive to the presence of biochemical processes that remove CSH from the extracellular space as long as the rates of the processes are constant and first order in CSH (see Appendix E for equation derivation). Thus, even though the analyte CSH may also be a substrate in one or more enzyme reactions or transport processes, the calibration will be accurate. If the processes removing CSH are significant and non-first order, the calibration graph would not be linear. CSH calibrations are linear in the examined concentration range (see Appendix F for a summary of calibration curves).

Other inferences are based on measurements of changes in PSH concentrations. PSH is neutral under our experimental conditions. Neutral thiols can in principle be determined by our measurement approach. However, because the separation is based on electrophoresis, neutral molecules are not separated from each other. As a result, a peak in the electropherogram can only be used for relative quantitation of a neutral compound when it can be certain that under the specific conditions used the change in the peak height of the neutral peak correlates with changes in the concentration of the sought for species. We have three observations that allow us to use the change in the height of the neutral peak to infer changes in pantetheine. Details are discussed below, but a statement of the observations here will support our use of changes in the neutral

peak height to infer changes in pantetheine concentration in the following discussion. (I) Perfusion with the disulfide pantetheine leads to an increase in the neutral peak height that is linearly related to the pantetheine concentration in the perfusate. This is consistent with the expectation that pantetheine engages in disulfide exchange reactions. (II) Perfusion with CoA leads to an increase in the neutral peak height. Other thiol products in the proposed catabolic pathway (Fig. 60) are charged, thus they cannot augment the neutral peak height. (III) Coperfusion of CoA and the pantetheinase inhibitor 8-cyclopentyl-1, 3-dipropylxanthine (DPCPX) leads to an increase in the neutral peak height with a corresponding decrease in the CSH peak height (Fig. 64). These observations permit us to use changes in the neutral peak height to infer changes in pantetheine.

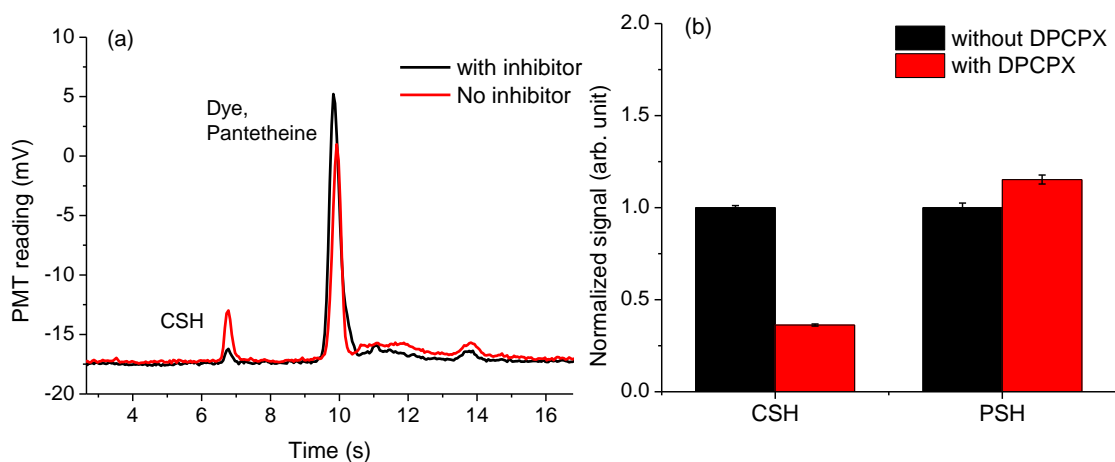


Figure 64. Inhibition of the pantetheinase by 8-cyclopentyl-1, 3-dipropylxanthine (DPCPX)

Petri dish contains 115.6 μM CoA with or without DPCPX 107.3 μM in ggACSF buffer. Other conditions are same as the online sampling of the CA3 in OHSCs. (a) Representative electropherograms obtained with and without inhibitor in the sampling buffer; (b) The peak height, H, (for CSH) and the peak height growth rate, dH/dt , around the inflection point of the sigmoid curve (for PSH) obtained with or without inhibitor are normalized for comparison. Data is shown as mean \pm SEM ($n \geq 16$). Two sample t-test of CSH peak height and ANCOVA analysis of the pantetheine peak growth rate indicate there are significant differences between results obtained with and without DPCPX treatment at $p = 0.04\%$.

5.3.2 CSSC is converted more rapidly than PSSP to CSH

Many bioactive functions of the disulfides cystamine and pantethine rely on their conversion to cysteamine through disulfide exchange with endogenous thiols and an additional metabolic step for pantethine with the help of pantetheinase as shown in Fig. 3.^{285, 289}

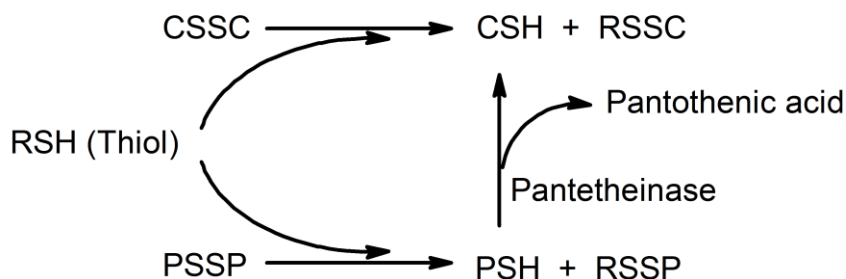


Figure 65. The formation of CSH from CSSC and PSSP through disulfide exchange and catalysis by pantetheinase.

RSSC and RSSP are mixed typed of disulfide aminothiols with CSH and PSH respectively.

CSH was determined in perfusate containing CSSC or PSSP. Fig. 66 demonstrates the electropherograms from all of the injections in a single measurement. ThioGlo-1, which is

neutral and weakly fluorescent, has a small peak with a migration time 9.4 s (Fig. 66 (a)). Because the source of the reagent is on the chip, it appears in the 5th injection, which is earlier than the arrival time of thiols coming from the tissue. Peaks from the latter compounds were not detected until the 16th injection. This is attributed to the time spent in the sampling capillary. Although the maleimide reagent (ThioGlo-1) is intended to react with thiols, it also reacts with amines at a much lower rate.²⁸⁰ Due to the relatively high concentration of Gly-Gly in ggACSF, we also observed the derivatized Gly-Gly peak in the electropherogram most easily seen in Fig. 66 (c) and Fig. 66 (d) with a migration time near 21 s. Fig. 66 (a) and Fig. 66 (b) show that cystamine is converted to cysteamine, while Fig. 66 (c) and Fig. 66 (d) show that PSSP is converted to PSH (increase in the neutral peak). Fig. 67 (a) shows that the dependence of measured CSH concentration on that of the initial CSSC concentration ($\Delta[\text{CSH}]/[\text{CSSC}]_0$) in the extracellular space is high ($91\% \pm 4\%$ with the assumption that one cysteamine is formed from a disulfide exchange reaction with cysteamine) and linearly related to the concentration of CSSC in the perfusate over the range investigated up to $\sim 700 \mu\text{M}$ (high concentration data not shown). The *in situ* measurement on intact tissue result reflects a biochemically relevant result for extracellular conversion. To determine the effect of added PSSP on PSH concentration, we use the peak height growth rate around the inflection point of the sigmoid progress curve, dH/dt which is directly proportional to $\Delta[\text{PSH}]$ (see Appendix D). Linear regression of dH/dt vs. the added concentration of PSSP yields Fig. 67 (b). We find that the production of PSH is linearly related to the concentration of PSSP introduced. This is consistent with an uncatalyzed disulfide exchange reaction being responsible for the conversion.

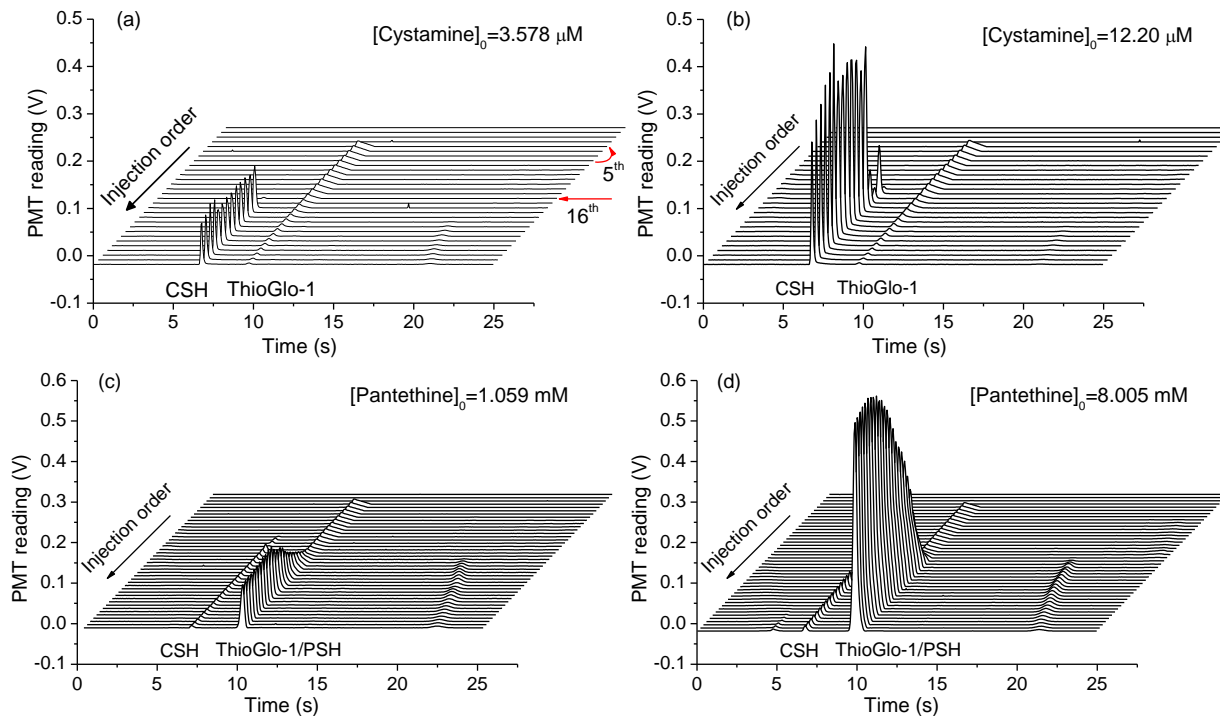


Figure 66. Series of electroperograms obtained from online sampling in the CA3 region of OHSCs

The initial CSSC or PSSP concentrations in the ggACSF that OHSCs imbibe are (a) CSSC: 3.578 μM ; (b) CSSC: 12.20 μM ; (c) PSSP: 1.059 mM; (d) PSSP: 8.005 mM.

In Fig. 67 (c), the concentration of CSH is plotted against the initial concentration of PSSP. The relationship is nonlinear implying the presence of an enzyme-catalyzed step. The dependence of measured CSH concentration on that of the initial PSSP concentration ($\Delta[\text{CSH}]/[\text{PSSP}]_0$) in the extracellular space is very low, from 0.03% to 0.01% when the concentration of PSSP varies from 1.1 mM to 8.0 mM. Pantetheinase, the ectoenzyme that creates CSH from PSH, is inhibited by disulfides. An uncompetitive inhibition of pantetheinase by PSSP at pH 8.0 has been observed and the inhibition effect is increased as the incubation time of the pantetheinase and PSSP is prolonged.³⁰⁰ Therefore the rate equation based on the production of CSH can be written as follows where $K_{M,C}$, $V_{\max,C}$, and $K_{i,C}$ are the Michaelis

constant, maximum reaction rate, and the inhibitor constant of pantetheinase with PSH as the substrate and PSSP as the uncompetitive inhibitor, respectively.²⁵⁰

$$\Delta[\text{CSH}] = \frac{t_S V_{\max,C} [\text{PSH}]}{K_{M,C} + [\text{PSH}] \left(1 + \frac{[\text{PSSP}]}{K_{i,C}}\right)} = \frac{t_S V_{\max,C} [\text{PSSP}]_0}{\frac{K_{M,C}}{\alpha} + [\text{PSSP}]_0 + [\text{PSSP}]_0^2 \frac{1-\alpha}{K_{i,C}}} \quad (29)$$

$$\Delta[\text{CSH}] \approx \frac{t_S V_{\max,C} [\text{PSSP}]_0}{\frac{K_{M,C}}{\alpha} + [\text{PSSP}]_0} \quad (30)$$

The factor α is the fraction of initial PSSP, $[\text{PSSP}]_0$, that is converted with 1:1 stoichiometry to PSH. $[\text{PSH}]$ and $[\text{PSSP}]$ are the concentrations of PSH and PSSP in the sampling fluid. The results of a nonlinear fitting of Eq. 29 to $\Delta[\text{CSH}]$ as a function of $[\text{PSSP}]_0$ indicates that the last term of the denominator, $[\text{PSSP}]_0^2(1-\alpha)/K_{i,C}$, is negligible compared to other two terms. By omitting this term, Eq. 29 is reduced to Eq. 30. A nonlinear fitting of Eq. 30 is plotted in Fig. 67 (c), which gives $K_{M,C}/\alpha = 4.4 \pm 1.1$ mM and $V_{\max,C} = 29 \pm 3$ nM/s. Reported $K_{M,C}$ values for pantetheinase in *in vitro* assays using pantetheine or its analogs as substrate are in the range of ~ 20 μM .³⁰¹⁻³⁰³ Based on that, we can estimate that the percentage yield, α , for pantetheine to pantetheine to be approximately 0.5%, which is much lower than that of CSSC to CSH.

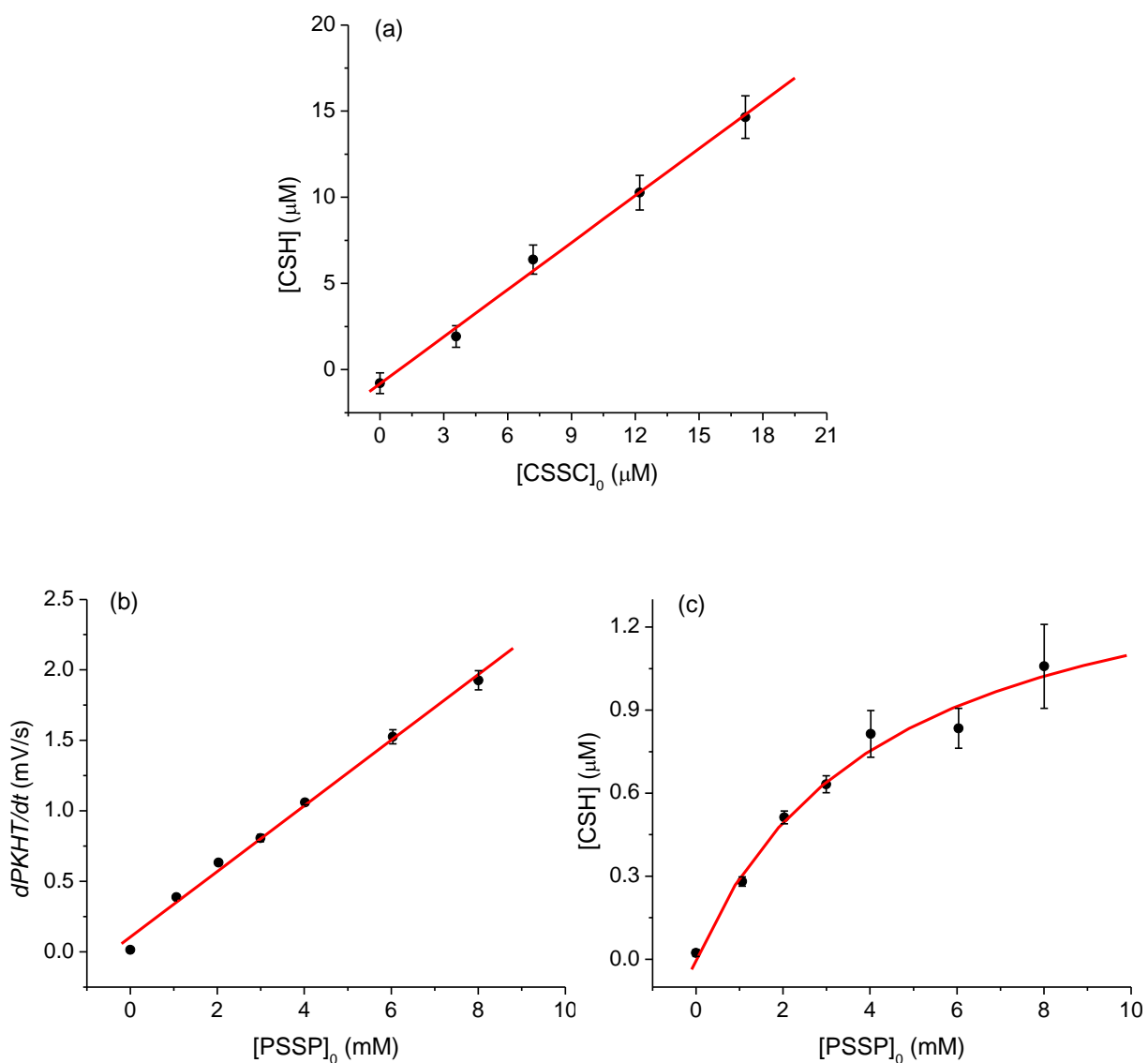


Figure 67. The conversion of drug compounds in the CA3 region of OHSCs during electroosmotic sampling (a) The conversion of CSSC to CSH; (b) PSSP to PSH, and (c) PSSP to CSH at different drug concentrations are given in plots. Error bar indicates \pm standard deviation ($n \geq 4$). Black dot indicates experimental data. Linear fitting or non-linear Michaelis-Menten fitting in red was performed based on the experimental data.

CSH is the active molecule in the treatment of cystinosis, however CSH is cytotoxic at high concentration; the LC50 of cysteamine to the human leukemia cell line B4D is $52 \mu\text{M}$.²⁸⁸,

³⁰⁴ CSH precursors CSSC and PSSP have also been used as drugs against cystinosis.^{285, 286, 305} Differences in the conversion rates of the two precursors to CSH in the OHSCs may well explain their distinct clinical profiles. The generation rate of CSH from precursors CSSC or PSSP will determine the concentration of active substance. PSSP is as effective as PSH in lowering cystine levels in cystinosis,²⁸⁵ however, PSSP is less effective.³⁰⁵ This is consistent with our observation that the production rate of CSH from PSSP is significantly lower than the production rate from CSSC. Side effects and toxicity are common in the treatment with CSH or CSSC.²⁸⁵⁻²⁸⁷ To the contrary, PSSP has no or limited side effects even at high doses.^{305, 306} The same rationale mentioned above can be used to explain this difference. Moreover, other beneficial effects of PSSP, such as its anti-catabolic effect and the acceleration of fatty acid oxidation, are related to its promotion of CoA concentration due to the biological conversion of PSSP to PSH, and the following metabolism of PSH to 4'-phospho-PSH and finally to CoA, which bypasses the first three steps in the CoA biosynthesis.^{286, 307}

5.3.3 Enzymatic degradation of CoA: CSH

Endogenous CSH, Hcy and Cys in the extracellular space of the OHSCs can be observed under the conditions used (Fig. 68 (a)). To monitor the metabolism of CoA in OHSCs, different concentrations of CoA were added to the ggACSF in Petri dish containing OHSCs. Fig. 68 shows the reconstructed plots of PMT reading vs. time for all injections in two experiments. Endogenous CSH, Hcy and Cys in the extracellular space of OHSCs were observed when only ggACSF was in the Petri dish (Fig. 68 (a)). ThioGlo-1 together with an unknown in the reagent solution appears earlier than all other peaks in the 5th injection as expected from the design of the microfluidic chip. Endogenous CSH peaks from OHSCs, followed by Hcy and Cys, were not

detected until the 17th injection, which is attributed to the sample's traveling time spent in the transporting capillary tube. As expected from the proposed pathway of CoA degradation, an increase in the CSH peak height was observed when ggACSF was spiked with 0.12 mM CoA as shown in Fig. 68 (b). CSH was first detected in the 16th injection and its height reached maximum in the 20th electropherogram and quickly formed a plateau thereafter. The abnormal heights for the first several CSH peaks are probably from the cation-specific preconcentration at the interface of different buffer zones along the flow path. To better elucidate the dependence of the plateau peak heights of CSH on the concentrations of CoA in ggACSF, four representative electropherograms from online electroosmotic sampling experiments under the same conditions except for the CoA concentration in ggACSF are shown in Fig. 69. There is a remarkable increase in the plateau peak height of CSH when CoA concentration in the ggACSF is elevated from 0 to 58 μ M. As the plateau peak height is directly proportional to the concentration of CSH produced from the CoA metabolism, we use it in determining the effect of CoA concentration on the CSH production rate. Thus by measuring the CSH concentration as a function of CoA concentration, we should observe a nonlinear dependence. The plateau concentration, $\Delta[\text{CSH}]$ was obtained from the calibration curve based on the plateau peak height of the analyte. $\Delta[\text{CSH}]$ is plotted against the initial $[\text{CoA}]_0$ concentration in Fig. 70 (a).

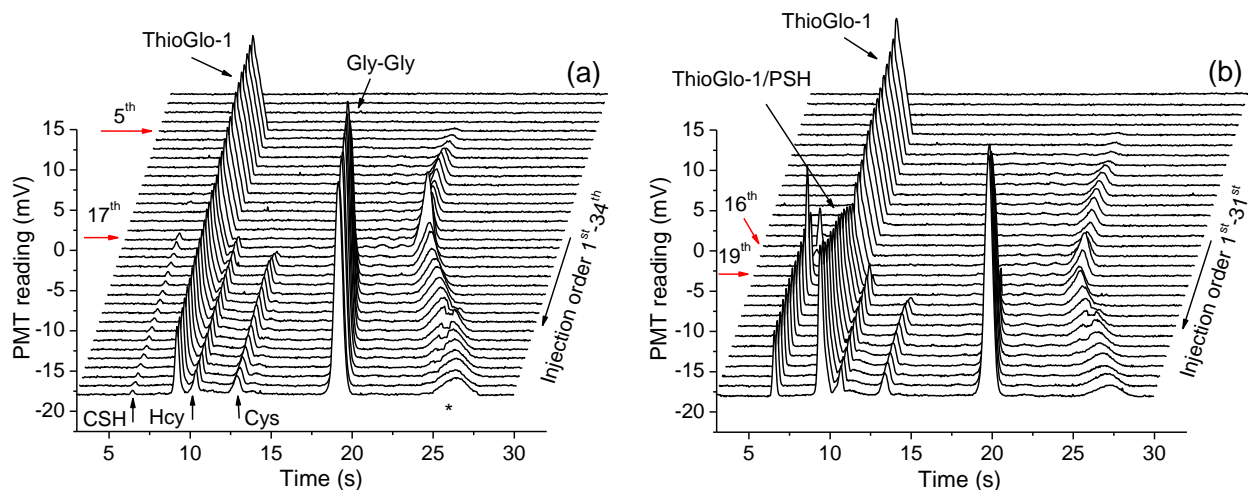


Figure 68. Electropherograms obtained from online electroosmotic sampling of the CA3 region in OHSCs. Initial CoA concentrations in the ggACSF that OHSCs imbibe are (a) 0 mM; (b) 0.12 mM. Peaks marked with ‘*’ are impurity in the dye.

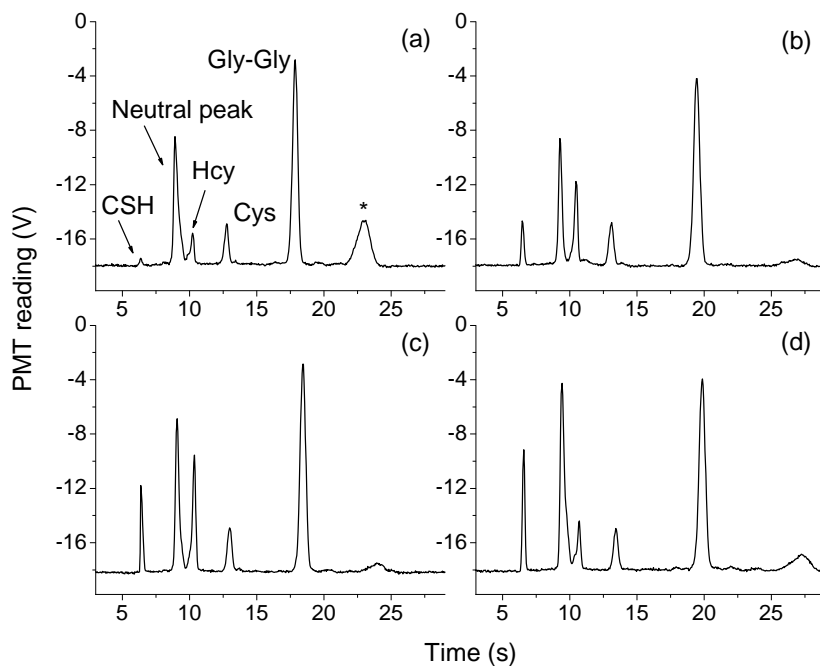


Figure 69. Representative electropherograms from online electroosmotic sampling of the CA3 region in OHSCs. All conditions are the same except the CoA concentrations in the ggACSF (a) 0 μM ; (b) 7.3 μM ; (c) 22 μM ; (d) 58 μM . Neutral peak is contributed from ThioGlo-1 and pantetheine.

As discussed above, it is appropriate to assume that CSH is the last product of a multi-enzyme reaction with CoA as the initial substance. Therefore, the overall initial reaction rate of a multi-enzyme reaction such as one of the paths shown in Fig. 60 can be obtained by noting the change in cysteamine concentration over the residence time of the substrate in the tissue, t_s . According to Michaelis-Menten kinetics, the overall reaction rate of the system $d[\text{CSH}]/dt$ is given by²⁵⁰

$$\frac{d[\text{CSH}]}{dt} \cong \frac{\Delta[\text{CSH}]}{t_s} = \frac{V'_{\max}[\text{CoA}]_0}{K'_M + [\text{CoA}]_0} \quad (31)$$

$$\Delta[\text{CSH}] = \frac{t_s V'_{\max} [\text{CoA}]_0}{K'_M + [\text{CoA}]_0} \quad (32)$$

where $\Delta[\text{CSH}]$ is the measured CSH concentration; $[\text{CoA}]_0$ represents the initial CoA concentration in the perfusate, K'_M and V'_{\max} and are the apparent Michaelis constant and apparent maximum reaction rate for the multi-enzyme reaction with CoA as the substrate, respectively. A nonlinear fit of Eq. 32 to the data shown in Fig. 70 (a) gave $K'_M = 16 \pm 4 \mu\text{M}$ and $V'_{\max} = 7.1 \pm 0.5 \text{ nM/s}$, respectively.

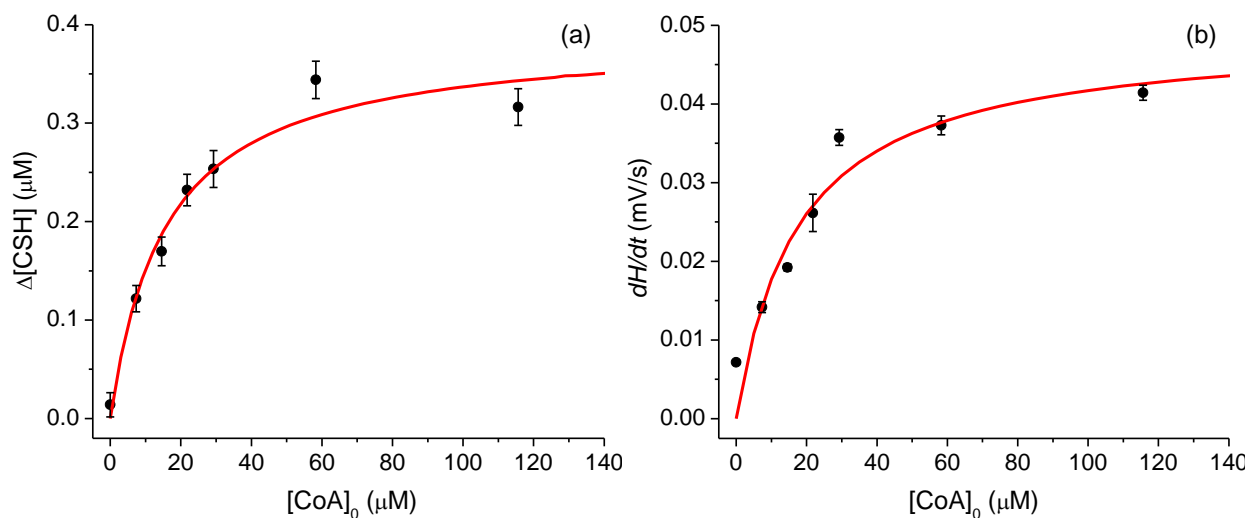


Figure 70. Michaelis-Menten fittings based on CSH and PSH

(a) $\Delta[\text{CSH}]$ vs. $[\text{CoA}]_0$ (b) dH/dt vs. $[\text{CoA}]_0$, were obtained by online sampling of the CA3 region in OHSCs. Error bar indicates \pm standard deviation ($n \geq 7$). Black dot indicates experimental data and red curves are the fitting result.

5.3.4 Enzymatic degradation of CoA: PSH

PSH is an intermediate molecule in the metabolic pathway of CoA (Fig. 60) and is expected to show up as a neutral molecule on the electropherogram. When CoA is added in sampling buffer, the height of the neutral peak stops decreasing around the 19th injection and starts to increase in Fig. 68 (b), which suggests that PSH elutes together with the unreacted ThioGlo-1 as expected. If the measured PSH signal is used to estimate the multi-enzyme reaction rate, a relationship analogous to Eq. 32 can be established. This relationship, Eq. 33, has the same form as the Michaelis-Menten equation, where $K'_{M,p}$ and $V'_{\max,p}$ are the apparent Michaelis constant and the apparent maximum reaction rate based on the production of pantetheine. As discussed above, peak height growth rate, dH/dt , is directly proportional to $\Delta[\text{PSH}]$.

$$\frac{dH}{dt} = q\Delta[\text{PSH}] = \frac{qt_s V'_{\max,p} [\text{CoA}]_0}{K'_{M,p} + [\text{CoA}]_0} \quad (33)$$

Here q is a constant that connects the steady state concentration of PSH with the PSH peak height growth rate. Fig. 70 (b) shows dH/dt for PSH plotted against $[\text{CoA}]_0$ with a nonlinear fitting of Eq. 33. From the fit, we find that $K'_{M,p}$ is $18 \pm 6 \mu\text{M}$. $K'_{M,p}$ is statistically indistinguishable from the K'_M obtained above based on CSH concentration. The fact that this constant is the same for the ultimate product formation rate, $\Delta[\text{CSH}]/t_s$ and the penultimate product formation rate, $\Delta[\text{PSH}]/t_s$, suggests that the final enzyme, pantetheinase, is not limiting and is operating in the first-order regime.

The electroosmotic perfusion technique used here is capable of collecting extracellular fluid under conditions that only cause minimal damage to the tissue.^{105, 297} The damage of tissue is mainly located in the region near the capillary lumen, where the fluid velocity in tissue is the highest and the substrate conversion to product is minimal. Therefore the damaged tissue will exert negligible effect on the total enzyme reaction. In addition, CoA and its metabolite 4'-phosphopantetheine are negatively charged. These molecules and their derivatives do not cross the cell membrane found in *E. coli*, rat liver and neuronal cells.³⁰⁷⁻³⁰⁹ Together with these facts, our results directly show that CoA can be completely degraded to CSH in the extracellular space. The proposed CoA metabolic routes I, II and III (Fig. 60) involve lysosomal acid phosphatase which is in lysosomes and nucleotide diphosphatase and pantetheinase which are ectoenzymes on the plasma membrane and nudix hydrolase which is in peroxisomes.^{65, 68, 88} Assuming that the *in vivo* degradation of CoA is carried out through one of these routes, there would be extensive trafficking of CoA and its metabolites between lysosomes or peroxisomes and outer surface of the plasma membrane. Due to the transport obstacles for intermediate metabolites to access these

enzymes in sequential reactions, it is quite difficult to envision these pathways in practice and to explain the efficient degradation of CoA found in rat liver.⁶⁸ Our results demonstrate that extracellular CoA is very likely to be degraded in a pathway similar to route I or III, but with all the dephosphorylation process taking place in the extracellular space. It is also possible that dephospho-CoA in lysosomes produced by lysosomal acid phosphatase is released to the extracellular space through lysosomal exocytosis^{310, 311} and is then metabolized outside the cells similar to route II. The nucleotide diphosphatase involved in this process prefers dephospho-CoA as a substrate over CoA.^{68, 312}

5.4 CONCLUSIONS

We have demonstrated here the successful integration of electroosmotic perfusion with online microfluidic analysis to study the metabolism of two drug compounds and CoA when these analytes passed through the extracellular space of OHSCs. The much higher percentage yields of cysteamine from cystamine than that from pantethine are directly correlated with the differences of these drug compounds in their effectiveness and toxicity observed clinically. The detection of cysteamine and pantetheine while perfusing CoA directly demonstrate the complete degradation of CoA to cysteamine in the extracellular space of OHSCs. Unlike other proposed pathways for CoA degradation, the route proposed here is easier to visualize *in vivo* as it does not involve extensive trafficking of CoA and related metabolites. The products of CoA biodegradation in the extracellular space, namely pantetheine, pantothenic acid and cysteamine can each be retaken by cells and reenter the CoA biosynthesis pathway or other metabolic pathways. The kinetic parameters of the overall sequential multi-enzyme reaction of CoA biodegradation obtained by

measuring the cysteamine formation rates in the OSHCs at different CoA concentrations are useful for evaluating the taurine flux through cysteamine pathway and for understanding and solving the challenges remaining in the mechanism, regulation and turnover rate of CoA degradation.

APPENDIX A

EQUIVALENT CIRCUIT OF THE MICROFLUIDIC CHIP

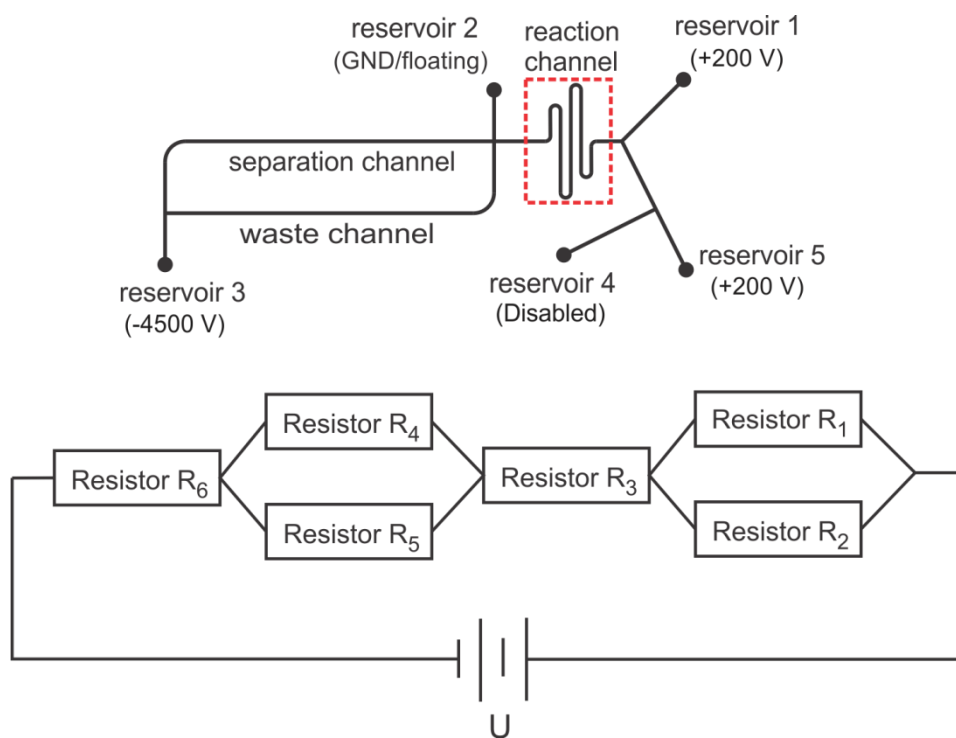


Figure A-1. Equivalent circuit of the microfluidic chip

R_1 , R_2 , R_3 , R_4 , R_5 , R_6 , are equivalent resistances of the derivatizing, the sample, the reaction, the separation, the waste and the final mixing channels, respectively.

$$R_i = \rho_i \frac{l_i}{A_i}, i = 1 \dots 6 \quad (\text{A-1})$$

ρ is the resistivity, l is the length, A is area of the cross section, i represents the equivalent resistor number;

U : is the voltage applied on the whole system;

Therefore the electric field E_i on resistor i is

$$E_i = \frac{\Delta U_i}{l_i} \quad (\text{A-2})$$

where ΔU_i : Voltage drop on resistor i ;

According to the equivalent circuit, the total resistance can be expressed by

$$R_t = \frac{R_1 R_2}{R_1 + R_2} + R_3 + \frac{R_4 R_5}{R_4 + R_5} + R_6 \quad (\text{A-3})$$

When reservoir 2 is floating,

Case 1: solution concentration is same everywhere in the microfluidic chip

We have

$$\rho_1 = \rho_2 = \rho_3 = \rho_4 = \rho_5 = \rho_6 \quad (\text{A-4})$$

$$A_1 = A_2 = A_3 = A_4 = A_5 = A_6 \quad (\text{A-5})$$

$$l_4 = l_5 \quad (\text{A-6})$$

According to Eq. A-1 to 6

$$E_3 = \frac{\Delta U_3}{l_3} = U \frac{R_3}{R_t l_3} = U \frac{\rho_3 \frac{l_3}{A_3}}{R_t l_3} = U \frac{\rho_3}{R_t A_3} \quad (\text{A-7})$$

$$E_4 = E_5 = \frac{\Delta U_4}{l_4} = U \frac{\frac{R_4 R_5}{R_4 + R_5}}{R_t l_4} = U \frac{\frac{\rho_4 \frac{l_4}{A_4} \rho_5 \frac{l_5}{A_5}}{\frac{l_4}{A_4} + \frac{l_5}{A_5}}}{R_t l_4} = U \frac{\frac{\rho_4}{2}}{R_t A_4} \quad (\text{A-8})$$

Therefore, divide Eq. 7 by Eq. 8 will give

$$\frac{E_3}{E_4} = \frac{E_3}{E_5} = 2$$

$$\text{Or } E_3 = E_4 + E_5 \quad (\text{A-9})$$

According to

$$v_i = -\frac{\varepsilon\zeta}{\eta} E_i \quad (\text{A-10})$$

We have

$$v_3 = v_4 + v_5 \quad (\text{A-11})$$

Case 2: reservoir 5 is replaced with high conductivity solution

After the solutions achieve steady state in each channel, we have

$$\rho_2 < \rho_3 \approx \rho_5 < \rho_6 < \rho_4 \approx \rho_1 \quad (\text{A-11})$$

$$A_1 = A_2 = A_3 = A_4 = A_5 = A_6 \quad (\text{A-12})$$

$$\rho_2 < \rho_3 \approx \rho_5 < \rho_6 < \rho_4 \approx \rho_1 \quad (\text{A-13})$$

$$l_4 = l_5 \quad (\text{A-14})$$

According to Eq. A-1 to 3 and Eq. A-12 to 14

$$E_3 = \frac{\Delta U_3}{l_3} = U \frac{R_3}{R_t l_3} = U \frac{\rho_3 \frac{l_3}{A_3}}{R_t l_3} = U \frac{\rho_3}{R_t A_3} \quad (\text{A-15})$$

$$E_4 = E_5 = \frac{\Delta U_4}{l_4} = U \frac{\frac{R_4 R_5}{R_4 + R_5}}{R_t l_4} = U \frac{\frac{\rho_4 \frac{l_4}{A_4} \rho_5 \frac{l_5}{A_5}}{\rho_4 \frac{l_4}{A_4} + \rho_5 \frac{l_5}{A_5}}}{R_t l_4} = U \frac{\rho_4 \rho_5}{R_t A_4} \quad (\text{A-16})$$

Similarly, divide Eq. A-15 by Eq. 16 will give

$$\frac{E_3}{E_4} = \frac{E_3}{E_5} = \frac{\rho_3}{\frac{\rho_4 \rho_5}{\rho_4 + \rho_5}} = 1 + \frac{\rho_5}{\rho_4} \quad (\text{A-17})$$

According to Eq. A-12, we will have

$$\frac{E_3}{E_4} = \frac{E_3}{E_5} < 2$$

$$\text{Or } E_3 < E_4 + E_5 \quad (\text{A-18})$$

Therefore, according to Eq. A-10 (to simplified the estimation, we assume that ζ -potential is the same for all channels)

$$v_3 < v_4 + v_5 \quad (\text{A-19})$$

APPENDIX B

STANDARD ADDITION METHOD

Standard addition method was applied to calculate the basal concentration of CSH, Hcy and Cys. Some main parameters used in the establishment of the calibration curve are listed in Table B-1. The standard curves for CSH, Hcy and CSH used in the standard addition method are given in Fig. B-1.

Table B-1. Parameters and results for the standard addition method

	CSH	Hcy	Cys
LOD (S/N=3)	5.4 nM	25 nM	1.4 μ M
Linear range	0 - 99.2 nM	0 - 2.43 μ M	0 - 98.4 μ M
# of concentrations measured (equals to # of slices used*)	5 <i>3 repeats at 0 nM</i>	6 <i>3 repeats at 0 μM</i>	8 <i>3 repeats at 0 μM</i>
# of points used in fitting	70	53	70
Calculated basal concentration	10.6 \pm 1.0 nM	0.18 \pm 0.01 μ M	11.1 \pm 1.2 μ M
Slope	2.56 $\times 10^1$	8.74	1.17 $\times 10^{-1}$
Slope SD	0.05 $\times 10^1$	0.13	0.03 $\times 10^{-1}$
Intercept	2.72 $\times 10^{-4}$	1.54 $\times 10^{-3}$	1.31 $\times 10^{-3}$
Intercept SD	0.25 $\times 10^{-4}$	0.12 $\times 10^{-3}$	0.14 $\times 10^{-3}$
Adjusted R ²	0.97	0.99	0.94

*Any single slice is only used at a particular concentration once

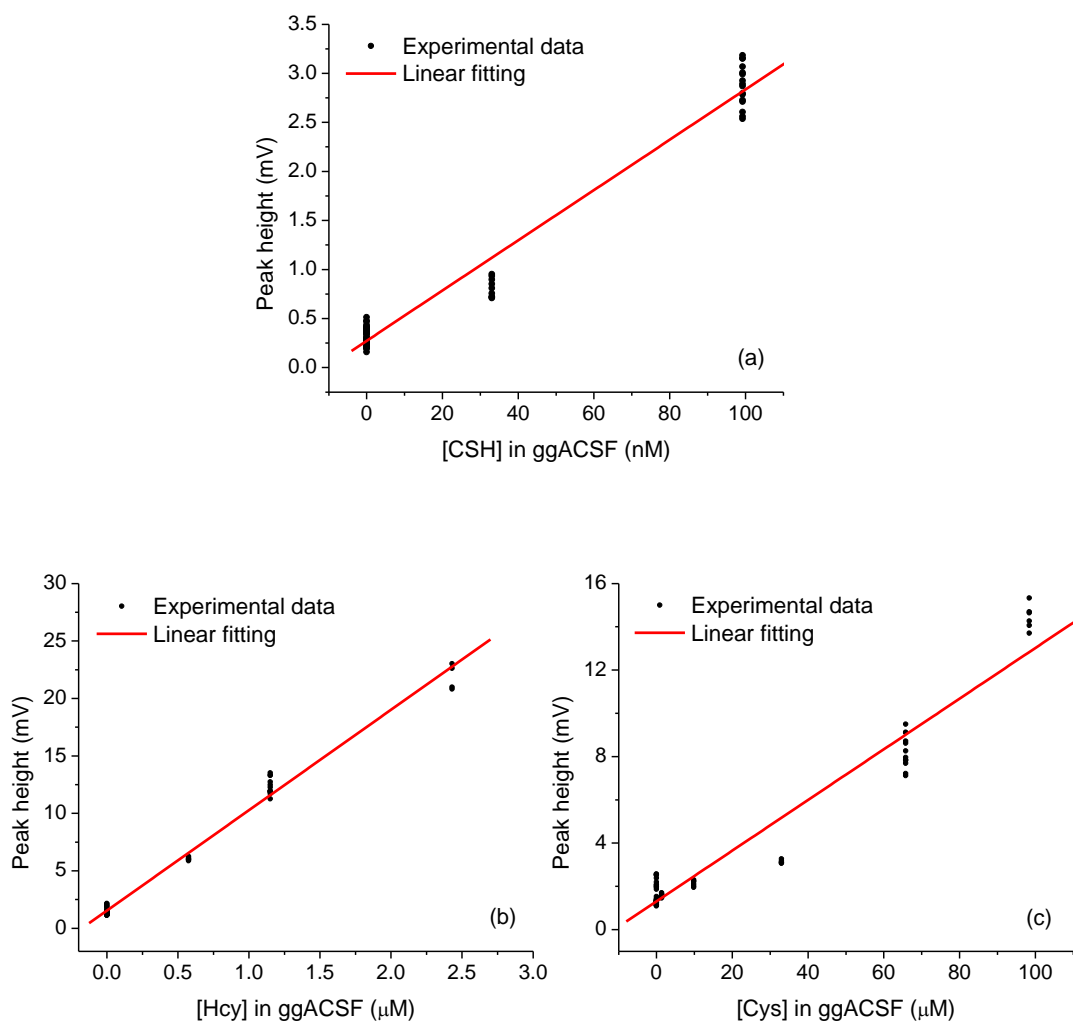


Figure B-1. Calibration curves used in the standard addition method for CSH, Hcy and Cys

APPENDIX C

ESTIMATION OF THE SAMPLED TISSUE VOLUME AND THE AVERAGE TIME THE ANALYTE SPENDS INSIDE OHSCS

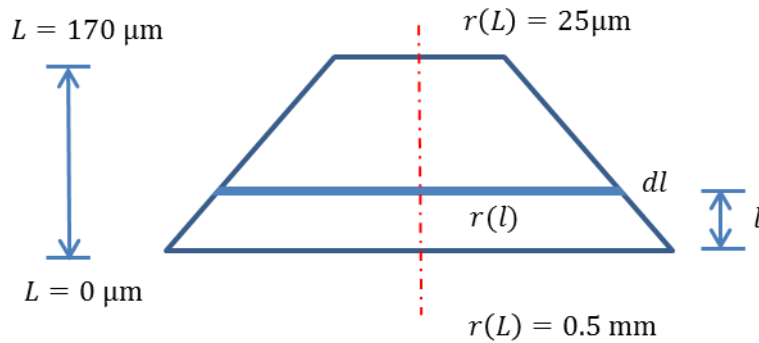


Figure C-1. Estimation the tissue volume being sampled

Assuming that the shape of the sampled tissue is a frustum of a cone with the top diameter equal to that of a sampling capillary, $50 \mu\text{m}$, and the bottom diameter is 1 mm (estimated from the tissue geometry). Fig. C-1 is a side view of the cross section of the sampled region in OHSCs. For illustration purpose, the shape is not drawn to scale. The thickness of the OSHC is L . Let's consider an element of the tissue slice with a thickness of dl . The volume of that element slice dV is a function of l (l is the distance between the element slice and the bottom of the tissue). According to the law of mass conservation, the sample flow rates F (m^3/s) at each any element

slice are the same. Therefore the time the analyte will be retained in the element tissue slice (or undergo enzyme catalyzed reaction) is given by

$$dt = \frac{\Phi}{F} dV \quad (C-1)$$

Therefore the total reaction time t_S (analyte will be exposed to the enzyme)

$$t_S = \int_{l=0}^{l=L} \frac{\Phi}{F} dV = \frac{\Phi V_{OHSC}}{F} = \frac{V_{eff}}{F} \quad (C-2)$$

Where V_{OHSC} is the volume of the sampled tissue and Φ is the porosity of the brain tissue. According to the given parameters, $V_{OHSC} = 4.7 \times 10^{-11} \text{ m}^3$. Assuming that the brain tissue has a porosity of 0.4,³¹³ the effective volume of the sampled tissue would be $V_{eff} = 19 \text{ nL}$. The average time required for PSH to arrive at the injection cross is 972 s and the total migration length for PSH is 170 mm. Therefore, the average linear velocity for PSH is 0.175 mm/s and the volume velocity in a 50 μm ID capillary would be 0.34 nL/s. Combining volume velocity with the effective volume of sampled tissue will give t_S to be 55 s.

APPENDIX D

RELATIONSHIP BETWEEN THE CORRECTED PANTETHEINE PEAK HEIGHT GROWTH RATE AND THE BULK CONCENTRATION

In our experiment, products of the enzyme reaction in OHSCs is collected by electroosmotic sampling and transported to the microfluidic channel by the sampling capillary. Sample stream with a spreading front will result in a sigmoid progress curve when the peak heights of an analyte from consecutive electropherograms in a single experiment are plotted against the time point of sample injection. There are many reasons that may result in a broadened frontal edge, such as the mass transfer in the enzyme reaction inside OHSCs, convective diffusion of analyte during the transport of sample in tissue, capillary and microfluidic channels due to non-uniform ζ -potential along the channel.^{255, 314, 315} For simplicity, all these effects are represented by an apparent axial diffusion coefficient, D_{app} . And the sigmoid curve can be mathematically expressed by the apparent axial diffusion of analyte from a continuous source at a velocity, v_{app} , along the flow path. The concentration profile $C(x, t)$ at any point on the flow path in the channel at time t is given by¹¹⁷

$$C(x, t) = \frac{C_0}{2} \operatorname{erfc} \frac{x - v_{app}t}{2\sqrt{D_{app}t}} \quad (\text{D-1})$$

Here x represents the distance between point and initial position of the frontal surface of the continuous source at $t = 0$, assuming there is no initial axial diffusion. C_0 is the bulk concentration of an analyte in the continuous source.

At any given location $x = x_p$, for example the injection cross, P, let

$$Z = \frac{x_p - v_{app}t}{2\sqrt{D_{app}t}} \quad (D-2)$$

The first derivative of concentration profile (D-1) with t as the independent variable can be written as follows:

$$C'(x_p, t) = \frac{C_0}{2} \frac{dZ}{dt} \frac{d}{dZ} \left(1 - \frac{2}{\sqrt{\pi}} \int_0^Z e^{-k^2} dk\right) \quad (D-3)$$

So that

$$C'(x_p, t) = \frac{C_0}{4\sqrt{\pi D_{app}}} e^{-Z^2} [x_p t^{-1.5} + v_{app} t^{-0.5}] \quad (D-4)$$

$C'(x_p, t)$ is a bell shaped curve with a maximum at $t = t_m$. t_m is the location of the inflexion point on the sigmoid curve $C(x_p, t)$. According to D-4,

$$C'(x_p, t_m) = kC_0 \text{ and } k = f(x_p, D_{app}, v_{app}) \quad (D-5)$$

For a specific analyte under same experimental conditions, k is a constant with a unit of 1/s. Meanwhile, it is obvious that the observed analyte peak height (H) directly proportional to concentration of analyte in the injected sample. Therefore, by introducing another coefficient g , which converts the concentration to voltage signal of PMT, and combining it with D-5, we have

$$\frac{dH}{dt} = gC'(x_p, t_m) = gkC_0 = qC_0 \quad (D-6)$$

where q is a coefficient contributed from both g and k .

Meanwhile, if we expand the function $C(x_p, t)$ at $t = t_m$ as N^{th} degree Taylor polynomials will give

$$C(x_p, t) = C(x_p, t_m) + C'(x_p, t_m)(t - t_m) + \frac{C''(x_p, t_m)}{2!}(t - t_m)^2 + \dots$$

$$+ \frac{C^{(n)}(x_p, t_m)}{n!}(t - t_m)^n + \dots$$
(D-7)

Then truncate D-7 at 2nd order, we have

$$C(x_p, t) = C(x_p, t_m) + C'(x_p, t_m)(t - t_m) + \frac{C''(x_p, t_m)}{2!}(t - t_m)^2$$
(D-8)

At $t = t_m$, we have

$$C''(x_p, t_m) = 0$$
(D-9)

Therefore

$$C(x_p, t) = C(x_p, t_m) + C'(x_p, t_m)(t - t_m)$$
(D-10)

When t is approaching t_m , $C(x_p, t)$ is a linear function of t , which explains the linear characteristic around the inflexion point of the sigmoid curve $C(x_p, t)$.

It is obvious that the plateau peak height, H , is also directly proportional to C_0 . Based on the above mathematical deduction, there should be a linear correlation between H and dH/dt . To prove that, in the following experiment, PSSP was added into the sampling buffer ggACSF in the Petri dish with concentration ranging from 0 mM to 8.0 mM. The peak height of PSH is obtained by subtracting the contribution from ThioGlo-1 based on the ThioGlo-1 peaks observed before PSH is observed on the electropherogram. Other conditions are the same as that of online sampling experiments described in experimental section. In Fig. D-1 (a), the plateau peak height of PSH is plotted against the peak # with the initial concentrations of PSSP in the sampling buffer varying from 0 to 8.0 mM; in Fig. D-1 (b) plateau peak height, H , is plotted as a function of dH/dt . Linear fitting proves the linear relationship between H and dH/dt .

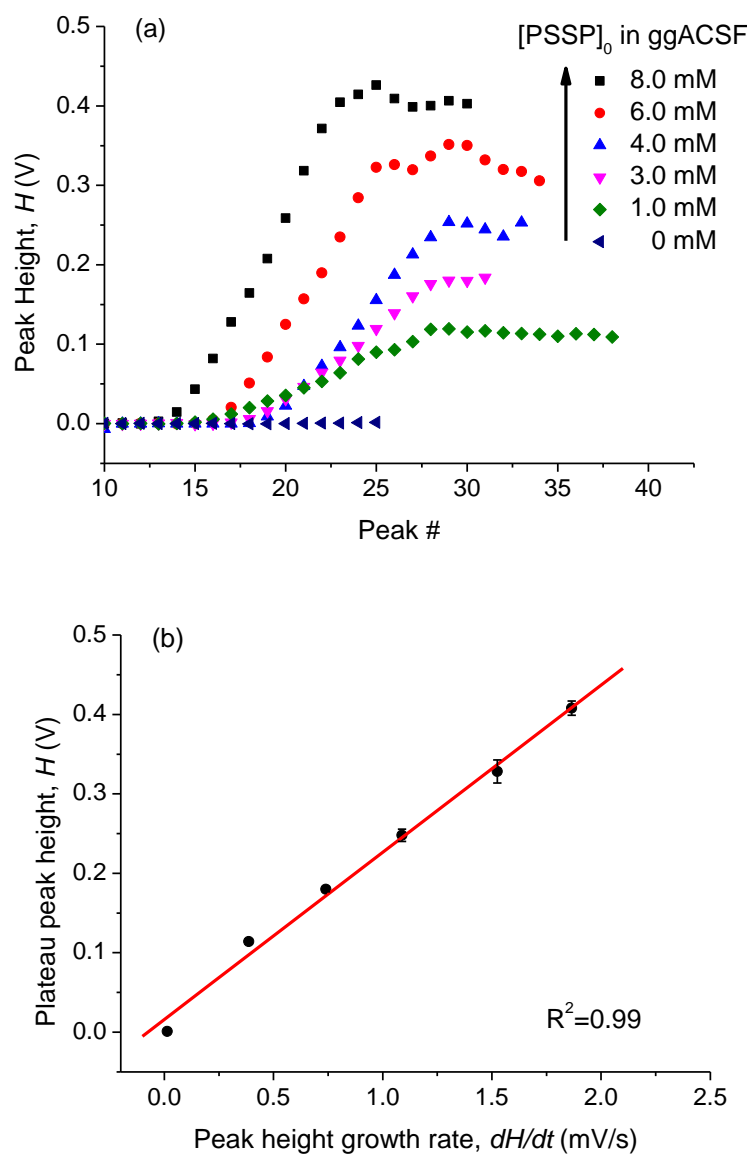


Figure D-1. Plot of plateau peak height, H , as a function of peak height growth rate, dH/dt

(a) Plateau peak height of PSH is plotted vs. the peak #; (b) plateau peak height, H , is plotted as a function of dH/dt around the inflection point of the sigmoid progress curve. Data is shown as mean \pm SD ($n \geq 4$).

APPENDIX E

QUANTITATIVE EXPLANATION OF CYSTEAMINE BEING TREATED AS THE FINAL PRODUCT

According to Michaelis–Menten kinetics

$$k = \frac{V_{max,ADO} [CSH]_0}{K_{M,ADO} + [CSH]_0} \quad (E-1)$$

Where $K_{M,ADO}$ and $V_{max,ADO}$, are Michaelis constant and maximum reaction rate of cysteamine dioxygenase (ADO, EC 1.13.11.19) with cysteamine as the substrate, respectively, $[CSH]_0$ is the initial cysteamine concentration and k is the initial reaction rate. The reported K_m of ADO at pH 8.0 with cysteamine as the substrate is around 3.8 mM,⁷⁰ while the highest concentration of cysteamine generated in experiments of CoA or pantethine metabolism is around 1 μ M. Because $[CSH]_0 \ll K_{M,ADO}$, E-1 can be reduced to

$$k = \frac{V_{max,ADO}}{K_{M,ADO}} [CSH]_0 = c [CSH]_0 \quad (E-2)$$

Where $c = V_{max,ADO}/K_{M,ADO}$. In the absence of ADO, the measured plateau peak height, H , is the function of the concentration of cysteamine as follows

$$H = a [CSH]_0 + b \quad (E-3)$$

where a and b are slope and intercept of the calibration curve, respectively.

Adding the effect of ADO, the relationship between peak height and the concentration of cysteamine becomes

$$H = a([\text{CSH}]_0 - t_s \cdot c[\text{CSH}]_0) + b = a(1 - t_s \cdot c)[S]_0 + b \quad (\text{E-4})$$

Where t_s is the average reaction time that the substrate spends interacting with the OHSCs during electroosmotic perfusion. It is clearly that peak height is still directly proportional to $[\text{CSH}]_0$ but with a modified slope in comparison to E-4. Therefore, if the calibration curve is established using the same conditions as that for the actual measurement (e.g. both are affected by the ADO), the analyte concentration read from the calibration curve reflects the value before a small portion of this compound is oxidized by ADO.

APPENDIX F

CALIBRATION CURVES USED IN THE METABOLISM OF COA AND TWO DRUG COMPOUNDS

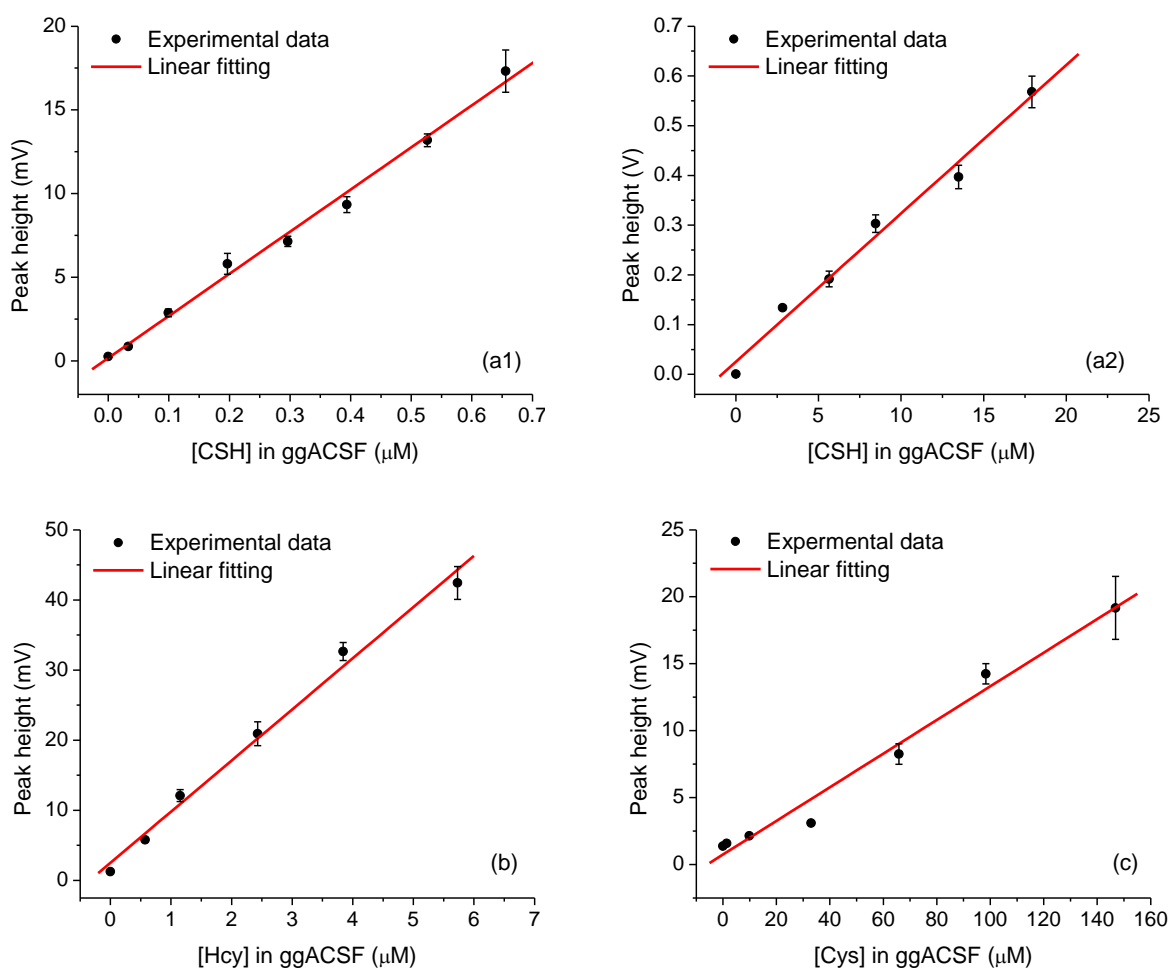


Figure F-1. Calibration curves CSH, Hcy and Cys

Table F-1. Linear fitting results for the calibration curves of CSH, Hcy and Cys

	CSH (low conc.)	CSH (high conc.)	Hcy	Cys
Slope (V/mV)	2.52×10^1	2.98×10^{-2}	7.29	1.26×10^{-1}
Slope SD (V/mV)	0.09×10^1	0.18×10^{-2}	0.36	0.08×10^{-1}
Intercept (V)	1.66×10^{-4}	2.52×10^{-2}	2.50×10^{-3}	7.39×10^{-4}
Intercept SD (V)	3.06×10^{-4}	1.79×10^{-2}	1.10×10^{-3}	5.78×10^{-4}
Adjusted R ²	0.99	0.98	0.99	0.98

APPENDIX G

ABBREVIATION LIST

ACSF	artificial cerebrospinal fluid	GSH	reduced glutathione
ADO	cysteamine dioxygenase	GSSG	oxidized glutathione
APD	avalanched photodiode	γ GT	γ -glutamyl transpeptidase
ATP	adenosine triphosphate	Hcy	homocysteine
BR/RR/SR/WR	buffer/reagent/sample/waste reservoir	LIF	laser induced fluorescence
CDO	cysteine dioxygenase	LOC	Lab on chip
CE	capillary electrophoresis	NADPH	β -nicotinamide adenine dinucleotide phosphate, reduced form
CoA	coenzyme A	NMDA	N-methyl-D-aspartate
CSH	cysteamine	OHSCs	organotypic hippocampal slice cultures
CSSC	cystamine	PD	photodiode
Cys	cysteine	PMT	Photomultiplier tube
CysGly	cysteinyglycine	PSH	pantetheine
1, 6-DAH	1, 6-diaminhexane	PSSP	pantethine
DPCPX	8-cyclopentyl-1, 3-dipropylxanthine	QE	quantum efficiencies
ggACSF	gly-gly modified ACSF	ROS	reactive oxygen species
Gly	glycine	RSSC/RSSP	mixed disulfide with CSH/ PSH
Gly-Gly	glycylglycine	SD	standard deviation
γ GluCys	γ -glutamylcysteine	SEM	standard error of the mean
GND	ground	μ TAS	miniaturized total analysis systems
GPx	glutathione peroxidase		
GR	glutathione reductase		

BIBLIOGRAPHY

- [1] Stipanuk MH (2004) Sulfur amino acid metabolism: Pathways for production and removal of homocysteine and cysteine. *Annu. Rev. Nutr.* 24:539-577.
- [2] Townsend DM, Tew KD, & Tapiero H (2004) Sulfur containing amino acids and human disease. *Biomed. Pharmacother.* 58(1):47-55.
- [3] Dringen R, Gutterer JM, & Hirrlinger J (2000) Glutathione metabolism in brain - metabolic interaction between astrocytes and neurons in the defense against reactive oxygen species. *Eur. J. Biochem.* 267(16):4912-4916.
- [4] Pastore A, Federici G, Bertini E, & Piemonte F (2003) Analysis of glutathione: Implication in redox and detoxification. *Clin. Chim. Acta* 333(1):19-39.
- [5] Wilson JX (1997) Antioxidant defense of the brain: A role for astrocytes. *Can. J. Physiol. Pharmacol.* 75(10-11):1149-1163.
- [6] Contestabile A (2001) Antioxidant strategies for neurodegenerative diseases. *Expert Opin. Ther. Pat.* 11(4):573-585.
- [7] Slemmer JE, Shacka JJ, Sweeney MI, & Weber JT (2008) Antioxidants and free radical scavengers for the treatment of stroke, traumatic brain injury and aging. *Curr. Med. Chem.* 15(4):404-414.
- [8] Ramirez A, *et al.* (2007) Extracellular cysteine/cystine redox potential controls lung fibroblast proliferation and matrix expression through upregulation of transforming growth factor-beta. *Am. J. Physiol.-Lung Cell. Mol. Physiol.* 293(4):L972-L981.
- [9] Forman HJ, Zhang H, & Rinna A (2009) Glutathione: Overview of its protective roles, measurement, and biosynthesis. *Mol. Asp. Med.* 30(1-2):1-12.
- [10] Dringen R (2000) Metabolism and functions of glutathione in brain. *Prog. Neurobiol.* 62(6):649-671.
- [11] Dringen R & Hamprecht B (1998) Glutathione restoration as indicator for cellular metabolism of astroglial cells. (Translated from English) *Dev. Neurosci.* 20(4-5):401-407 (in English).

- [12] Rice ME & Russo-Menna I (1997) Differential compartmentalization of brain ascorbate and glutathione between neurons and glia. *Neuroscience* 82(4):1213-1223.
- [13] Cooper AJ (1998) Role of astrocytes in maintaining cerebral glutathione homeostasis and in protecting the brain against xenobiotics and oxidative stress. *Glutathione in the nervous system*, ed Shaw CA (Taylor & Francis, Washington DC), pp 91-115.
- [14] Lu SC (2009) Regulation of glutathione synthesis. *Mol. Asp. Med.* 30(1–2):42-59.
- [15] Morgan B, *et al.* (2013) Multiple glutathione disulfide removal pathways mediate cytosolic redox homeostasis. *Nat. Chem. Biol.* 9(2):119-125.
- [16] Jones DP (2002) Redox potential of gsh/gssg couple: Assay and biological significance. *Methods enzymol.*, eds Helmut S & Lester P (Academic Press), Vol 348, pp 93-112.
- [17] Meister A (1994) Glutathione ascorbic-acid antioxidant system in animals. *J. Biol. Chem.* 269(13):9397-9400.
- [18] Rice ME, Perezpinzon MA, & Lee EJK (1994) Ascorbic-acid, but not glutathione, is taken up by brain-slices and preserves cell morphology. *J. Neurophysiol.* 71(4):1591-1596.
- [19] Swanson RA, Ying W, & Kauppinen TM (2004) Astrocyte influences on ischemic neuronal death. *Curr. Mol. Med.* 4(2):193-205.
- [20] Cooper AJL & Kristal BS (1997) Multiple roles of glutathione in the central nervous system. *Biol. Chem.* 378(8):793-802.
- [21] Meister A & Anderson ME (1983) Glutathione. *Annu. Rev. Biochem* 52:711-760.
- [22] Cotgreave IA & Gerdes RG (1998) Recent trends in glutathione biochemistry - glutathione-protein interactions: A molecular link between oxidative stress and cell proliferation? *Biochem. Biophys. Res. Commun.* 242(1):1-9.
- [23] Moriarty-Craige SE & Jones DP (2004) Extracellular thiols and thiol/disulfide redox in metabolism. *Annu. Rev. Nutr.* 24:481-509.
- [24] Shih AY, *et al.* (2006) Cystine/glutamate exchange modulates glutathione supply for neuroprotection from oxidative stress and cell proliferation. *J. Neurosci.* 26(41):10514-10523.
- [25] Filomeni G, Aquilano K, Rotilio G, & Ciriolo MR (2005) Glutathione-related systems and modulation of extracellular signal-regulated kinases are involved in the resistance of ags adenocarcinoma gastric cells to diallyl disulfide-induced apoptosis. *Cancer Res.* 65(24):11735-11742.
- [26] Sies H (1999) Glutathione and its role in cellular functions. *Free Radical Biol. Med.* 27(9-10):916-921.

- [27] Hall AG (1999) Glutathione and the regulation of cell death. *Drug resistance in leukemia and lymphoma*, Advances in experimental medicine and biology, eds Kaspers GJL, Pieters R, & Veerman AJP (Kluwer Academic Publishers, Dordrecht), Vol III, pp 199-203.
- [28] Schafer FQ & Buettner GR (2001) Redox environment of the cell as viewed through the redox state of the glutathione disulfide/glutathione couple. *Free Radical Biol. Med.* 30(11):1191-1212.
- [29] Lada MW & Kennedy RT (1997) In vivo monitoring of glutathione and cysteine in rat caudate nucleus using microdialysis on-line with capillary zone electrophoresis-laser induced fluorescence detection. *J. Neurosci. Methods* 72(2):153-159.
- [30] Yang CS, *et al.* (1994) Determination of extracellular glutathione in rat-brain by microdialysis and high-performance liquid-chromatography with fluorescence detection. *J Chromatogr B Biomed Appl.* 661(2):231-235.
- [31] Dringen R & Hirrlinger J (2003) Glutathione pathways in the brain. *Biol. Chem.* 384(4):505-516.
- [32] Orwar O, *et al.* (1994) Increased intracellular and extracellular concentrations of gamma-glutamylglutamate and related dipeptides in the ischemic rat striatum - involvement of beta-glutamyl transpeptidase. *J. Neurochem.* 63(4):1371-1376.
- [33] Li XY, Orwar O, Revesjo C, & Sandberg M (1996) Gamma-glutamyl peptides and related amino acids in rat hippocampus in vitro: Effect of depolarization and gamma-glutamyl transpeptidase inhibition. *Neurochem. Int.* 29(2):121-128.
- [34] Li XY, Wallin C, Weber SG, & Sandberg M (1999) Net efflux of cysteine, glutathione and related metabolites from rat hippocampal slices during oxygen/glucose deprivation: Dependence on gamma-glutamyl transpeptidase. *Brain Res.* 815(1):81-88.
- [35] Varga V, Jenei Z, Janaky R, Saransaari P, & Oja SS (1997) Glutathione is an endogenous ligand of rat brain n-methyl-d-aspartate (nmda) and 2-amino-3-hydroxy-5-methyl-4-isoxazolepropionate (ampa) receptors. *Neurochem. Res.* 22(9):1165-1171.
- [36] Ogita K, Enomoto R, Nakahara F, Ishitsubo N, & Yoneda Y (1995) A possible role of glutathione as an endogenous agonist at the n-methyl-d-aspartate recognition domain in rat-brain. *J. Neurochem.* 64(3):1088-1096.
- [37] Wallin C, *et al.* (2003) Searching for mechanisms of n-methyl-d-aspartate-induced glutathione efflux in organotypic hippocampal cultures. *Neurochem. Res.* 28(2):281-291.
- [38] Robillard JM, Gordon GR, Choi HB, Christie BR, & MacVicar BA (2011) Glutathione restores the mechanism of synaptic plasticity in aged mice to that of the adult. *PLoS One* 6(5):e20676.

- [39] Anderson ME, Underwood M, Bridges RJ, & Meister A (1989) Glutathione metabolism at the blood-cerebrospinal fluid barrier. *The FASEB Journal* 3:2527-2531.
- [40] Landolt H, *et al.* (1992) Extracellular antioxidants and amino-acids in the cortex of the rat - monitoring by microdialysis of early ischemic changes. *Journal of Cerebral Blood Flow and Metabolism* 12(1):96-102.
- [41] Juurlink BHJ (1997) Response of glial cells to ischemia: Roles of reactive oxygen species and glutathione. *Neuroscience and Biobehavioral Reviews* 21(2):151-166.
- [42] Bains JS & Shaw CA (1997) Neurodegenerative disorders in humans: The role of glutathione in oxidative stress-mediated neuronal death. *Brain Res. Rev.* 25(3):335-358.
- [43] Benzi G & Moretti A (1995) Are reactive oxygen species involved in alzheimers-disease. *Neurobiol. Aging* 16(4):661-674.
- [44] Do KQ, *et al.* (2000) Schizophrenia: Glutathione deficit in cerebrospinal fluid and prefrontal cortex in vivo. *Eur. J. Neurosci.* 12(10):3721-3728.
- [45] Richman PG & Meister A (1975) Regulation of gamma-glutamyl-cysteine synthetase by nonallosteric feedback inhibition by glutathione. *J. Biol. Chem.* 250(4):1422-1426.
- [46] Wang XF & Cynader MS (2000) Astrocytes provide cysteine to neurons by releasing glutathione. *J. Neurochem.* 74(4):1434-1442.
- [47] Chen YM, *et al.* (2001) Astrocytes protect neurons from nitric oxide toxicity by a glutathione-dependent mechanism. *J. Neurochem.* 77(6):1601-1610.
- [48] Hertz L & Zielke HR (2004) Astrocytic control of glutamatergic activity: Astrocytes as stars of the show. *Trends Neurosci.* 27(12):735-743.
- [49] Kranich O, Dringen R, Sandberg M, & Hamprecht B (1998) Utilization of cysteine and cysteine precursors for the synthesis of glutathione in astroglial cultures: Preference for cystine. *Glia* 22(1):11-18.
- [50] Dringen R, Pfeiffer B, & Hamprecht B (1999) Synthesis of the antioxidant glutathione in neurons: Supply by astrocytes of cysgly as precursor for neuronal glutathione. *J. Neurosci.* 19(2):562-569.
- [51] Kranich O, Hamprecht B, & Dringen R (1996) Different preferences in the utilization of amino acids for glutathione synthesis in cultured neurons and astroglial cells derived from rat brain. *Neurosci. Lett.* 219(3):211-214.
- [52] Dringen R, Gutterer JM, Gros C, & Hirrlinger J (2001) Aminopeptidase n mediates the utilization of the gsh precursor cysgly by cultured neurons. *J. Neurosci. Res.* 66(5):1003-1008.

- [53] Dringen R, Kussmaul L, & Hamprecht B (1998) Rapid clearance of tertiary butyl hydroperoxide by cultured astroglial cells via oxidation of glutathione. *Glia* 23(2):139-145.
- [54] Salinas AE & Wong MG (1999) Glutathione s-transferases - a review. *Curr. Med. Chem.* 6(4):279-309.
- [55] Awasthi YC, Sharma R, & Singhal SS (1994) Human glutathione s-transferases. *Int. J. Biochem.* 26(3):295-308.
- [56] Rushmore TH & Pickett CB (1993) Glutathione s-transferases, structure, regulation, and therapeutic implications. *J. Biol. Chem.* 268(16):11475-11478.
- [57] Juurlink BHJ, Schultke E, & Hertz L (1996) Glutathione release and catabolism during energy substrate restriction in astrocytes. *Brain Res.* 710(1-2):229-233.
- [58] Sagara JI, Makino N, & Bannai S (1996) Glutathione efflux from cultured astrocytes. *J. Neurochem.* 66(5):1876-1881.
- [59] Hirrlinger J, Schulz JB, & Dringen R (2002) Effects of dopamine on the glutathione metabolism of cultured astroglial cells: Implications for parkinson's disease. *J. Neurochem.* 82(3):458-467.
- [60] Stridh MH, Tranberg M, Weber SG, Blomstrand F, & Sandberg M (2008) Stimulated efflux of amino acids and glutathione from cultured hippocampal slices by omission of extracellular calcium - likely involvement of connexin hemichannels. *J. Biol. Chem.* 283(16):10347-10356.
- [61] Hirrlinger J, Schulz JB, & Dringen R (2002) Glutathione release from cultured brain cells: Multidrug resistance protein 1 mediates the release of gsh from rat astroglial cells. *J. Neurosci. Res.* 69(3):318-326.
- [62] Stewart VC, *et al.* (2002) Preservation of extracellular glutathione by an astrocyte derived factor with properties comparable to extracellular superoxide dismutase. *J. Neurochem.* 83(4):984-991.
- [63] Hirrlinger J, *et al.* (2001) The multidrug resistance protein mrp1 mediates the release of glutathione disulfide from rat astrocytes during oxidative stress. *J. Neurochem.* 76(2):627-636.
- [64] Minich T, *et al.* (2006) The multidrug resistance protein 1 (mrp1), but not mrp5, mediates export of glutathione and glutathione disulfide from brain astrocytes. *J. Neurochem.* 97(Copyright (C) 2013 American Chemical Society (ACS). All Rights Reserved.):373-384.
- [65] Leonardi R, Zhang YM, Rock CO, & Jackowski S (2005) Coenzyme a: Back in action. *Prog. Lipid Res.* 44(2-3):125-153.

- [66] Tokutake Y, Onizawa N, Katoh H, Toyoda A, & Chohnan S (2010) Coenzyme a and its thioester pools in fasted and fed rat tissues. *Biochem. Biophys. Res. Commun.* 402(1):158-162.
- [67] Deutsch J, Rapoport SI, & Rosenberger TA (2002) Coenzyme a and short-chain acyl-coa species in control and ischemic rat brain. *Neurochem. Res.* 27(12):1577-1582.
- [68] Robishaw JD & Neely JR (1985) Coenzyme a metabolism. *Am. J. Physiol. Endocrinol. Metabol.* 248(1):E1-E9.
- [69] Pinto JT, *et al.* (2009) Measurement of sulfur-containing compounds involved in the metabolism and transport of cysteamine and cystamine. Regional differences in cerebral metabolism. *J. Chromatogr. B: Anal. Technol. Biomed. Life Sci.* 877(28):3434-3441.
- [70] Dominy J, *et al.* (2007) Discovery and characterization of a second mammalian thiol dioxygenase, cysteamine dioxygenase. *J. Biol. Chem.* 282(35):25189-25198.
- [71] Gibrat C & Cicchetti F (2011) Potential of cystamine and cysteamine in the treatment of neurodegenerative diseases. *Prog. Neuro-Psychopharmacol. Biol. Psychiatry* 35(2):380-389.
- [72] Ida S, Tanaka Y, Ohkuma S, & Kuriyama K (1984) Determination of cystamine by high-performance liquid chromatography. *Anal. Biochem.* 136(2):352-356.
- [73] Pinto JT, *et al.* (2005) Treatment of yac128 mice and their wild-type littermates with cystamine does not lead to its accumulation in plasma or brain: Implications for the treatment of huntington disease. *J. Neurochem.* 94(4):1087-1101.
- [74] Ogony J, Mare S, Wu W, & Ercal N (2006) High performance liquid chromatography analysis of 2-mercaptoethylamine (cysteamine) in biological samples by derivatization with n-(1-pyrenyl) maleimide (npm) using fluorescence detection. *J. Chromatogr. B: Anal. Technol. Biomed. Life Sci.* 843(1):57-62.
- [75] Lewerenz J, Maher P, & Methner A (2012) Regulation of xct expression and system x(c)(-) function in neuronal cells. (Translated from English) *Amino Acids* 42(1):171-179 (in English).
- [76] Eskelinen EL, Tanaka Y, & Saftig P (2003) At the acidic edge: Emerging functions for lysosomal membrane proteins. *Trends Cell Biol.* 13(3):137-145.
- [77] Bannai S (1984) Transport of cystine and cysteine in mammalian cells. *Biochim. Biophys. Acta.* 779(3):289-306.
- [78] Janaky R, Varga V, Hermann A, Saransaari P, & Oja SS (2000) Mechanisms of l-cysteine neurotoxicity. *Neurochem. Res.* 25(9-10):1397-1405.

- [79] Tesseraud S, Metayer-Coustard S, Collin A, & Seiliez I (2009) Role of sulfur amino acids in controlling nutrient metabolism and cell functions: Implications for nutrition. *Br. J. Nutr.* 101(8):1132-1139.
- [80] Brosnan JT & Brosnan ME (2006) The sulfur-containing amino acids: An overview. *J. Nutr.* 136(6):1636S-1640S.
- [81] Jonas CR, Ziegler TR, Gu LiH, & Jones DP (2002) Extracellular thiol/disulfide redox state affects proliferation rate in a human colon carcinoma (caco2) cell line. *Free Radical Biol. Med.* 33(11):1499-1506.
- [82] Jones DP, *et al.* (2000) Redox state of glutathione in human plasma. *Free Radical Biol. Med.* 28(4):625-635.
- [83] Wu G, Fang Y-Z, Yang S, Lupton JR, & Turner ND (2004) Glutathione metabolism and its implications for health. *J. Nutr.* 134(3):489-492.
- [84] Lash LH & Jones DP (1985) Distribution of oxidized and reduced forms of glutathione and cysteine in rat plasma. *Arch. Biochem. Biophys.* 240(2):583-592.
- [85] Iyer SS, Jones DP, Brigham KL, & Rojas M (2009) Oxidation of plasma cysteine/cystine redox state in endotoxin-induced lung injury. (Translated from English) *Am. J. Respir. Cell Mol. Biol.* 40(1):90-98 (in English).
- [86] Medina MÁ, Urdiales JL, & Amores-Sánchez MI (2001) Roles of homocysteine in cell metabolism. *Eur. J. Biochem.* 268(14):3871-3882.
- [87] Nekrassova O, Lawrence NS, & Compton RG (2003) Analytical determination of homocysteine: A review. *Talanta* 60(6):1085-1095.
- [88] Stipanuk MH, Dominy JE, Lee J-I, & Coloso RM (2006) Mammalian cysteine metabolism: New insights into regulation of cysteine metabolism. *J. Nutr.* 136(6):1652S-1659S.
- [89] Spry C, Kirk K, & Saliba KJ (2008) Coenzyme a biosynthesis: An antimicrobial drug target. *FEMS Microbiol. Rev.* 32(1):56-106.
- [90] Stipanuk MH (1986) Metabolism of sulfur-containing amino-acids. *Annu. Rev. Nutr.* 6:179-209.
- [91] Selhub J (1999) Homocysteine metabolism. *Annu. Rev. Nutr.* 19:217-246.
- [92] Banjac A, *et al.* (2008) The cystine/cysteine cycle: A redox cycle regulating susceptibility versus resistance to cell death. *Oncogene* 27(11):1618-1628.
- [93] Camera E & Picardo M (2002) Analytical methods to investigate glutathione and related compounds in biological and pathological processes. *J. Chromatogr. B: Anal. Technol. Biomed. Life Sci.* 781(1-2):181-206.

- [94] Kuster A, *et al.* (2008) Simultaneous determination of glutathione and cysteine concentrations and h-2 enrichments in microvolumes of neonatal blood using gas chromatography-mass spectrometry. *Anal. Bioanal. Chem.* 390(5):1403-1412.
- [95] Hogan BL & Yeung ES (1992) Determination of intracellular species at the level of a single erythrocyte via capillary electrophoresis with direct and indirect fluorescence detection. *Anal. Chem.* 64(22):2841-2845.
- [96] Gao J, Yin XF, & Fang ZL (2004) Integration of single cell injection, cell lysis, separation and detection of intracellular constituents on a microfluidic chip. *Lab Chip* 4(1):47-52.
- [97] Ling YY, Yin XF, & Fang ZL (2005) Simultaneous determination of glutathione and reactive oxygen species in individual cells by microchip electrophoresis. *Electrophoresis* 26(24):4759-4766.
- [98] Carru C, Deiana L, Sotgia S, Pes GM, & Zinellu A (2004) Plasma thiols redox status by laser-induced fluorescence capillary electrophoresis. *Electrophoresis* 25(6):882-889.
- [99] Sakhi AK, Blomhoff R, & Gundersen TE (2007) Simultaneous and trace determination of reduced and oxidized glutathione in minute plasma samples using dual mode fluorescence detection and column switching high performance liquid chromatography. *J. Chromatogr. A* 1142(2):178-184.
- [100] Nozal MJ, *et al.* (1997) Determination of glutathione, cysteine and n-acetylcysteine in rabbit eye tissues using high-performance liquid chromatography and post-column derivatization with 5,5'-dithiobis(2-nitrobenzoic acid). *J. Chromatogr. A* 778(1-2):347-353.
- [101] Wallin C, Weber SG, & Sandberg M (1999) Glutathione efflux induced by nmda and kainate: Implications in neurotoxicity? *J. Neurochem.* 73(4):1566-1572.
- [102] Chaurasia CS, *et al.* (2007) Aaps-fda workshop white paper: Microdialysis principles, application, and regulatory perspectives report from the joint aaps-fda workshop, november 4-5, 2005, nashville, tn. *Aaps Journal* 9(1):E48-E59.
- [103] Han JL, Cheng FC, Yang ZL, & Dryhurst G (1999) Inhibitors of mitochondrial respiration, iron (ii), and hydroxyl radical evoke release and extracellular hydrolysis of glutathione in rat striatum and substantia nigra, potential implications to parkinson's disease. *J. Neurochem.* 73(4):1683-1695.
- [104] Shi GY, *et al.* (1999) Determination of glutathione in vivo by microdialysis using liquid chromatography with a cobalt hexacyanoferrate chemically modified electrode. *Anal. Chim. Acta* 391(3):307-313.
- [105] Hamsher AE, Xu HJ, Guy Y, Sandberg M, & Weber SG (2010) Minimizing tissue damage in electroosmotic sampling. *Anal. Chem.* 82(15):6370-6376.

- [106] Xu HJ, *et al.* (2010) Electroosmotic sampling. Application to determination of ectopeptidase activity in organotypic hippocampal slice cultures. *Anal. Chem.* 82(15):6377-6383.
- [107] Monostori P, Wittmann G, Karg E, & Turi S (2009) Determination of glutathione and glutathione disulfide in biological samples: An in-depth review. *J. Chromatogr. B: Anal. Technol. Biomed. Life Sci.* 877(28):3331-3346.
- [108] Senft AP, Dalton TP, & Shertzer HG (2000) Determining glutathione and glutathione disulfide using the fluorescence probe o-phthalaldehyde. *Anal. Biochem.* 280(1):80-86.
- [109] Yoshida T (1996) Determination of reduced and oxidized glutathione in erythrocytes by high-performance liquid chromatography with ultraviolet absorbance detection. *J Chromatogr B Biomed Appl.* 678(2):157-164.
- [110] Wang SS, Hung Y-T, & Lin Y-C (2010) Kinetic studies of the oxidation of glutathione in protein refolding buffer. (Translated from English) *Bioprocess Biosystems Eng.* 33(2):277-286 (in English).
- [111] Abedinzadeh Z, Gardes-Albert M, & Ferradini C (1989) Kinetic study of the oxidation mechanism of glutathione by hydrogen peroxide in neutral aqueous medium. *Can. J. Chem.* 67(7):1247-1255.
- [112] Hanaki A, Kinoshita T, & Ozawa T (2000) Kinetic studies on the autoxidation of cysteine catalyzed by copper complexes: Catecholamines stimulate the autoxidation. *Bull. Chem. Soc. Jpn.* 73(1):73-80.
- [113] Hogg N (1999) The effect of cyst(e)ine on the auto-oxidation of homocysteine. *Free Radical Biol. Med.* 27(1-2):28-33.
- [114] Toyo'oka T (2009) Recent advances in separation and detection methods for thiol compounds in biological samples. *J. Chromatogr. B: Anal. Technol. Biomed. Life Sci.* 877(28):3318-3330.
- [115] Antwi C, Johnson AS, Selimovic A, & Martin RS (2011) Use of microchip electrophoresis and a palladium/mercury amalgam electrode for the separation and detection of thiols. *Anal. Methods* 3(5):1072-1078.
- [116] Shimada K & Mitamura K (1994) Derivatization of thiol-containing compounds. *J Chromatogr B Biomed Appl.* 659(1-2):227-241.
- [117] Karger BL, Snyder LR, & Horvath C (1973) *An introduction to separation science* (John Wiley & Sons, Inc, New York), pp 129-146; 501-505.
- [118] Kusmierk K, Chwatko G, Glowacki R, & Bald E (2009) Determination of endogenous thiols and thiol drugs in urine by hplc with ultraviolet detection. *J. Chromatogr. B: Anal. Technol. Biomed. Life Sci.* 877(28):3300-3308.

- [119] Landers JP (2008) *Handbook of capillary and microfluidic electrophoresis and associated microtechniques* (CRC Press, New York) 3rd Ed, pp 4-19.
- [120] Koesdjojo MT, Gonzalez CF, & Remcho VT (2008) Principles and practice of capillary electrochromatography. *Handbook of capillary and microchip electrophoresis and associated microtechniques*, ed Landers JP (CRC press, Boca Raton), 3rd Ed, pp 184-187.
- [121] Schwartz HE & Wanders BJ (1998) Capillary electrophoresis. *Handbook of hplc*, eds Katz E, Eksteen R, Schoenmakers P, & Miller N (Marcel Dekker, Inc., New York), Vol 78, pp 169-191.
- [122] Landers JP (2008) Introduction to capillary electrophoresis. *Handbook of capillary and microchip electrophoresis and associated microtechniques*, ed Landers JP (CRC press, Boca Raton), 3rd Ed, pp 7-8.
- [123] Zinellu A, *et al.* (2007) Protein-bound glutathione measurement in cultured cells by cze with lif detection. *Electrophoresis* 28(18):3277-3283.
- [124] Lada MW & Kennedy RT (1995) Quantitative in vivo measurements using microdialysis on-line with capillary zone electrophoresis. *J. Neurosci. Methods* 63(1-2):147-152.
- [125] Tietze F (1969) Enzymic method for quantitative determination of nanogram amounts of total and oxidized glutathione: Applications to mammalian blood and other tissues. *Anal. Biochem.* 27(3):502-522.
- [126] Liang SC, Wang H, Zhang ZM, Zhang X, & Zhang HS (2002) Direct spectrofluorimetric determination of glutathione in biological samples using 5-maleimidyl-2-(m-methylphenyl) benzoxazole. *Anal. Chim. Acta* 451(2):211-219.
- [127] Albrecht SC, Barata AG, Grosshans J, Teleman AA, & Dick TP (2011) In vivo mapping of hydrogen peroxide and oxidized glutathione reveals chemical and regional specificity of redox homeostasis. *Cell Metab.* 14(Copyright (C) 2013 American Chemical Society (ACS). All Rights Reserved.):819-829.
- [128] Morgan B, Sobotta MC, & Dick TP (2011) Measuring egsh and h2o2 with rogfp2-based redox probes. *Free Radical Biol. Med.* 51(Copyright (C) 2013 American Chemical Society (ACS). All Rights Reserved.):1943-1951.
- [129] Back P, *et al.* (2012) Exploring real-time in vivo redox biology of developing and aging caenorhabditis elegans. *Free Radical Biol. Med.* 52(Copyright (C) 2013 American Chemical Society (ACS). All Rights Reserved.):850-859.
- [130] Meyer AJ, *et al.* (2007) Redox-sensitive gfp in arabidopsis thaliana is a quantitative biosensor for the redox potential of the cellular glutathione redox buffer. *Plant J.* 52(5):973-986.

- [131] Inoue T & Kirchhoff JR (2000) Electrochemical detection of thiols with a coenzyme pyrroloquinoline quinone modified electrode. *Anal. Chem.* 72(23):5755-5760.
- [132] Joshi KA, Pandey PC, Chen W, & Mulchandani A (2004) Ormosil encapsulated pyrroloquinoline quinone-modified electrochemical sensor for thiols. *Electroanalysis* 16(23):1938-1943.
- [133] Trabesinger AH & Boesiger P (2001) Improved selectivity of double quantum coherence filtering for the detection of glutathione in the human brain in vivo. *Magn. Reson. Med.* 45(4):708-710.
- [134] Kennett EC, Bubb WA, Bansal P, Alewood P, & Kuchel PW (2005) Nmr studies of exchange between intra- and extracellular glutathione in human erythrocytes. *Redox Rep* 10(2):83-90.
- [135] Manz A, Graber N, & Widmer HM (1990) Miniaturized total chemical-analysis systems - a novel concept for chemical sensing. *Sens. Actuators, B* 1(1-6):244-248.
- [136] Tabeling P (2005) *Introduction to microfluidics* (Oxford University Press, New York); trans Chen S, pp 1-68.
- [137] Reyes DR, Iossifidis D, Auroux PA, & Manz A (2002) Micro total analysis systems. 1. Introduction, theory, and technology. *Anal. Chem.* 74(12):2623-2636.
- [138] Auroux PA, Iossifidis D, Reyes DR, & Manz A (2002) Micro total analysis systems. 2. Analytical standard operations and applications. *Anal. Chem.* 74(12):2637-2652.
- [139] Vilckner T, Janasek D, & Manz A (2004) Micro total analysis systems. Recent developments. *Anal. Chem.* 76(12):3373-3385.
- [140] Dittrich PS, Tachikawa K, & Manz A (2006) Micro total analysis systems. Latest advancements and trends. *Anal. Chem.* 78(12):3887-3907.
- [141] Hansen EH & Wang JH (2004) The three generations of flow injection analysis. (Translated from English) *Anal. Lett.* 37(3):345-359 (in English).
- [142] Chen XG, Fan LY, & Hu Z (2004) The combination of flow injection with electrophoresis using capillaries and chips. *Electrophoresis* 25(23-24):3962-3969.
- [143] Reid VR & Synovec RE (2008) High-speed gas chromatography: The importance of instrumentation optimization and the elimination of extra-column band broadening. *Talanta* 76(4):703-717.
- [144] Probstein RF (1994) *Physicochemical hydrodynamics: An introduction, 2nd ed.* (John Wiley & Sons, Inc, New York), pp 53-103.
- [145] Kuban P & Dasgupta PK (2000) Capillary separations. *Kirk-othmer encyclopedia of chemical technology*, (John Wiley & Sons, Inc.), Vol 4, pp 602-647.

- [146] Kostal V, Katzenmeyer J, & Arriaga EA (2008) Capillary electrophoresis in bioanalysis. (Translated from English) *Anal. Chem.* 80(12):4533-4550 (in English).
- [147] Manz A, Harrison DJ, Verpoorte E, & Widmer HM (1993) Planar chips technology for miniaturization of separation systems - a developing perspective in chemical monitoring. *Adv. Chromatogr.* 33:1-66.
- [148] Bruus H (2008) *Theoretical microfluidics* (Oxford University Press, New York), pp 1-15.
- [149] Rios A, Escarpa A, & Simonet B (2009) *Miniaturization of analytical systems : Principles, designs and applications* (Wiley, Hoboken, NJ, USA), pp 165-208.
- [150] Uchiyama K, Nakajima H, & Hobo T (2004) Detection method for microchip separations. *Anal. Bioanal. Chem.* 379(3):375-382.
- [151] Johnson ME & Landers JP (2004) Fundamentals and practice for ultrasensitive laser-induced fluorescence detection in microanalytical systems. *Electrophoresis* 25(21-22):3513-3527.
- [152] Ingle JDJ & Crouch SR (1988) *Spectrochemical analysis* (Prentice Hall, Inc., Upper Saddle River), pp 98-105, 106-117, 135-161, 438-473.
- [153] Sandlin ZD, Shou MS, Shackman JG, & Kennedy RT (2005) Microfluidic electrophoresis chip coupled to microdialysis for in vivo monitoring of amino acid neurotransmitters. *Anal. Chem.* 77(23):7702-7708.
- [154] Ocvirk G, Tang T, & Harrison DJ (1998) Optimization of confocal epifluorescence microscopy for microchip-based miniaturized total analysis systems. *Analyst* 123(7):1429-1434.
- [155] Semwogerere D & Weeks ER (2005) Confocal microscopy. *Encyclopedia of biomaterials and biomedical engineering* eds Wnek G & Bowlin G (Taylor and Francis, London), pp 1-10.
- [156] Nicholson C & Tao L (1993) Hindered diffusion of high-molecular-weight compounds in brain extracellular microenvironment measured with integrative optical imaging. *Biophys. J.* 65(6):2277-2290.
- [157] Böhmer M & Enderlein J (2003) Fluorescence spectroscopy of single molecules under ambient conditions: Methodology and technology. *ChemPhysChem* 4(8):793-808.
- [158] Földes-Papp Z, Demel U, & Tilz GP (2003) Laser scanning confocal fluorescence microscopy: An overview. *Int. Immunopharmacol.* 3(13-14):1715-1729.
- [159] Prasad V, Semwogerere D, & Eric RW (2007) Confocal microscopy of colloids. *J. Phys.: Condens. Matter* 19(11):113102-113127.

- [160] Hewlett SJ & Wilson T (1991) Resolution enhancement in three-dimensional confocal microscopy. (Translated from English) *Machine Vis. Apps.* 4(4):233-242 (in English).
- [161] Wilson T (2011) Resolution and optical sectioning in the confocal microscope. *J. Microsc.* 244(2):113-121.
- [162] Ferrando M & Spiess WEL (2000) Review: Confocal scanning laser microscopy. A powerful tool in food science revision: Microscopía láser confocal de barrido. Una potente herramienta en la ciencia de los alimentos. *Food Sci. Technol. Int.* 6(4):267-284.
- [163] Paddock S (2000) Principles and practices of laser scanning confocal microscopy. (Translated from English) *Mol. Biotechnol.* 16(2):127-149 (in English).
- [164] Cox G (1993) Trends in confocal microscopy. *Micron* 24(3):237-247.
- [165] GASSMANN E, KUO JE, & ZARE RN (1985) Electrokinetic separation of chiral compounds. *Science* 230(4727):813 - 814.
- [166] Cheng Y-f & Dovichi NJ (1988) Subattomole amino acid analysis by capillary zone electrophoresis and laser-induced fluorescence. *Science* 242(4878):562-564.
- [167] Wu SL & Dovichi NJ (1989) High-sensitivity fluorescence detector for fluorescein isothiocyanate derivatives of amino-acids separated by capillary zone electrophoresis. *J. Chromatogr.* 480:141-155.
- [168] Peck K, Stryer L, Glazer AN, & Mathies RA (1989) Single-molecule fluorescence detection: Autocorrelation criterion and experimental realization with phycoerythrin. *Proc. Natl. Acad. Sci. USA* 86(11):4087-4091.
- [169] Mathies RA, Peck K, & Stryer L (1990) Optimization of high-sensitivity fluorescence detection. *Anal. Chem.* 62(17):1786-1791.
- [170] Hernandez L, Escalona J, Joshi N, & Guzman N (1991) Laser-induced fluorescence and fluorescence microscopy for capillary electrophoresis zone detection. *J. Chromatogr. A* 559(1-2):183-196.
- [171] Huang XC, Quesada MA, & Mathies RA (1992) DNA sequencing using capillary array electrophoresis. *Anal. Chem.* 64(18):2149-2154.
- [172] Nie S, Dadoo R, & Zare RN (1993) Ultrasensitive fluorescence detection of polycyclic aromatic hydrocarbons in capillary electrophoresis. *Anal. Chem.* 65(24):3571-3575.
- [173] Legendre BL, Moberg DL, Williams DC, & Soper SA (1997) Ultrasensitive near-infrared laser-induced fluorescence detection in capillary electrophoresis using a diode laser and avalanche photodiode. *J. Chromatogr. A* 779(1-2):185-194.

- [174] Jiang GF, Attiya S, Ocvirk G, Lee WE, & Harrison DJ (2000) Red diode laser induced fluorescence detection with a confocal microscope on a microchip for capillary electrophoresis. *Biosens. Bioelectron.* 14(10-11):861-869.
- [175] Gotz S & Karst U (2007) Wavelength-resolved fluorescence detector for microchip capillary electrophoresis separations. *Sensor Actuat. B-Chem* 123(1):622-627.
- [176] Fu JL, Fang Q, Zhang T, Jin XH, & Fang ZL (2006) Laser-induced fluorescence detection system for microfluidic chips based on an orthogonal optical arrangement. *Anal. Chem.* 78(11):3827-3834.
- [177] Hellmich W, Greif D, Pelargus C, Anselmetti D, & Ros A (2006) Improved native uv laser induced fluorescence detection for single cell analysis in poly(dimethylsiloxane) microfluidic devices. *J. Chromatogr. A* 1130(2):195-200.
- [178] Xu CX & Yin XF (2011) Continuous cell introduction and rapid dynamic lysis for high-throughput single-cell analysis on microfluidic chips with hydrodynamic focusing. *J. Chromatogr. A* 1218(5):726-732.
- [179] Sun Y & Yin XF (2006) Novel multi-depth microfluidic chip for single cell analysis. *J. Chromatogr. A* 1117(2):228-233.
- [180] Yu LF, *et al.* (2008) Simple, fast and high-throughput single-cell analysis on pdms microfluidic chips. *Electrophoresis* 29(24):5055-5060.
- [181] Xu CX, Wang M, & Yin XF (2011) Three-dimensional (3d) hydrodynamic focusing for continuous sampling and analysis of adherent cells. *Analyst* 136(19):3877-3883.
- [182] Qin JH, *et al.* (2005) Simultaneous and ultrarapid determination of reactive oxygen species and reduced glutathione in apoptotic leukemia cells by microchip electrophoresis. *Electrophoresis* 26(6):1155-1162.
- [183] Gao N, Li L, Shi ZK, Zhang XL, & Jin WR (2007) High-throughput determination of glutathione and reactive oxygen species in single cells based on fluorescence images in a microchannel. *Electrophoresis* 28(21):3966-3975.
- [184] Chen ZZ, *et al.* (2010) Potent method for the simultaneous determination of glutathione and hydrogen peroxide in mitochondrial compartments of apoptotic cells with microchip electrophoresis-laser induced fluorescence. *Anal. Chem.* 82(5):2006-2012.
- [185] Zhao SL, Li XT, & Liu YM (2009) Integrated microfluidic system with chemiluminescence detection for single cell analysis after intracellular labeling. *Anal. Chem.* 81(10):3873-3878.
- [186] Chen G, Zhang LY, & Wang J (2004) Miniaturized capillary electrophoresis system with a carbon nanotube microelectrode for rapid separation and detection of thiols. *Talanta* 64(4):1018-1023.

- [187] Vickers JA & Henry CS (2005) Simplified current decoupler for microchip capillary electrophoresis with electrochemical and pulsed amperometric detection. *Electrophoresis* 26(24):4641-4647.
- [188] Chand R, *et al.* (2013) Analytical detection of biological thiols in a microchip capillary channel. *Biosens. Bioelectron.* 40(1):362-367.
- [189] Pasas SA, Lacher NA, Davies MI, & Lunte SM (2002) Detection of homocysteine by conventional and microchip capillary electrophoresis/electrochemistry. *Electrophoresis* 23(5):759-766.
- [190] Miyaki K, Zeng HL, Nakagama T, & Uchiyama K (2007) Steady surface modification of polydimethylsiloxane microchannel and its application in simultaneous analysis of homocysteine and glutathione in human serum. *J. Chromatogr. A* 1166(1-2):201-206.
- [191] Guan Q, Noblitt SD, & Henry CS (2012) Electrophoretic separations in poly(dimethylsiloxane) microchips using a mixture of ionic and zwitterionic surfactants. *Electrophoresis* 33(2):379-387.
- [192] Zhao SL, Huang Y, Ye FG, Shi M, & Liu YM (2010) Determination of intracellular sulphhydryl compounds by microchip electrophoresis with selective chemiluminescence detection. *J. Chromatogr. A* 1217(36):5732-5736.
- [193] Gunasekara DB, Hulvey MK, & Lunte SM (2011) In-channel amperometric detection for microchip electrophoresis using a wireless isolated potentiostat. *Electrophoresis* 32(8):832-837.
- [194] Xu JJ, Peng Y, Bao N, Xia XH, & Chen HY (2005) Simple method for the separation and detection of native amino acids and the identification of electroactive and non-electroactive analytes. *J. Chromatogr. A* 1095(1-2):193-196.
- [195] Zeng HL, Li HF, Wang X, & Lin JM (2006) Development of a gel monolithic column polydimethylsiloxane microfluidic device for rapid electrophoresis separation. *Talanta* 69(1):226-231.
- [196] Huang Y, Zhao SL, Shi M, & Liang H (2011) A microchip electrophoresis strategy with online labeling and chemiluminescence detection for simultaneous quantification of thiol drugs. *J. Pharm. Biomed. Anal.* 55(5):889-894.
- [197] Kinsey JL (1977) Laser-induced fluorescence. *Annu. Rev. Phys. Chem.* 28:349-372.
- [198] Slater JB, Tedesco JM, Fairchild RC, & Lewis IR (2001) Handbook of raman spectroscopy: From the research laboratory to the process line. *Pract. Spectrosc.*, eds Lewis IR & Edwards HGM (Marcel Dekker, Inc, New York), pp 41-49.
- [199] Donati S (2006) Photomultipliers. *Wiley encyclopedia of biomedical engineering*, (John Wiley & Sons, Inc.), pp 1-17.

- [200] Lawrence WG, Varadi G, Entine G, Podniesinski E, & Wallace PK (2008) Enhanced red and near infrared detection in flow cytometry using avalanche photodiodes. *Cytometry Part A* 73A(8):767-776.
- [201] Kaufmann K (2005) Choosing your detector: Signal-to-noise ratio, active area, and cost requirements drive the choice of detectors. in *SPIE's OEMagazine*, pp 25-27.
- [202] Kasap S, Ruda H, & Boucher Y (2009) *Cambridge illustrated handbook of optoelectronics and photonics* (Cambridge University Press, Cambridge), pp 196-197.
- [203] Siegman AE (1993) Defining, measuring, and optimizing laser beam quality. *Proc. SPIE* 1868:2-12.
- [204] Self SA (1983) Focusing of spherical gaussian beams. *Appl. Opt.* 22(5):658-661.
- [205] Umer H & Muhammad Sabieh A (2010) Reducing noise by repetition: Introduction to signal averaging. *Eur. J. Phys.* 31(3):453.
- [206] Anonymous (2013) Analog sampling basics (white paper).
- [207] Morgan DM & Weber SG (1984) Noise and signal-to-noise ratio in electrochemical detectors. *Anal. Chem.* 56(13):2560-2567.
- [208] Aoyama K, Watabe M, & Nakaki T (2008) Regulation of neuronal glutathione synthesis. *J Pharmacol Sci* 108(3):227-238.
- [209] Yap LP, Garcia JV, Han D, & Cadenas E (2009) The energy-redox axis in aging and age-related neurodegeneration. *Adv. Drug Del. Rev.* 61(14):1283-1298.
- [210] Ballatori N, *et al.* (2009) Glutathione dysregulation and the etiology and progression of human diseases. *Biol. Chem.* 390(3):191-214.
- [211] Wallin C, Puka-Sundvall M, Hagberg H, Weber SG, & Sandberg M (2000) Alterations in glutathione and amino acid concentrations after hypoxia-ischemia in the immature rat brain. *Dev. Brain Res.* 125(1-2):51-60.
- [212] Kim D, Joe CO, & Han PL (2003) Extracellular and intracellular glutathione protects astrocytes from zn²⁺-induced cell death. *Neuroreport* 14(2):187-190.
- [213] Sofic E, Lange KW, Jellinger K, & Riederer P (1992) Reduced and oxidized glutathione in the substantia-nigra of patients with parkinsons-disease. *Neurosci. Lett.* 142(2):128-130.
- [214] Lakritz J, Plopper CG, & Buckpitt AR (1997) Validated high-performance liquid chromatography electrochemical method for determination of glutathione and glutathione disulfide in small tissue samples. *Anal. Biochem.* 247(1):63-68.

- [215] Orwar O, Fishman HA, Ziv NE, Scheller RH, & Zare RN (1995) Use of 2,3-naphthalenedicarboxaldehyde derivatization for single-cell analysis of glutathione by capillary electrophoresis and histochemical-localization ion by fluorescence microscopy. *Anal. Chem.* 67(23):4261-4268.
- [216] Winters RA, Zukowski J, Ercal N, Matthews RH, & Spitz DR (1995) Analysis of glutathione, glutathione disulfide, cysteine, homocysteine, and other biological thiols by high-performance liquid-chromatography following derivatization by n-(1-pyrenyl)maleimide. *Anal. Biochem.* 227(1):14-21.
- [217] Vegvari A & Hjerten S (2002) A hybrid microdevice for electrophoresis and electrochromatography using uv detection. *Electrophoresis* 23(20):3479-3486.
- [218] Parmentier C, Wellman M, Nicolas A, Siest G, & Leroy P (1999) Simultaneous measurement of reactive oxygen species and reduced glutathione using capillary electrophoresis and laser-induced fluorescence detection in cultured cell lines. *Electrophoresis* 20(14):2938-2944.
- [219] Toyo'oka T, Tanabe J, & Jinno H (2001) Determination of rat hepatocellular glutathione by reversed-phase liquid chromatography with fluorescence detection and cytotoxicity evaluation of environmental pollutants based on the concentration change. *Biomed. Chromatogr.* 15(4):240-247.
- [220] Kand'ar R, Zakova P, Lotkova H, Kucera O, & Cervinkova Z (2007) Determination of reduced and oxidized glutathione in biological samples using liquid chromatography with fluorimetric detection. *J. Pharm. Biomed. Anal.* 43(4):1382-1387.
- [221] Kamencic H, Lyon A, Paterson PG, & Juurlink BHJ (2000) Monochlorobimane fluorometric method to measure tissue glutathione. *Anal. Biochem.* 286(1):35-37.
- [222] Nolin TD, McMenamin ME, & Himmelfarb J (2007) Simultaneous determination of total homocysteine, cysteine, cysteinylglycine, and glutathione in human plasma by high-performance liquid chromatography: Application to studies of oxidative stress. *J. Chromatogr., B: Anal. Technol. Biomed. Life Sci.* 852(1-2):554-561.
- [223] Yang JR & Langmuir ME (1991) Synthesis and properties of a maleimide fluorescent thiol reagent derived from a naphthopyranone. *J. Heterocycl. Chem.* 28(5):1177-1180.
- [224] Storey BT, Alvarez JG, & Thompson KA (1998) Human sperm glutathione reductase activity in situ reveals limitation in the glutathione antioxidant defense system due to supply of nadph. *Mol. Reprod. Dev* 49(4):400-407.
- [225] Kagan VE, *et al.* (2001) Pro-oxidant and antioxidant mechanisms of etoposide in hl-60 cells: Role of myeloperoxidase. *Cancer Res.* 61(21):7777-7784.
- [226] Agarwal A, Zudans I, Orwar O, & Weber SG (2007) Simultaneous maximization of cell permeabilization and viability in single-cell electroporation using an electrolyte-filled capillary. *Anal. Chem.* 79(1):161-167.

- [227] Lantz RC, Lemus R, Lange RW, & Karol MH (2001) Rapid reduction of intracellular glutathione in human bronchial epithelial cells exposed to occupational levels of toluene diisocyanate. *Toxicol. Sci.* 60(2):348-355.
- [228] Penugonda S, Wu W, Mare S, & Ercal N (2004) Liquid chromatography analysis of n-(2-mercaptopropionyl)-glycine in biological samples by thioglo (tm) 3 derivatization. *J. Chromatogr. B: Anal. Technol. Biomed. Life Sci.* 807(2):251-256.
- [229] Massey V & Williams CH, Jr. (1965) On the reaction mechanism of yeast glutathione reductase. *J. Biol. Chem.* 240(11):4470-4480.
- [230] Tandogan B & Ulusu NN (2006) Kinetic mechanism and molecular properties of glutathione reductase. *FABAD Journal of Pharmaceutical Sciences* 31:230-237.
- [231] Mannervik B (1973) A branching reaction mechanism of glutathione reductase. *Biochem. Biophys. Res. Commun.* 53(4):1151-1158.
- [232] Montero S, de Arriaga D, Busto F, & Soler J (1990) A study of the kinetic mechanism followed by glutathione reductase from mycelium of phycomyces blakesleeanus. *Arch. Biochem. Biophys.* 278(1):52-59.
- [233] Racker E (1955) Glutathione reductase from bakers' yeast and beef liver. *J. Biol. Chem.* 217(2):855-866.
- [234] Jacobson SC, Ermakov SV, & Ramsey JM (1999) Minimizing the number of voltage sources and fluid reservoirs for electrokinetic valving in microfluidic devices. *Anal. Chem.* 71(15):3273-3276.
- [235] Pei J, *et al.* (2008) Microfabricated channel array electrophoresis for characterization and screening of enzymes using rgs-g protein interactions as a model system. *Anal. Chem.* 80(13):5225-5231.
- [236] Anonymous (General information and usage guidelines of thioglo).
- [237] Beutler E, Srivastava SK, & West C (1970) The reversibility of n-ethylmaleimide (nem) alkylation of red cell glutathione. *Biochem. Biophys. Res. Commun.* 38(2):341-347.
- [238] Jacobson SC, Koutny LB, Hergenroder R, Moore AW, & Ramsey JM (1994) Microchip capillary electrophoresis with an integrated postcolumn reactor. *Anal. Chem.* 66(20):3472-3476.
- [239] Wenclawiak BW & Puschl R (2006) Sample injection for capillary electrophoresis on a micro fabricated device/on chip ce injection. *Anal. Lett.* 39(1):3-16.
- [240] Slentz BE, Penner NA, & Regnier F (2002) Sampling bias at channel junctions in gated flow injection on chips. *Anal. Chem.* 74(18):4835-4840.

- [241] Du H, Fuh RCA, Li JZ, Corkan LA, & Lindsey JS (1998) Photochemcad: A computer-aided design and research tool in photochemistry. *Photochem. Photobiol.* 68(2):141-142.
- [242] Landers JP, Oda RP, Madden BJ, & Spelsberg TC (1992) High-performance capillary electrophoresis of glycoproteins - the use of modifiers of electroosmotic flow for analysis of microheterogeneity. *Anal. Biochem.* 205(1):115-124.
- [243] Watson E & Yao F (1993) Capillary electrophoretic separation of human recombinant erythropoietin (rhuepo) glycoforms. *Anal. Biochem.* 210(2):389-393.
- [244] Mize CE & Langdon RG (1962) Hepatic glutathione reductase. I. Purification and general kinetic properties. *J. Biol. Chem.* 237(5):1589-1595.
- [245] Staal GEJ & Veeger C (1969) The reaction mechanism of glutathione reductase from human erythrocytes. *Biochim. Biophys. Acta. Enzymol.* 185(1):49-62.
- [246] Lopez-Barea J & Lee C (1979) Mouse liver glutathione reductase. *Eur. J. Biochem.* 98:487-499.
- [247] Savvides SN & Karplus PA (1996) Kinetics and crystallographic analysis of human glutathione reductase in complex with a xanthene inhibitor. *J. Biol. Chem.* 271(14):8101-8107.
- [248] Ulusu NN & Tandogan B (2007) Purification and kinetic properties of glutathione reductase from bovine liver. *Mol. Cell. Biochem.* 303(1-2):45-51.
- [249] Jin WR & Chen HF (2000) A new method of determination of diffusion coefficients using capillary zone electrophoresis (peak-height method). *Chromatographia* 52(1-2):17-21.
- [250] Segel IH (1975) *Enzyme kinetics, behavior and analysis of rapid equilibrium and steady-state enzyme systems* (John Wiley & Sons, New York) 1st Ed, pp 1-29; pp 136-143.
- [251] Mavis RD & Stellwagen E (1968) Purification and subunit structure of glutathione reductase from bakers' yeast. *J. Biol. Chem.* 243(4):809-814.
- [252] Cellar NA, Burns ST, Meiners JC, Chen H, & Kennedy RT (2005) Microfluidic chip for low-flow push-pull perfusion sampling in vivo with on-line analysis of amino acids. *Anal. Chem.* 77(21):7067-7073.
- [253] Mecker LC & Martin RS (2008) Integration of microdialysis sampling and microchip electrophoresis with electrochemical detection. *Anal. Chem.* 80(23):9257-9264.
- [254] Nandi P, Desaias DP, & Lunte SM (2010) Development of a pdms-based microchip electrophoresis device for continuous online in vivo monitoring of microdialysis samples. *Electrophoresis* 31(8):1414-1422.

- [255] Kirby BJ & Hasselbrink EF (2004) Zeta potential of microfluidic substrates: 1. Theory, experimental techniques, and effects on separations. *Electrophoresis* 25(2):187-202.
- [256] Chang CC & Yang RJ (2007) Electrokinetic mixing in microfluidic systems. *Microfluid. Nanofluid.* 3(5):501-525.
- [257] Bousse L, *et al.* (2000) Electrokinetically controlled microfluidic analysis systems. *Annu. Rev. Biophys. Biomol. Struct.* 29:155-181.
- [258] Sherbet GV, Rao KV, & Lakshmi MS (1972) Characterization of ionogenic groups and estimation of net negative electric charge on surface of cells using natural pH gradients. *Exp. Cell Res.* 70(1):113-123.
- [259] Guy Y, Muha RJ, Sandberg M, & Weber SG (2009) Determination of zeta-potential and tortuosity in rat organotypic hippocampal cultures from electroosmotic velocity measurements under feedback control. *Anal. Chem.* 81(8):3001-3007.
- [260] Liu MC, *et al.* (2004) Determination of thiol compounds in rat striatum microdialysate by hplc with a nanosized cohf-modified electrode. *Anal. Bioanal. Chem.* 380(5-6):742-750.
- [261] Houze P, Gamra S, Madelaine I, Bousquet B, & Gourmel B (2001) Simultaneous determination of total plasma glutathione, homocysteine, cysteinylglycine, and methionine by high-performance liquid chromatography with electrochemical detection. *J. Clin. Lab. Anal.* 15(3):144-153.
- [262] Lochman P, Adam T, Friedecky D, Hlidkova E, & Skopkova Z (2003) High-throughput capillary electrophoretic method for determination of total aminothiols in plasma and urine. *Electrophoresis* 24(7-8):1200-1207.
- [263] Kusmerek K, Glowacki R, & Bald E (2006) Analysis of urine for cysteine, cysteinylglycine, and homocysteine by high-performance liquid chromatography. *Anal. Bioanal. Chem.* 385(5):855-860.
- [264] Guan XM, Hoffman B, Dwivedi C, & Matthees DP (2003) A simultaneous liquid chromatography/mass spectrometric assay of glutathione, cysteine, homocysteine and their disulfides in biological samples. *J. Pharm. Biomed. Anal.* 31(2):251-261.
- [265] Carlucci F & Tabucchi A (2009) Capillary electrophoresis in the evaluation of aminothiols in body fluids. *J. Chromatogr. B: Anal. Technol. Biomed. Life Sci.* 877(28):3347-3357.
- [266] Kessler A, *et al.* (2008) Antioxidant effect of cysteamine in brain cortex of young rats. *Neurochem. Res.* 33(5):737-744.
- [267] Ricci G, Nardini M., Chiaraluce R., Dupre S., Cavallini D. (1983) Detection and determination of cysteamine at the nanomole level. *J. Appl. Biochem.* 5(4-5):320-329.

- [268] Garcia RAG, Hirschberger LL, & Stipanuk MH (1988) Measurement of cyst(e)amine in physiological samples by high performance liquid chromatography. *Anal. Biochem.* 170(2):432-440.
- [269] Pitari G, *et al.* (2000) Pantetheinase activity of membrane-bound vanin-1: Lack of free cysteamine in tissues of vanin-1 deficient mice. *FEBS Lett.* 483(2-3):149-154.
- [270] Coloso RM, Hirschberger LL, Dominy JE, Lee JI, & Stipanuk MH (2006) Cysteamine dioxygenase: Evidence for the physiological conversion of cysteamine to hypotaurine in rat and mouse tissues. *Taurine 6*, Advances in experimental medicine and biology, eds Oja SS & Saransaari P (Springer-Verlag Berlin, Berlin), Vol 583, pp 25-36.
- [271] Pastore A, *et al.* (1998) Fully automated assay for total homocysteine, cysteine, cysteinylglycine, glutathione, cysteamine, and 2-mercaptopropionylglycine in plasma and urine. *Clin. Chem.* 44(4):825-832.
- [272] Stridh MH, *et al.* (2010) Enhanced glutathione efflux from astrocytes in culture by low extracellular Ca^{2+} and curcumin. *Neurochem. Res.* 35(8):1231-1238.
- [273] Gogolla N, Galimberti I, DePaola V, & Caroni P (2006) Preparation of organotypic hippocampal slice cultures for long-term live imaging. *Nat. Protoc.* 1(3):1165-1171.
- [274] Wu J, Ferrance JP, Landers JP, & Weber SG (2010) Integration of a precolumn fluorogenic reaction, separation, and detection of reduced glutathione. *Anal. Chem.* 82(17):7267-7273.
- [275] McClain MA, *et al.* (2003) Microfluidic devices for the high-throughput chemical analysis of cells. *Anal. Chem.* 75(21):5646-5655.
- [276] Xuan XC, Xu B, Sinton D, & Li DQ (2004) Electroosmotic flow with joule heating effects. *Lab Chip* 4(3):230-236.
- [277] Morin M, Rivard C, & Keillor JW (2006) Gamma-glutamyl transpeptidase acylation with peptidic substrates: Free energy relationships measured by an hplc kinetic assay. *Org. Biomol. Chem.* 4(20):3790-3801.
- [278] Smith JH & Humphrey JAC (2007) Interstitial transport and transvascular fluid exchange during infusion into brain and tumor tissue. (Translated from English) *Microvasc Res* 73(1):58-73 (in English).
- [279] Lide DR (1997) *Crc handbook of chemistry and physics* (CRC Press, Boca Raton, New York) 78th Ed, pp 8(45)-8(55).
- [280] Sharpless NE & Flavin M (1966) The reactions of amines and amino acids with maleimides. Structure of the reaction products deduced from infrared and nuclear magnetic resonance spectroscopy. *Biochemistry* 5(9):2963-2971.

- [281] Nolkrantz K, *et al.* (2001) Electroporation of single cells and tissues with an electrolyte-filled capillary. *Anal. Chem.* 73(18):4469-4477.
- [282] Bousquet M, *et al.* (2010) Cystamine metabolism and brain transport properties: Clinical implications for neurodegenerative diseases. *J. Neurochem.* 114(6):1651-1658.
- [283] Pillai A, Veeranan-Karmegam R, Dhandapani KM, & Mahadik SP (2008) Cystamine prevents haloperidol-induced decrease of bdnf/trkb signaling in mouse frontal cortex. *J. Neurochem.* 107(4):941-951.
- [284] Jézégou A, *et al.* (2012) Heptahelical protein pqlc2 is a lysosomal cationic amino acid exporter underlying the action of cysteamine in cystinosis therapy. *Proc. Natl. Acad. Sci. USA* 109(50):E3434–E3443.
- [285] Butler JD & Zatz M (1984) Pantethine and cystamine deplete cystine from cystinotic fibroblasts via efflux of cysteamine-cysteine mixed disulfide. *J. Clin. Invest.* 74(2):411-416.
- [286] Horvath Z & Vecsei L (2009) Current medical aspects of pantethine-treatment strategies. *Ideggyogy Sz. (Clin. Neurosci.)* 62(7-8):220-229.
- [287] Kuna P, *et al.* (2004) Acute toxicity and radioprotective effects of amifostine (wr-2721) or cystamine in single whole body fission neutrons irradiated rats. *J. Appl. Biomed.* 2(1):43-49.
- [288] Jeitner TM, Delikatny EJ, Bartier WA, Capper HR, & Hunt NH (1998) Inhibition of drug-naive and -resistant leukemia cell proliferation by low molecular weight thiols. *Biochem. Pharmacol.* 55(6):793-802.
- [289] Wood PL, Khan MA, & Moskal JR (2007) Cellular thiol pools are responsible for sequestration of cytotoxic reactive aldehydes: Central role of free cysteine and cysteamine. *Brain Res.* 1158:158-163.
- [290] Reibel DK, Wyse BW, Berkich DA, & Neely JR (1982) Coenzyme a metabolism in pantothenic acid-deficient rats. *J. Nutr.* 112(6):1144-1150.
- [291] Deutsch J, Rapoport S, & Rosenberger T (2002) Coenzyme a and short-chain acyl-coa species in control and ischemic rat brain. *Neurochem. Res.* 27(12):1577-1582.
- [292] Leonardi R, Rock CO, Jackowski S, & Zhang Y-M (2007) Activation of human mitochondrial pantothenate kinase 2 by palmitoylcarnitine. *Proc. Natl. Acad. Sci. USA* 104(5):1494-1499.
- [293] Goding JW, Grobden B, & Slegers H (2003) Physiological and pathophysiological functions of the ecto-nucleotide pyrophosphatase/phosphodiesterase family. *Biochimica et Biophysica Acta (BBA) - Molecular Basis of Disease* 1638(1):1-19.

- [294] Strauss E (2010) Coenzyme a biosynthesis and enzymology. *Comprehensive natural products ii: Chemistry and biology*, eds Mander L & Liu H-W (Elsevier Ltd., Oxford), 1st Ed Vol 7.11, pp 351-410.
- [295] Cartwright JL, Gasmi L, Spiller DG, & McLennan AG (2000) The *saccharomyces cerevisiae* *pcd1* gene encodes a peroxisomal nudix hydrolase active toward coenzyme a and its derivatives. *J. Biol. Chem.* 275(42):32925-32930.
- [296] Freeman MF, Moshos KA, Bodner MJ, Li R, & Townsend CA (2008) Four enzymes define the incorporation of coenzyme a in thienamycin biosynthesis. *Proc. Natl. Acad. Sci. USA* 105(32):11128-11133.
- [297] Wu J, Xu K, Landers JP, & Weber SG (2013) An in situ measurement of extracellular cysteamine, homocysteine, and cysteine concentrations in organotypic hippocampal slice cultures by integration of electroosmotic sampling and microfluidic analysis. *Anal. Chem.* 85(6):3095-3103.
- [298] Schoffelen S & van Hest JCM (2012) Multi-enzyme systems: Bringing enzymes together in vitro. *Soft Matter* 8(6):1736-1746.
- [299] Tetko IV, *et al.* (2005) Virtual computational chemistry laboratory - design and description. *J. Comput. Aided Mol. Des.* 19(6):453-463.
- [300] Pitari G, Maurizi G, Ascenzi P, Ricci G, & Dupre S (1994) A kinetic-study on pantetheinase inhibition by disulfides. *Eur. J. Biochem.* 226(1):81-86.
- [301] Wittwer C, Wyse B, & Hansen RG (1982) Assay of the enzymatic-hydrolysis of pantetheine. *Anal. Biochem.* 122(2):213-222.
- [302] Dupre S, *et al.* (1984) Continuous spectrophotometric assay of pantetheinase activity. *Anal. Biochem.* 142(1):175-181.
- [303] Ruan BH, *et al.* (2010) A fluorescent assay suitable for inhibitor screening and vanin tissue quantification. *Anal. Biochem.* 399(2):284-292.
- [304] Jeitner TM & Lawrence DA (2001) Mechanisms for the cytotoxicity of cysteamine. *Toxicol. Sci.* 63(1):57-64.
- [305] Wittwer CT, Gahl WA, Butler JD, Zatz M, & Thoene JG (1985) Metabolism of pantethine in cystinosis. *J. Clin. Invest.* 76(4):1665-1672.
- [306] Penet MF, *et al.* (2008) Protection against cerebral malaria by the low-molecular-weight thiol pantethine. *Proc. Natl. Acad. Sci. USA* 105(4):1321-1326.
- [307] Balibar CJ, Hollis-Symynkywicz MF, & Tao JS (2011) Pantethine rescues phosphopantothienoylcysteine synthetase and phosphopantothienoylcysteine decarboxylase deficiency in *escherichia coli* but not in *pseudomonas aeruginosa*. *J. Bacteriol.* 193(13):3304-3312.

- [308] Domschke W, Liersch N, & Decker K (1971) Lack of permeation of coenzyme a from blood into liver cells. *Hoppe-Seyler's Z. Physiol. Chem.* 253:85-88.
- [309] Kropf M, *et al.* (2008) Subunit-specific surface mobility of differentially labeled ampa receptor subunits. *Eur. J. Cell Biol.* 87(10):763-778.
- [310] Reddy A, Caler EV, & Andrews NW (2001) Plasma membrane repair is mediated by ca²⁺-regulated exocytosis of lysosomes. *Cell* 106(2):157-169.
- [311] Zhang ZJ, *et al.* (2007) Regulated atp release from astrocytes through lysosome exocytosis. *Nat. Cell Biol.* 9(8):945-U115.
- [312] Skrede S (1973) The degradation of coa: Subcellular localization and kinetic properties of coa-and dephospho-coa pyrophosphatase. *Eur. J. Biochem.* 38(3):401-407.
- [313] Sykova E & Nicholson C (2008) Diffusion in brain extracellular space. *Physiol. Rev.* 88(4):1277-1340.
- [314] Herr AE, *et al.* (2000) Electroosmotic capillary flow with nonuniform zeta potential. *Anal. Chem.* 72(5):1053-1057.
- [315] Ghosal S (2002) Band broadening in a microcapillary with a stepwise change in the ζ -potential. *Anal. Chem.* 74(16):4198-4203.